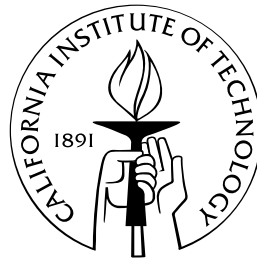


Simulations and Analysis of Two- and Three-Dimensional Single-Mode Richtmyer-Meshkov Instability using Weighted Essentially Non-Oscillatory and Vortex Methods

Thesis by
Marco Latini

In Partial Fulfillment of the Requirements
for the Degree of
Doctor of Philosophy



California Institute of Technology
Pasadena, California

2007
(Defended September 22, 2006)

To my parents Giovanni and Carole Latini

Acknowledgements

This thesis would not be here without the support, guidance, and encouragement of my advisers Dr. Daniel Meiron and Dr. Oleg Schilling.

I will always be grateful to my adviser Dr. Daniel Meiron for the incredible opportunities afforded during these five years at Caltech, both in terms of the research opportunities, including the terrific problem that I worked on and the guidance provided as we resolved many scientific questions, but also in terms of the interactions that have taught me the importance of scientific judgment and also have served as a model of temperament and leadership.

I will always remember the care, support, patience, and dedication that Dr. Oleg Schilling has shown me, including the constant exhortations to extract greater understanding from my work and always do my best. I also thank Dr. Schilling for welcoming me in the turbulence group at the Lawrence Livermore National Laboratory (LLNL) and for providing me with a great sense of purpose and impact for this research.

I wish to thank my colleagues in the Compressible Turbulence Group in the Accelerated Strategic Computing (ASC) Center at Caltech. The Tuesday lunches and discussions are part of the most vivid and important learning experiences in my graduate career, allowing me to be part of an integrated, large-scale scientific effort of unparalleled quality and impact.

A special thanks also to the members of my thesis committee, Dr. Pullin, Dr. Hou, and Dr. Pierce, whose comments and suggestions have greatly improved this work.

I would also like to thank my parents, Giovanni and Carole Latini, for their unconditional support during all my life. I would not be here, if it were not for their help and knowing that no matter what they would always be there for me.

Finally, I need to thank all of my friends who shared with me some of the happiest moments in my graduate career and also provided relief from the intensity of research.

During my first three years, I was supported by the Air Force Office of Scientific Research (AFOSR) through the National Defense Science and Engineering Graduate (NDSEG) Fellowship. This work was also supported by the Academic Strategic Alliance Program (ASAP) of the ASC Center under subcontract B3441492 of DOE contract W-7405-ENG-48. Summer visits to the LLNL were hosted by the Institute for Scientific Computing and Research (ISCR).

Abstract

An incompressible vorticity-streamfunction (VS) method is developed to investigate the single-mode Richtmyer-Meshkov instability in two and three dimensions. The initial vortex sheet (representing the initial shocked interface) is thickened to regularize the limit of classical Lagrangian vortex methods. In the limit of smaller thickness, the initial velocity converges to the velocity of a vortex sheet. The vorticity on the Cartesian grid follows the vorticity evolution equation augmented by the baroclinic vorticity production term (to capture the effects of the instability on the layer) and a viscous dissipation term. The equations are discretized using a fourth-order in space and third-order in time semi-implicit Adams-Bashforth backward differentiation scheme. The convergence properties of the method with respect to varying the diffuse interface thickness and viscosity are investigated. It is shown that the small-scale structures within the roll-up are more sensitive to the diffuse interface thickness than to the viscosity. By contrast, the large-scale quantities, including the perturbation, bubble, and spike amplitudes are less sensitive. Fourth-order point-wise convergence is achieved, provided that a sufficiently fine grid is used.

In two dimensions, the VS method is applied to investigate late-time nonlinear effects of the single-mode Mach 1.3 air(acetone)/SF₆ shock tube experiment of Jacobs and Krivets [62]. The results are also compared to those from compressible ninth-order weighted essentially non-oscillatory (WENO) simulations. The density fields from the WENO and VS methods agree with the experimental PLIF images in the large-scale structures but differ in the small-scale structures. The WENO method exhibits small-scale disordered structure similar to that in the experiment, while the VS method does not capture such structure, but shows a strong rotating core. The perturbation amplitudes from the two methods are in good agreement and match the experimental data points well. The WENO bubble amplitude is smaller than the VS amplitude and vice versa for the spike amplitude. Comparing amplitudes from simulations with varying Mach number shows that as the Mach number increases, the differences in the bubble and spike amplitudes increase due to intensifying pressure perturbations not present in the incompressible VS method. The perturbation amplitude from the WENO and VS methods is also compared to the predictions of nonlinear amplitude growth models in which the growth rate was reduced to account for the diffuse initial interface. In general, the model predictions agree with the simulation amplitudes at early-to-intermediate times and

underpredict at later times, corresponding to the late nonlinear regime.

The WENO simulation is used to investigate reshock, which occurs when the transmitted shock reflects from the end wall of the test section and interacts with the evolving layer. The post-reshock mixing layer width agrees well with the predictions of reshock models for short times until the interaction of the reflected rarefaction with the layer.

The VS simulation was also compared to classical Lagrangian and vortex-in-cell simulations as the Atwood number was varied. For low Atwood numbers, all three simulations agree. As the Atwood number increases, the VS simulation shows differences in the bubble and spike amplitudes compared to the Lagrangian and VIC simulations, as the baroclinic vorticity production for a diffuse layer is different from that of a thin layer. The simulation amplitudes agree with the predictions of nonlinear amplitude growth models at early times. The growth models underpredict the amplitudes at later times.

The investigation is extended to three dimensions, where the initial perturbation is a product of sinusoids and the initial vorticity deposition is given by linear instability analysis. The instability evolution and dynamics of vorticity are visualized using the mass fraction and enstrophy isosurface, respectively. For the WENO and VS methods, two roll-ups corresponding to the bubble and spike regions form, and the vorticity shows the formation of a ring-like structure. The perturbation amplitudes from the WENO and VS methods are in excellent agreement. The bubble and spike amplitude are in good agreement at early times. At later times, the WENO bubble amplitude is smaller than the VS amplitude and vice versa for the spike. The nonlinear three-dimensional Zhang-Sohn model [157] agrees with the simulation amplitudes at early times, and underpredicts later. In three dimensions, the enstrophy iso-surface after reshock shows significant fragmentation and the formation of small, short, tubular structures. Simulations with different initial amplitudes show that the mixing layer width after reshock does not depend on the pre-shock amplitude. Finally, the effects of Atwood number are investigated using the VS method and the amplitudes are compared to the predictions of the Zhang-Sohn model. The simulation and the models are in agreement at early times, while the models underpredict later.

The VS method constitutes a useful numerical approach to investigate the Richtmyer-Meshkov instability in two and three dimensions. The VS method and, more generally, vortex methods are valid tools for predicting the large-scale instability features, including the perturbation amplitudes, into the late nonlinear regime.

Contents

Acknowledgements	iv
Abstract	v
Contents	vii
Figures	xi
Tables	xxi
Symbols	xxv
1 Introduction	1
1.1 Overview of the Richtmyer-Meshkov instability	1
1.1.1 Linear instability analysis	1
1.1.2 Single-mode instability dynamics	4
1.2 Goals of this thesis	8
1.2.1 Development of the vorticity-streamfunction method	9
1.2.2 Investigation of the two-dimensional single-mode instability	10
1.2.3 Investigation of the three-dimensional single-mode instability	11
1.3 Organization of thesis	12
2 Development and Numerical Implementation of the Vorticity-Streamfunction Method	13
2.1 Overview of vortex methods	14
2.1.1 Literature survey on vortex methods applied to the Rayleigh-Taylor and Richtmyer-Meshkov instabilities	15
2.1.2 The classical Lagrangian vortex method	18
2.1.3 The hybrid Lagrangian-Eulerian vortex method based on the vortex-in-cell algorithm	19
2.2 Convergence study for the vortex-in-cell algorithm	21

2.2.1	Convergence study for a thin vortex sheet	22
2.2.2	Convergence study for a thick vortex layer	24
2.2.3	Vortex-sheet evolution by the vortex-in-cell and Lagrangian vortex methods	29
2.3	The vorticity-streamfunction method	29
2.3.1	Motivation for developing the method	31
2.3.2	Governing equations	31
2.3.3	Spatial and temporal discretization	33
3	Investigation of Convergence of the Vorticity-Streamfunction Method	36
3.1	Spatial and temporal convergence for fixed vortex-layer thickness	36
3.1.1	Results for zero viscosity and mass diffusivity	37
3.1.2	Results with nonzero viscosity and mass diffusivity for zero Atwood number	44
3.1.3	Results with nonzero viscosity and mass diffusivity for nonzero Atwood number	49
3.2	Convergence study using different diffuse interface thicknesses and viscosities	56
3.2.1	Dynamics of the instability evolution	57
3.2.2	Convergence study as the diffuse interface thickness is reduced	64
3.2.3	Effects of viscosity and diffuse-interface thickness on the perturbation, bubble, and spike amplitudes, circulation, and Reynolds numbers	69
4	Investigation of the Two-Dimensional Single-Mode Richtmyer-Meshkov Instability	76
4.1	The weighted essentially non-oscillatory (WENO) method	77
4.1.1	Literature survey	77
4.1.2	Overview of the WENO method	79
4.2	Initial and boundary conditions	81
4.2.1	Late-time Mach 1.3 air(acetone)/SF ₆ Richtmyer-Meshkov instability experiment of Jacobs and Krivets	81
4.2.2	Mix and upstream initial conditions for the WENO method	82
4.2.3	Baroclinic circulation deposition on the interface and comparison to the predictions of models	87
4.2.4	Initial conditions for the vorticity-streamfunction, Lagrangian, and vortex-in-cell methods	89
4.3	Comparison of fifth- and ninth-order WENO simulations for different grid resolutions	91
4.3.1	Comparison of the instability evolution and fields	91
4.3.2	Comparison of the perturbation, bubble, and spike amplitudes, circulation, and Reynolds number	95
4.4	Dynamics of the instability evolution	98

4.4.1	Comparison of density fields to experimental PLIF images	100
4.4.2	Visualization of the vorticity and baroclinic vorticity production fields	100
4.5	Comparison of the perturbation, bubble, and spike amplitudes with experimental data and to the predictions of amplitude growth models	106
4.5.1	Literature survey on Richtmyer-Meshkov instability growth models	106
4.5.1.1	Impulsive and linear models	106
4.5.1.2	Perturbation and empirical models	107
4.5.1.3	Potential models	108
4.5.2	Comparison of amplitudes to experimental data and to the predictions of amplitude growth models	109
4.5.3	Comparison of the mix and upstream initial conditions for the WENO method	116
4.6	Comparison of WENO and vorticity-streamfunction simulations for different Mach numbers	120
4.7	Investigation of reshock using the WENO method	123
4.7.1	Dynamics of the reshock process	123
4.7.2	Comparison of the mixing layer amplitude to the predictions of reshock models	127
4.8	Atwood number study using the vorticity-streamfunction method and comparison to the Lagrangian and vortex-in-cell methods	129
4.8.1	Comparison of instability evolution from the Lagrangian, vortex-in-cell, and vorticity-streamfunction methods	129
4.8.2	Comparison of the perturbation, bubble, and spike amplitudes to the predictions of amplitude growth models	143
5	Investigation of the Three-Dimensional Single-Mode Richtmyer-Meshkov Instability	157
5.1	Initial and boundary conditions	157
5.1.1	Initial conditions for the WENO method	158
5.1.2	Baroclinic circulation deposition on the interface and comparison to linear theory	160
5.1.3	Initial conditions for the vorticity-streamfunction method	164
5.2	Dynamics of the instability evolution	165
5.3	Comparison of the perturbation, bubble, and spike amplitudes to the predictions of an amplitude growth model	169
5.4	Investigation of reshock using the WENO method	173
5.4.1	Dynamics of the reshock process	174
5.4.2	Comparison of the mixing layer amplitude to the predictions of reshock models	180
5.5	Atwood number study using the vorticity-streamfunction method	182

5.5.1	Comparison of instability evolution and vorticity dynamics	182
5.5.2	Comparison of the perturbation, bubble, and spike amplitudes to the predic- tions of amplitude growth models	189
6	Conclusions	194
6.1	Development and numerical implementation of the vorticity-streamfunction method	194
6.2	Investigation of convergence of the vorticity-streamfunction method	196
6.3	Investigation of the two-dimensional single-mode Richtmyer-Meshkov instability . . .	197
6.4	Investigation of the three-dimensional single-mode Richtmyer-Meshkov instability . .	199
6.5	Implications	200
	Bibliography	202

Figures

1.1	Sinusoidal interface for the linear instability problem in two dimensions.	2
1.2	The shock tube test section and computational domain for the two-dimensional simulations of the Richtmyer-Meshkov instability	4
1.3	Time-evolution of the density $\rho(x, y)$, vorticity $\omega(x, y)$, and simulated density Schlieren $\phi(x, y)$ fields illustrating the development of the single-mode Richtmyer-Meshkov instability before reshock at 0.06, 1.76, 3.06, and 5.26 ms (top panel) and after reshock at 5.6, 5.7, 5.9, and 6.5 ms (bottom panel).	6
1.4	The shock tube test section and computational domain for the three-dimensional simulations of the Richtmyer-Meshkov instability	7
2.1	Vorticity field on the Cartesian grid using the $M_4(x)$ interpolant for a thin vortex sheet as the grid is refined with $N_x = 64, 128,$ and 256	23
2.2	Comparison of the horizontal velocity $u(e)$ and velocity gradient $\partial u/\partial e$ on the interface for the VIC algorithm applied to the thin vortex sheet using the M_4 interpolant. Also shown is the ℓ^∞ -error for the horizontal velocity and velocity gradient	23
2.3	Vorticity field on the Cartesian grid using the $M_4(x)$ interpolant for a thick vortex layer with $\delta_T = 0.15$, as the grid is refined with $N_x = 64, 128,$ and 256	24
2.4	Comparison of the horizontal velocity $u(e)$ and velocity gradient $\partial u/\partial e$ on the interface for the VIC algorithm applied to the thick vortex sheet using the M_4 interpolant and with fixed $\delta_T = 0.15$. Also shown is the ℓ^∞ -error for the horizontal velocity and velocity gradient	25
2.5	Vorticity field on the Cartesian grid using the $M_4(x)$ interpolant for a thick vortex layer as the thickness is decreased keeping $\delta_T/\Delta x$ fixed for $N_x = 64, 128,$ and 256	26
2.6	Comparison of the horizontal velocity $u(e)$ and velocity gradient $\partial u/\partial e$ on the interface for the VIC algorithm applied to the thick vortex sheet using the M_4 interpolant and with fixed $\delta_T/\Delta x$. Also shown is the ℓ^∞ -error for the horizontal velocity and velocity gradient	26
2.7	The ℓ^∞ -error for the horizontal velocity and velocity gradient with fixed $\delta_T/\Delta x$ and Richardson extrapolation	27

2.8	Time-evolution of the interface for the Richtmyer-Meshkov instability with $A = 0$ using the Lagrangian- γ formulation with $N = 256$ and 512 vortex markers and the vortex-in-cell iterative-time-step (VIC-ITS) formulation at 0, 1, 2, 3, 4, and 5 ms with a grid resolution of $N_x \times N_y = 32 \times 128$ with $N = 256$ vortex markers and $N_x \times N_y = 64 \times 256$ with $N = 512$ vortex markers when the $M_4(x)$ interpolant is used.	28
2.9	Same as Figure 2.8 but with $A = 0.4$	30
3.1	Time-evolution of the mass fraction field $m(x, y)$ for the Richtmyer-Meshkov instability with $A = 0$ and initial diffuse layer thickness $\delta_T = 0.4$ cm at 0, 1, 3, 5, 7, and 9 ms. The results are obtained using the VS method with grid resolutions $N_x = 64, 128, 256,$ and 512.	38
3.2	Time-evolution of the mass fraction contour corresponding to $m_1 = 1/2$ for the Richtmyer-Meshkov instability with $A = 0$ and initial diffuse-interface thickness $\delta_T = 0.4$ cm at 0, 1, 3, 5, 7, and 9 ms. The results are obtained using the VS method with grid resolutions $N_x = 64, 128, 256,$ and 512.	40
3.3	Time-evolution of the vorticity field $\omega(x, y)$ for the Richtmyer-Meshkov instability with $A = 0$ and initial thickness $\delta_T = 0.4$ cm at 0, 1, 3, 5, 7, and 9 ms. The results are obtained using the VS method with grid resolutions $N_x = 64, 128, 256,$ and 512.	41
3.4	Temporal and spatial convergence for the vorticity ω and density ρ fields when $\nu = \mathcal{D} = 0$ for $A = 0$. For temporal convergence, $\Delta t_f = 0.005$ ms at 0.8 ms when $\Delta t = 0.16, 0.08, 0.04, 0.02,$ and 0.01 ms. The dashed green line represents Δt^3 , indicating third-order convergence in time. For spatial convergence, $N_{xf} = 512$ at 1, 3, 5, and 7 ms when $N_x = 32, 64, 128,$ and 256. The red line represents N_x^{-2} , indicating second-order convergence, and the blue line represents N_x^{-4} , indicating fourth-order convergence.	42
3.5	Comparison of the perturbation amplitude $a(t)$ and circulation $\Gamma^+(t)$ as the grid is refined for $A = 0$ using the VS method with $\nu = 0$ and $\delta_T = 0.4$ cm for $N_x = 32, 64, 128, 256,$ and 512 (left column). Also shown is the rms-norm of the difference between results obtained on the $N_{xf} \times N_{yf} = 512 \times 1024$ grid and results on coarser grids. See Figure 3.4 for the legend.	43
3.6	Time-evolution of the mass fraction field $m(x, y)$ for the Richtmyer-Meshkov instability with $A = 0$, initial diffuse-interface thickness $\delta_T = 0.4$ cm, and $\nu = \mathcal{D} = 3 \times 10^{-3}$ cm ² /ms at 0, 1, 3, 5, 7, and 9 ms. The results are obtained using the VS method with grid resolutions $N_x = 64, 128, 256,$ and 512.	45

3.7 Time-evolution of the mass fraction contour corresponding to $m_1 = 1/2$ for the Richtmyer-Meshkov instability with $A = 0$, initial diffuse-interface thickness $\delta_T = 0.4$ cm, and $\nu = \mathcal{D} = 3 \times 10^{-3}$ cm²/ms at 0, 1, 3, 5, 7, and 9 ms. The results are obtained using the VS method with grid resolutions $N_x = 64, 128, 256,$ and 512 46

3.8 Time-evolution of the vorticity field $\omega(x, y)$ for the Richtmyer-Meshkov instability with $A = 0$, initial thickness $\delta_T = 0.4$ cm, and $\nu = \mathcal{D} = 3 \times 10^{-3}$ cm²/ms at 0, 1, 3, 5, 7, and 9 ms. The results are obtained using the VS method with grid resolutions $N_x = 64, 128, 256,$ and 512 47

3.9 Temporal and spatial convergence for the vorticity ω and density ρ fields with $\nu = \mathcal{D} = 3 \times 10^{-4}$ cm²/ms when $A = 0$. For temporal convergence, $\Delta t_f = 0.005$ ms at 0.8 ms when $\Delta t = 0.16, 0.08, 0.04, 0.02,$ and 0.01 ms. For spatial convergence, $N_{xf} = 512$ at 1, 3, 5, and 7 ms when $N_x = 32, 64, 128,$ and 256 . See Figure 3.4 for the legend. 48

3.10 Comparison of the perturbation amplitude $a(t)$ and circulation $\Gamma^+(t)$ as the grid is refined for $A = 0$ using the VS method with $\nu = \mathcal{D} = 3 \times 10^{-3}$ cm²/ms and $\delta_T = 0.4$ cm for $N_x = 32, 64, 128, 256,$ and 512 (left column). Also shown is the rms-norm of the difference between results obtained on the $N_{xf} \times N_{yf} = 512 \times 1024$ grid and results on coarser grids. See Figure 3.4 for the legend. 49

3.11 Time-evolution of the density field $\rho(x, y)$ for the Richtmyer-Meshkov instability with $A = 0.4$, initial diffuse-interface thickness $\delta_T = 0.4$ cm, and $\nu = \mathcal{D} = 3 \times 10^{-3}$ cm²/ms at 0, 1, 3, 5, 7, and 9 ms. The results are obtained using the VS method with grid resolutions $N_x = 64, 128, 256,$ and 512 50

3.12 Time-evolution of the mass fraction contour $m_1 = 1/2$ for the Richtmyer-Meshkov instability with $A = 0.4$, initial thickness $\delta_T = 0.4$ ms, and $\nu = \mathcal{D} = 3 \times 10^{-3}$ cm²/ms at 0, 1, 3, 5, 7, and 9 ms. The results are obtained using the VS method with grid resolutions $N_x = 64, 128, 256,$ and 512 52

3.13 Time-evolution of the vorticity field $\omega(x, y)$ for the Richtmyer-Meshkov instability with $A = 0.4$, initial diffuse-interface thickness $\delta_T = 0.4$ cm, and $\nu = \mathcal{D} = 3 \times 10^{-3}$ cm²/ms at 0, 1, 3, 5, 7, and 9 ms. The results are obtained using the VS method with grid resolutions $N_x = 64, 128, 256,$ and 512 53

3.14 Temporal and spatial convergence for the vorticity ω and density ρ fields with $\nu = \mathcal{D} = 3 \times 10^{-3}$ cm²/ms for $A = 0.4$. For temporal convergence, $\Delta t_f = 0.005$ ms with $\Delta t = 0.16, 0.08, 0.04, 0.02,$ and 0.01 ms. For spatial convergence, $N_{xf} = 512$ at 1, 3, 5, and 7 ms when $N_x = 32, 64, 128$ and 256 . See Figure 3.4 for the legend. 54

3.15	Comparison of the perturbation, bubble, and spike amplitudes $a(t)$, $a_b(t)$, and $a_s(t)$, respectively, as the grid is refined for $A = 0.4$ using the VS method with $\nu = 3 \times 10^{-3}$ cm^2/ms and $\delta_T = 0.4$ cm for $N_x = 32, 64, 128, 256,$ and 512 (left column). Also shown is the rms-norm of the difference between results obtained on the $N_{xf} \times N_{yf} = 512 \times 1024$ grid and results on coarser grids. See Figure 3.4 for the legend.	55
3.16	Comparison of the circulation $\Gamma^+(t)$ as the grid is refined for $A = 0.4$ using the VS method with $\nu = 3 \times 10^{-3}$ cm^2/ms and $\delta_T = 0.4$ cm for $N_x = 32, 64, 128, 256,$ and 512 (left column). Also shown is the rms-norm of the difference between results obtained on the $N_{xf} \times N_{yf} = 512 \times 1024$ grid and results on coarser grids. See Figure 3.4 for the legend.	56
3.17	The density field $\rho(x, y)$ at 3 ms for different values of the diffuse-interface thickness δ_T and viscosity ν . The results were obtained with grid resolution 512×1024 using the VS method.	58
3.18	The mass fraction contour at 3 ms for different values of the diffuse-interface thickness δ_T and viscosity ν using the VS method.	59
3.19	The vorticity field $\omega(x, y)$ at 3 ms for different values of the diffuse-interface thickness δ_T and viscosity ν using the VS method.	60
3.20	Same as Figure 3.17 but at 5 ms.	61
3.21	Same as Figure 3.18 but at 5 ms.	62
3.22	Same as Figure 3.19 but at 5 ms.	63
3.23	Same as Figure 3.17 but at 7 ms.	65
3.24	Same as Figure 3.18 but at 7 ms.	66
3.25	Same as Figure 3.19 but at 7 ms.	67
3.26	Time-evolution of the spatial convergence rate for the vorticity ω and density ρ when $\nu = 10^{-4}$ cm^2/ms as the grid is refined for $\delta_T = 0.4, 0.3,$ and 0.2 cm at 1, 3, 5, and 7 ms. For the fine-grid simulation $N_{xf} \times N_{yf} = 1024 \times 2048$ when $N_x = 32, 64, 128, 256, 512$. The dashed red line represents N_x^{-2} , the green line N_x^{-3} , and the blue line N_x^{-4} , indicating, second-, third-, and fourth-order convergence.	68
3.27	Comparison of the perturbation amplitude $a(t)$ when the viscosity ν and diffuse-interface interface thickness δ_T are varied (top). Comparison when ν is changed keeping $\delta_T = 0.3$ cm fixed (middle). Comparison when δ_T is changed keeping $\nu = 2 \times 10^{-4}$ cm^2/ms fixed (bottom). Quantities obtained using $\delta_T = 0.4, 0.3,$ and 0.2 cm are shown in blue, red, and green, respectively; quantities obtained using $\nu = 8 \times 10^{-4}, 4 \times 10^{-4}, 2 \times 10^{-4},$ and 10^{-4} (cm^2/ms) are shown using a solid, dashed, dash-dot, and dotted lines respectively.	70

3.28	Comparison of the bubble and spike amplitudes $a_b(t)$ and $a_s(t)$ when the viscosity ν and diffuse-interface interface thickness δ_T are varied (top). Comparison when ν is changed keeping $\delta_T = 0.3$ cm fixed (middle). Comparison when δ_T is changed keeping $\nu = 2 \times 10^{-4}$ cm ² /ms fixed (bottom). See Figure 3.27 for legend.	71
3.29	Comparison of the circulation $\Gamma(t)$ and Reynolds number $Re_\Gamma(t)$ when the viscosity ν and diffuse-interface interface thickness δ_T are varied (top). Comparison when ν is changed keeping $\delta_T = 0.3$ cm fixed (middle). Comparison when δ_T is changed keeping $\nu = 2 \times 10^{-4}$ cm ² /ms fixed (bottom). See Figure 3.27 for legend.	72
3.30	Comparison of the Reynolds numbers $Re_h(t)$ and $Re_{\Delta x}(t)$ when the viscosity ν and diffuse-interface interface thickness δ_T are varied (top). Comparison when ν is changed keeping $\delta_T = 0.3$ cm fixed (middle). Comparison when δ_T is changed keeping $\nu = 2 \times 10^{-4}$ cm ² /ms fixed (bottom). See Figure 3.27 for legend.	74
4.1	The initial deposition of circulation on the interface $\langle \omega \rangle(y, 0^+)$ from the incident shock at time $t = 0^+$ from the WENO simulation (solid black line), together with the predictions of the Samtaney-Zabusky model (dashed line) and linear instability theory (solid blue line) (left). The initial baroclinic vorticity production $\langle \mathcal{P} \rangle(y, 0^+)$ is also shown (right).	88
4.2	Comparison of the initial circulation deposition $\langle \omega \rangle(y, 0^+)$ and baroclinic production $\langle \mathcal{P} \rangle(y, 0^+)$ from the fifth- and ninth-order WENO simulations at different grid resolutions. See Table 4.6 for the legend.	92
4.3	Comparison of the density fields and mass fraction contours at 5.26 ms from the fifth- and ninth-order WENO simulations using different grid resolutions.	93
4.4	Comparison of the vorticity $\omega(x, y)$ and baroclinic vorticity production $\mathcal{P}(x, y)$ fields at 5.26 ms from the fifth- and ninth-order WENO simulations using different grid resolutions.	94
4.5	Comparison of the mass fraction contours as the order and resolution are varied. See Table 4.6 for the legend.	95
4.6	The x - t diagram showing the position of the interface $\ell_{\text{int}}(t)$ (solid line), shock (dotted line), and bubble and spike locations $\ell_b(t)$ and $\ell_s(t)$ (dash-dot and dashed lines, respectively). The horizontal distance between the spike and the bubble location is the perturbation width $h(t)$	96

4.7	Comparison of the time-evolution of the perturbation, bubble, and spike amplitudes $a(t)$, $a_b(t)$, and $a_s(t)$, respectively, as the grid is refined and the order of flux reconstruction is varied (left). Also shown is the rms-norm of the difference between results obtained on the $N_x = 768$ grid and results obtained on coarser grids for the WENO5 (red) and WENO9 (blue) simulations. The dashed black line indicates N_x^{-1} , the dashed red line N_x^{-2} , and the dashed green line N_x^{-3} . See Table 4.6 for the legend.	97
4.8	Comparison of the time-evolution of the positive circulation $\Gamma^+(t)$ before reshock as the grid is refined and the order of reconstruction is varied (left). Also shown is the rms-norm of the difference between results obtained on the $N_x = 768$ grid and those on coarser grids for the WENO5 (red) and WENO9 (blue) simulations. See Table 4.6 for the legend.	98
4.9	Comparison of the numerical Reynolds numbers $Re_{\Delta x}(t)$ for the fifth- and ninth-order simulations at different resolutions. See Table 4.6 for the legend.	99
4.10	Comparison of the corrected PLIF images from the Jacobs and Krivets experiment with the density fields $\rho(x, y)$ from the ninth- and fifth-order WENO simulations at a resolution of 512 points per wavelength and the density field $\rho(x, y)$ from the VS simulation at 1.16, 3.06, and 5.26 ms. The experimental images are taken from Figure 5 of Jacobs and Krivets [62] (reprinted with permission of the American Institute of Physics).	101
4.11	Comparison of the mass fraction contour from the ninth- and fifth-order WENO simulations and the VS simulation at 0.06, 1.16, 3.06, and 5.26 ms.	102
4.12	Comparison of the vorticity fields $\omega(x, y)$ and the baroclinic vorticity production fields $\mathcal{P}(x, y)$ from the ninth- and fifth-order WENO simulation and the VS simulation at 0.06, 1.16, 3.06, and 5.26 ms.	103
4.13	Comparison of the vortex sheet strength $\gamma(e, t)$ on the mass fraction contour from the fifth- and ninth-order WENO and VS simulations at 0.06, 1.16, 3.06, and 5.26 ms. . .	104
4.14	Comparison of the interface position $z(e)$, vortex-sheet strength $\gamma(e)$, and horizontal and vertical components of the velocity, $u(e)$ and $v(e)$, respectively, from the ninth-order WENO (red) and VS (blue) simulations at 0.06, 1.16, 3.06, and 5.26 ms.	105
4.15	Comparison of the perturbation amplitude $a(t)$ from the WENO and VS methods with the experimental data points (top). Also shown is a comparison of the bubble and spike amplitudes $a_b(t)$ and $a_s(t)$, respectively, from the simulations (bottom).	110
4.16	The perturbation amplitude $a(t) - a_0^+$ versus time t from the WENO and VS methods and the experimental data points, together with the predictions of the linear and nonlinear models.	111

4.17	Comparison of the WENO and VS bubble and spike amplitudes $a_b(t)$ and $a_s(t)$ with the predictions of the Zhang-Sohn, Sadot et al., Matsuoka et al., and Mikaelian models.	113
4.18	Comparison of the WENO and VS bubble velocity $da_b(t)/dt$ with the predictions of the Zhang-Sohn, Sadot et al., Matsuoka et al., Mikaelian, Sohn-Layzer, Goncharov, and Sohn-Zufiria models.	114
4.19	Comparison of the circulation $\Gamma^+(t)$ and Reynolds number $Re_{\Delta x}(t)$ from the WENO (red) and VS (blue) simulations.	117
4.20	Comparison of the Reynolds number $Re_h(t)$ (solid black) and $Re_\Gamma(t)$ (dashed line) from the VS simulation.	118
4.21	The initial deposition of circulation on the interface $\langle\omega\rangle(y, 0^+)$ from the incident shock at time 0^+ from the WENO simulation using mix initial conditions (solid black line) and upstream initial conditions (solid gray line), together with the predictions of the Samtaney-Zabusky and linear instability models. The initial baroclinic vorticity production $\langle\mathcal{P}\rangle(y, 0^+)$ on the interface is also shown (right).	118
4.22	Comparison of the the $x-t$ diagram (left) and perturbation amplitude $a(t)$ (right) for the mix (black) and the upstream (gray) initial conditions.	119
4.23	Comparison of the perturbation, bubble, and spike amplitudes $a(t)$, $a_b(t)$, $a_s(t)$, and circulation $\Gamma^+(t)$ from the WENO (solid line) and VS (dashed line) simulations for $Ma = 1.05$ (blue), 1.15 (red), 1.31 (green), and 1.45 (light blue).	122
4.24	Time-evolution of the density and simulated density Schlieren fields from the WENO9-512 simulation illustrating the reshock process at 5.6, 5.7, 5.8, 5.9, 6, 6.2, 6.5, and 7 ms.	124
4.25	Time-evolution of the vorticity $\omega(x, y)$ and baroclinic vorticity production $\mathcal{P}(x, y)$ fields from the WENO9-512 simulation during reshock at 5.6, 5.7, 5.8, 5.9, 6, 6.2, 6.5, and 7 ms.	126
4.26	Time-evolution of the density $\rho(x, y)$, vorticity $\omega(x, y)$, and baroclinic vorticity production $\mathcal{P}(x, y)$ fields from the WENO9-512 simulation at 8 and 10 ms.	127
4.27	The mixing layer amplitude $a(t)$ versus time t from the WENO9-512 simulation together with the predictions of the linear models following reshock.	128
4.28	Time-evolution of the interface for the Richtmyer-Meshkov instability when $A = 0$ at 0, 1, 2, 3, 4, and 5 ms using the Lagrangian- γ method with $N = 256$ markers and $\delta = 0.15$, the VIC method with grid resolution $N_x \times N_y = 32 \times 128$ and $N = 256$ vortex markers, and of the mass fraction contour corresponding to $m_1 = 1/2$ from the VS method with grid resolution $N_x \times N_y = 128 \times 512$. Also shown is the evolution of the mass fraction field $m(x, y)$ from the VS method.	131

4.29	Time-evolution of the vorticity field $\omega(x, y)$ for the Richtmyer-Meshkov instability when $A = 0$ at 0, 1, 3, and 5 ms using the VS method and the VIC method with grid resolution $N_x \times N_y = 32 \times 128$ and $N = 256$ vortex markers and the VS method with a grid resolution $N_x \times N_y = 128 \times 512$ (top two rows). Also shown is the circulation on the interface $\gamma(e)$ at 0, 1, 3, and 5 ms for the VIC, VS, and Lagrangian- γ methods with $N = 256$ markers and $\delta = 0.15$ (bottom three rows).	132
4.30	Same as Figure 4.28 but for $A = 0.4$	134
4.31	Same as Figure 4.29 but for $A = 0.4$	135
4.32	Same as Figure 4.28 but for $A = 0.6$	136
4.33	Same as Figure 4.29 but for $A = 0.6$	137
4.34	Same as Figure 4.28 but for $A = 0.8$	139
4.35	Same as Figure 4.29 but for $A = 0.8$	140
4.36	Time-evolution of the interface for the Richtmyer-Meshkov instability when $A = 1$ at 0, 1, 2, 3, 4, and 5 ms using the Lagrangian- γ and Lagrangian- μ methods with $N = 256$ markers (these simulations only converge for $t < 3.4$ ms, so that visualizations at late times are not shown), and the VIC method with grid resolution $N_x \times N_y = 32 \times 128$ and $N = 256$ vortex markers.	141
4.37	Time-evolution of the vorticity field $\omega(x, y)$ for the Richtmyer-Meshkov instability when $A = 1$ at 0, 1, 2, 3, 4, and 5 ms using the VIC method with grid resolution $N_x \times N_y = 32 \times 128$ and $N = 256$ vortex markers. Also shown is the circulation on the interface $\gamma(e)$ at 0, 1, 3, and 5 ms for the VIC, Lagrangian- γ , and Lagrangian- μ methods with $N = 256$ markers.	142
4.38	Comparison of the perturbation amplitude $a(t)$, bubble amplitude $a_b(t)$, and spike amplitude $a_s(t)$ for $A = 0, 0.2, 0.4, 0.6, 0.8,$ and 1 from the Lagrangian, VIC, and VS methods.	143
4.39	The perturbation amplitude $a(t) - a_0^+$ from the Lagrangian- γ , VIC, and VS simulations with the predictions of the nonlinear models for $A = 0$ and 0.4.	145
4.40	Same as Figure 4.39 but with $A = 0.8$ and 1.	146
4.41	The bubble amplitude $a_b(t) - a_b(0^+)$ from the Lagrangian- γ , VIC, and VS simulations with the predictions of the nonlinear models for $A = 0$ and 0.4.	148
4.42	The bubble growth $da_b(t)/dt$ from the Lagrangian- γ , VIC, and VS simulations with the predictions of the nonlinear models for $A = 0$ and 0.4.	149
4.43	Same as Figure 4.41 but for $A = 0.8$ and 1.	150
4.44	Same as Figure 4.42 but for $A = 0.8$ and 1.	151
4.45	The spike amplitude $a_s(t) - a_s(0^+)$ from the Lagrangian- γ , VIC, and VS simulations with the predictions of the nonlinear models for $A = 0$ and 0.4.	153

4.46	Same as Figure 4.45 but with $A = 0.8$ and 1.	154
5.1	The $x-t$ diagram showing the position of the interface $\ell_{\text{int}}(t)$ (solid line), shock (dotted line), and bubble and spike locations $\ell_b(t)$ and $\ell_s(t)$ (dash-dot and dashed lines, respectively) for the three-dimensional simulation with $a_0^- = 0.205$ cm (red) and $a_0^- = 0.29$ cm (green).	159
5.2	Visualization of the mass fraction isosurface corresponding to $m = 1/2$, the density cross-section at $z_{\text{mid}} = L_z/2$, the enstrophy isosurface $\Omega = 10^8 \text{ s}^{-2}$ at 0.06 ms, and the enstrophy cross-section at z_{mid} using the WENO method.	161
5.3	The initial deposition of circulation on the interface from the three-dimensional WENO simulation with $a_0^- = 0.205$ cm, as measured by the averaged components of the vorticity vector $\langle \omega_1 \rangle(y, z, 0^+)$, $\langle \omega_2 \rangle(y, z, 0^+)$, $\langle \omega_3 \rangle(y, z, 0^+)$, and the enstrophy $\langle \Omega \rangle(y, z, 0^+)$ from the incident shock at time 0^+ (left column) with the comparison from linear instability theory (center column). Also shown is the surface-plot comparison of the results from the simulation (green) with the results from linear instability theory (blue) (right column).	162
5.4	Visualization of the mass fraction isosurface corresponding to $m = 1/2$ and enstrophy isosurface corresponding to $\Omega = 10 \text{ ms}^{-2}$ at 0 ms from the VS simulation.	166
5.5	Time-evolution of the mass fraction isosurface $m_{\text{SF}_6} = 1/2$ and enstrophy isosurface $\Omega = 10^8 \text{ s}^{-2}$ for the single-mode Richtmyer-Meshkov instability at 1, 3, 4.5, and 5.6 ms from the WENO simulation. The spike side facing the air(acetone) (top two rows), and the bubble side facing SF_6 (bottom two rows) are shown.	167
5.6	Time-evolution of the mass fraction isosurface $m_{\text{SF}_6} = 1/2$ and enstrophy isosurface $\Omega = 10^2 \text{ ms}^{-2}$ for the single-mode Richtmyer-Meshkov instability at 1, 3, 4.5, 5.6, and 7 ms from the VS simulation. The spike side facing the air(acetone) (top two rows), and the bubble side facing SF_6 (bottom two rows) are shown	168
5.7	Comparison of the perturbation amplitude from the WENO and VS simulations with $a_0^- = 0.205$ and 0.29 cm (top). The bubble and spike amplitudes $a_b(t)$ and $a_s(t)$, respectively, for $a_0^- = 0.205$ cm (middle) and for $a_0^- = 0.29$ cm (bottom) are also shown.	170
5.8	Comparison of the amplitudes $a(t) - a_0^+$, $a_b(t) - a_b(0^+)$, and $a_s(t) - a_s(0^+)$ from the WENO and VS simulations with $a_0^- = 0.205$ cm and the predictions of the Zhang-Sohn model.	171
5.9	Same as Figure 5.8 but for simulations with $a_0^- = 0.29$ cm.	172

5.10	Time-evolution of the mass fraction isosurface $m_{SF_6} = 1/2$ and enstrophy isosurface $\Omega = 10^8 \text{ s}^{-2}$ at 5.7, 5.8, and 5.9 ms using the WENO method. The spike side facing the air(acetone) (top two rows) and the bubble side facing SF ₆ (bottom two rows) are shown.	175
5.11	Same as Figure 5.10 but at 6, 6.2, and 6.5 ms.	176
5.12	Same as Figure 5.10 but at 7, 8, and 10 ms.	177
5.13	Time-evolution of the density in the (x, y) -plane at 5.7, 5.8, 5.9, 6, 6.1, 6.3, and 6.5 ms using the WENO method. Both the evolution of the spike (first and third row) and of the bubble (second and fourth row) are shown.	178
5.14	Same as Figure 5.13 but at 7, 8, and 10 ms.	179
5.15	The mixing layer amplitude $a(t)$ versus time t from the three-dimensional WENO simulation with $a_0^- = 0.205 \text{ cm}$ (top) and $a_0^- = 0.29 \text{ cm}$ (bottom), together with the predictions of the Mikaelian, Brouillette-Sturtevant, and Charakhch'yan reshock models.	181
5.16	Time-evolution of the mass fraction and enstrophy isosurfaces for $A = 0$ at 1, 3, 5, and 7 ms from the VS simulation.	183
5.17	Same as Figure 5.16 but with $A = 0.4$	184
5.18	The density cross-section $\rho(x, y_{\text{mid}}, z)$ and cross-sections for the three components of the vorticity field, $\omega_1(x, y_{\text{mid}}, z)$, $\omega_2(x, y_{\text{mid}}, z)$ at 0 ms and $\omega_3(x, y_{\text{mid}}, z)$ at 0.2 ms.	185
5.19	Time-evolution of the (x, z) -cross-section of the density field $\rho(x, y_{\text{mid}}, z)$ for $A = 0$, 0.2, 0.4, 0.6, and 0.8 at 1, 3, 5, 7, and 9 ms from the VS simulation.	186
5.20	Time-evolution of the (x, z) -cross-section for the first component of the vorticity field $\omega_1(x, y_{\text{mid}}, z)$ for $A = 0$, 0.2, 0.4, 0.6, and 0.8 at 1, 3, 5, 7, and 9 ms from the VS simulation.	187
5.21	Same as Figure 5.20 but for the second component of the vorticity field $\omega_2(x, y_{\text{mid}}, z)$	188
5.22	Same as Figure 5.20 but for the third component of the vorticity field $\omega_3(x, y_{\text{mid}}, z)$	190
5.23	Comparison of the perturbation, bubble, and spike amplitudes, $a(t)$, $a_b(t)$ and $a_s(t)$, respectively, for $A = 0, 0.2, 0.4, 0.6$, and 0.8 from the three-dimensional VS simulation.	191
5.24	The perturbation, bubble, and spike amplitudes $a(t) - a(0^+)$, $a_b(t) - a_b(0^+)$, and $a_s(t) - a_s(0^+)$, respectively, from the VS simulations with $A = 0, 0.4$, and 0.8 and the predictions of the Zhang-Sohn model.	192

Tables

2.1	The computational stencil for the fourth-order finite-difference modified nine-point scheme used to discretize the Helmholtz equation [Eq. (2.48)] in two dimensions. The table presents a 3×3 block corresponding to the coefficients of $u_{k,\ell}$ and $f_{k,\ell}$	35
2.2	The computational stencil for the fourth-order finite-difference modified nine-point scheme used to discretize the Helmholtz equation [Eq. (2.48)] in three dimensions. The table presents three 3×3 block grids corresponding to the coefficients of $u_{k,\ell,m}$ and $f_{k,\ell,m}$. The first block contains the coefficients for $u_{k,\ell,m+1}$ and $f_{k,\ell,m+1}$, the second block the coefficients for $u_{k,\ell,m}$ and $f_{k,\ell,m}$, and the third block the coefficients for $u_{k,\ell,m-1}$ and $f_{k,\ell,m-1}$	35
3.1	Keys used to denote simulations for the convergence study using different grid resolutions.	37
3.2	Average fractional deviation Δ between the results on the $N_{xf} = 512$ grid and those on coarser grids for the perturbation, bubble, and spike amplitudes $a(t)$, $a_b(t)$, and $a_s(t)$, respectively, and the circulation $\Gamma^+(t)$ for the VS method with $A = 0$ and $\nu = \mathcal{D} = 0$.	44
3.3	Average fractional deviation Δ between the results on the $N_{xf} = 512$ grid and those on coarser grids for the perturbation, bubble, and spike amplitudes $a(t)$, $a_b(t)$, and $a_s(t)$, respectively, and the circulation $\Gamma^+(t)$ for the VS method with $A = 0$ and $\nu = \mathcal{D} = 3 \times 10^{-3}$ cm ² /ms.	51
3.4	Average fractional deviation Δ between the results on the $N_{xf} = 512$ grid and those on coarser grids for the perturbation, bubble, and spike amplitudes $a(t)$, $a_b(t)$, and $a_s(t)$, respectively, and the circulation $\Gamma^+(t)$ for the VS method with $A = 0.4$ and $\nu = \mathcal{D} = 3 \times 10^{-3}$ cm ² /ms.	54
3.5	Keys used to denote simulations with different values of the viscosity ν and initial diffuse-interface thickness δ_T for the VS method.	56
3.6	Average fractional deviations for the perturbation amplitude $a(t)$, bubble and spike amplitudes, $a_b(t)$ and $a_s(t)$, and circulation $\Gamma(t)$ as the viscosity ν and diffuse-interface thickness δ_T are varied.	75

- 4.1 The physical properties of air, acetone vapor, SF₆, and air(acetone) mixture, including the molecular weight M , the density ρ , the adiabatic exponent γ , the particular gas constant R_g , the heat capacity at constant volume c_v , the heat capacity at constant pressure c_p , the dynamic viscosity μ , and the kinematic viscosity ν . The properties of air, acetone vapor, and SF₆ were obtained from the NIST Chemistry Webbook [87] at a temperature of $T_1 = 296$ K. 83
- 4.2 The gas constant R , heat capacity at constant pressure c_p , and heat capacity at constant volume c_v for the air(acetone) mixture and SF₆ gas when $\gamma_1 = \gamma_2 = 1.1405$ for a mixture of 50% air(acetone) and 50% SF₆ by volume (*mix initial conditions*); and when $\gamma_1 = \gamma_2 = 1.2776$ of the air(acetone) mixture is used (*upstream initial conditions*). 85
- 4.3 Comparison of flow properties, including the shock Mach numbers, shock velocities, interface velocity, pre- and post-shock initial amplitudes, pre- and post-shock Atwood numbers when initial conditions from the experiments of Jacobs and Krivets are adopted in one-dimensional refraction theory. Results are presented for two different values of the adiabatic exponents corresponding to air(acetone) and SF₆, and when the upstream and mix initial conditions are used. Also shown are the corresponding values obtained in the experiments of Jacobs and Krivets 86
- 4.4 Initial interface perturbation properties, including the pre-shock amplitude a_0^- , wavelength λ , and wavenumber k ; additional initial physical parameters, including the shock Mach number Ma for the mix and upstream initial conditions, and the temperature T_1 ahead of the shock, and; numerical parameters, including the number of grid points N , grid separation h , and domain size for the longitudinal L_x , and transverse (periodic) direction L_y , used in the two-dimensional simulations. The numerical parameters are based on 128, 256, 512, and 1024 points per initial perturbation wavelength λ . For three-dimensional simulations in Chapter 5, the values for the periodic z direction are the same as the values for the periodic y dimension. 87
- 4.5 Initial perturbation and vortex sheet properties for the VS and vortex simulations, including the initial sheet amplitude a_0 , the wavelength λ , the wavenumber k , and the initial growth rate v_0 for the Atwood number study and for the comparison with the experiment of Jacobs and Krivets with $A = 0.604$. Also shown are the properties of the Lagrangian method, including the number of markers N , the regularization parameter δ , and the time step Δt , the properties of the VIC method, including the dimension of the Cartesian grid, and the number of grid points, and grid spacing $h = \Delta x = \Delta y$, and; the properties of the VS method, including the CFL number, thickness of the layer δ_T , and the viscosity and mass diffusivity ν and \mathcal{D} , respectively. 90

4.6	Keys used to denote simulations with different order of WENO flux reconstruction and grid resolution. The number after the dash is the number of grid points per initial perturbation wavelength λ	91
4.7	Comparison of the initial circulation deposition $\max[\langle\omega\rangle(y, 0^+)]$ and baroclinic production $\max[\langle\mathcal{P}\rangle(y, 0^+)]$ from the fifth- and ninth-order simulations for different grid resolutions.	91
4.8	Average fractional deviation Δ from the WENO9-768 results as the order and grid resolution are varied for the perturbation amplitude $a(t)$, bubble and spike amplitudes $a_b(t)$ and $a_s(t)$, respectively, and the positive circulation $\Gamma^+(t)$	99
4.9	Average fractional deviations Δ_{exp} between the experimental amplitude $a_{\text{exp}}(t)$ and the amplitude from the WENO and VS simulations a_{sim} and the predictions from nonlinear models $a_{\text{mod}}(t)$ obtained using the mix initial conditions, respectively. Also shown is the average fractional deviation Δ_{sim} between the simulation amplitude $a_{\text{sim}}(t)$, and the amplitude from the nonlinear models $a_{\text{mod}}(t)$	115
4.10	Comparison of the initial circulation deposition $\max[\langle\omega\rangle(y, 0^+)]$ from the WENO simulations using mix and upstream initial conditions with the predictions of the Samtaney-Zabusky model $\Gamma_1' a_0^+$ and the prediction from linear instability theory $\max(\gamma)$. Also shown is $\max[\langle\mathcal{P}\rangle(y, 0^+)]$, which measures the initial circulation deposition on the interface.	116
4.11	Average fractional deviations Δ_{exp} between the experimental amplitude $a_{\text{exp}}(t)$ and the amplitude from the nonlinear models $a_{\text{mod}}(t)$ obtained using the upstream and mix initial conditions. Also shown is the average fractional deviations Δ_{sim} between the simulation amplitudes and the predictions of the Zhang-Sohn, Matsuoka et al., Sadot et al., and Mikaelian models.	120
4.12	Comparison of flow properties, including the shock Mach numbers, shock velocities, interface velocity, pre- and post-shock initial amplitudes, pre- and post-shock Atwood numbers for $Ma = 1.05, 1.15, 1.31,$ and 1.45	121
4.13	The average fractional deviation Δ between the perturbation, bubble, and spike amplitudes $a(t)$, $a_b(t)$, $a_s(t)$, and circulation $\Gamma^+(t)$ from the WENO and VS simulations for $Ma_i = 1.05, 1.15, 1.31,$ and 1.45	123
4.14	The growth rate da/dt and the normalized growth rate $k da/d\tau$ for the Richtmyer model before reshock for the mix initial conditions. Also shown is the growth rate and the normalized growth rates from the Mikaelian, Brouillette-Sturtevant, and Charakhch'yan reshock models.	129

4.15	Average fractional deviations Δ_{sim} between the simulation amplitudes from the Lagrangian- γ , VIC, and VS methods $a_{\text{sim}}(t)$ and the amplitudes from the nonlinear models $a_{\text{mod}}(t)$ for $A = 0, 0.2$, and 0.4	155
4.16	Same as Table 4.15 but for $A = 0.6$ and 0.8 . For $A = 1$ the average fractional deviation from the Lagrangian- γ , Lagrangian- μ , and VIC methods is shown.	156
5.1	Initial conditions for the three-dimensional simulations	159
5.2	Number of nodes, CPUs, and time steps for the WENO simulations. Also shown is the grid size, total number of cells, and CPU times for advancing the simulations by $\Delta t = 0.1$ ms for the WENO5 and WENO9 simulations.	160
5.3	Comparison of the initial circulation deposition $\max[\langle\omega_1\rangle(y, z, 0^+)]$, $\max[\langle\omega_2\rangle(y, z, 0^+)]$, and $\max[\langle\omega_3\rangle(y, z, 0^+)]$ from the three-dimensional WENO simulations with $a_0^- = 0.205$ and $a_0^- = 0.29$ cm together with the predictions of linear instability theory. Also shown is the baroclinic circulation deposition on the interface $\max[\langle\Omega\rangle(y, z, 0^+)]$	163
5.4	Initial surface and vortex sheet properties for the VS simulations of the Atwood number study and the comparison with the WENO method in three dimensions, including the initial amplitude a_0 , the wavelength λ , the wavenumber k , and the initial vortex sheet strength parameter v_0 . Also shown are the properties of the VS method, including the CFL number, thickness of the sheet δ_T , and the viscosity ν	165
5.5	Average fractional deviation Δ_{sim} between the WENO and VS simulation amplitudes for $a_0^- = 0.205$ and 0.29 cm and the predictions of the Zhang-Sohn model.	173
5.6	The growth rate da/dt and the normalized growth rate $k da/d\tau$ for the Richtmyer model before reshock for the three-dimensional WENO simulations with $a_0^- = 0.205$ and 0.29 cm. Also shown are the growth rates and the normalized growth rates for the Mikaelian, Brouillette-Sturtevant, and the Charakhch'yan reshock models.	180
5.7	Average fractional deviation Δ_{sim} between the VS amplitude and the predictions of the Zhang-Sohn model for $A = 0, 0.2, 0.4, 0.6$, and 0.8	193

Symbols

Greek letters

α	weighting parameter in vortex sheet computations, page 18
δ	regularization parameter for Lagrangian vortex method simulations, page 18
Δs_n	arclength between vortex markers, defined in Equation (2.20), page 21
$\delta_T^{-(+)}$	pre-shock (post-shock) diffuse-interface thickness, page 84
Δx	grid spacing, page 24
η_{comp}	compression factor, defined in Equation (4.15), page 84
$\eta(y)$	initial interface in two dimensions, defined in Equation (1.1), page 2
Γ_n	vortex marker circulation, defined in Equation (2.19), page 21
γ_r	adiabatic exponent of fluid r , page 80
$\gamma(e, t)$	vortex-sheet strength, page 18
λ	perturbation wavelength, page 2
μ	dynamic viscosity, page 31
$\mu(e, t)$	vortex dipole, defined in Equation (2.18), page 21
ν	kinematic viscosity, page 31
$\omega(\mathbf{x}, t)$	vorticity field, page 5
$\Omega(\mathbf{x}, t)$	enstrophy field, defined in Equation (5.5), page 161
$\phi(x, y)$	interpolation function, defined in Equation (2.13), page 20
$\Phi(x, y, t)$	density Schlieren field, defined in Equation (4.41), page 123
$\psi(x, y, t)$	streamfunction, page 20

$\psi^{-(+)}$	pre-shock (post-shock) growth reduction factor, page 85
ρ_r	density of fluid r , page 2
$\rho(\mathbf{x}, t)$	density field, defined in Equation (1.17), page 5
τ	rescaled time, defined in Equation (1.17), page 4

Operators

$\bar{\phi}$	average over the periodic direction, defined in Equation (4.24), page 95
\mathcal{D}_x	derivative operator, page 34
Δ	Laplacian operator, page 20
Δ_0	central difference operator, page 34
Δ_{sim}	average fractional deviation, defined in Equation (3.5), page 43
$\frac{d}{dt}$	convective derivative, defined in Equation (1.19), page 5
$\gamma^{+(-)}$	upwind (downwind) finite values, defined in Equation (2.8), page 19

Roman letters

$A^{-(+)}$	pre-shock (post-shock) Atwood number, defined in Equation (1.13), page 3
$a_0^{-(+)}$	pre-shock (post-shock) initial perturbation amplitude, page 2
$a_{b(s)}(t)$	bubble (spike) amplitude, page 42
$a(t)$	perturbation amplitude, defined in Equation (3.4), page 42
$\mathcal{C}(\mathbf{x}, t)$	vortex compression, defined in Equation (1.18), page 5
$c_{p(v)}$	heat capacity at constant pressure (volume), page 82
\mathcal{D}	mass diffusivity, page 32
$h(t)$	mixing layer width, defined in Equation (3.4), page 42
k	perturbation wavenumber, page 2
$\mathbf{L}(\mathbf{x}, t)$	linear diffusion term in the vorticity equation, defined in Equation (2.42), page 33
$L_\rho(\mathbf{x}, t)$	linear diffusion term in the density equation, defined in Equation (2.45), page 33
$L_g(x, \delta_T, \Delta x)$	Gaussian interpolant, defined in Equation (2.26), page 24

ℓ_{int}	position of the interface obtained from a simulation without an initial perturbation, page 95
$\ell_{b(s)}(t)$	bubble (spike) location, page 95
$L_{x,y,z}$	domain length in the x , y , and z directions, respectively, page 37
$M_n(x)$	interpolation kernel based on central B-splines, defined in Equation (2.15), page 20
M_r	molecular weight of fluid r , page 83
m_r	mass fraction of fluid r , page 83
$m(\mathbf{x}, t)$	mass fraction field, page 79
$\mathbf{N}(\mathbf{x}, t)$	nonlinear transport term in the vorticity equation, defined in Equation (2.41), page 33
$N_\rho(\mathbf{x}, t)$	nonlinear transport term in the density equation, defined in Equation (2.44), page 33
$N_{x,y,z}$	number of grid points in the x , y , and z directions, respectively, page 37
$\mathcal{P}(\mathbf{x}, t)$	baroclinic vorticity production field, defined in Equation (1.18), page 5
$p(\mathbf{x}, t)$	pressure field, page 5
$q(e)$	velocity of vortex sheet in complex notation, page 18
$Re_{\Gamma,h,\Delta x}(t)$	Reynolds number based on the circulation, perturbation width, and grid spacing, defined in Equations (3.6), (3.7), and (3.8), respectively, page 73
$R_{g(u)}$	particular (universal) gas constant, page 83
$\mathcal{S}(\mathbf{x}, t)$	vortex stretching, defined in Equation (1.18), page 5
Sc	Schmidt number, page 32
$S(x, y)$	thickness function in the WENO method, defined in Equation (4.10), page 82
t	time, page 2
$\mathbf{u}(\mathbf{x}, t)$	velocity field, page 5
v_0	initial growth rate for the Richtmyer-Meshkov instability, defined in Equation (1.16), page 4

X_r	mole fraction of fluid r , defined in Equation (4.12), page 83
$X(\mathbf{x}, t)$	mole fraction field, defined in Equation (4.23), page 95
$z(e)$	position of vortex sheet in complex notation, page 18

Chapter 1

Introduction

The *Richtmyer-Meshkov instability* denotes the growth of perturbations on an interface separating two fluids following an impulsive acceleration [78]. In the laboratory, the impulsive acceleration is typically provided by a shock. As a result, this instability is usually studied in shock tubes where, at the entrance of the test section, an interface with a perturbation separates a light gas and a heavy gas. The instability derives its name from the linear instability analysis of Richtmyer [121], who first considered the growth rate of a perturbation following an impulsive acceleration and later numerically verified these predictions by solving the compressible linear instability equations, and by the shock tube experiments of Meshkov [96], who verified the predictions of Richtmyer. The instability has been extensively studied for its relevance to inertial confinement fusion [31, 85, 86], supernovae dynamics in astrophysics [37, 5, 6, 4], supersonic combustion [56, 152], as well as for its fundamental interest [154, 17]. Developed in this thesis is a vorticity-streamfunction method for the numerical investigation of the Richtmyer-Meshkov instability in two and three dimensions.

This introductory chapter is organized as follows. An overview of the Richtmyer-Meshkov instability, including the linear instability analysis, and the development of the single-mode instability is presented in Section 1.1. The goals of this thesis are discussed in Section 1.2. The organization of the thesis is presented in Section 1.3.

1.1 Overview of the Richtmyer-Meshkov instability

An overview of the Richtmyer-Meshkov instability is presented here, including the linear instability analysis (Sec. 1.1.1) and instability dynamics (Sec. 1.1.2).

1.1.1 Linear instability analysis

Presented here is the linear instability analysis for the Richtmyer-Meshkov instability, taken from Pullin and Wheatley [148, 149]. Additional information on linear instability theory can be found in Drazin and Reid [33, 32] and Saffman [123].

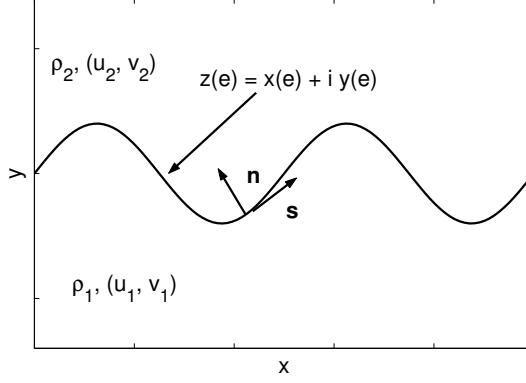


Figure 1.1. Sinusoidal interface for the linear instability problem in two dimensions.

Consider two incompressible, inviscid, irrotational fluids separated by an interface

$$\eta(y) = a_0^- \sin(k y), \quad (1.1)$$

where a_0^- is the pre-shock amplitude, $k = 2\pi/\lambda$ is the wavenumber, and λ is the perturbation wavelength (Fig. 1.1). Let 1 and 2 denote the fluids below and above the interface, respectively. In two dimensions, let x denote the horizontal coordinate and let y denote the vertical coordinate. Let the interface be parametrized as $\mathbf{x}(e, t) = [x(e, t), y(e, t)]$, where e is the parameter of the interface, and t is time.

The Richtmyer-Meshkov instability develops following an impulsive acceleration $g = [u]\delta(t)$, where $\delta(t)$ is the Dirac δ -function, and $[u]$ is a velocity difference created by the acceleration. A time dependence is introduced, so that the ansatz used in classical linear instability analysis for the Kelvin-Helmholtz and Rayleigh-Taylor instabilities can no longer be used. To derive the new ansatz, consider the boundary conditions for a flow at rest following an impulsive acceleration

$$\nabla\phi(z \rightarrow \pm\infty) \rightarrow 0, \quad (1.2)$$

$$\frac{\partial\phi'_r}{\partial z} = \frac{\partial\eta}{\partial t}, \quad (1.3)$$

$$\rho_1 \left[\frac{\partial\phi'_1}{\partial t} + [u]\delta(t)\eta \right] = \rho_2 \left[\frac{\partial\phi'_2}{\partial t} + [u]\delta(t)\eta \right]. \quad (1.4)$$

To solve the linear instability equations use the ansatz

$$(\eta, \phi'_1, \phi'_2) = \left[\widehat{\eta}(z) a(t), \widehat{\phi}'_1(z) f_1(t), \widehat{\phi}'_2(z) f_2(t) \right] e^{i(k_x x + k_y y)} \quad (1.5)$$

and solve the initial-value problem to determine the time-dependent functions $f_1(t)$, $f_2(t)$, and $a(t)$. To satisfy the boundary condition [Eq. (1.2)] with initial conditions $f_1(0) = f_2(0) = 0$ and $a(0) = a_0$,

choose $\widehat{\phi}'_1$ and $\widehat{\phi}'_2$

$$\widehat{\phi}'_2 = B_2 e^{-kz}, \quad \widehat{\phi}'_1 = B_1 e^{kz}, \quad (1.6)$$

and substitute in Equations (1.3)–(1.4) (for $B_1 = B_2 = \widehat{\eta}(z)$) to obtain

$$-k f_2(t) = \frac{da}{dt}, \quad (1.7)$$

$$k f_1(t) = \frac{da}{dt}, \quad (1.8)$$

$$\rho_1 \left[\frac{df_1}{dt} + [u] \delta(t) a(t) \right] = \rho_2 \left[\frac{df_2}{dt} + [u] \delta(t) a(t) \right]. \quad (1.9)$$

To solve the system of first-order ordinary differential equations, apply the Laplace transform in time

$$\widetilde{F}(s) = \int_0^\infty f(t) e^{-st} ds, \quad (1.10)$$

to Equations (1.7)–(1.9) to give the algebraic system

$$-k \widetilde{F}_2(s) = s \widetilde{A}(s) - a_0, \quad k \widetilde{F}_1(s) = \widetilde{A}(s) - a_0, \quad (1.11)$$

$$\rho_1 \left[s \widetilde{F}_1(s) + [u] a_0 \right] = \rho_2 \left[s \widetilde{F}_2(s) + [u] a_0 \right].$$

The system can be solved to give

$$\widetilde{F}_1(s) = \frac{A a_0 [u]}{s}, \quad \widetilde{F}_2(s) = -\frac{A a_0 [u]}{s}, \quad \widetilde{A}(s) = \frac{a_0}{s} + k \frac{A a_0 [u]}{s^2}, \quad (1.12)$$

where

$$A \equiv \frac{\rho_2 - \rho_1}{\rho_1 + \rho_2}, \quad (1.13)$$

is the *Atwood number*. Taking the inverse Laplace transform along the Bromwich contour

$$a(t) = \frac{1}{2\pi i} \int_{c-i\infty}^{c+i\infty} \widetilde{A}(s) e^{st} ds, \quad (1.14)$$

yields

$$a(t) = a_0 (1 + k [u] A t), \quad (1.15)$$

indicating that the instability grows linearly in time. It follows that:

1. if $\rho_2 > \rho_1$, corresponding to $A > 0$, the instability immediately grows;
2. if $\rho_2 < \rho_1$, corresponding to $A < 0$, the instability initially decreases in a process called

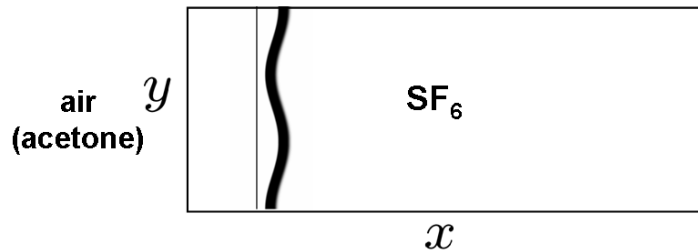


Figure 1.2. The shock tube test section and computational domain for the two-dimensional simulations of the Richtmyer-Meshkov instability. The diffuse sinusoidal interface separates the light air(acetone) gas from the heavier SF_6 gas, x denotes the direction of shock propagation, and y denotes the transverse (periodic) direction.

inversion, and then exhibits linear growth;

3. if $\rho_1 = \rho_2$, corresponding to $A = 0$, the instability does not grow (called *freeze-out*).

In the case of a shock passing through an interface, $[u]$ is the speed of the interface following the passage of the shock, and a_0 is the initial perturbation amplitude. However, it is unclear whether the Atwood number A and the initial perturbation amplitude a_0 should be formed from the pre-shock values A^- and a_0^- , or the post-shock values A^+ and a_0^+ . Richtmyer [121] (based on numerical simulations of the linearized equations) concluded that the best agreement between the model prediction and the simulation data is obtained with the post-shock values A^+ and a_0^+ :

$$v_0 \equiv k [u] A^+ a_0^+. \quad (1.16)$$

It is therefore customary to use the post-shock values in all of the models for both the linear and nonlinear instability. The initial velocity is used to define the rescaled time

$$\tau \equiv k v_0 t, \quad (1.17)$$

which is used to distinguish the linear regime ($\tau < 1$) from the weakly-nonlinear regime ($1 < \tau < 4$) and the fully nonlinear regime ($\tau > 4$). The initial growth [Eq. (1.16)] only applies to the linear regime.

1.1.2 Single-mode instability dynamics

Presented here is an overview of the development of the reshocked single-mode Richtmyer-Meshkov instability in two dimensions. The description is taken from a more comprehensive discussion in Chapter 4.

The configuration considered here is the classical single-mode case, where air seeded with acetone

[air(acetone)] is separated from sulfur hexafluoride (SF_6) by a diffuse sinusoidal perturbation [Eq. (1.1)], where a_0^- , k , and the diffuse-interface thickness δ_T [Eq. (4.10)] are chosen to closely match the parameters in the shock tube experiments of Jacobs and Krivets [62] (Sec. 4.2.1). In two dimensions, a schematic of the shock tube test section and of the computational domain used in the present simulations is shown in Figure 1.2. Also shown is the shock entering the test section before refracting at the interface separating the light air(acetone) gas and the heavier SF_6 gas.

Figure 1.3 illustrates the instability evolution through the density $\rho(x, y)$, vorticity $\omega(x, y)$, and simulated density Schlieren fields $\phi(x, y)$ [Eq. (4.41)]. First, following the shock interface interaction, *shock refraction* occurs, in which a transmitted shock continues into the SF_6 and a reflected shock returns back into the air(acetone) and exits the computational domain. As the shock passes through the interface, the misalignment of the density and pressure gradients causes a deposition of vorticity through the baroclinic vorticity production mechanism. Consider the three-dimensional evolution equation for the vorticity $\boldsymbol{\omega} = \nabla \times \mathbf{u}$ (in the absence of dissipation terms):

$$\begin{aligned} \frac{d\boldsymbol{\omega}}{dt} &= \mathcal{P} + \mathcal{S} + \mathcal{C} \\ &= \frac{\nabla\rho \times \nabla p}{\rho^2} + (\boldsymbol{\omega} \cdot \nabla) \mathbf{u} - \boldsymbol{\omega} \nabla \cdot \mathbf{u}, \end{aligned} \quad (1.18)$$

where

$$\frac{d}{dt} \equiv \frac{\partial}{\partial t} + \mathbf{u} \cdot \nabla \quad (1.19)$$

is the *convective derivative*. The first term on the right side is the *baroclinic vorticity production* \mathcal{P} and constitutes the main mechanism for vorticity generation in the Richtmyer-Meshkov instability. The second term is the *vortex stretching* \mathcal{S} . Vortex stretching is identically zero in two dimensions, as the vorticity field is perpendicular to the velocity field. The absence of vortex stretching in two dimensions causes an inverse cascade from small scales to larger scales [70], resulting in the generation of larger and more coherent structures [129]. Thus, the dynamics of the Richtmyer-Meshkov in three dimensions are different from the dynamics in two dimensions. The third term is the *vortex compression* \mathcal{C} and is small in the present simulations. In fact, compressibility effects are not significant in the Richtmyer-Meshkov instability following the passage of the shock for the moderate Mach numbers considered in the present work [93, 94, 57].

The baroclinic vorticity production is large when the shock passes through the interface, as a shock causes a jump in pressure, depositing positive vorticity on one side of the interface and negative vorticity on the other side of the interface. As the positive vorticity represents a counter-clockwise rotation, while the negative vorticity represents a clockwise rotation, the distribution of vorticity on the interface drives the evolution of the instability. In particular, the heavy SF_6 penetrates into the air(acetone) causing the formation of *spikes*, while the lighter air(acetone) “rises” into the SF_6

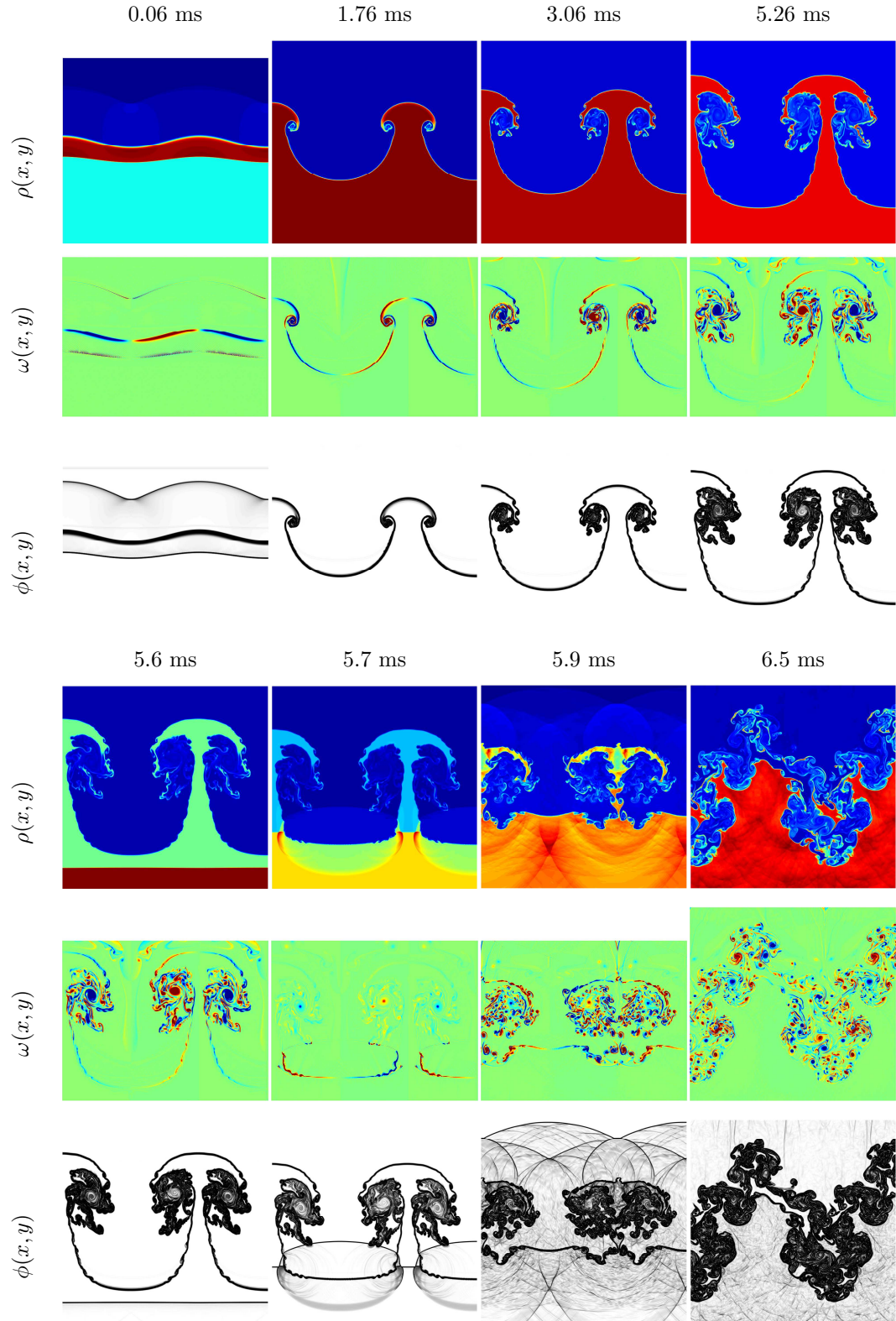


Figure 1.3. Time-evolution of the density $\rho(x, y)$, vorticity $\omega(x, y)$, and simulated density Schlieren $\phi(x, y)$ fields illustrating the development of the single-mode Richtmyer-Meshkov instability before reshock at 0.06, 1.76, 3.06, and 5.26 ms (top panel) and after reshock at 5.6, 5.7, 5.9, and 6.5 ms (bottom panel).

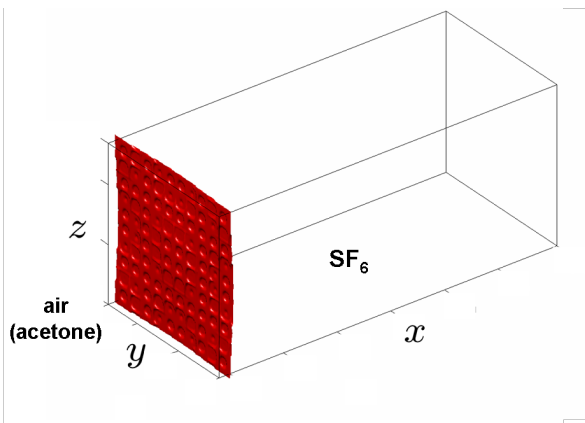


Figure 1.4. The shock tube test section and computational domain for the three-dimensional simulations of the Richtmyer-Meshkov instability. The initial $\eta(y, z)$ interface separates the light air(acetone) gas from the heavier SF_6 gas, x denotes the direction of shock propagation, and y and z denote the transverse (periodic) directions.

causing the formation of *bubbles*. This can be seen in the instability evolution at 1.76 ms (Fig. 1.3). Subsequently, the spike rolls up forming the characteristic “mushroom” shape and the vorticity rolls up into strong positive and negative cores. As the roll-up occurs, the baroclinic vorticity production generates additional vorticity on the interface, in a mechanism also called *vortex-accelerated-vorticity-deposition* (VAVD) [115]. The baroclinic vorticity production causes the deposition of vorticity of opposite sign in the roll-up, contributing to the formation of complex structures within the roll-up that eventually fragment, as seen at 5.26 ms in Fig. 1.3. Additional deposition of vorticity occurs and additional complex structure forms in a process called *reshock*. The transmitted shock that entered the SF_6 following the initial shock refraction travels faster than the interface, reflects from the end wall of the test section, and interacts with the interface. At reshock, the shock refraction is from the heavier SF_6 into the lighter air(acetone). As a result, a transmitted shock continues into the air(acetone) and a reflected rarefaction wave returns back into the SF_6 . The passage of the shock causes deposition of vorticity of opposite sign on the interface. As a result, the spike now transforms into a bubble and vice versa in a process called *inversion*. This process is visible at 5.6 ms, when the reflected shock is observed prior to interacting with the interface, and also at 5.7 and 5.9 ms. The transmitted shock and the reflected rarefaction waves are visualized through the density Schlieren fields at these times, which also show the complex system of reflected and transmitted waves in the layer. Following reshock, the instability grows faster, and by 6.5 ms a complex layer develops.

In this thesis the single-mode case is extended from two dimensions to three dimensions (Chapter 5). In three dimensions, a schematic of the shock tube test section and of the computational domain used in the present simulations is shown in Figure 1.4. The interface separating the light air(acetone) and the heavier SF_6 gas is visualized through the mass fraction isosurface. The mass fraction is a

scalar field advected by the velocity field and is initially zero in the air(acetone) gas and unity in the SF₆ gas. The mass fraction iso-surface corresponding to $m = 1/2$ is used to visualize the evolution of the instability in three dimensions. The perturbed interface separating the two gases is

$$\eta(y, z) = a_0^- \sin(k_y y) \sin(k_z z) , \quad (1.20)$$

where k_y and k_z are the wavenumbers in the y and z direction, and a_0^- is the pre-shock perturbation amplitude. The values of $k_y = k_z = k_{2D}$, and a_0^- are chosen to match the values in the two-dimensional study.

1.2 Goals of this thesis

The Richtmyer-Meshkov instability is a complex phenomenon that has been extensively investigated numerically, analytically, and experimentally [154, 17]. As the instability contains a wide range of scales developing from small interfacial perturbations in the presence of shocks, a high-resolution compressible shock-capturing method is needed to capture the dynamics and multi-scale properties of the instability. In previous work [78, 129], the ninth-order weighted essentially non-oscillatory method was used to investigate the physics of the two-dimensional single-mode Richtmyer-Meshkov instability with reshock using a model of the Collins and Jacobs [27] Mach 1.2 air(acetone)/SF₆ experiment. Concurrent with this investigation, a study was also performed to quantify the effects of resolution and order of WENO flux reconstruction on the instability dynamics and other characteristic quantities [77]. This study underscored how physical and numerical effects are closely linked and concluded that the ninth-order WENO method is well suited for investigating the instability dynamics.

The single-mode Richtmyer-Meshkov instability is numerically investigated into the late nonlinear regime in this thesis by simulating a model of the late-time Mach 1.3 air(acetone)/SF₆ Jacobs and Krivets [62] shock tube experiment (Sec. 4.2.1). These experiments were previously considered by Peng, Zabusky, and Zhang [115] as part of a numerical investigation of the effects of the vortex-accelerated secondary baroclinic vorticity deposition (VAVD) using a piece-wise parabolic method. The present investigation is performed in the spirit of a previous study of the Collins and Jacobs [27] experiment using the WENO method [78, 129], but the present work is different in two important ways. (1) The Jacobs and Krivets experiments have a higher Mach number, so that a later nonlinear regime is reached (by contrast, reshock occurs at an earlier time in the instability development in the Collins and Jacobs experiment). (2) The instability is investigated from a perspective complementary to the compressible WENO approach by considering the incompressible dynamics of the underlying vorticity deposited by the passage of the shock. In fact, following the passage of

the shock, the Richtmyer-Meshkov instability is essentially an incompressible phenomenon [94, 57]. Furthermore, for a high Reynolds number flow (including the Richtmyer-Meshkov instability), the vorticity is concentrated in a small layer, so that a vorticity distribution can be used to model the dynamics of the underlying complex flow [124]. However, modeling such a flow using a vorticity approach raises questions of well-posedness of the initial conditions, long-time existence of the solution, and convergence [11]. In fact, the linear instability of an inviscid plane vortex sheet in two dimensions is ill-posed [35, 73]. Furthermore, Samtaney and Pullin [126] numerically examined the convergence of initial-value solutions for vortex sheets in compressible Euler equations and reported that pointwise convergence is not achieved. Developed in this thesis is a vorticity-streamfunction method to investigate the dynamics of the vorticity in the Richtmyer-Meshkov instability in two and three dimensions, where the initial vortex sheet is thickened to regularize the singular limit of classical thin sheet representations. The vorticity on the Cartesian grid is evolved using the vorticity equation augmented by the baroclinic vorticity production term to capture the effects of the instability.

Presented in this section are the goals for the development of the VS method (Sec. 1.2.1). A comparison of simulation results using the VS and WENO methods is performed (Sec. 1.2.2). The investigation is also extended to three dimensions (Sec. 1.2.3).

1.2.1 Development of the vorticity-streamfunction method

A vorticity dynamics approach for investigating the Richtmyer-Meshkov instability has many advantages including: (1) recognizing that vorticity is a fundamental instability driving mechanism and; (2) as vorticity exists only in a small region of the domain, the numerical method is computationally efficient. Developed in this thesis is a vorticity-streamfunction (VS) method for the simulation of the Richtmyer-Meshkov instability. The initial interface is thickened to model the diffuse thickness of the Jacobs and Krivets experiments (Sec. 4.2.1). The goals for the development of this method are presented here.

1. A goal of this thesis is the *development of a high-order VS method* for increased accuracy and resolution of structures as the instability develops (Chapter 2). In addition, the numerical method must be efficient.
2. In the present investigation, vortex layers with finite diffuse-interface thickness are adopted to model the diffuse-interface experiments of Jacobs and Krivets [62]. Vortex layers are well-posed and exist in time [11]. The goal is to show that the vortex layer under appropriate conditions *converges to the solution of a vortex sheet* as the diffuse-interface thickness is decreased (Sec. 2.2).
3. One of the goals for developing the VS method is to *extend the formulation to three dimensions*.

4. Once the method is developed, a goal is the *investigation of the numerical properties* (Chapter 3). A convergence study must be performed to verify the numerical properties of the method (Sec. 3.1) and investigate how these properties change in time. In addition, a systematic and self-consistent convergence study is performed for variable diffuse-interface thickness and viscosity (Sec. 3.2). The goal of these convergence studies is to ensure that simulations are performed with sufficient resolution so that fourth-order pointwise convergence of the solution is obtained.

1.2.2 Investigation of the two-dimensional single-mode instability

Compressible WENO and incompressible VS simulations are performed for the two-dimensional Richtmyer-Meshkov instability (Chapter 4). The simulations are modeled after the single-mode Mach 1.3 air(acetone)/SF₆ shock tube experiment of Jacobs and Krivets [62] (Sec. 4.2.1), which investigated *late-time effects* of the instability.

The main goals of this study are presented here.

1. One of the purposes of this study is the *accurate construction and evaluation of initial conditions* (Sec. 4.2). First, the properties of the air(acetone) mixture are constructed based on thermodynamic properties of the constitutive air and acetone vapor. As the WENO method employed here allows the specification of a single value for the adiabatic exponent γ , the *mix initial conditions* corresponding to a 50% mixture of air(acetone) and SF₆ by volume are adopted. As the VS method simulates the evolution of the instability following the passage of the shock, results from linear instability theory, the Samtaney-Zabusky [127, 128] circulation deposition model, and the WENO simulations are used to determine the circulation deposition at the interface.
2. Another goal is to *assess the properties of the ninth-order WENO method* by comparing with the fifth-order WENO method at different grid resolutions (Sec. 4.3). Visualization of the instability evolution, as well as comparison of perturbation, bubble, and spike amplitudes are performed to ensure that these amplitudes do not vary as the grid is refined and the order of flux reconstruction is varied.
3. A *comparison of the instability evolution from the incompressible VS method with results from the compressible WENO simulation and the experimental PLIF images* constitutes is another goal (Sec. 4.4).
4. A *comparison of the perturbation, bubble, and spike amplitudes with experimental data and with the predictions of linear and nonlinear growth models* is another goal of this investigation (Sec. 4.5).

5. To further interpret *the agreement between the VS and WENO methods*, the effects of varying Mach numbers (Sec. 4.6) are investigated.
6. Another goal of the simulations is the *investigation of reshock* using the WENO method (Sec. 4.7), including comparison of the mixing layer width with the predictions of reshock models.
7. As the VS method introduces a thickened vortex layer to model a thin vortex sheet, *results are compared with the Lagrangian- γ and vortex-in-cell method* for different Atwood numbers (Sec. 4.8). Different values of A correspond to different levels of baroclinic vorticity production, so that this study also investigates the effects of A on the instability evolution.

1.2.3 Investigation of the three-dimensional single-mode instability

Three-dimensional simulations using the WENO and VS methods (Chapter 5) are performed using the same shock tube dimensions as in the two-dimensional investigation. The initial interface is given by a product of sine functions [Eq. (1.20)], as it represents a generalization in three dimensions of the two-dimensional perturbation [84, 157].

The goals for the investigation in three dimensions are presented here.

1. A goal of this study is the *construction of appropriate initial conditions* (Sec. 5.1). In particular, as three-dimensional simulations have larger effective wavenumbers, two simulations are performed: (1) the initial amplitude is the same as the two-dimensional simulations, and; (2) the initial amplitude is reduced so that the initial growth matches the two-dimensional value.
2. Another goal is *the visualization of the instability evolution in three dimensions* through the evolution of a mass fraction iso-surface (Sec. 5.2). The vorticity is visualized using an enstrophy iso-surface. Additional quantities are also considered to determine the principal mechanisms of instability evolution in three dimensions.
3. The *comparison of the perturbation, bubble, and spike amplitudes with the predictions of non-linear growth models in three dimensions* (Sec. 5.3) constitutes a central objective of this study.
4. The *dynamics of reshock* are also investigated in three dimensions (Sec. 5.4) and the mixing layer width is compared to the predictions of reshock models.
5. An *Atwood number study* is performed to assess the effects of this parameter on the instability evolution and the dynamics of vorticity (Sec. 5.5). Visualizations of the density cross-sections also illustrate the dynamics of the bubble and spike. Cross-sections of the components of the vorticity field are also shown. The perturbation, bubble, and spike amplitudes are also compared with the predictions of models.

1.3 Organization of thesis

In Chapter 2 the vorticity-streamfunction method is developed and the numerical implementation is discussed. Properties of the method, including pointwise convergence and the effects of numerical and physical parameters are discussed in Chapter 3. Simulations and analysis of the single-mode Richtmyer-Meshkov instability in two dimensions, including a comparison to the experiments of Jacobs and Krivets [62], to WENO simulations, and to classical Lagrangian and hybrid Lagrangian/Eulerian vortex method simulations are presented in Chapter 4. Simulations and analysis of the single-mode Richtmyer-Meshkov instability in three dimensions, including a comparison to WENO simulations, are presented in Chapter 5. Finally, conclusions and implications of this research are presented in Chapter 6.

Chapter 2

Development and Numerical Implementation of the Vorticity-Streamfunction Method

Presented here is the development of the vorticity-streamfunction method used in this thesis for the numerical investigation of the Richtmyer-Meshkov instability. This method was developed in the context of vortex methods for the simulation of the interface dynamics of this instability. Vortex methods are used because the vorticity deposition-evolution viewpoint provides physical insight into the instability [51, 154] and is also numerically advantageous [29] when compared with the more expensive weighted essentially non-oscillatory (WENO) compressible simulations considered in the present investigation.

The vorticity evolution viewpoint recognizes that the main physical mechanism driving the classical Richtmyer-Meshkov instability is the deposition of localized vorticity at the interface during shock refraction through the baroclinic vorticity production mechanism. Following the passage of the shock, a transmitted shock enters the second fluid and a reflected wave returns back into the first fluid. A second mechanism of vorticity deposition is the interaction of the interface with the pressure perturbations from the *stable perturbed shock fronts* [150, 151], including the reflected and transmitted shocks, but not a reflected rarefaction. Typically, the pressure perturbations from the stable shock front decrease the growth rate, causing in some cases “freeze-out” [104]. This second mechanism of vorticity generation is not captured by the present incompressible simulations. However, the results from this thesis suggest that such a contribution is not significant for the classical Richtmyer-Meshkov instability. Velikovich et al. [147] discuss *Richtmyer-Meshkov-like* instabilities, including “anti-collisions”, where such a mechanism becomes relevant.

Vortex methods allow the investigation of late-time stages of the instability development not tractable via analytical approaches. For example, current analytical treatments are limited to weakly-nonlinear analysis [156, 145] or Layzer-type expansions [52, 105, 155, 42, 137, 134, 135]

(Sec. 4.5). Such weakly-nonlinear treatments are shown to be valid up to $\tau = 4$ [Eq. (1.17)]. By contrast, vortex methods offer an alternative strategy to describe the interface dynamics from the linear to the weakly-nonlinear and fully-nonlinear stages. In the fully-nonlinear stage, for $A \neq 1$ the spike rolls up into a spiral due to the nonuniform vorticity distribution on the interface.

This chapter is organized as follows. An overview, including a discussion of vortex methods applied to the Richtmyer-Meshkov instability and a description of the classical Lagrangian and hybrid Lagrangian-Eulerian vortex methods based on the vortex-in-cell (VIC) algorithm, is presented in Section 2.1. A convergence study for the VIC method demonstrating that this method does not converge to the Biot-Savart velocity under grid refinement, and that the method can be applied to the Richtmyer-Meshkov instability for coarse grids is presented in Section 2.2. The development of the vorticity-streamfunction method, including the equations solved and the semi-implicit third-order in time and fourth-order in space discretization adopted here is presented in Section 2.3.

2.1 Overview of vortex methods

Vortex methods are based on the discretization of the incompressible vorticity equation (presented here in two dimensions in the absence of viscosity and for constant density flows)

$$\frac{\partial \omega}{\partial t} + \nabla \cdot (\mathbf{u} \omega) = 0, \quad (2.1)$$

$$\omega(\mathbf{x}, 0) = \omega_0. \quad (2.2)$$

In particular, Equation (2.1) states that vorticity is constant along particle paths. This combined with the fact that vorticity is advected along particle paths [53] suggests a natural *Lagrangian formulation* for vortex methods based on the following simple algorithm: (1) discretize the initial vorticity distribution ω_0 using vortex markers; (2) next, compute the velocity field \mathbf{u} induced by the vorticity field through the Biot-Savart law; (3) advect the point markers under the self-induced velocity field; (4) since vorticity is advected along particle paths and does not evolve in time, the procedure can be repeated. To compute the velocity from the vorticity field in a Lagrangian formulation [step (2) above] two methods can be used: (1) the Biot-Savart law based on the Green's function is adopted in purely Lagrangian vortex-marker methods, and; (2) the vortex-in-cell algorithm (which uses an auxiliary Cartesian grid and the vorticity-streamfunction formulation) is adopted in the hybrid Lagrangian/Eulerian vortex methods.

Vortex methods have been widely applied to investigate Richtmyer-Meshkov instability dynamics (Sec. 2.1.1). In classical Lagrangian vortex methods for the Richtmyer-Meshkov instability, the vorticity (circulation) on the markers is updated due to the action of density and pressure gradients using a coupled system of integral equations (Sec. 2.1.2). This formulation has also been extended

to the hybrid Lagrangian/Eulerian methods based on the vortex-in-cell algorithm (Sec. 2.1.3).

2.1.1 Literature survey on vortex methods applied to the Rayleigh-Taylor and Richtmyer-Meshkov instabilities

Since the work of Rosenhead [122], who computed the evolution of a Kelvin-Helmholtz [54, 67] unstable vortex sheet by hand, the evolution of a vortex sheet has been a principal application of vortex methods. Vortex sheets also form when a heavy fluid pushes on a light fluid in the *Rayleigh-Taylor instability* [119, 139] and for impulsive accelerations in the Richtmyer-Meshkov instability (Sec. 1.1.1). Presented here is a brief overview of the applications of vortex methods to the Rayleigh-Taylor and Richtmyer-Meshkov instability.

The early interest in the classical Kelvin-Helmholtz vortex sheet dynamics was related to mathematical questions of well-posedness and singularity formation. The problem of a vortex sheet roll-up idealizing the Kelvin-Helmholtz instability is formally ill-posed (as first reported by Birkhoff [15]), as there is no mechanism to stabilize small-scale motions and short wave disturbances grow at increasing rates. Saffman and Baker [124] speculated that a singularity develops in a finite time. Moore [111] expanded the interface as a Fourier series and showed that at a critical time t_c the coefficients of the Fourier series decay algebraically, indicating that the interface is no longer analytic. Meiron, Baker, and Orszag [92] analyzed the vortex sheet dynamics when a tangential shear is applied to a sharp flat interface. The analysis of the Taylor series coefficients indicated that a singularity formed at a critical time t_c slightly larger than the critical time predicted by Moore. Krasny [71, 72] desingularized the equations governing the motion of the vortex sheet to investigate the possible evolution past the critical time t_c . As no rigorous theory exists to justify the procedure and guarantee that the solution obtained is physical or even convergent, this procedure was treated as an experimental work. However, this work was conducted in the spirit of Anderson [3], who replaced the exact equations by a set of regularized equations. The regularized equations can overcome the breaking of analyticity at the critical time t_c and can mitigate the short-wavelength instability of the Kelvin-Helmholtz instability. Before Krasny, Moore [110] proposed modeling the inner-most part of the roll-up as a single strong vortex that would absorb all point vortices within a certain distance from it. Chorin and Bernard [23] proposed using vortex blobs. Fink and Soh [38] redistributed the points on the interface. The Krasny regularization is used in the present computations. Tryggvason [142] later compared the simulations of the vortex sheet roll-up using the vortex-in-cell (VIC) method and the vortex blob method of Krasny [71], and showed that the VIC method gave similar and accurate results.

Birkhoff [14, 15, 16] and later Baker, Meiron, and Orszag [8] extended the point vortex method to study the Rayleigh-Taylor instability in inviscid, incompressible flows. The density interface was

represented by a vortex sheet of strength γ across which the tangential component of the velocity became discontinuous. In two-dimensional layered flow, the vorticity is no longer constant along particle paths (as in the Kelvin-Helmholtz instability). The evolution equation for the vortex sheet strength was shown to depend on the density difference through the Atwood number and was coupled with the Biot-Savart law to determine the velocity from the vorticity. To compute the change in vortex sheet strength, an iterative procedure based on the flow acceleration from the previous time level was used. This iteration procedure was shown to be globally convergent, provided that the interface and vorticity were sufficiently smooth. This vortex method had a cost of $O(N^2)$ operations. For $A = 1$, corresponding to a fluid falling in a vacuum, the acceleration of the spikes approached the free-fall limit. For small Atwood numbers, the spikes began to roll-up due to the Kelvin-Helmholtz instability. Capturing the roll-up structure proved difficult, due to the small number of point vortices. Increasing the number of point vortices led to a deterioration of the results. Baker, Meiron, and Orszag [9] later presented a generalized vortex method to compute flows modeled using vortex sheets (Sec. 2.1.2). The approach was later extended to the axisymmetric three-dimensional Rayleigh-Taylor instability [10].

Kerr [68] simulated the Rayleigh-Taylor instability using vortex blobs to smooth the Green's function, second-order central differences to accommodate spikes in the vorticity, a method to spread the nodes evenly along the interface to suppress clustering and maintain resolution and accuracy, and filtering similar to Krasny [72] to eliminate numerical instabilities. The method predicted the development of bubbles and spikes for a single-mode initial perturbation.

Tryggvason [141] simulated the Rayleigh-Taylor instability using the vortex-in-cell (VIC) algorithm. As stabilization mechanisms (such as viscosity and surface tension) were neglected, difficulties associated with infinitely small perturbations growing infinitely fast were resolved through the regularization introduced by the algorithm. In addition, the VIC algorithm is less computationally intensive than a blob method. A Poisson solver has a cost of $O(M^2 \log M)$ for an $M \times M$ grid. However, since the size of the grid is linear with the number of point vortices N , so that $M^2 \sim N$, the overall cost of the VIC method is $O(N \log N)$, which is significantly less than the $O(N^2)$ cost for a direct summation method in the Biot-Savart law. Tryggvason used a fixed Cartesian grid and assigned the vorticity from the interface to the grid through the area-weighting-rule (AWR) of Christiansen [24]. Thus, the vortex sheet had been replaced by a smoother vortex representation. However, the area-weighting-rule created an anisotropic distribution on the smallest scales. This can be corrected using smooth or quiet VIC methods [81], but Tryggvason used the smoother Peskin interpolant [116] to remove the anisotropy. Tryggvason described two VIC methods based on whether the acceleration is computed on the Lagrangian interface as in the *iterative-time-step* formulation (VIC-ITS), or is computed on the Cartesian grid and then interpolated onto the interface as in the *acceleration-potential* formulation (VIC-AP). The Rayleigh-Taylor test problem was compared with

solutions from the point vortex method of Baker, Meiron, and Orszag [9] and the conformal mapping method of Menikoff and Zemach [95]. Excellent agreement was found at early times. For $A = 1$, the results were compared with the the point vortex method solution indicating that the spikes were less sharp in the VIC simulations. Zufria [160] explained this through a linear instability analysis, which linked the effects of the Cartesian grid to numerical surface tension. As a result, the spike velocity decreased, falling short of the “exact” results from the point vortex method. The bubble velocity was very similar to the exact value. A closer analysis of the spike dynamics showed that vorticity of opposite signs formed near the spike tip, akin to a dipole. When this vorticity was distributed on the Cartesian grid, a cancellation of the negative and positive vorticity occurred, resulting in a weaker dipole.

Zufria [159] also considered the VIC-ITS method and noted that the discretization of the γ^2 term [Eq. (2.5)] developed a very steep profile. Reminiscent of a shock-like behavior, Zufria applied a Godunov upwind technique to differentiate this term [41, 83]. This small change significantly improved the method, allowing the simulation to run to times one order of magnitude larger than previous schemes. Prior to the introduction of this upwind finite differencing, Tryggvason [141] solved this problem using a five-point moving average of the vortex sheet strength γ . Following the modification introduced by Zufria, the iterative time-step method gave superior results, even in the case of a roll-up. Zufria [159] investigated the bubble competition in the Rayleigh-Taylor instability using the VIC algorithm in the limit $A \rightarrow 1$. The study was motivated by experiments by Read [120], where a multi-mode initial condition gave rise to bubbles that grew in time and changed in number. The bubbles did not break, indicating that they were stable to small-scale perturbations, and that the change in number was due to *bubble competition*. In the case of a single-mode initial condition, the results were compared with the ITS method of Tryggvason [141] and with the results of Baker, Meiron, and Orszag [9], showing that the bubble position was captured very accurately, but the spike grew at a slower speed in the VIC simulations. In the case of multi-mode initial conditions, Zufria observed bubble competition with the larger bubbles overcoming the smaller ones.

Kotelnikov, Ray, and Zabusky [69] explored vortex dynamics and interfacial evolution of reshocked and reaccelerated single-mode Richtmyer-Meshkov flows using an incompressible VIC method, a vortex blob method, and a compressible second-order Godunov method. The configuration was based on the experiments of Jacobs and Niederhaus [112, 113], where liquid-liquid interfaces were impulsively accelerated giving rise to the Richtmyer-Meshkov instability. The impulsive and incompressible approach was justified because the flow was incompressible [93] following the passage of the shock.

Sohn [136] applied the point vortex method of Baker, Meiron, and Orszag [92] to investigate the single-mode Rayleigh-Taylor and Richtmyer-Meshkov instability evolution for $A < 1$. Sohn concluded that this method provided accurate and reliable results in agreement with analytical predictions of potential models [134]. The method used Eulerian time stepping, the Krasny [71]

regularization to remove the singularity at the core and stabilize the method, and the Zufria [159] Godunov-like flux splitting for the γ^2 term [Eq. (2.5)].

2.1.2 The classical Lagrangian vortex method

The classical Lagrangian vortex method for the Richtmyer-Meshkov instability uses a coupled system of integral equations first derived by Birkhoff [14, 15, 16]. The formulation presented here was derived from Baker, Meiron, and Orszag [9]. Consider a sinusoidal vortex sheet with position $z = x + iy$, velocity $q = u + iv$ (in complex notation), and vortex-sheet strength $\gamma(e)$. The *weighting parameter* α measures whether the interface moves with the lower fluid ($\alpha = 1$) or with the upper fluid ($\alpha = -1$). The equations of motion are

$$\tilde{q}^* = q^* + \frac{\alpha \gamma}{2 z_e}, \quad \frac{dz^*}{dt} = \tilde{q}^*. \quad (2.3)$$

The velocity q^* is obtained from the circulation $\gamma(e)$ via the *Biot-Savart* law

$$q^*(e) = \frac{1}{4\pi i} \int_0^{2\pi} \frac{\gamma(e') \cos \left[\frac{z(e) - z(e')}{2} \right]}{\sin \left[\frac{z(e) - z(e')}{2} \right] + \delta^2} de', \quad (2.4)$$

where δ is a regularization parameter introduced by Krasny [71, 72], which transforms the singular vortex cores into *vortex blobs*.

The circulation on the interface is obtained by iteratively solving the coupled system of Fredholm integral equations

$$\frac{\partial \gamma}{\partial t} = \frac{\alpha}{2} \frac{\partial}{\partial e} \left(\frac{\gamma^2}{z_e z_e^*} \right) - 2A \left[\operatorname{Re} \left(z_e \frac{\partial q^*}{\partial t} \right) - \frac{\alpha \gamma}{2} \operatorname{Re} \left(\frac{q_e}{z_e} \right) + \frac{1}{8} \frac{\partial}{\partial e} \left(\frac{\gamma^2}{z_e z_e^*} \right) \right], \quad (2.5)$$

$$\frac{\partial q^*(e)}{\partial t} = \frac{1}{4\pi i} \int_0^{2\pi} \frac{\partial \gamma(e')}{\partial t} \cot \left[\frac{z(e) - z(e')}{2} \right] de' - \frac{1}{8\pi i} \int_0^{2\pi} \frac{\gamma(e') [\tilde{q}(e) - \tilde{q}(e')]}{\sin^2 \left[\frac{z(e) - z(e')}{2} \right]} de'. \quad (2.6)$$

For $A \neq 1$, instead of regularizing $\partial q^*/\partial t$ [Eq. (2.6)], this value is obtained from q^* [Eq. (2.4)] through the leap-frog scheme

$$\frac{\partial (q^*)^n}{\partial t} = \begin{cases} \frac{(q^*)^2 - (q^*)^1}{\Delta t} \\ \frac{(q^*)^{n+1} - (q^*)^{n-1}}{2\Delta t} \quad \text{for } n \geq 2 \end{cases}, \quad (2.7)$$

where n indicates the time step. Zufria [159] first noted that the discretization of the $F = \gamma^2$ term [Eq. (2.5)] needs to be treated carefully. In fact, this term becomes very steep, developing a shock-like behavior. By analogy with the Burgers equation, a Godunov upwind method [41, 83] is

used:

$$F_{i+1/2} = \max \left[(\gamma_i^+)^2, (\gamma_{i+1}^-)^2 \right], \quad \gamma^+ = \max(-\gamma, 0), \quad \gamma^- = \min(-\gamma, 0), \quad (2.8)$$

where i indicates the index of the vortex marker discretizing the sheet. This method approximates the flux at the midpoints between the vortex markers and ensures a proper upwind finite difference relative to the “shock” position. This small change significantly improves the method, allowing the simulation to run to times one order of magnitude larger than schemes based on pure finite differences.

2.1.3 The hybrid Lagrangian-Eulerian vortex method based on the vortex-in-cell algorithm

In vortex-in-cell (VIC) methods, a Cartesian grid is super-imposed onto the Lagrangian vortex markers. The Cartesian grid is used to rapidly compute the velocity field from the vorticity field through the *velocity-streamfunction* formulation. This step avoids the Biot-Savart integral and the complex regularizations needed to overcome the singularity in the kernel. Furthermore, as discussed in Section 2.1.1 the VIC algorithm has a cost of $O(N \log N)$ compared to the $O(N^2)$ cost for the Biot-Savart law.

The VIC algorithm is a special case of a more general class of algorithms developed to compute the force field from charge distributions in *particle-mesh methods* [60]. In these methods, the Laplacian operator is replaced by grid-based finite-difference approximations, resulting in rapid force calculations (or in rapid computations of the velocity field from the vorticity field). In addition, the Cartesian mesh introduces a physical lengthscale, Δx , that eliminates the unphysical correlations as particles come close to each other. In this spirit, Harlow [45, 46] introduced the *particle-in-cell* (PIC) method to overcome the disadvantages of Eulerian formulations that could not track interfaces, and Lagrangian formulations that could not represent regions of shear due to mesh distortions. Harlow simulated advection by moving particles, and used the Eulerian mesh for all non-advective terms, eliminating the problem of mesh distortion. Christiansen [24] later performed hydrodynamic simulations using the area-weighting-rule interpolant and called the algorithm *vortex-in-cell*.

The VIC algorithm consists of the following four steps.

1. The vorticity is assigned from the markers onto the Cartesian grid

$$\omega(x_i, y_j) = \sum_n \frac{\Gamma_n}{h^2} \phi(x_n - x_i, y_n - y_j), \quad (2.9)$$

where (x_n, y_n) is the location of the vortex marker, (x_i, y_j) is the location of the grid point, ϕ is the assignment function, and Γ_n is the circulation [Eq. (2.19)].

2. The Poisson equation

$$\Delta\psi = -\omega \quad (2.10)$$

is solved for the streamfunction $\psi(x, y)$.

3. The velocity field on the Cartesian grid is obtained from the streamfunction

$$\mathbf{u} = \nabla \times \psi. \quad (2.11)$$

4. The velocity field is interpolated onto the markers

$$\mathbf{u}_n = \sum_{i,j} \mathbf{u}_{i,j} \phi(x_n - x_i, y_n - y_i). \quad (2.12)$$

The interpolation and assignment steps are performed using the same function

$$\phi(x, y) = M_i(x) M_i(y), \quad (2.13)$$

where $M_n(x)$ are interpolation kernels based on central B-splines [130]. These kernels are obtained by taking successive partial sums of the polynomial

$$p(x) = \sum_{k=0}^n (-1)^k \binom{n}{k} \left(x + \frac{n}{2} - k\right)^{n-1}, \quad (2.14)$$

yielding the interpolation kernels

$$(n-1)! M_n(x) = \begin{cases} 0 & \text{for } x \leq -\frac{n}{2}, \\ \left(x + \frac{n}{2}\right)^{n-1} & \text{for } -\frac{n}{2} \leq x \leq -\frac{n}{2} + 1, \\ \vdots & \vdots \\ \sum_{k=0}^j (-1)^k \binom{n}{k} \left(x + \frac{n}{2} - k\right)^{n-1} & \text{for } -\frac{n}{2} + j - 1 \leq x \leq -\frac{n}{2} + j. \end{cases} \quad (2.15)$$

The interpolation kernel $M_n(x)$ is an even function of x . The first three interpolation kernels are

$$M_1(x) = \begin{cases} 1 & \text{for } 0 \leq x \leq \frac{1}{2}, \\ 0 & \text{for } x > \frac{1}{2}, \end{cases} \quad M_2(x) = \begin{cases} 1 - |x| & \text{for } |x| \leq 1, \\ 0 & \text{for } |x| > 1, \end{cases} \quad (2.16)$$

$$M_3(x) = \begin{cases} -|x|^2 + \frac{3}{4} & \text{for } 0 \leq |x| \leq 1/2, \\ \frac{1}{2} \left(-|x| + \frac{3}{2}\right)^2 & \text{for } 1/2 \leq |x| \leq 3/2, \\ 0 & \text{for } |x| > 3/2, \end{cases}$$

and are called the *nearest-grid-point* (NGP), *area-weighting-rule* (AWR), and *triangular-shaped-cloud* (TSC) interpolants, respectively.

Here, the vorticity-streamfunction Poisson equation [Eq. (2.10)] is discretized using a fourth-order modified nine-point scheme [61]. The fast Fourier transform is used to invert the block-Toeplitz-symmetric-tridiagonal (TST) finite-difference matrices using *Hockney's method* [59].

2.2 Convergence study for the vortex-in-cell algorithm

Presented here is a convergence study for the vortex-in-cell (VIC) algorithm. This study establishes that in the case of a thin vortex sheet (Sec. 2.2.1), the VIC velocity field does not converge to the Biot-Savart velocity field under grid refinement. To correct this problem, the vortex sheet is thickened to give a *vortex layer*. The velocity from the vortex layer converges to the velocity from the Biot-Savart law as the grid is refined and the thickness of the layer is decreased (Sec. 2.2.2). The classical VIC algorithm can only be used to investigate the Richtmyer-Meshkov instability when fairly coarse Cartesian grids are used. As finer grids are used, the results fail to converge (Sec. 2.2.3)

Consider a vortex sheet with an initial sinusoidal perturbation

$$[x(e), y(e)] = \{x(e), a_0 \cos [k x(e)]\} , \quad (2.17)$$

where a_0 is the perturbation amplitude and k is the perturbation wavenumber. For the Richtmyer-Meshkov instability the initial vortex dipole and vortex sheet strength are

$$\mu(e) = 2 v_0 \cos [k x(e)] , \quad \gamma(e) = \frac{\partial \mu}{\partial e} , \quad (2.18)$$

respectively, where v_0 is a constant. In the present convergence study, the velocity and velocity gradients are determined using the VIC algorithm, as the Cartesian grid is refined ($N_x = 32, 64, 128, 256$) keeping the number of markers $N = 4 N_x$, and are compared with the results from the Biot-Savart law. Results varying the number of markers from $N = 2 N_x$ to $8 N_x$ showed no difference. Each vortex marker has circulation

$$\Gamma_n = \gamma_n \Delta s_n , \quad (2.19)$$

where

$$\Delta s_n = \frac{1}{2} \sqrt{(x_{n+1} - x_{n-1})^2 + (y_{n+1} - y_{n-1})^2} \quad (2.20)$$

is the arclength on the interface. For the VIC algorithm, the circulation is assigned onto the grid using

$$\omega(x_i, y_j) = \sum_n \frac{\Gamma_n}{h^2} M_i(x_n - x_i) M_i(y_n - y_i) , \quad (2.21)$$

where M_i are the interpolation functions [Eq. (2.15)]. To assess the effects of the interpolation functions, the assignment and interpolation steps are performed using the second-order M_4 and M_5 functions

$$M_4(x) = \begin{cases} \frac{2}{3} - |x|^2 + \frac{|x|^3}{2} & \text{for } |x| \leq 1 \\ \frac{1}{6} (-|x| + 2)^3 & \text{for } 1 \leq |x| \leq 1, \\ 0 & \text{for } |x| > 2 \end{cases}, \quad (2.22)$$

$$M_5(x) = \begin{cases} \frac{|x|^4}{4} - \frac{5|x|^2}{8} + \frac{115}{192} & \text{for } |x| \leq \frac{1}{2} \\ -\frac{|x|^4}{6} + \frac{5|x|^3}{6} - \frac{5|x|^2}{4} + \frac{5|x|}{24} + \frac{55}{96} & \text{for } \frac{1}{2} \leq |x| \leq \frac{3}{2} \\ \frac{1}{24} (|x| - \frac{5}{2})^4 & \text{for } \frac{3}{2} \leq |x| \leq \frac{5}{2} \\ 0 & \text{for } |x| > \frac{5}{2} \end{cases}, \quad (2.23)$$

and the third-order modified \widetilde{M}_4 , and fourth-order modified \widetilde{M}_5 interpolants

$$\widetilde{M}_4(x) = \begin{cases} 1 - \frac{5}{2} |x|^2 + \frac{3}{2} |x|^3 & \text{for } |x| \leq 1 \\ \frac{1}{2} (2 - |x|)^2 (1 - |x|) & \text{for } 1 \leq |x| \leq 2, \\ 0 & \text{for } |x| > 2 \end{cases}, \quad (2.24)$$

$$\widetilde{M}_5(x) = \begin{cases} \frac{1}{48} \left(\frac{345}{8} - 75 |x|^2 + 42 |x|^4 \right) & \text{for } |x| \leq \frac{1}{2} \\ \frac{1}{48} \left(\frac{165}{4} + 20 |x| - 150 |x|^2 + 120 |x|^3 - 28 |x|^4 \right) & \text{for } \frac{1}{2} \leq |x| \leq \frac{3}{2} \\ \frac{1}{48} \left(|x| - \frac{5}{2} \right)^3 \left(7 |x| - \frac{15}{2} \right) & \text{for } \frac{3}{2} \leq |x| \leq \frac{5}{2} \\ 0 & \text{for } |x| > \frac{5}{2} \end{cases}. \quad (2.25)$$

The modified interpolants were derived by Monaghan [109] using Richardson extrapolation to improve the second-order convergence of B-spline kernels [Eq. (2.15)].

2.2.1 Convergence study for a thin vortex sheet

Figure 2.2 shows the horizontal velocity $u(e)$ and velocity gradient $\partial u/\partial e$ obtained using the M_4 [Eq. (2.22)] interpolant. As the grid is refined, the velocity converges; however, the velocity gradient does not converge, as indicated by the large oscillations that develop on the finer grids because the thin vortex sheet is singular. For coarse grids, the smoothing introduced by the grid spacing Δx is sufficient to stabilize the low wavenumber instabilities associated with the evolution of a vortex sheet. In fact, Zufiria [160] showed that the Cartesian grid stabilizes the computation by an effect that is equivalent to surface tension. However, as the grid is refined, the effective surface tension decreases and the method becomes progressively more unstable. The convergence study can be

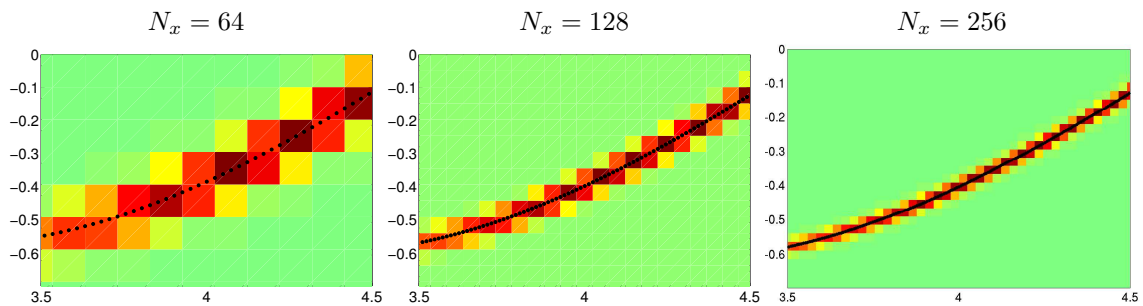


Figure 2.1. Vorticity field on the Cartesian grid using the $M_4(x)$ interpolant for a thin vortex sheet as the grid is refined with $N_x = 64$, 128, and 256.

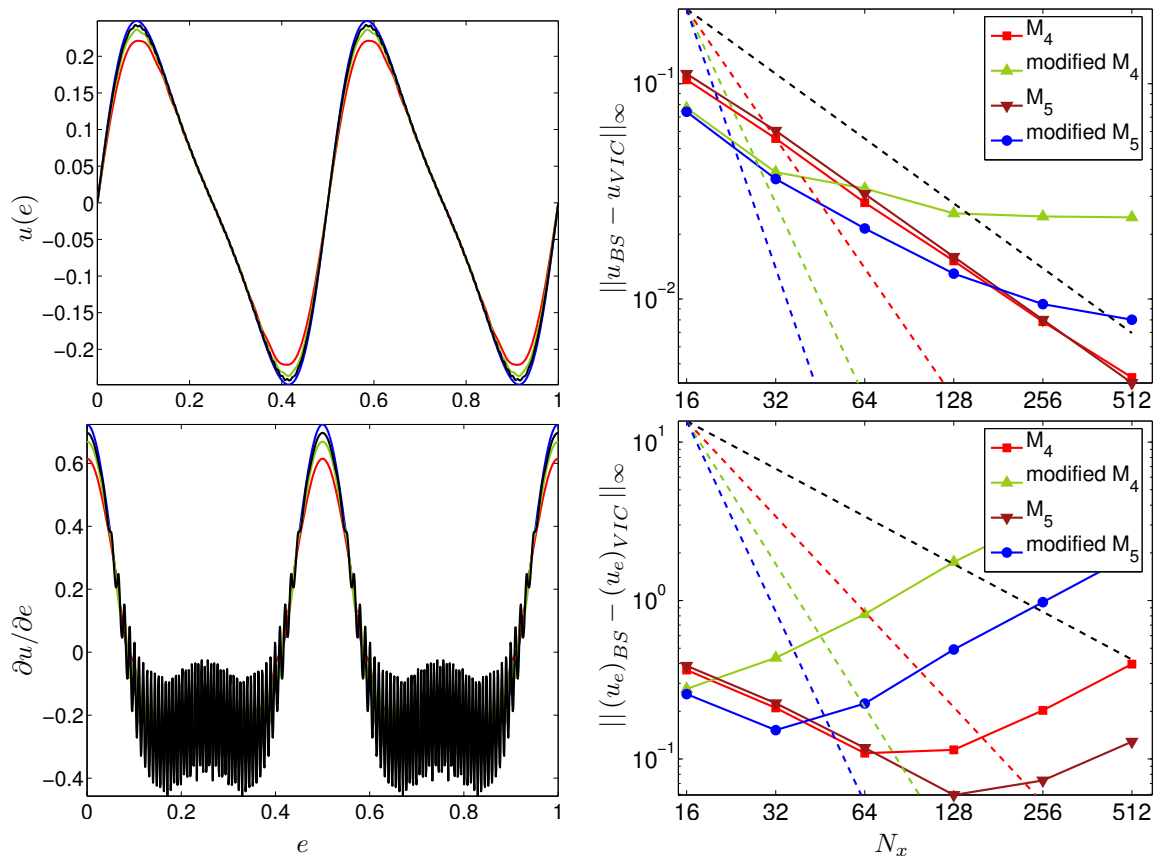


Figure 2.2. Comparison of the horizontal velocity $u(e)$ and velocity gradient $\partial u/\partial e$ on the interface for the VIC algorithm applied to the thin vortex sheet using the M_4 interpolant (left). The blue line is the Biot-Savart solution, the red line is the VIC solution with $N_x = 64$ and $N = 256$, the green line is the solution with $N_x = 128$ and $N = 512$, and the black line represents the solution for $N_x = 256$ and $N = 1024$. Also shown is the ℓ^∞ -error for the horizontal and vertical velocity fields for the VIC algorithm applied to the thin vortex sheet as the Eulerian grid is refined (right): dotted black line N_x^{-1} , dotted red line N_x^{-2} , dotted green line N_x^{-3} , and dotted blue line N_x^{-4} .

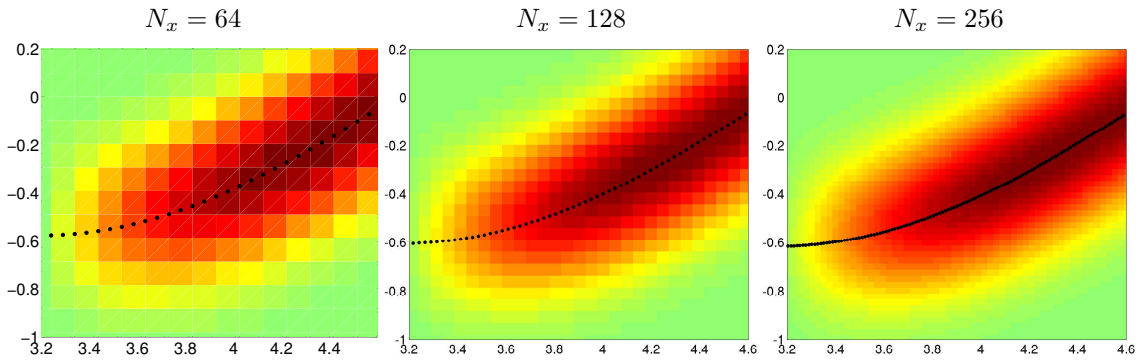


Figure 2.3. Vorticity field on the Cartesian grid using the $M_4(x)$ interpolant for a thick vortex layer with $\delta_T = 0.15$, as the grid is refined with $N_x = 64$, 128, and 256.

made quantitative by computing the ℓ^∞ -norm of the difference between the velocity from the Biot-Savart law and the velocity from the VIC algorithm under different interpolation algorithms. As the grid is refined, the horizontal and vertical velocities show first-order convergence to the Biot-Savart velocity using the M_4 and M_5 interpolants, while no convergence is observed for \widetilde{M}_4 and \widetilde{M}_5 . This is in contrast to the second-order convergence rate expected for M_4 and M_5 and the third- and fourth-order convergence rates expected for \widetilde{M}_4 and \widetilde{M}_5 , respectively. The velocity gradient diverges as oscillations develop. Thus, the velocity obtained from the classical VIC algorithm does not converge to the velocity obtained from the Biot-Savart law for the thin vortex sheet.

2.2.2 Convergence study for a thick vortex layer

The divergence in the VIC method applied to the (thin) vortex sheet is resolved here by thickening the vorticity, creating a thick vortex layer. Thickening is obtained using the Gaussian interpolant

$$L_g(x, \delta_T, \Delta x) = \frac{\Delta x}{\delta_T \sqrt{2\pi}} \exp\left(-\frac{x^2}{2\delta_T^2}\right), \quad (2.26)$$

where δ_T is the thickness and Δx is the grid spacing, to assign the vorticity onto the Cartesian grid. This provides a lengthscale δ_T for the vortex layer that is independent of the grid resolution Δx . It is shown here that the simultaneous reduction of the grid spacing Δx and interface thickness δ_T produces initial conditions that converge to the Biot-Savart solution.

The convergence study is divided into three parts. In the first part, the convergence of the VIC algorithm is demonstrated for a fixed width ($\delta_T = 0.15$). Next, the convergence to the Biot-Savart solution as $\delta_T \rightarrow 0$ and $\Delta x/\delta_T$ is kept fixed, is demonstrated. Finally, to increase the rate of convergence, Richardson extrapolation is used.

Consider the case of a thickened vortex layer, as the grid is refined keeping the layer thickness $\delta_T = 0.15$ fixed. An illustration of the vortex markers and the vorticity assigned on the Cartesian

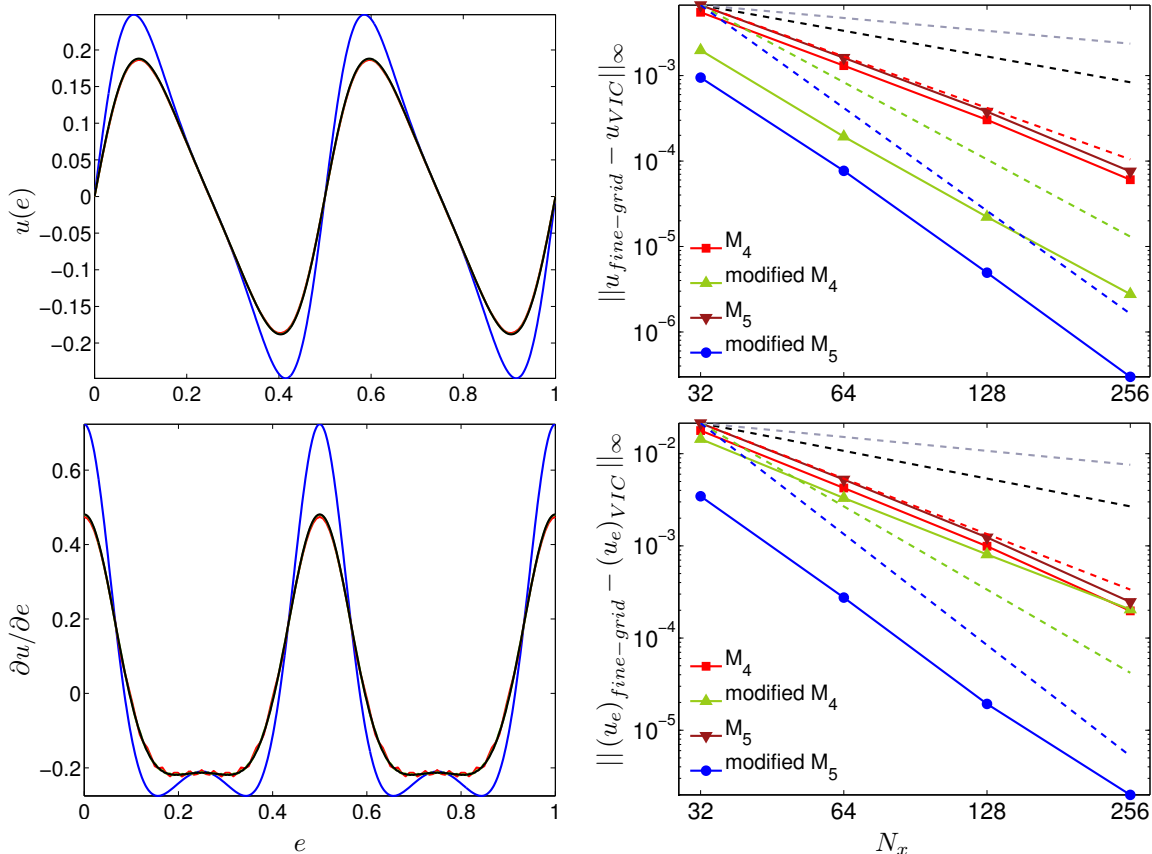


Figure 2.4. Comparison of the horizontal velocity $u(e)$ and velocity gradient $\partial u / \partial e$ on the interface for the VIC algorithm applied to the thick vortex sheet using the M_4 interpolant and with fixed $\delta_T = 0.15$ (left). Also shown is the ℓ^∞ -error for the horizontal and vertical velocity fields for the VIC algorithm applied to the thin vortex sheet as the Eulerian grid is refined (right). See Figure 2.2 for the legend.

grid is shown in Figure 2.3. Figure 2.4 shows the convergence results for fixed thickness $\delta_T = 0.15$. The velocity does not converge to the Biot-Savart result, but to a smaller value. The convergence analysis provides the ℓ^∞ -norm of the difference between the solution on the fine grid and the solution on the coarser grids. The expected rates of convergence are obtained: second-order for the M_4 and M_5 interpolants, third-order for \widetilde{M}_4 , and fourth-order for \widetilde{M}_5 .

In the second part of the convergence study, the width of the vortex layer δ_T is decreased simultaneously with the reduction of the grid spacing Δx . Figure 2.5 shows the vorticity assigned on the Cartesian grid, indicating that as the grid resolution is doubled, the thickness is halved.

Figure 2.6 shows that the velocity field approaches the Biot-Savart result. The ℓ^∞ -norm of the difference between the Biot-Savart and VIC results shows first-order convergence. Richardson extrapolation is applied to the initial vorticity distribution to accelerate the convergence rate of the velocity and velocity gradients on the interface to the Biot-Savart results. Richardson extrapolation

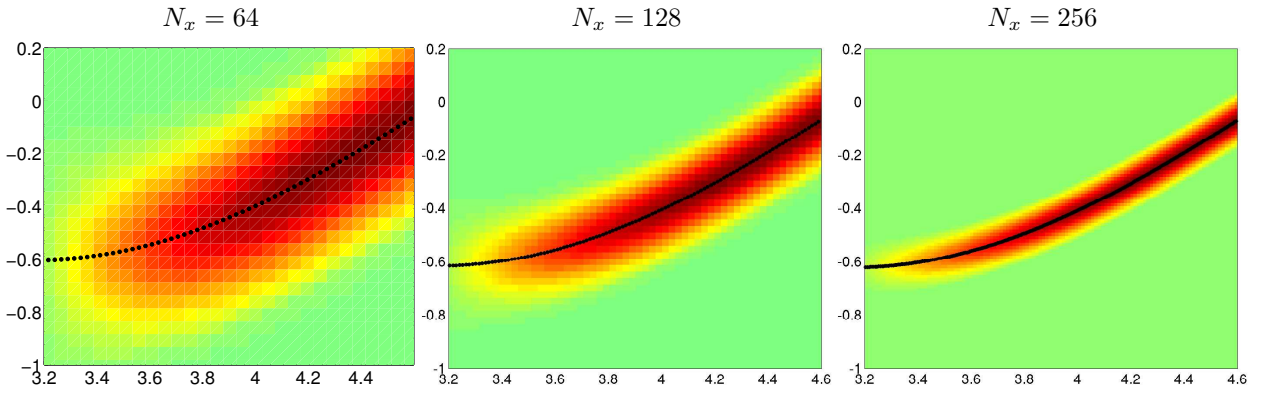


Figure 2.5. Vorticity field on the Cartesian grid using the $M_4(x)$ interpolant for a thick vortex layer as the thickness is decreased keeping $\delta_T/\Delta x$ fixed for $N_x = 64, 128,$ and 256 .

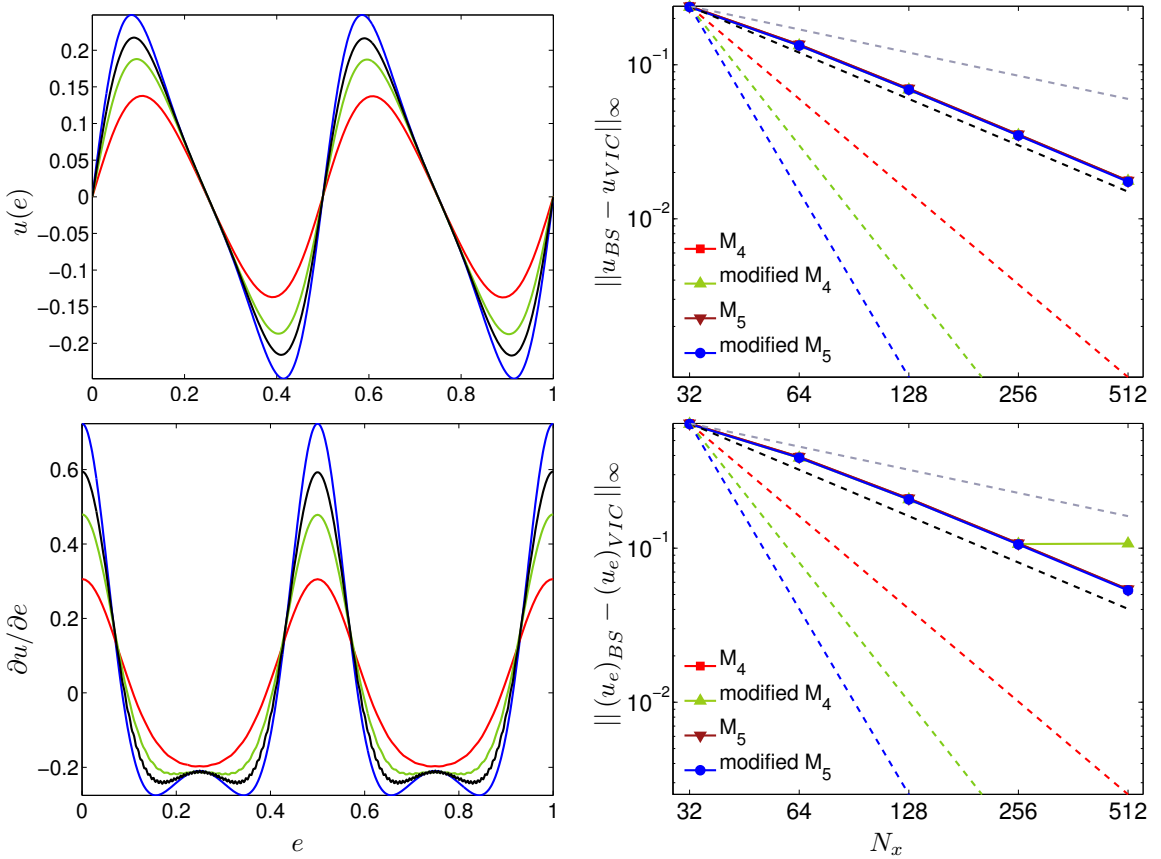


Figure 2.6. Comparison of the horizontal velocity $u(e)$ and velocity gradient $\partial u/\partial e$ on the interface for the VIC algorithm applied to the thick vortex sheet using the M_4 interpolant and with fixed $\delta_T/\Delta x$ (left). Also shown is the ℓ^∞ -error for the horizontal and vertical velocity fields for the VIC algorithm applied to the thin vortex sheet as the Eulerian grid is refined (right). See Figure 2.2 for the legend.

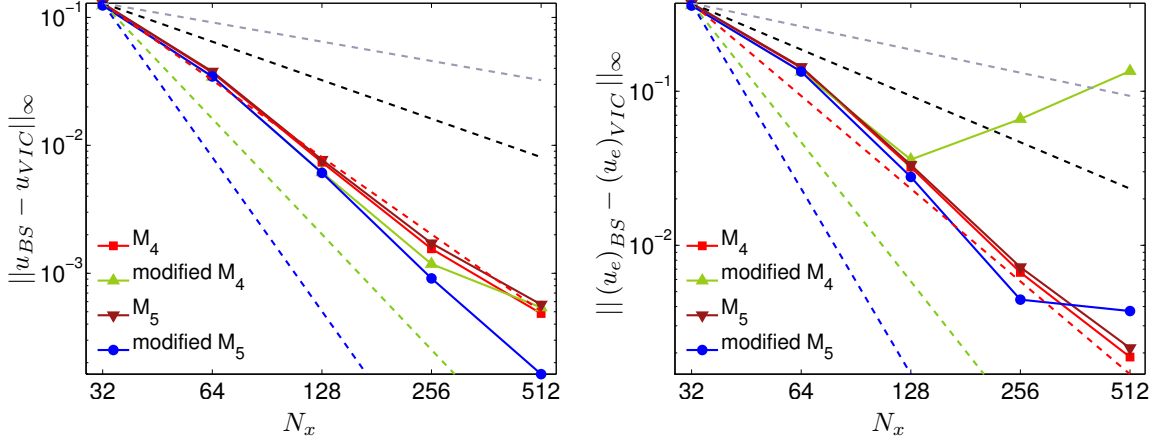


Figure 2.7. The ℓ^∞ -error for the horizontal velocity and velocity gradient with fixed $\delta_T/\Delta x$ and Richardson extrapolation. See Figure 2.2 for the legend.

eliminates the leading error in the first-order convergence as δ_T . Consider two vorticity distributions ω_{δ_T} and $\omega_{\delta_T/2}$. Let q_{δ_T} and $q_{\delta_T/2}$ be the corresponding velocity fields. As shown in the previous section, the velocity field has expansion

$$q = q_{\delta_T} + K \delta_T + K_1 \delta_T^n, \quad (2.27)$$

which is first-order in δ_T . For $\delta_T/2$ the velocity has expansion

$$q = q_{\delta_T/2} + K \frac{\delta_T}{2} + K_1 \left(\frac{\delta_T}{2}\right)^n. \quad (2.28)$$

Combining (2.27) and (2.28) gives the new Richardson extrapolation for the velocity

$$q_{new} = 2q_{\delta_T/2} - q_{\delta_T} + O(\delta_T^n). \quad (2.29)$$

Equation (2.29) removes the first-order error and leaves an error of order n . The results using Richardson extrapolation are shown in Figure 2.7, indicating that the convergence rate for the velocity and velocity gradient fields is improved to second order for the M_4 and M_5 interpolants. When the \widetilde{M}_4 and \widetilde{M}_5 interpolants are used, the convergence rate for the velocity increases to third order, but as the grid is refined no convergence is observed in the gradients. As \widetilde{M}_4 is fourth-order, this indicates that $n = 3$ in Equation (2.29).

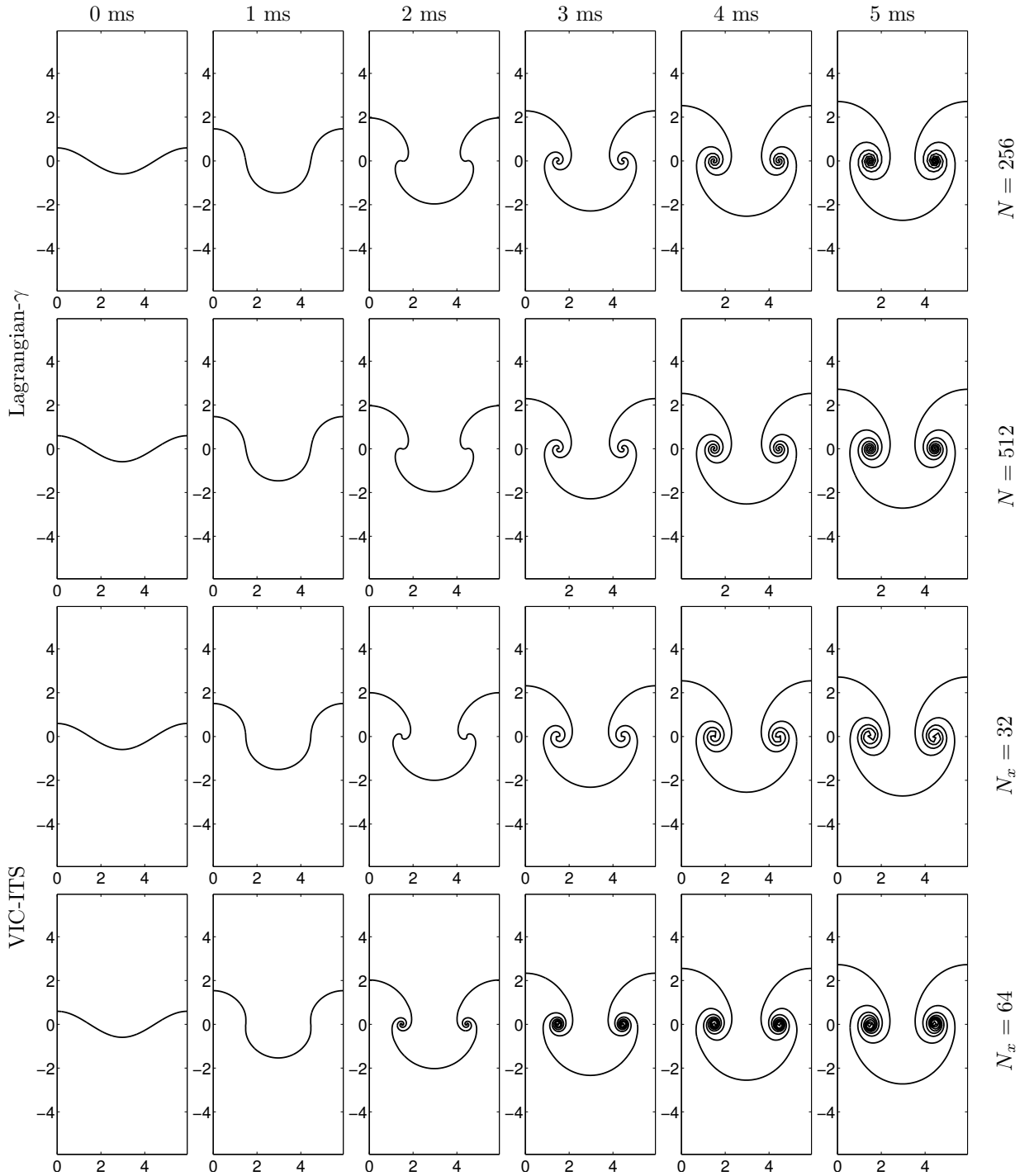


Figure 2.8. Time-evolution of the interface for the Richtmyer-Meshkov instability with $A = 0$ using the Lagrangian- γ formulation with $N = 256$ and 512 vortex markers and the vortex-in-cell iterative-time-step (VIC-ITS) formulation at $0, 1, 2, 3, 4,$ and 5 ms with a grid resolution of $N_x \times N_y = 32 \times 128$ with $N = 256$ vortex markers and $N_x \times N_y = 64 \times 256$ with $N = 512$ vortex markers when the $M_4(x)$ interpolant is used.

2.2.3 Vortex-sheet evolution by the vortex-in-cell and Lagrangian vortex methods

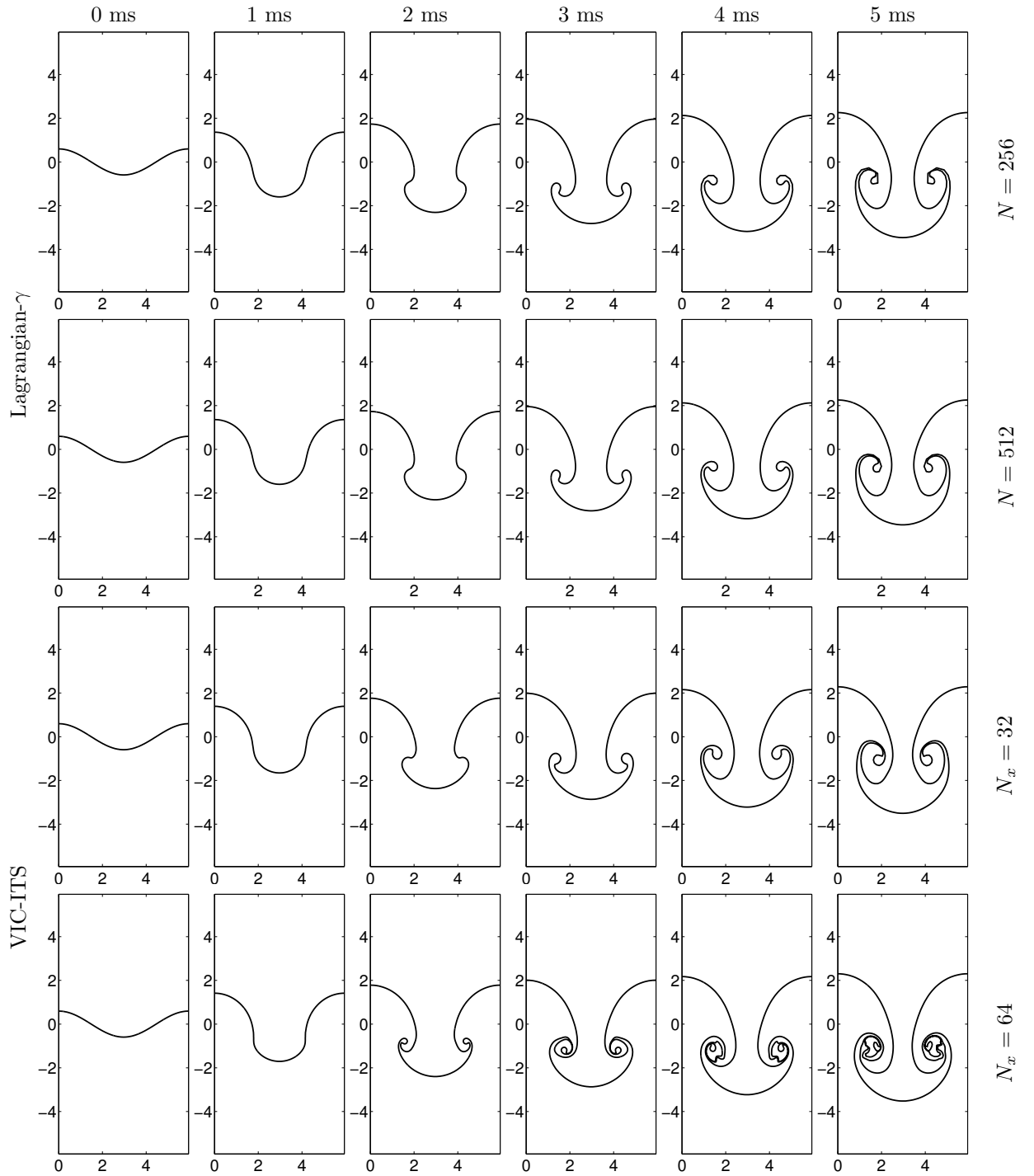
Although the initial velocity gradient from the VIC algorithm does not converge to that from the Biot-Savart law, this algorithm has been successfully applied to the Richtmyer-Meshkov instability (Sec. 2.1.1). Here a comparison of the classical Lagrangian and VIC algorithm is presented for $A = 0$ and 0.4 as the grid is refined.

Figure 2.8 shows the time-evolution of the vortex sheet for $A = 0$ when the Lagrangian- γ method is used with $N = 256$ and 512 markers. The Lagrangian- γ method gives similar results as the number of markers is doubled, including details inside the roll-up. The parameter governing the evolution of the vortex sheet in the Lagrangian- γ method is the length-scale δ (used to form vortex blobs in the regularization of the Biot-Savart law). Also shown are the results from the VIC method using the iterative-time-step formulation (VIC-ITS) [141] as the grid is refined from $N_x = 32$ (corresponding to $N = 256$ markers) to $N_x = 64$ (corresponding to $N = 512$ markers). As the grid is refined, additional structure is observed in the roll-up. In fact, the length-scale governing the VIC method is the grid spacing Δx .

Figure 2.9 shows the time-evolution of the Richtmyer-Meshkov instability under the Lagrangian- γ method for $A = 0.4$ with $N = 256$ and 512 markers. For $A = 0.4$, the Lagrangian- γ method gives identical results as the number of markers increases. This is expected as the length-scale affecting the instability development is the size of the vortex blob δ . Also shown is the time-evolution of the instability when the VIC-ITS method is used. The results for $N_x = 32$ are very similar to the results from the Lagrangian- γ method. However, for $N_x = 64$ the VIC-ITS method shows the development of additional unstable structure inside the roll-up. In fact, the only stabilization mechanism in the VIC algorithm is provided by the grid spacing Δx . For $N_x = 32$ such a grid spacing is sufficient to give results comparable with the Lagrangian- γ methods. However, for $N_x = 64$, the smaller grid spacing is no longer sufficient, so that oscillations develop on the interface.

2.3 The vorticity-streamfunction method

Developed in this thesis is a vorticity-streamfunction (VS) method for the simulation of the Richtmyer-Meshkov instability, motivated by limitations of the classical (thin) vortex sheet approaches (Sec. 2.3.1). In this method, the vorticity equation on the Cartesian grid is augmented by the baroclinic vorticity production term to capture the effects of the instability (Sec. 2.3.2). The equations are discretized using a semi-implicit fourth-order in space and third-order in time Adams-Bashforth backward differentiation scheme (Sec. 2.3.3).

Figure 2.9. Same as Figure 2.8 but with $A = 0.4$.

2.3.1 Motivation for developing the method

Vorticity-streamfunction methods solve the vorticity transport equation [Eq. (2.30)] and are part of a wider class of methods developed for incompressible flows (i.e. when the velocity, as measured by the Mach number, is $Ma < 0.3$ [25]). These methods constitute an alternative to *velocity-pressure* methods. The vorticity-streamfunction and velocity-pressure formulations are equivalent [44]. One advantage of VS methods is that the velocity is divergence-free by construction. Furthermore, the mathematical properties of the equations allow the construction of robust solution methods [117].

The VS method is motivated by current limitations in classical vortex method approaches for simulating this instability. (1) In the classical Lagrangian vortex method (Sec. 2.1.2), the evolution of the vortex sheet requires complex regularizations to mitigate the formation of the singularity during the rollup. In addition, a redistribution of the vortex markers may be necessary, and the numerical method may cease to provide solutions at late times. Classical Lagrangian vortex methods have been extended to three dimensions for the evolution of a vortex sheet [47]. (2) It was shown in Section 2.2 that the VIC method does not converge under grid refinement. This result is due to the singular limit of the vortex sheet. Furthermore, the VIC method does not constitute a valid computational method for the simulation of vortex sheet dynamics, as the method breaks down upon grid refinement. The VIC method has not been extended to three dimensions for the Richtmyer-Meshkov instability.

The VS method resolves the singular limit of a vortex sheet by thickening it to obtain a vortex layer (Sec. 2.2.2). This has the desirable feature of providing a “physical” solution to the instability problem (the thickening of the vortex sheet may be equivalent to the diffuse interface in the Jacobs and Krivets [62] experiments). This is in contrast to the “unphysical” length-scale introduced by using vortex blobs (in the Lagrangian- γ method) and the grid spacing Δx (in the VIC method). Furthermore, the numerical method can be easily extended to three dimensions.

2.3.2 Governing equations

The three-dimensional vorticity equation for an incompressible viscous flow is

$$\frac{\partial \boldsymbol{\omega}}{\partial t} + \mathbf{u} \cdot \nabla \boldsymbol{\omega} = \boldsymbol{\omega} \cdot \nabla \mathbf{u} + \frac{\nabla \rho \times \nabla p}{\rho^2} + \nu \Delta \boldsymbol{\omega}, \quad (2.30)$$

where $\nu = \mu/\rho$ is the kinematic viscosity and μ is the dynamic viscosity. To formulate a numerical method, additional equations for the velocity $\mathbf{u} = (u, v, w)$, pressure p , and density ρ need to supplement Equation (2.30).

The density is obtained by solving the continuity equation

$$\frac{\partial \rho}{\partial t} + \nabla \cdot (\rho \mathbf{u}) = 0. \quad (2.31)$$

As the gases are miscible, diffusion is modeled as Fickian so that the mass flux of the heavy gas is

$$\mathbf{j} = -\rho \mathcal{D} \nabla m, \quad (2.32)$$

where \mathcal{D} is the *mass diffusivity* and m is the mass fraction. This gives the modified density equation (see Cabot, Schilling, and Zhou [20] and Cook and Dimotakis [28] for the derivation)

$$\frac{\partial \rho}{\partial t} + \mathbf{u} \cdot \nabla \rho = -\frac{\mathcal{D}}{\rho} (\nabla \rho \cdot \nabla \rho) + \mathcal{D} \Delta \rho, \quad (2.33)$$

where the mass diffusivity is chosen so that the *Schmidt number* $Sc \equiv \nu/\mathcal{D} = 1$ is consistent with gas properties. The velocity is obtained from the vorticity-streamfunction Poisson equation

$$\Delta \psi = -\omega, \quad (2.34)$$

$$\mathbf{u} = \nabla \times \psi, \quad (2.35)$$

where $\psi = (\psi_1, \psi_2, \psi_3)$ is the vector streamfunction. The pressure is obtained by taking the divergence of the momentum equation

$$\frac{\partial \mathbf{u}}{\partial t} + \mathbf{u} \cdot \nabla \mathbf{u} = -\frac{\nabla p}{\rho} + \nu \Delta \mathbf{u} \quad (2.36)$$

to obtain the pressure Poisson equation

$$\Delta p = -\rho \nabla \cdot (\mathbf{u} \cdot \nabla \mathbf{u}). \quad (2.37)$$

To determine the boundary conditions for Equations (2.34) and (2.37), consider a periodic box in the x and y directions with rigid walls at the top and bottom (z direction) $[0, L_x] \times [0, L_y] \times [0, L_z]$. The boundary value problem for the streamfunction is

$$\begin{cases} \Delta \psi = -\omega \\ \psi(x, y, 0) = 0, \quad \psi(x, y, L_z) = 0 \end{cases}, \quad (2.38)$$

which represents three separate boundary value problems for each ψ_1 , ψ_2 , and ψ_3 .

The boundary value problem for the pressure is

$$\begin{cases} \Delta p = -\rho \nabla \cdot (\mathbf{u} \cdot \nabla \mathbf{u}) \\ \frac{\partial p}{\partial y}(x, y, 0) = 0, \quad \frac{\partial p}{\partial y}(x, y, L_z) = 0 \end{cases}. \quad (2.39)$$

Equations (2.30) and (2.33) supplemented by the boundary value problems for the streamfunction

and pressure [Eqs. (2.38) and (2.39)] and for the velocity from the streamfunction [Eq. (2.35)] constitute a complete VS method in three dimensions.

2.3.3 Spatial and temporal discretization

In the vorticity and density equations [Eqs. (2.30) and (2.33)], separate the spatial operator into linear diffusion and nonlinear transport terms:

$$\frac{\partial \boldsymbol{\omega}}{\partial t} = \mathbf{N}(\boldsymbol{\omega}, \rho) + \mathbf{L}(\nu, \boldsymbol{\omega}), \quad (2.40)$$

$$\mathbf{N}(\boldsymbol{\omega}, \rho) = -\mathbf{u} \cdot \nabla \boldsymbol{\omega} + \boldsymbol{\omega} \cdot \nabla \mathbf{u} + \frac{\nabla \rho \times \nabla p}{\rho^2}, \quad (2.41)$$

$$\mathbf{L}(\nu, \boldsymbol{\omega}) = \nu \Delta \boldsymbol{\omega}, \quad (2.42)$$

and

$$\frac{\partial \rho}{\partial t} = N_\rho(\mathbf{u}, \rho) + L_\rho(\mathcal{D}, \rho), \quad (2.43)$$

$$N_\rho(\mathbf{u}, \rho) = -\nabla \cdot (\rho \mathbf{u}) - \frac{\mathcal{D}}{\rho} (\nabla \rho \cdot \nabla \rho), \quad (2.44)$$

$$L_\rho(\mathcal{D}, \rho) = \mathcal{D} \Delta \rho. \quad (2.45)$$

The governing equations are discretized using a *semi-implicit* scheme where the linear viscous part $\mathbf{L}(\nu, \boldsymbol{\omega})$ is treated implicitly and the nonlinear part $\mathbf{N}(\rho, \boldsymbol{\omega})$ is treated explicitly. This overcomes the time-step limitations of a purely explicit formulation, and the need for complex nonlinear solvers for a fully implicit formulation.

The third-order Adams-Bashforth backward differentiation (AB/BDI3) scheme is adopted for the time-stepping, which uses multiple time-levels for both the temporal and spatial operators:

$$\begin{aligned} \frac{1}{\Delta t} \left(\frac{11}{6} \omega^{n+1} - 3 \omega^n + \frac{3}{2} \omega^{n-1} - \frac{1}{3} \omega^{n-2} \right) &= 3 N(\omega^n, \rho^n) - 3 N(\omega^{n-1}, \rho^{n-1}) \\ &+ N(\omega^{n-2}, \rho^{n-2}) + L(\nu, \omega^{n+1}), \end{aligned} \quad (2.46)$$

$$\begin{aligned} \frac{1}{\Delta t} \left(\frac{11}{6} \rho^{n+1} - 3 \rho^n + \frac{3}{2} \rho^{n-1} - \frac{1}{3} \rho^{n-2} \right) &= 3 N_\rho(u^n, v^n, \rho^n) \\ &- 3 N_\rho(u^{n-1}, v^{n-1}, \rho^{n-1}) \\ &+ N_\rho(u^{n-2}, v^{n-2}, \rho^{n-2}) + L_\rho(\mathcal{D}, \rho^{n+1}). \end{aligned} \quad (2.47)$$

An analysis shows that the region of stability is largest among the Adams-Bashforth backward differentiation methods.

The final implicit linear equation that must be solved is a Helmholtz equation of the form

$$\Delta u + \lambda u = f. \quad (2.48)$$

A modified nine-point method is used to solve this equation by following the same procedure as in the derivation of the modified nine-point method for the Poisson equation [61].

Consider the error for a second-order finite-difference for the second derivative,

$$\Delta_{0,x}^2 = h^2 \mathcal{D}_x^2 + \frac{h^4}{12} \mathcal{D}_x^4 + O(h^6), \quad (2.49)$$

where $\mathcal{D}_x \equiv d/dx$ is the derivative operator and $\Delta_{0,x}$ is the central difference operator (so that $\Delta_{0,x} x_i = x_{i+\frac{1}{2}} - x_{i-\frac{1}{2}}$). Applying Equation (2.49) to a second-order nine-point scheme shows that the error scales as

$$\frac{1}{h^2} \left(\Delta_{0,x}^2 + \Delta_{0,y}^2 + \frac{\Delta_{0,x}^2 \Delta_{0,y}^2}{6} \right) = \Delta + \frac{h^2}{12} \Delta^2 + O(h^4). \quad (2.50)$$

As a result, a second-order nine-point scheme can be made fourth-order by considering the nine-point scheme for

$$\left(\Delta + \frac{h^2}{12} \Delta^2 \right) u = f - \lambda u. \quad (2.51)$$

After inversion, the solution of

$$\Delta u = \left(I + \frac{h^2}{12} \Delta \right) (f - \lambda u) \quad (2.52)$$

leads to the modified nine-point scheme for the Helmholtz equation [Eq. (2.48)],

$$\begin{aligned} \frac{1}{h^2} \left(\Delta_{0,x}^2 + \Delta_{0,y}^2 + \frac{\Delta_{0,x}^2 + \Delta_{0,y}^2}{6} \right) u_{k,\ell} &= \left(I + \frac{\Delta_{0,x}^2 + \Delta_{0,y}^2}{12} \right) f_{k,\ell} \\ &\quad - \lambda \left(I + \frac{\Delta_{0,x}^2 + \Delta_{0,y}^2}{12} \right) u_{k,\ell}, \end{aligned} \quad (2.53)$$

or re-arranging terms,

$$\begin{aligned} &\frac{1}{h^2} \left[\frac{u_{k+1,\ell+1}}{6} + \left(\frac{2}{3} + \frac{\lambda h^2}{12} \right) u_{k+1,\ell} + \frac{u_{k,\ell-1}}{6} + \left(\frac{2}{3} + \frac{\lambda h^2}{12} \right) u_{k,\ell+1} \right. \\ &+ \left. \left(\frac{2\lambda h^2}{3} - \frac{10}{3} \right) u_{k,\ell} + \left(\frac{2}{3} + \frac{\lambda h^2}{12} \right) u_{k,\ell-1} + \frac{u_{k-1,\ell+1}}{6} + \left(\frac{2}{3} + \frac{\lambda h^2}{12} \right) u_{k-1,\ell} + \frac{u_{k,\ell-1}}{6} \right] = \\ &\quad \frac{f_{k+1,\ell}}{12} + \frac{f_{k,\ell+1}}{12} + \frac{2f_{k,\ell}}{3} + \frac{f_{k,\ell-1}}{12} + \frac{f_{k,\ell-1}}{12}. \end{aligned} \quad (2.54)$$

This stencil for the scheme is represented in Table 2.1. A similar procedure is followed to derive the scheme in three dimensions. The stencil in three dimensions is shown in Table 2.2.

Modified nine-point stencil for the Helmholtz equation in two dimensions								
$\frac{1}{6}$	$\frac{2}{3} + \frac{\lambda h^2}{12}$	$\frac{1}{6}$			$\frac{1}{12}$			
$\frac{2}{3} + \frac{\lambda h^2}{12}$	$-\frac{10}{3} + \frac{2\lambda h^2}{3}$	$\frac{2}{3} + \frac{\lambda h^2}{12}$	$u_{k,\ell} = h^2$	$\frac{1}{12}$	$\frac{2}{3}$	$\frac{1}{12}$	$f_{k,\ell}$	
$\frac{1}{6}$	$\frac{2}{3} + \frac{\lambda h^2}{12}$	$\frac{1}{6}$			$\frac{1}{12}$			

Table 2.1. The computational stencil for the fourth-order finite-difference modified nine-point scheme used to discretize the Helmholtz equation [Eq. (2.48)] in two dimensions. The table presents a 3×3 block corresponding to the coefficients of $u_{k,\ell}$ and $f_{k,\ell}$.

Modified nine-point stencil for the Helmholtz equation in three dimensions								
$\frac{1}{6}$	$\frac{1}{3} + \frac{\lambda h^2}{12}$	$\frac{1}{6}$			$\frac{1}{12}$			$m+1$
$\frac{1}{6}$	$\frac{1}{3} + \frac{\lambda h^2}{12}$	$\frac{1}{6}$	$u_{k,\ell,m} = h^2$	$\frac{1}{12}$	$\frac{1}{2}$	$\frac{1}{12}$	$f_{k,\ell,m}$	m
$\frac{1}{3} + \frac{\lambda h^2}{12}$	$-4 + \frac{\lambda h^2}{2}$	$\frac{1}{3} + \frac{\lambda h^2}{12}$			$\frac{1}{12}$	$\frac{1}{2}$		
$\frac{1}{6}$	$\frac{1}{3} + \frac{\lambda h^2}{12}$	$\frac{1}{6}$			$\frac{1}{12}$			$m-1$

Table 2.2. The computational stencil for the fourth-order finite-difference modified nine-point scheme used to discretize the Helmholtz equation [Eq. (2.48)] in three dimensions. The table presents three 3×3 block grids corresponding to the coefficients of $u_{k,\ell,m}$ and $f_{k,\ell,m}$. The first block contains the coefficients for $u_{k,\ell,m+1}$ and $f_{k,\ell,m+1}$, the second block the coefficients for $u_{k,\ell,m}$ and $f_{k,\ell,m}$, and the third block the coefficients for $u_{k,\ell,m-1}$ and $f_{k,\ell,m-1}$.

Chapter 3

Investigation of Convergence of the Vorticity-Streamfunction Method

The vorticity-streamfunction (VS) method developed here depends on several numerical and physical parameters. The numerical parameters include the grid spacing Δx , the time step Δt , the CFL number, and the number of grid points N_x . The physical parameters are divided into parameters for the vortex layer, including the layer thickness δ_T , the viscosity ν , and the mass diffusivity \mathcal{D} , and physical parameters for the problem, including the initial perturbation amplitude and wavenumber, a_0 and λ , respectively, the Atwood number A , and the initial vortex sheet velocity v_0 . All of these parameters affect the evolution of the vortex layer. In this chapter, the dependence of the solution on the numerical and vortex-layer parameters is investigated. The dependence on A , v_0 , and a_0 is investigated in Chapter 4.

This chapter is organized as follows. The dependence of the evolution of a vortex layer on numerical parameters is investigated in Section 3.1. The dependence on vortex-layer parameters is investigated in Section 3.2.

3.1 Spatial and temporal convergence for fixed vortex-layer thickness

Investigated here are the effects of grid spacing Δx and time step size Δt on the evolution of a vortex layer with fixed thickness $\delta_T = 0.4$ cm under the VS method. The initial vorticity is

$$\omega(x_i, y_j) = \sum_n \frac{\Gamma_n}{h^2} L_{g,2D}(x_n - x_i, y_n - y_i, h, \delta_T), \quad (3.1)$$

where $L_{g,2D}$ is the two-dimensional Gaussian [Eq. (2.26)] and Γ_i is the initial circulation of the markers used to discretize the center of the layer [Eq. (2.19)]. The initial density is a hyperbolic

A	ν	$N_x = 32$	$N_x = 64$	$N_x = 128$	$N_x = 256$	$N_x = 512$
0	0	VS-00-32 (solid blue)	VS-00-64 (dashed blue)	VS-00-128 (solid red)	VS-00-256 (dashed red)	VS-00-512 (solid green)
0	3×10^{-3}	VS-03-32 (solid blue)	VS-03-64 (dashed blue)	VS-03-128 (solid red)	VS-03-256 (dashed red)	VS-03-512 (solid green)
0.4	3×10^{-3}	VS-43-32 (solid blue)	VS-43-64 (dashed blue)	VS-43-128 (solid red)	VS-43-256 (dashed red)	VS-43-512 (solid green)

Table 3.1. Keys used to denote simulations for the convergence study using different grid resolutions.

tangent previously used by Saffman and Meiron [125] and Meloon [94],

$$\rho(x_i, y_j) = \frac{\rho_1 + \rho_2}{2} \left\{ 1 + A \tanh \left[\frac{y_j - a_0 \cos(k x_i)}{\delta_T} \right] \right\}, \quad (3.2)$$

where A is the Atwood number [Eq. (1.13)] and $k = 2\pi/\lambda$ is the wavenumber with wavelength $\lambda = 5.94$ cm. In the present simulations, $\rho_2 = 1$ and $\rho_1 = (\rho_2 - A\rho_2)/(1 + A)$.

Simulations are performed in a rectangular domain $[0, L_x] \times [-L_b, L_t] = [0, 5.94] \times [-11.88, 11.88]$ for grid resolutions $N_x \times 4N_x$ where $N_x = 32, 64, 128, 256,$ and 512 , so that N_x is the number of points per initial perturbation wavelength. When $\nu = \mathcal{D} = 0$ (Sec. 3.1.1), oscillations develop due to the formation of steep density and vorticity gradients. As the grid is refined, the oscillations occur at later times. Thus, viscosity and mass diffusivity are introduced to prevent the formation of oscillations. Both in the case of zero Atwood number (Sec. 3.1.2) and nonzero Atwood number (Sec. 3.1.3), similar small-scale features form as the grid is refined and the thickness δ_T is kept fixed. Third-order in time and fourth-order in space point-wise convergence is demonstrated. Table 3.1 shows the simulations performed, together with the keys used to denote the simulations.

3.1.1 Results for zero viscosity and mass diffusivity

Figure 3.1 shows the time-evolution of the mass fraction field for the evolution of a vortex layer when the viscosity ν and mass diffusivity \mathcal{D} are zero as the grid is refined keeping the layer thickness $\delta_T = 0.4$ cm fixed. The results are obtained using the VS method for $A = 0$. For $N_x = 64$, the change in color at 1 ms for the mass fraction field $m(x, y)$ corresponds to the onset of oscillations. The red color at 0 ms corresponds to $m = 1$, and the blue color to $m = 0$. At 1 ms, the change in color indicates that regions with values larger than unity and smaller than zero form due to oscillations that develop in the presence of steep gradients. These steep gradients form when the instability develops, as the top fluid pushes onto the bottom fluid in the spike region, and the bottom fluid “rises” into the top fluid in the bubble region. These oscillations become stronger at later times, as demonstrated by the lighter colors at later times. For $N_x = 128$, oscillations are not present at 1 ms, but are already visible at 3 ms. For the $N_x = 256$ and 512 cases, the change in color

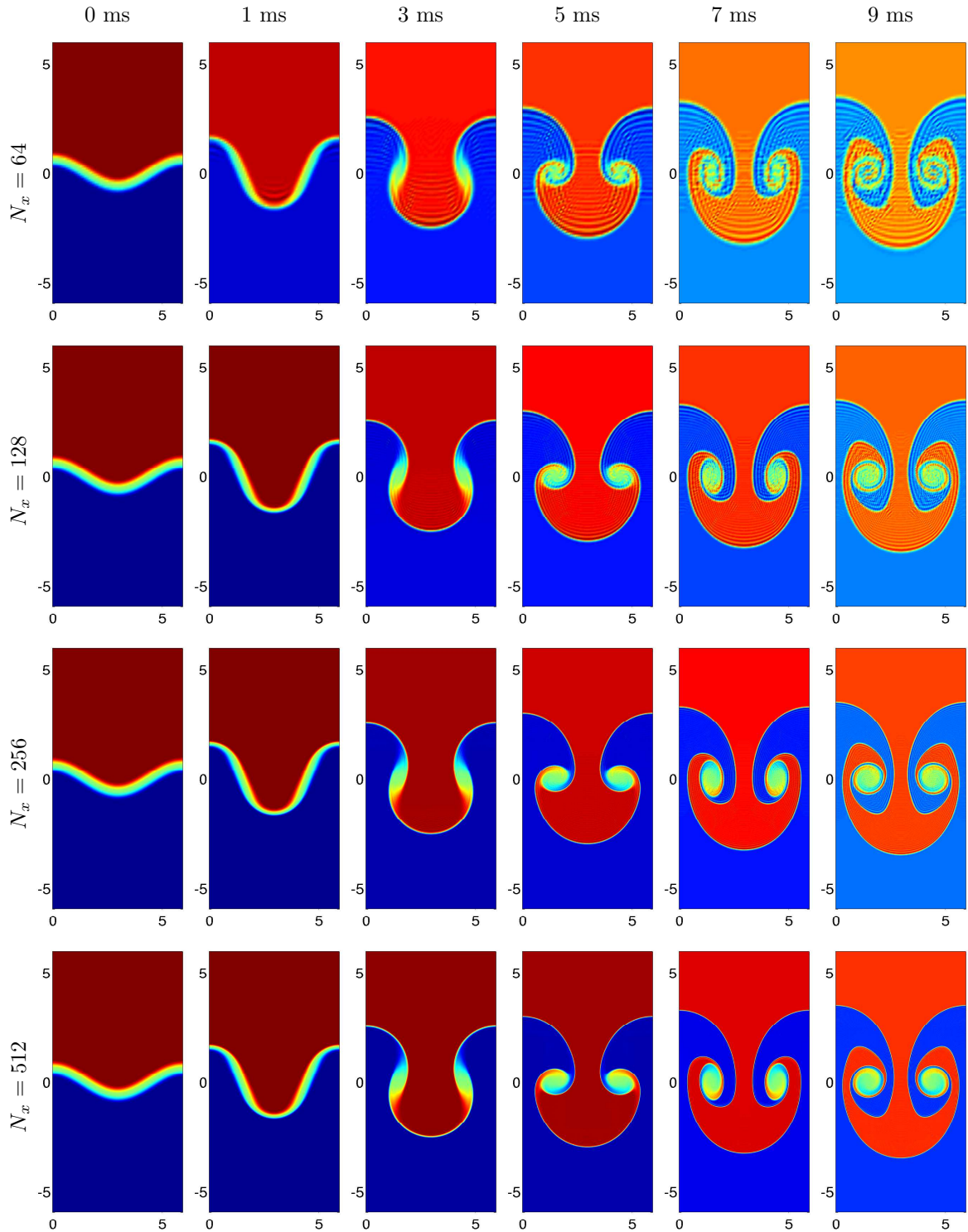


Figure 3.1. Time-evolution of the mass fraction field $m(x, y)$ for the Richtmyer-Meshkov instability with $A = 0$ and initial diffuse layer thickness $\delta_T = 0.4$ cm at 0, 1, 3, 5, 7, and 9 ms. The results are obtained using the VS method with grid resolutions $N_x = 64, 128, 256,$ and 512 .

occurs at later times. This demonstrates that as the resolution is increased, the scheme can tolerate steeper gradients before developing oscillations. For sufficiently high resolution, it may be possible to simulate the Richtmyer-Meshkov instability without developing these oscillations. However, the formation of the roll-up region with successively smaller structures guarantees that sufficiently steep gradients develop, introducing oscillations in the flow. In the absence of dissipation, the Euler equations do not have a length-scale so that progressively finer scales develop, despite the use of a layer with finite thickness.

Figure 3.2 shows the time-evolution of the mass fraction contours for the vortex layer evolution using the VS method for $A = 0$. Complex small-scale structure develops within the roll-up regions. The large-scale structure is not affected by the oscillations introduced by the small-scale structures. Figure 3.3 shows the time-evolution of the vorticity field $\omega(x, y)$ for $A = 0$. For $N_x = 64$, the vorticity shows areas of higher concentration at 5, 7, and 9 ms. For higher grid resolutions, the vorticity does not show similar concentrations. However, differences in structure are visible at 9 ms.

It was shown in Section 2.2.2 that a Gaussian thickening of the vortex layer converges in the limit of decreasing thickness δ_T and decreasing grid spacing Δx to the velocity given by the Biot-Savart law for a vortex sheet. Figure 3.4 shows that the VS method is third-order in time and fourth-order in space when δ_T is kept fixed. For the temporal convergence (first row), simulations were performed until 0.8 ms using decreasing values of the time-step Δt . The rms-norm of the difference between the simulations obtained using the smallest $\Delta t_f = 0.005$ ms and the simulations obtained using larger values of Δt are shown for the vorticity $\omega(x, y)$ and density $\rho(x, y)$. The results demonstrate third-order convergence in time, as indicated by the fiducial (green). For the spatial convergence (second row), simulations were performed for $N_x = 32, 64, 128, 256$, and 512 (fine grid). The rms-norm of the difference between the vorticity and density from the simulations on the fine and coarser grids are shown at 1, 3, 5, and 7 ms. Fourth-order convergence is obtained at 1 ms as the grid is refined. At 3 ms, second-order convergence is observed between $N_x = 32$ and 128 and higher-order convergence between $N_x = 128$ and 256, indicating that for coarser grids, fourth-order convergence is not achieved. At 5 ms, first-order convergence is observed between $N_x = 32$ and $N_x = 128$ and higher order convergence between $N_x = 128$ and 256. At 7 ms, first-order convergence is observed for all grid resolutions. Thus, fourth-order convergence is lost in time for $A = 0$ when $\nu = \mathcal{D} = 0$, as expected, due to the oscillations (as shown in Fig. 3.1).

Figure 3.5 shows the time-evolution of the perturbation amplitude $a(t)$ as the grid is refined (left). The perturbation amplitude is computed for $A = 0$ as follows. The mass fraction is averaged across the periodic direction,

$$\bar{m}(y, t) = \frac{1}{L_x} \int_0^{L_x} m(x, y, t) dy, \quad (3.3)$$

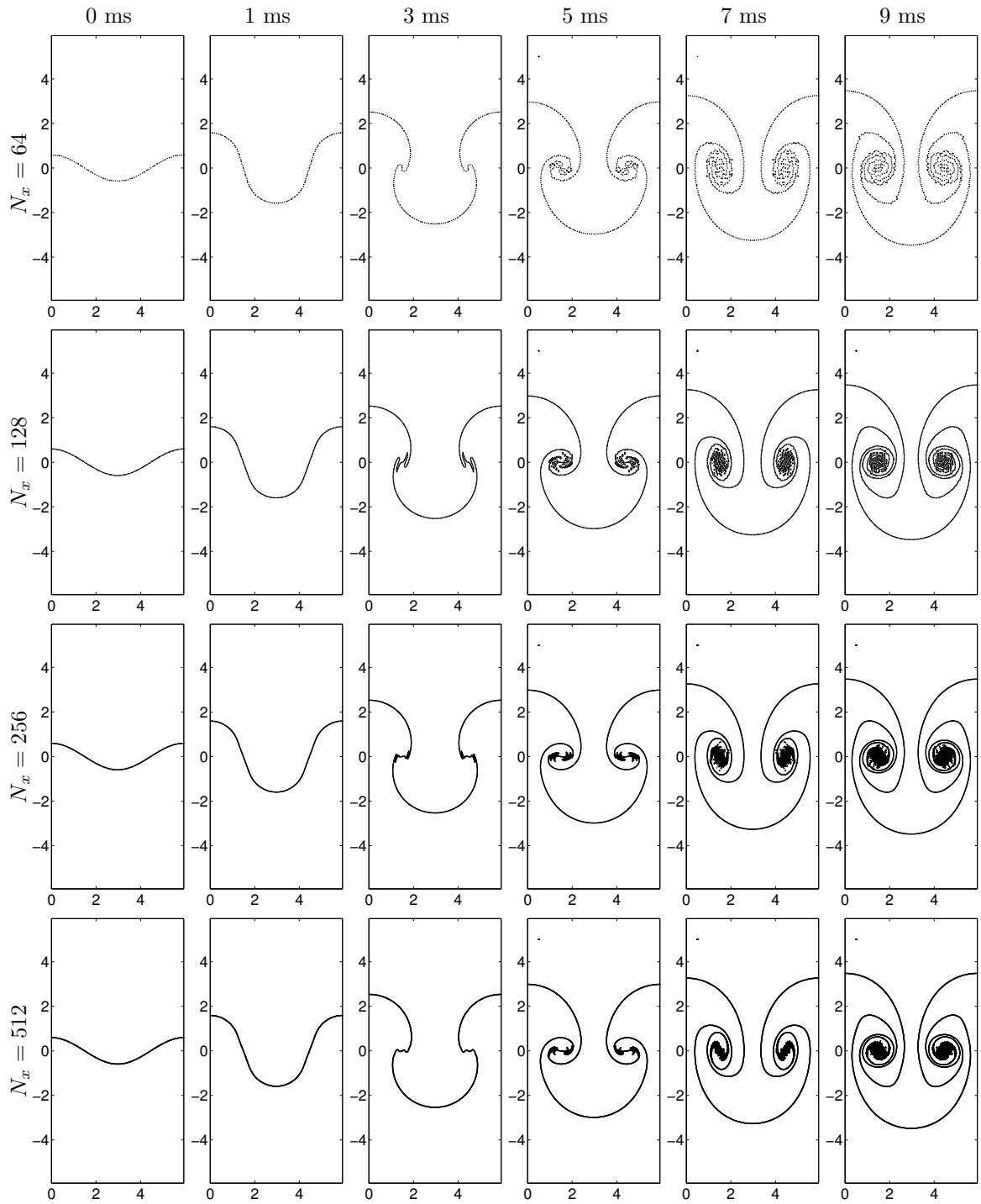


Figure 3.2. Time-evolution of the mass fraction contour corresponding to $m_1 = 1/2$ for the Richtmyer-Meshkov instability with $A = 0$ and initial diffuse-interface thickness $\delta_T = 0.4$ cm at 0, 1, 3, 5, 7, and 9 ms. The results are obtained using the VS method with grid resolutions $N_x = 64$, 128, 256, and 512.

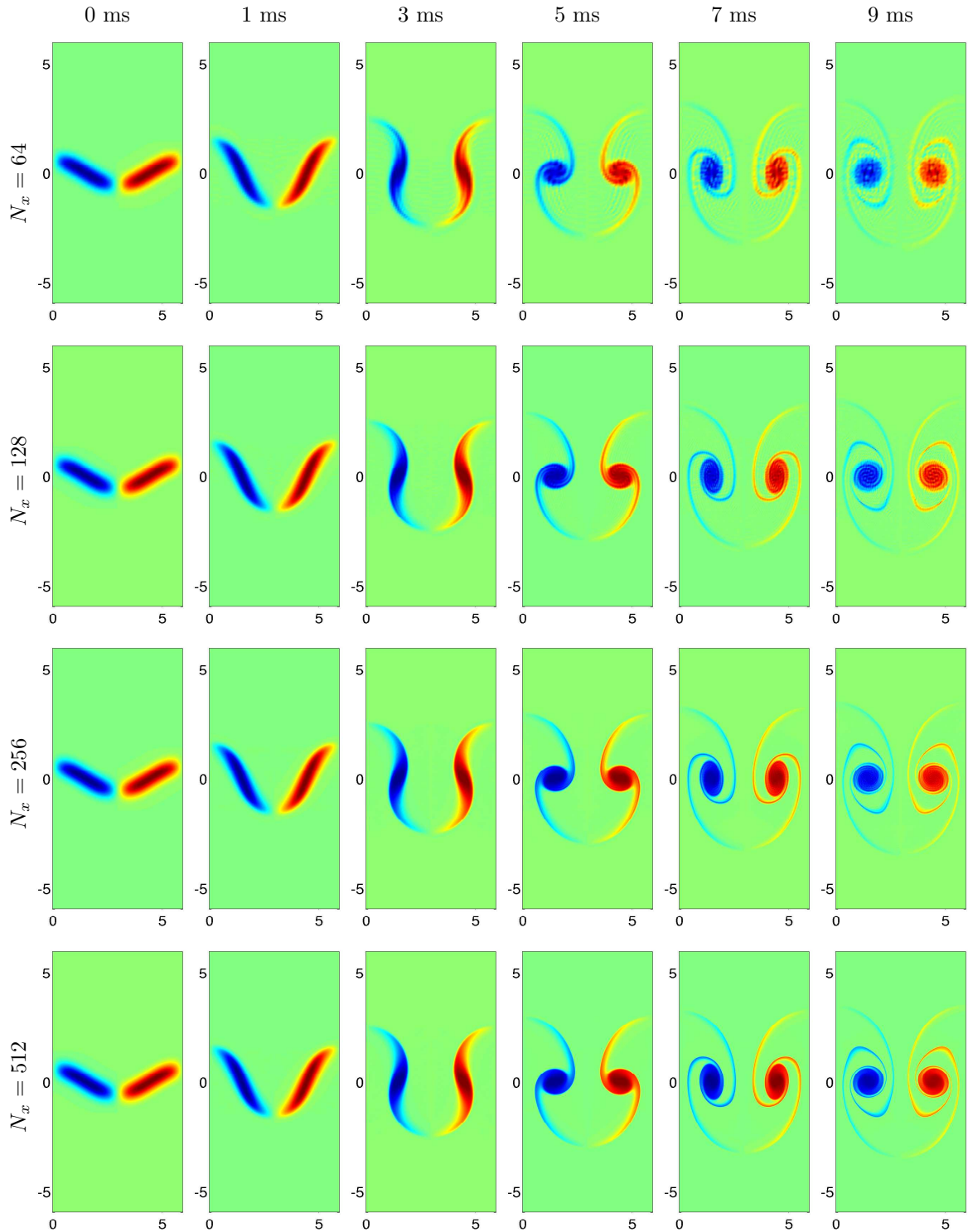


Figure 3.3. Time-evolution of the vorticity field $\omega(x, y)$ for the Richtmyer-Meshkov instability with $A = 0$ and initial thickness $\delta_T = 0.4$ cm at 0, 1, 3, 5, 7, and 9 ms. The results are obtained using the VS method with grid resolutions $N_x = 64, 128, 256,$ and 512 .

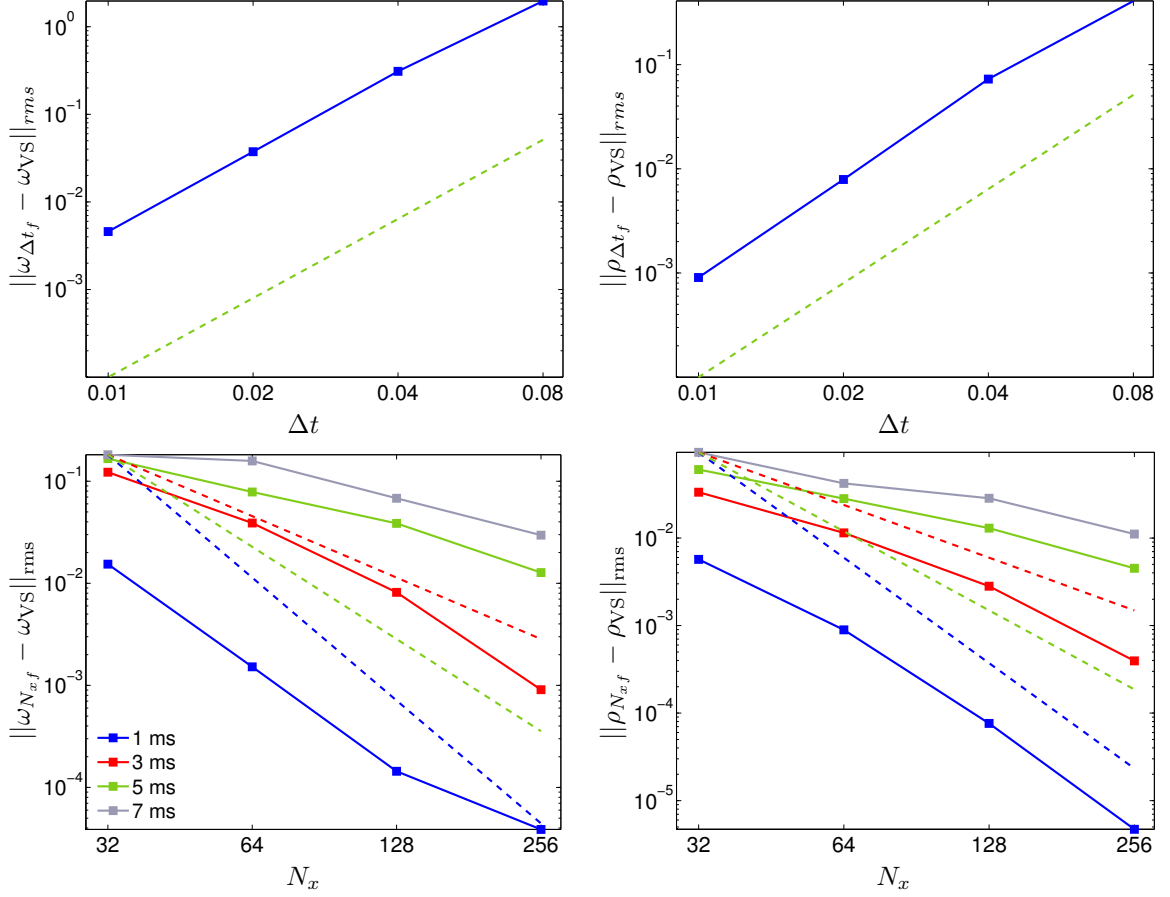


Figure 3.4. Temporal and spatial convergence for the vorticity ω and density ρ fields when $\nu = \mathcal{D} = 0$ for $A = 0$. For temporal convergence, $\Delta t_f = 0.005$ ms at 0.8 ms when $\Delta t = 0.16, 0.08, 0.04, 0.02,$ and 0.01 ms. The dashed green line represents Δt^3 , indicating third-order convergence in time. For spatial convergence, $N_{x_f} = 512$ at 1, 3, 5, and 7 ms when $N_x = 32, 64, 128,$ and 256 . The red line represents N_x^{-2} , indicating second-order convergence, and the blue line represents N_x^{-4} , indicating fourth-order convergence.

and the amplitude of the bubble and spike, $a_b(t)$ and $a_s(t)$, respectively correspond to the location where $\bar{m} \geq \epsilon$ and $\bar{m} \leq 1 - \epsilon$, respectively with $\epsilon = 0.01$. Define and spike amplitudes, the *perturbation width* and *perturbation amplitude*

$$h(t) = a_b(t) + a_s(t), \quad a(t) = \frac{h(t)}{2}, \quad (3.4)$$

respectively. The amplitude is not significantly affected as the grid is refined, even in the presence of oscillations. The rms-norm of the difference between the amplitudes on the fine and coarser grids (right) shows that first-order convergence is recovered in $a(t)$ as the grid is refined. This is expected, as the oscillations introduced by the steep gradients reduce the convergence rates for all quantities, including $a(t)$. The bubble and spike amplitudes are not shown, as they are equal for $A = 0$. Figure

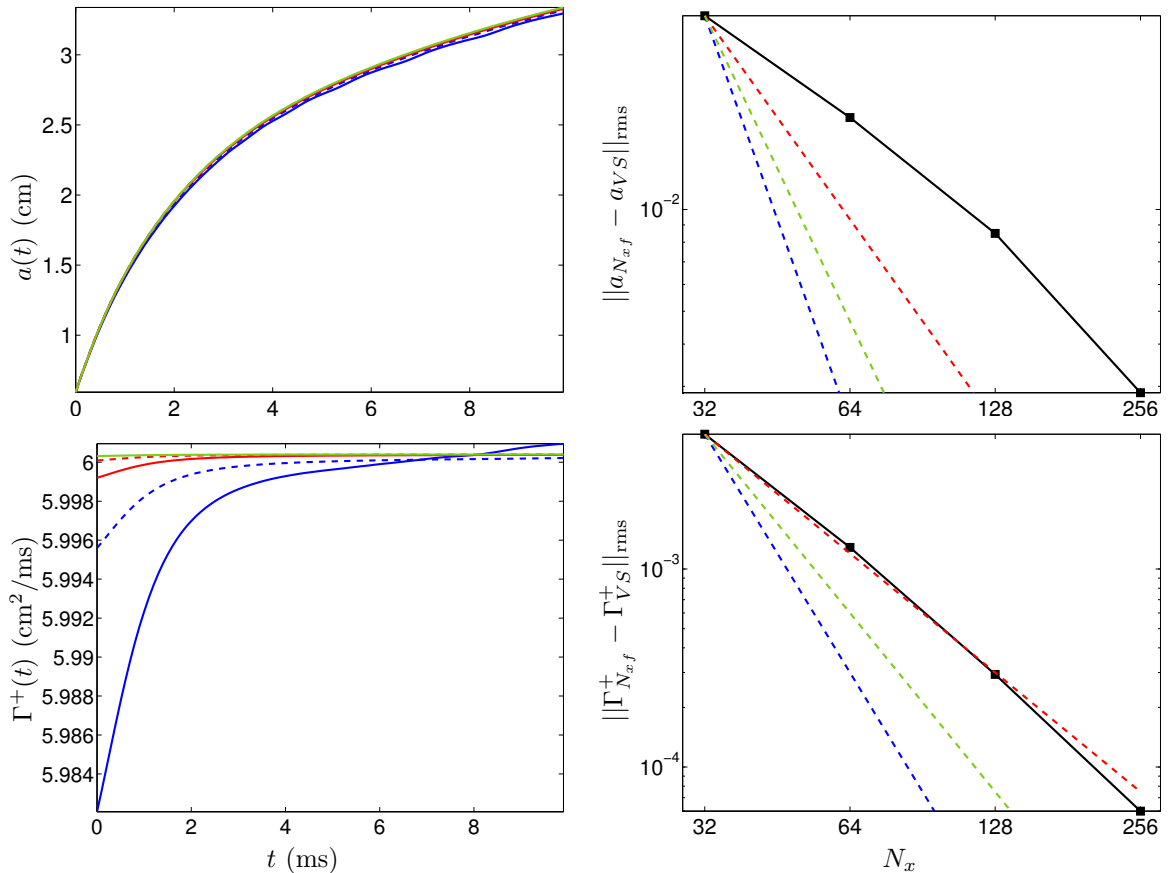


Figure 3.5. Comparison of the perturbation amplitude $a(t)$ and circulation $\Gamma^+(t)$ as the grid is refined for $A = 0$ using the VS method with $\nu = 0$ and $\delta_T = 0.4$ cm for $N_x = 32, 64, 128, 256,$ and 512 (left column). Also shown is the rms-norm of the difference between results obtained on the $N_{xf} \times N_{yf} = 512 \times 1024$ grid and results on coarser grids. See Figure 3.4 for the legend.

3.5 also shows that the positive circulation $\Gamma^+(t)$ remains constant as the grid is refined. For $\nu = 0$, there is no mechanism to dissipate the circulation so that it remains constant. The rms-norm of the difference between the circulation on the fine grid and that on coarser grids shows second-order convergence.

To make the agreement between the results on the fine grid and the results on the coarser grids more quantitative, the *average fractional deviation* [62, 78]

$$\Delta = \frac{1}{N} \sum_{i=1}^N \frac{|a_{N_x}(t_i) - a_{N_{xf}}(t_i)|}{a_{N_{xf}}(t_i)} \quad (3.5)$$

is computed, where N is the number of sample points used. The results indicate that the coarser grids values approach the fine grid value.

Δ (%)	$N_x = 32$	$N_x = 64$	$N_x = 128$	$N_x = 256$
$a(t)$	1.408	0.661	0.275	0.086
$a_b(t)$	1.408	0.661	0.276	0.086
$a_s(t)$	1.407	0.661	0.275	0.086
$\Gamma^+(t)$	0.0427	0.014	0.00288	0.000583

Table 3.2. Average fractional deviation Δ between the results on the $N_{xf} = 512$ grid and those on coarser grids for the perturbation, bubble, and spike amplitudes $a(t)$, $a_b(t)$, and $a_s(t)$, respectively, and the circulation $\Gamma^+(t)$ for the VS method with $A = 0$ and $\nu = \mathcal{D} = 0$.

3.1.2 Results with nonzero viscosity and mass diffusivity for zero Atwood number

To prevent the formation of steep gradients as the instability develops, viscosity ν and mass diffusivity \mathcal{D} are introduced so that the Schmidt number $Sc \equiv \nu/\mathcal{D} = 1$ is consistent with gas properties. Figure 3.6 shows the time-evolution of a thickened vortex layer under the VS method for $A = 0$, as the grid is refined keeping the thickness of the layer $\delta_T = 0.4$ cm fixed. For $A = 0$, the density is equal across the two fluids and the baroclinic vorticity production is zero, so that the mass fraction field $m(x, y)$ is shown. The mass fractions across the fields are very similar. The mass fraction field corresponding to $N_x = 64$ shows a lighter color starting from 1 ms, indicating the presence of oscillations in the simulation. At later times, the red and blue colors become lighter, indicating that the oscillations intensify. At 7 and 9 ms, the oscillations are visible near the tips of the bubble and spike. As the grid is refined, the additional points used to discretize the layer, combined with the action of viscosity, prevent the formation of these oscillations. Starting from $N_x = 128$, the red and blue colors remain dark at all times, indicating that no oscillations develop. Furthermore, as the grid is refined, the roll-up retains the same shape, indicating that the results are converged.

Figure 3.7 shows the mass fraction contours corresponding to the fields in Figure 3.6. The contours are used to visualize the small-scale structure within the roll-ups. The contours show convergence under grid refinement, including similar characterizations of the small-scale roll-ups at late times, further confirming that the results are converged under grid refinement. The contour corresponding to $N_x = 64$ shows a different structure within the roll-ups at 7 and 9 ms, with the inner core exhibiting oscillations, due to the underlying oscillations in the field. No oscillations are observed at 1 ms, although oscillations are present in the field. Figure 3.8 shows a comparison of the vorticity field as the grid is refined. The vorticity forms cores at late times with a well-defined center. The cores become larger at late times. For $N_x = 64$ the cores show a fragmented core with small disordered structures.

The temporal and spatial convergence properties for the VS method are shown in Figure 3.9. For the temporal convergence, the vorticity and mass fraction are computed up to a fixed time 0.8 ms as Δt is decreased. The rms-norm of the difference between fields obtained with $\Delta t_f = 0.005$ ms

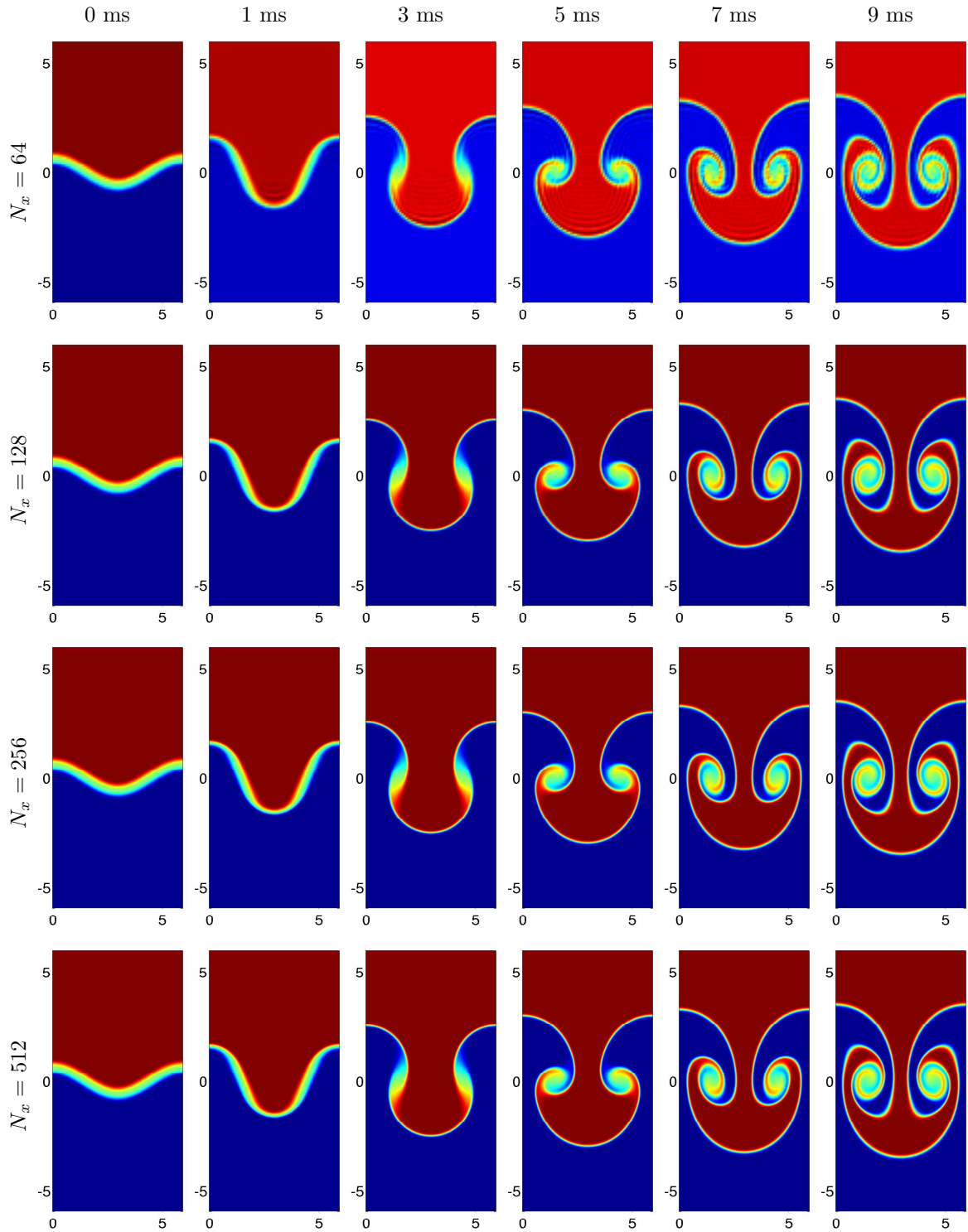


Figure 3.6. Time-evolution of the mass fraction field $m(x, y)$ for the Richtmyer-Meshkov instability with $A = 0$, initial diffuse-interface thickness $\delta_T = 0.4$ cm, and $\nu = \mathcal{D} = 3 \times 10^{-3}$ cm²/ms at 0, 1, 3, 5, 7, and 9 ms. The results are obtained using the VS method with grid resolutions $N_x = 64$, 128, 256, and 512.

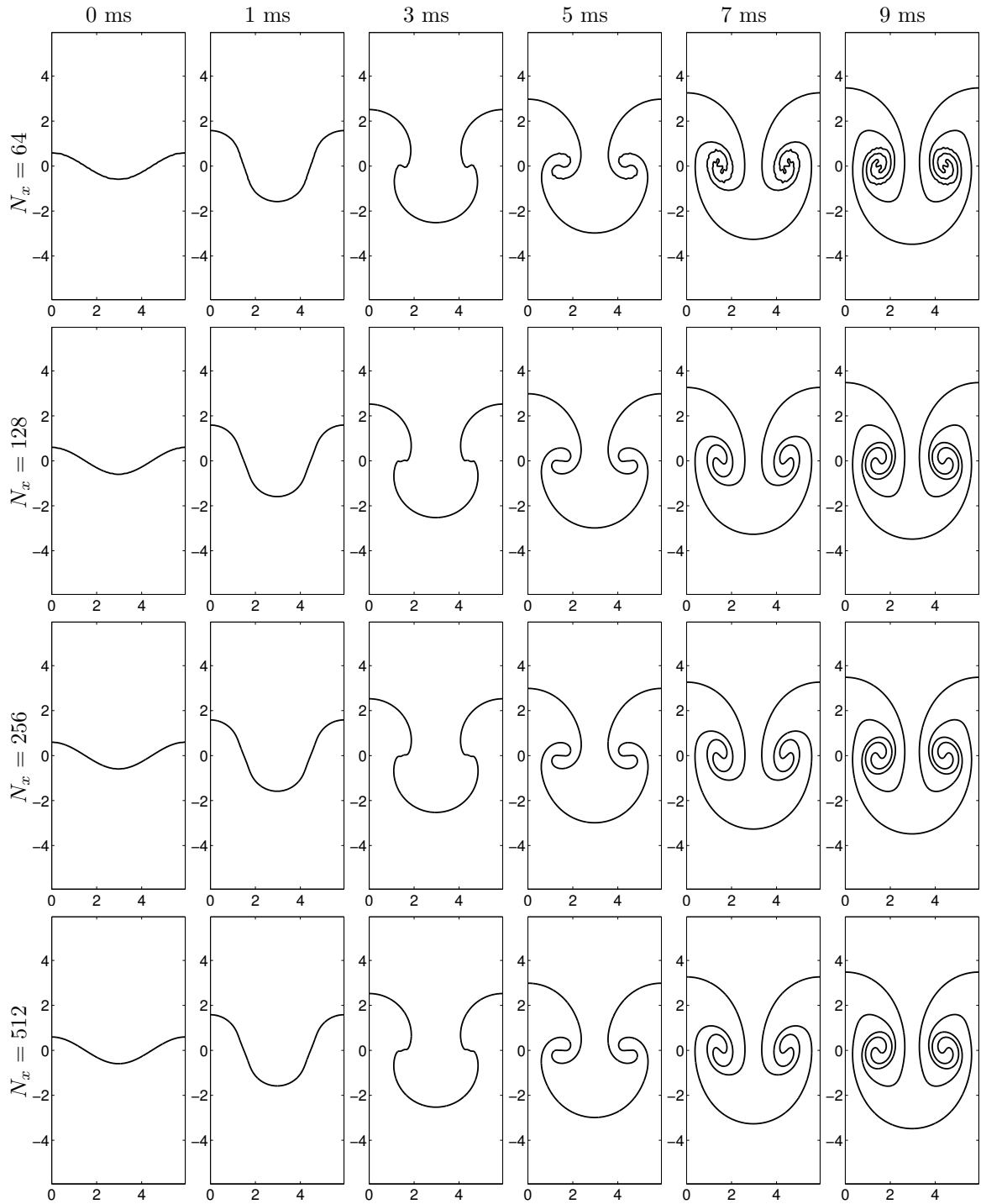


Figure 3.7. Time-evolution of the mass fraction contour corresponding to $m_1 = 1/2$ for the Richtmyer-Meshkov instability with $A = 0$, initial diffuse-interface thickness $\delta_T = 0.4$ cm, and $\nu = \mathcal{D} = 3 \times 10^{-3}$ cm²/ms at 0, 1, 3, 5, 7, and 9 ms. The results are obtained using the VS method with grid resolutions $N_x = 64, 128, 256,$ and 512 .

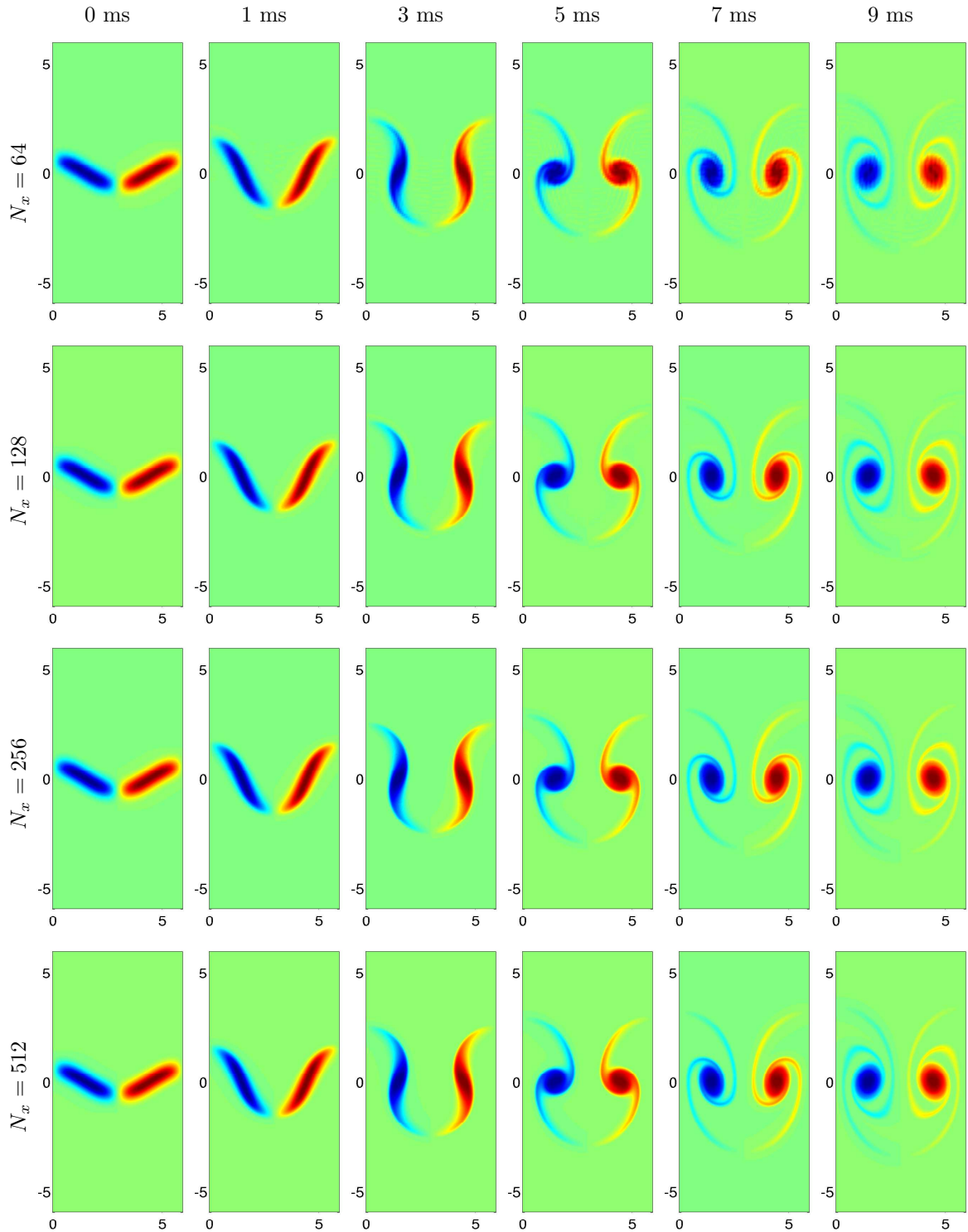


Figure 3.8. Time-evolution of the vorticity field $\omega(x, y)$ for the Richtmyer-Meshkov instability with $A = 0$, initial thickness $\delta_T = 0.4$ cm, and $\nu = \mathcal{D} = 3 \times 10^{-3}$ cm²/ms at 0, 1, 3, 5, 7, and 9 ms. The results are obtained using the VS method with grid resolutions $N_x = 64, 128, 256,$ and 512 .

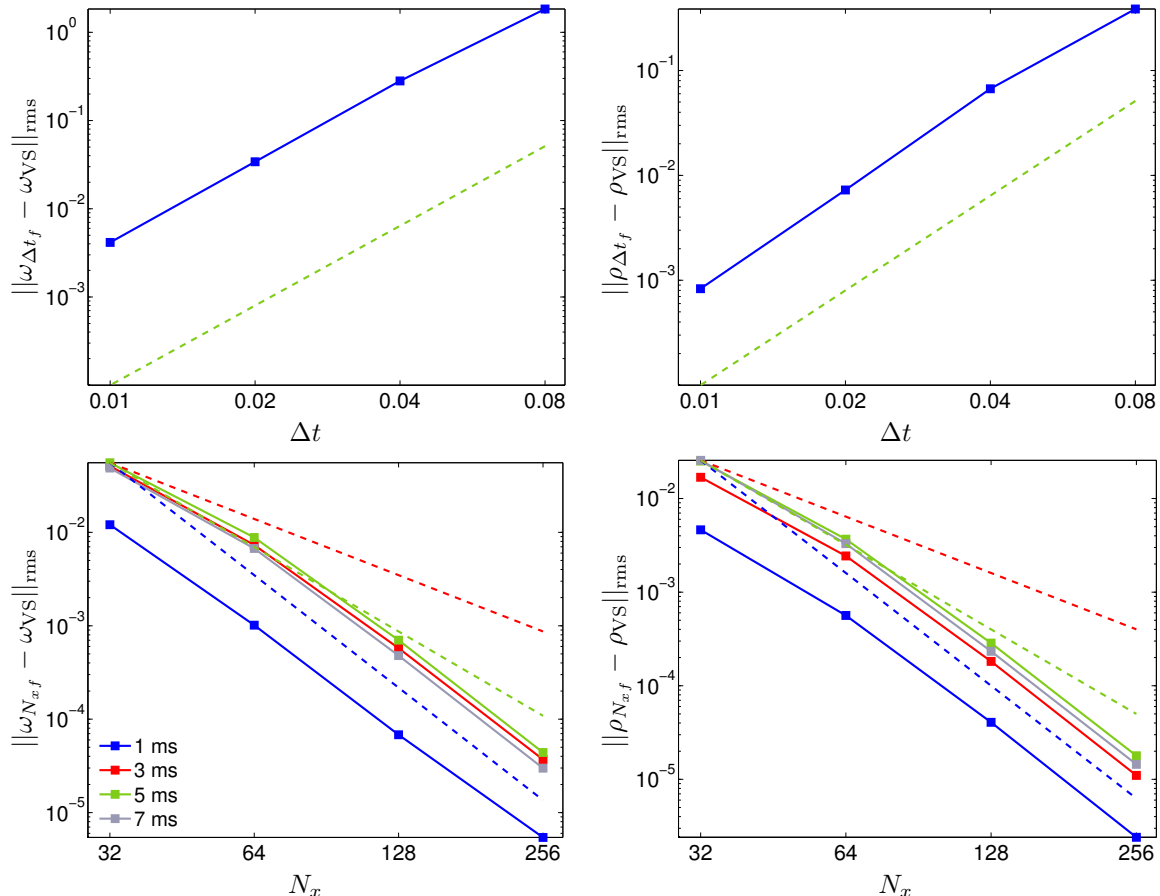


Figure 3.9. Temporal and spatial convergence for the vorticity ω and density ρ fields with $\nu = \mathcal{D} = 3 \times 10^{-4}$ cm²/ms when $A = 0$. For temporal convergence, $\Delta t_f = 0.005$ ms at 0.8 ms when $\Delta t = 0.16, 0.08, 0.04, 0.02$, and 0.01 ms. For spatial convergence, $N_{x_f} = 512$ at 1, 3, 5, and 7 ms when $N_x = 32, 64, 128$, and 256. See Figure 3.4 for the legend.

and with larger time steps is shown, indicating third-order convergence. For the spatial convergence, the results are compared at 1, 3, 5, and 7 ms as the grid is refined. The ℓ^∞ -norm of the difference between results on the $N_{x_f} = 512$ grid and results on coarser grids shows fourth-order convergence for all times. This is in contrast to the results with zero viscosity (Fig. 3.4), where fourth-order convergence was obtained at 1 ms and lower-order convergence at later times.

Figure 3.10 shows a comparison of the perturbation amplitude $a(t)$, indicating that differences as the grid is refined are small. The rms-norm of the difference between the amplitude on the fine grid and on the coarser grids is also shown, indicating fourth-order convergence. Also shown is a comparison of the circulations $\Gamma^+(t)$ as the grid is refined. The circulation decreases as time evolves, due to the dissipation of vorticity. For $A = 0$ and $\nu = 0$, the circulation is expected to remain constant (Fig. 3.5). A viscosity of 3×10^{-3} cm²/ms contributes a 0.5% decrease in circulation in 10 ms. The rms-norm of the difference between results on the fine and coarser grids shows fourth-order

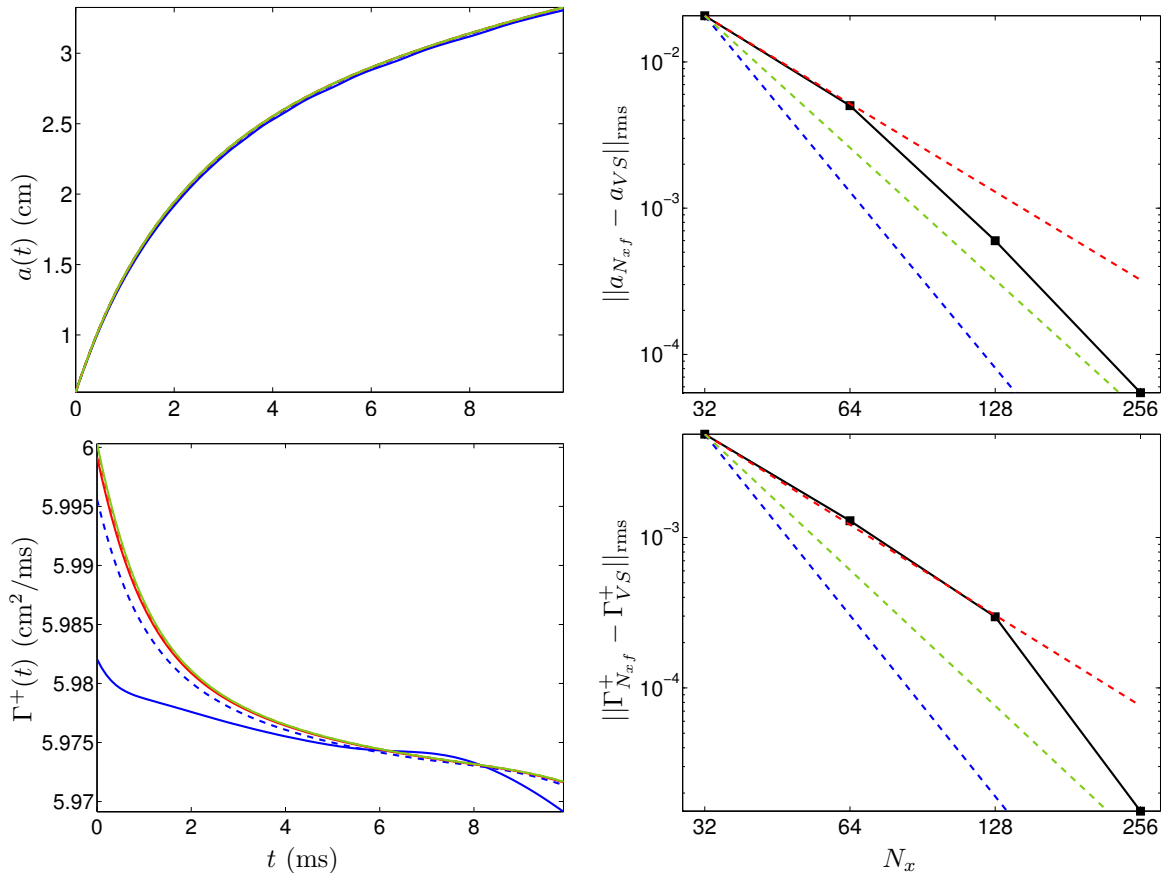


Figure 3.10. Comparison of the perturbation amplitude $a(t)$ and circulation $\Gamma^+(t)$ as the grid is refined for $A = 0$ using the VS method with $\nu = \mathcal{D} = 3 \times 10^{-3}$ cm²/ms and $\delta_T = 0.4$ cm for $N_x = 32, 64, 128, 256,$ and 512 (left column). Also shown is the rms-norm of the difference between results obtained on the $N_{xf} \times N_{yf} = 512 \times 1024$ grid and results on coarser grids. See Figure 3.4 for the legend.

convergence. The average fractional deviation Δ [Eq. (3.5)] is shown in Table 3.3.

3.1.3 Results with nonzero viscosity and mass diffusivity for nonzero Atwood number

Figure 3.11 shows the time-evolution of the density field from the VS simulations of the Richtmyer-Meshkov instability for $A = 0.4$ and $\nu = \mathcal{D} = 3 \times 10^{-3}$ cm²/ms. Results for $\nu = \mathcal{D} = 0$ are not shown since the oscillations for $A = 0$ intensify as the density is differentiated to compute the baroclinic vorticity production \mathcal{P} . The computation of \mathcal{P} also requires the determination of the pressure gradient, which is computed by solving the pressure Poisson equation [Eq. (2.37)] with Neumann boundary conditions. For $A = 0.4$, the densities are very similar under grid refinement, indicating converged results. The density also exhibits the expected differences between bubbles and spikes. In particular, at early times, the bubble expands and the spike contracts. At later times, the

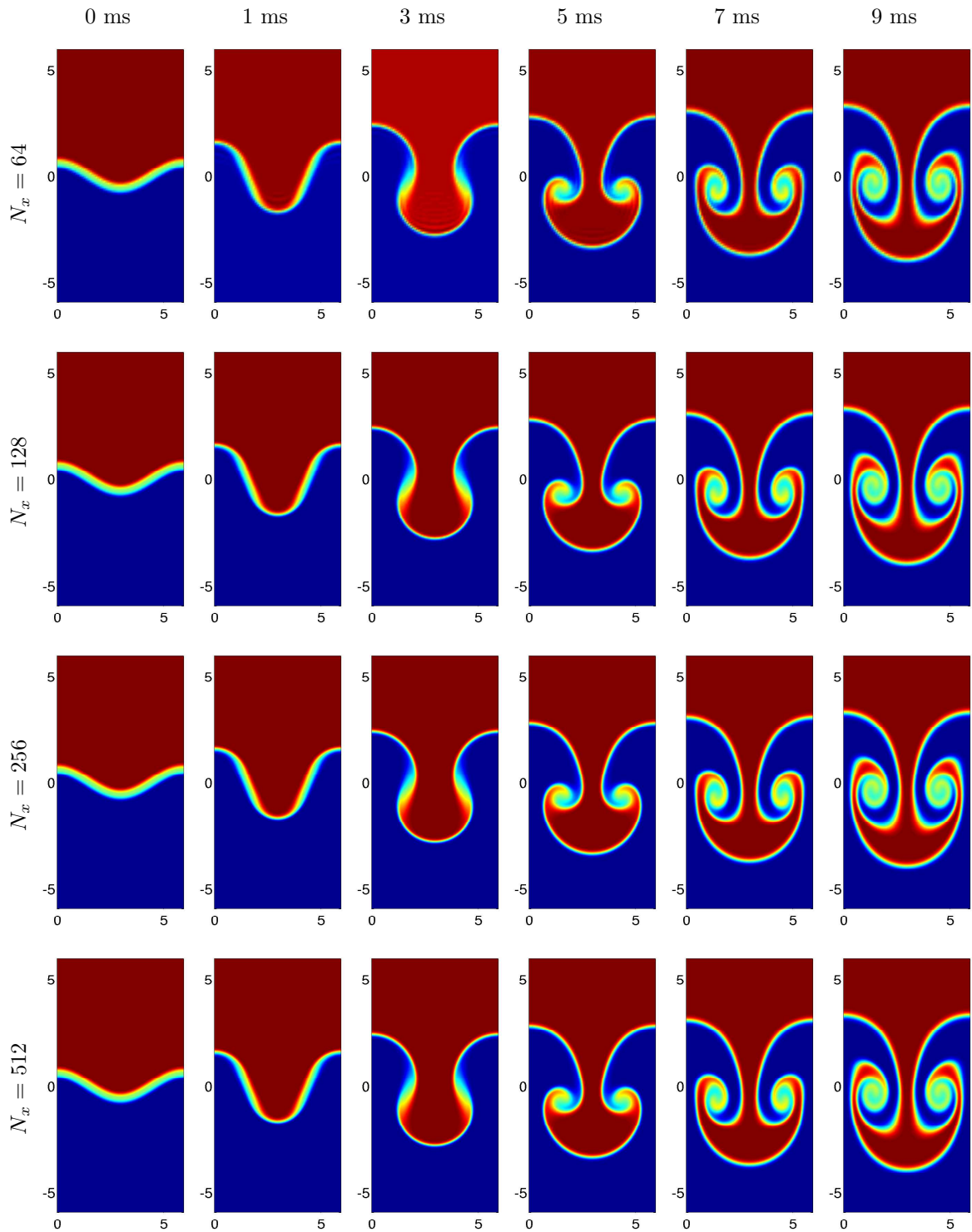


Figure 3.11. Time-evolution of the density field $\rho(x, y)$ for the Richtmyer-Meshkov instability with $A = 0.4$, initial diffuse-interface thickness $\delta_T = 0.4$ cm, and $\nu = \mathcal{D} = 3 \times 10^{-3}$ cm²/ms at 0, 1, 3, 5, 7, and 9 ms. The results are obtained using the VS method with grid resolutions $N_x = 64, 128, 256,$ and 512 .

Δ (%)	$N_x = 32$	$N_x = 64$	$N_x = 128$	$N_x = 256$
$a(t)$	0.84	0.198	0.023	2.21×10^{-3}
$a_b(t)$	0.84	0.199	0.0231	2.22×10^{-3}
$a_s(t)$	0.84	0.198	0.023	2.22×10^{-3}
$\Gamma^+(t)$	0.045	0.014	0.003	6.16×10^{-3}

Table 3.3. Average fractional deviation Δ between the results on the $N_{xf} = 512$ grid and those on coarser grids for the perturbation, bubble, and spike amplitudes $a(t)$, $a_b(t)$, and $a_s(t)$, respectively, and the circulation $\Gamma^+(t)$ for the VS method with $A = 0$ and $\nu = \mathcal{D} = 3 \times 10^{-3}$ cm²/ms.

bubble has a smaller amplitude than the spike. For $A = 0$, the bubbles and spikes were identical. For $N_x = 64$, oscillations are observed at 3 ms. These oscillations are mitigated at later times due to dissipation. For all other values of N_x , no oscillations are observed.

Figure 3.12 shows the mass fraction contours corresponding to the densities in Figure 3.11. As the grid is refined, the contours provide similar characterizations of the roll-up structure, including the $N_x = 64$ case, where oscillations were observed at 3 ms. Figure 3.13 shows the time-evolution of $\omega(x, y)$ for $A = 0.4$ under grid refinement. The vorticity field does not show differences, indicating that similar characterizations of the vorticity are provided by the method. In particular, the vorticity for $N_x = 64$ at 3 ms does not show oscillations, indicating that the oscillations in the density were mitigated by the viscosity. At late times, the vorticity rolls up into strong cores.

The temporal and grid convergence properties of the density and vorticity in the VS method for $A = 0.4$ are shown in Figure 3.14. For the temporal convergence (first row), the rms-norm of the difference between results obtained using $\Delta t_f = 0.05$ ms and larger values shows third-order convergence as the time-step is decreased. For the spatial convergence (second row), the rms-norm of the difference between results on the fine grid $N_{xf} = 512$ and results on coarser grids shows fourth-order convergence for all times.

Figure 3.15 shows a comparison of the perturbation, bubble, and spike amplitudes, $a(t)$, $a_b(t)$, and $a_s(t)$, respectively, as the grid is refined. For $A \neq 0$, distinctive bubble and spike amplitudes develop. As the grid is refined, the amplitudes do not vary significantly. Also shown in the figure is the rms-norm of the difference between the amplitudes on the fine and coarser grids, indicating fourth-order convergence.

Shown in Figure 3.16 is a comparison of the circulation $\Gamma^+(t)$ as the grid is refined. Following the baroclinic vorticity deposition, Γ^+ decreases and then increases. Also shown is the rms-norm of the difference between the circulation on the fine and coarser grids, indicating fourth-order convergence. The average fractional deviation Δ [Eq. (3.5)] is shown in Table 3.4.

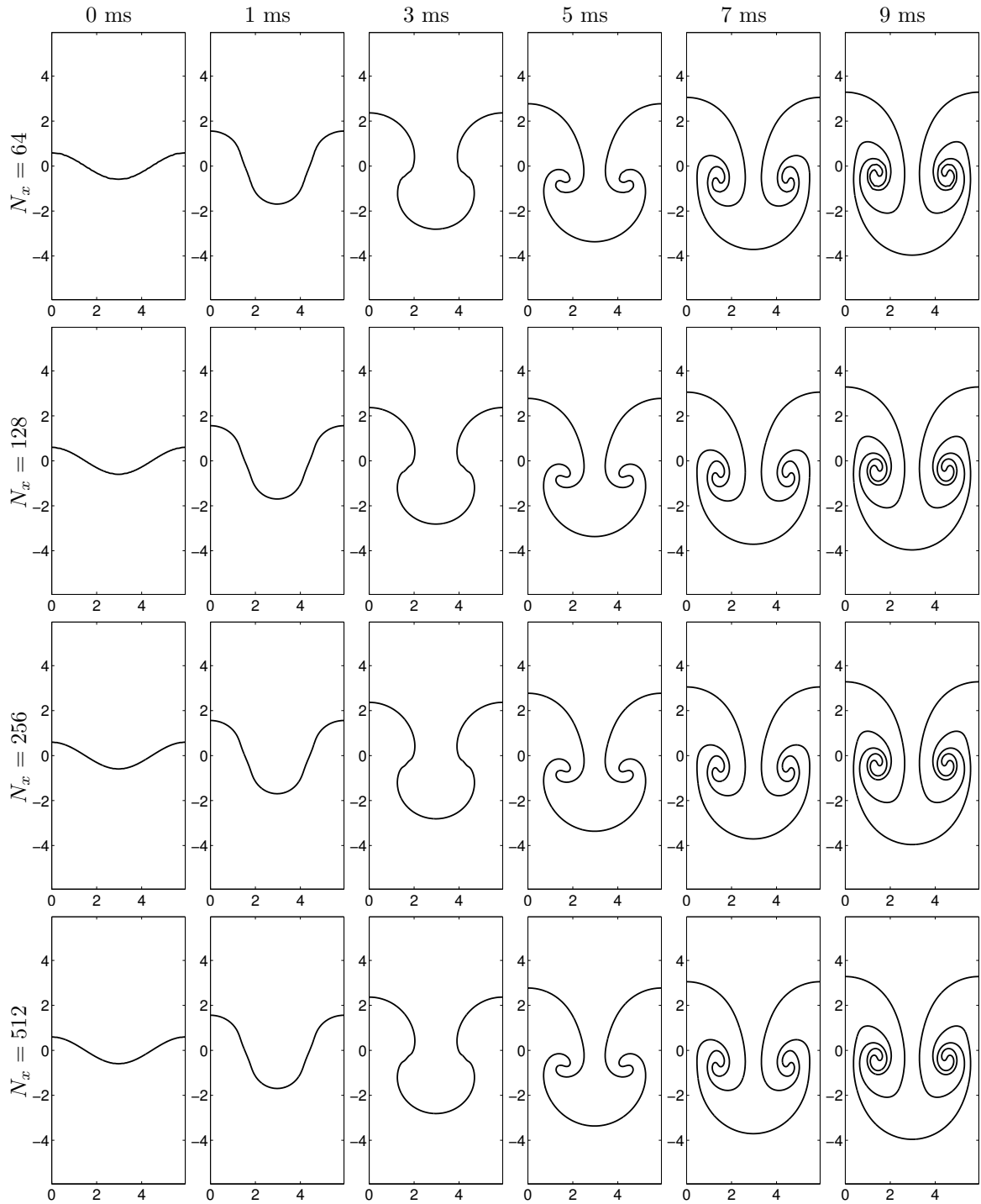


Figure 3.12. Time-evolution of the mass fraction contour $m_1 = 1/2$ for the Richtmyer-Meshkov instability with $A = 0.4$, initial thickness $\delta_T = 0.4$ ms, and $\nu = \mathcal{D} = 3 \times 10^{-3}$ cm²/ms at 0, 1, 3, 5, 7, and 9 ms. The results are obtained using the VS method with grid resolutions $N_x = 64$, 128, 256, and 512.

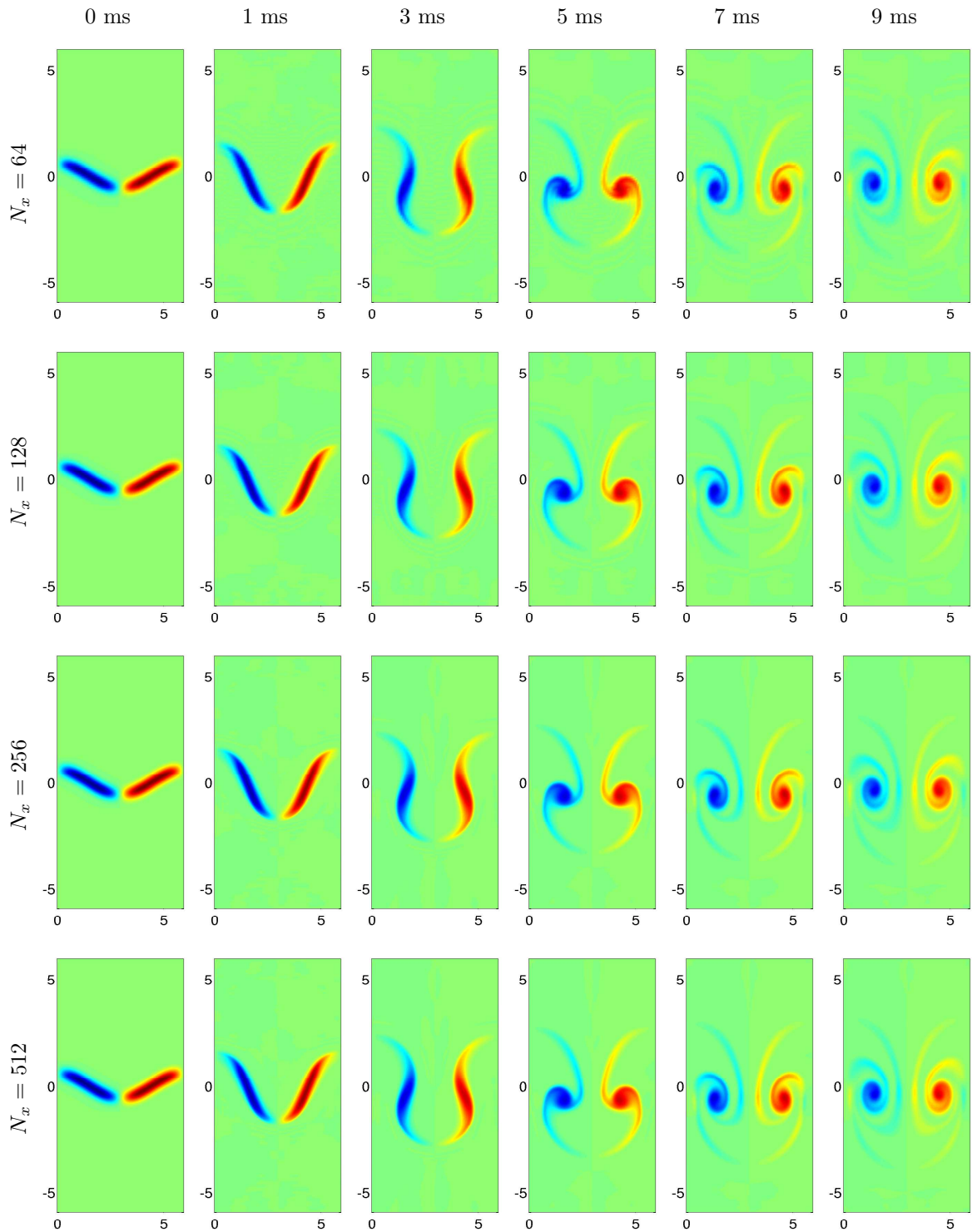


Figure 3.13. Time-evolution of the vorticity field $\omega(x, y)$ for the Richtmyer-Meshkov instability with $A = 0.4$, initial diffuse-interface thickness $\delta_T = 0.4$ cm, and $\nu = \mathcal{D} = 3 \times 10^{-3}$ cm²/ms at 0, 1, 3, 5, 7, and 9 ms. The results are obtained using the VS method with grid resolutions $N_x = 64, 128, 256,$ and 512 .

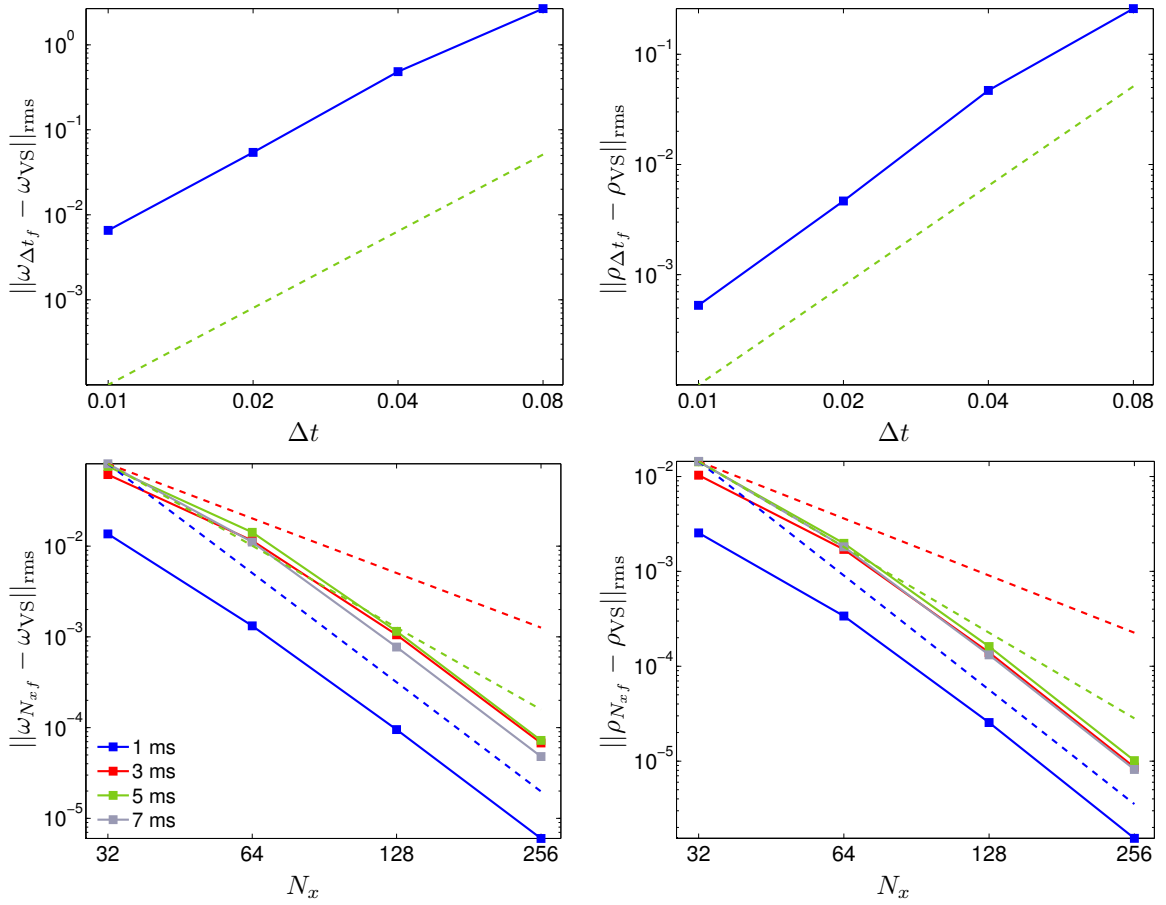


Figure 3.14. Temporal and spatial convergence for the vorticity ω and density ρ fields with $\nu = \mathcal{D} = 3 \times 10^{-3} \text{ cm}^2/\text{ms}$ for $A = 0.4$. For temporal convergence, $\Delta t_f = 0.005 \text{ ms}$ with $\Delta t = 0.16, 0.08, 0.04, 0.02$, and 0.01 ms . For spatial convergence, $N_{x_f} = 512$ at 1, 3, 5, and 7 ms when $N_x = 32, 64, 128$ and 256. See Figure 3.4 for the legend.

Δ (%)	$N_x = 32$	$N_x = 64$	$N_x = 128$	$N_x = 256$
$a(t)$	1.05	0.171	0.047	3.97×10^{-3}
$a_b(t)$	0.192	0.45	0.106	2.12×10^{-3}
$a_s(t)$	2.16	0.72	0.18	5.62×10^{-3}
$\Gamma^+(t)$	0.476	0.047	5.3×10^{-3}	8.31×10^{-4}

Table 3.4. Average fractional deviation Δ between the results on the $N_{x_f} = 512$ grid and those on coarser grids for the perturbation, bubble, and spike amplitudes $a(t)$, $a_b(t)$, and $a_s(t)$, respectively, and the circulation $\Gamma^+(t)$ for the VS method with $A = 0.4$ and $\nu = \mathcal{D} = 3 \times 10^{-3} \text{ cm}^2/\text{ms}$.

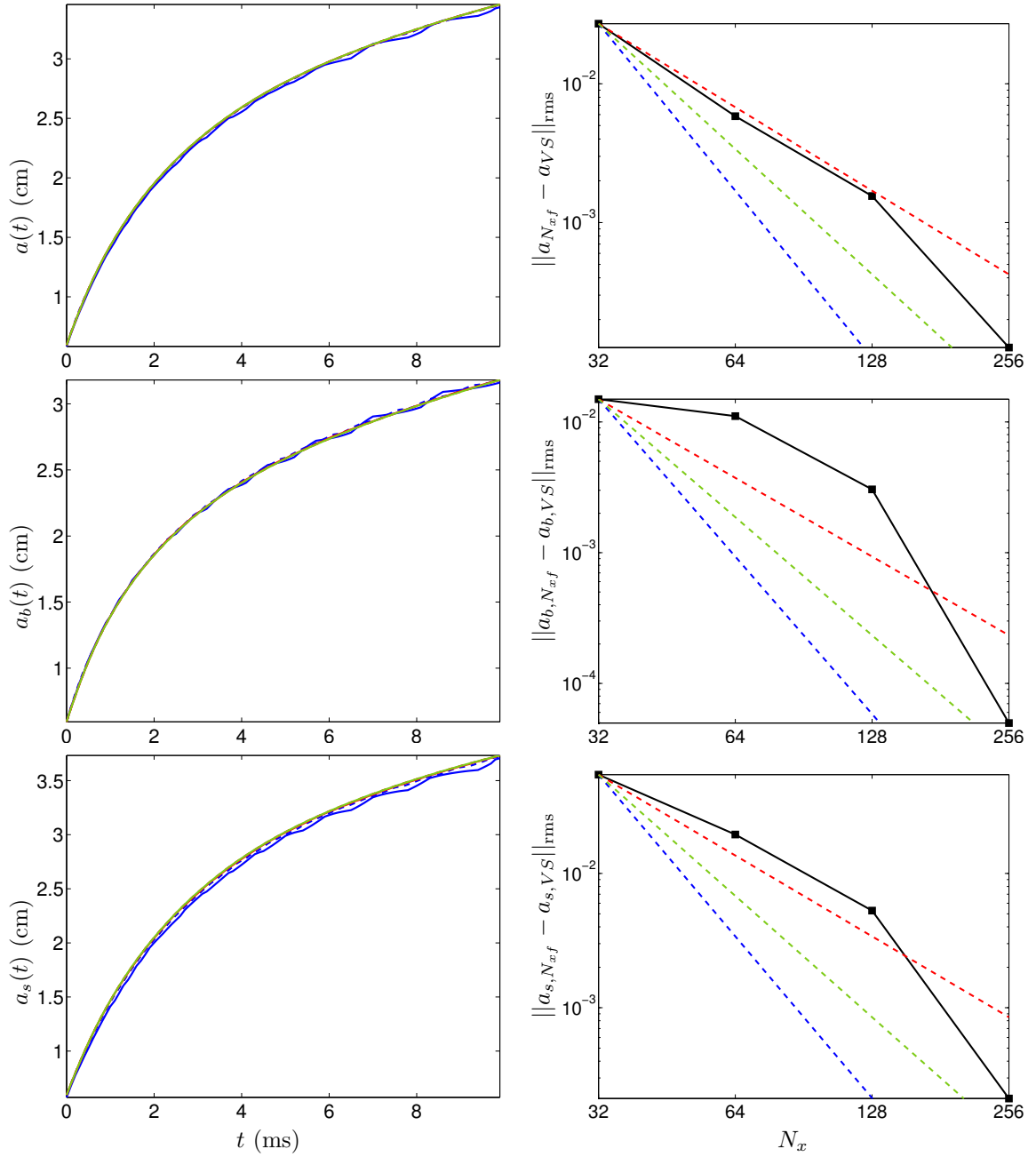


Figure 3.15. Comparison of the perturbation, bubble, and spike amplitudes $a(t)$, $a_b(t)$, and $a_s(t)$, respectively, as the grid is refined for $A = 0.4$ using the VS method with $\nu = 3 \times 10^{-3}$ cm²/ms and $\delta_T = 0.4$ cm for $N_x = 32, 64, 128, 256$, and 512 (left column). Also shown is the rms-norm of the difference between results obtained on the $N_{x_f} \times N_{y_f} = 512 \times 1024$ grid and results on coarser grids. See Figure 3.4 for the legend.

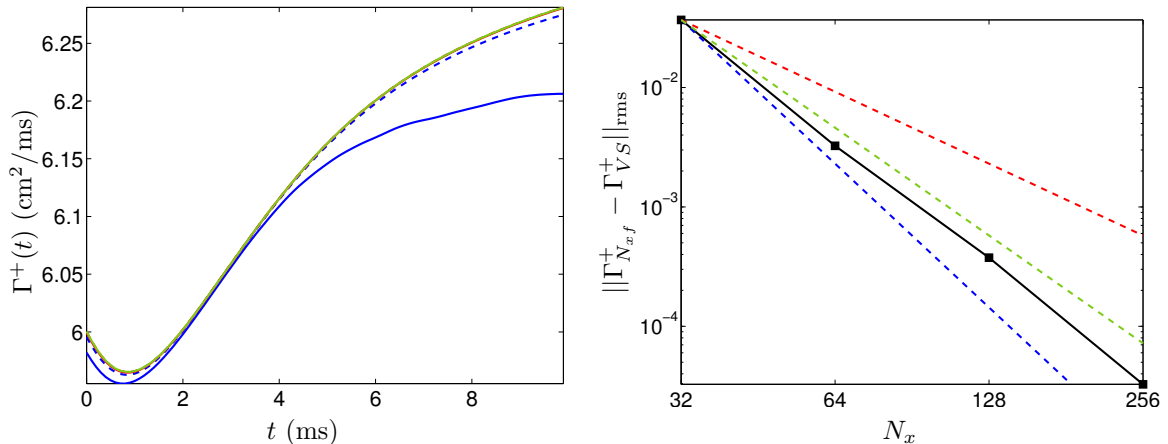


Figure 3.16. Comparison of the circulation $\Gamma^+(t)$ as the grid is refined for $A = 0.4$ using the VS method with $\nu = 3 \times 10^{-3} \text{ cm}^2/\text{ms}$ and $\delta_T = 0.4 \text{ cm}$ for $N_x = 32, 64, 128, 256,$ and 512 (left column). Also shown is the rms-norm of the difference between results obtained on the $N_{xf} \times N_{yf} = 512 \times 1024$ grid and results on coarser grids. See Figure 3.4 for the legend.

	$\nu = 8 \times 10^{-4} \frac{\text{cm}^2}{\text{ms}}$	$\nu = 4 \times 10^{-4} \frac{\text{cm}^2}{\text{ms}}$	$\nu = 2 \times 10^{-4} \frac{\text{cm}^2}{\text{ms}}$	$\nu = 10^{-4} \frac{\text{cm}^2}{\text{ms}}$
$\delta_T = 0.4 \text{ cm}$	VS-04-80 (solid blue)	VS-04-40 (dashed blue)	VS-04-20 (dash-dot blue)	VS-04-10 (dotted blue)
$\delta_T = 0.3 \text{ cm}$	VS-03-80 (solid red)	VS-03-40 (dashed red)	VS-03-20 (dash-dot red)	VS-04-10 (dotted red)
$\delta_T = 0.2 \text{ cm}$	VS-02-80 (solid green)	VS-02-40 (dashed green)	VS-02-20 (dash-dot green)	VS-04-10 (dotted green)

Table 3.5. Keys used to denote simulations with different values of the viscosity ν and initial diffuse-interface thickness δ_T for the VS method.

3.2 Convergence study using different diffuse interface thicknesses and viscosities

Presented here is a convergence study as the diffuse interface thickness δ_T is varied from 0.4 to 0.2 cm and the viscosity ν is varied from 8×10^{-4} to $10^{-4} \text{ cm}^2/\text{ms}$ for $A = 0.4$ (keeping $\mathcal{D} = \nu$). First, the density, mass fraction contours, and vorticities are compared at 3, 5, and 7 ms (Sec. 3.2.1). Next, a convergence study is performed for the smallest value of the viscosity, as the diffuse interface thickness is reduced (Sec. 3.2.2). Finally, the effects of varying the diffuse interface thickness and the viscosity on the perturbation, bubble, and spike amplitudes, on the circulation, and on the Reynolds numbers is investigated (Sec. 3.2.3).

3.2.1 Dynamics of the instability evolution

Presented here is a visualization of the instability development as the diffuse-interface width δ_T and viscosity ν are varied. Table 3.5 shows the keys used to denote the simulations. Each simulation is performed at a resolution of $N_x = 512$, and it is shown in Section 3.2.2 that this resolution is guaranteed to be in the region of fourth-order point-wise convergence of the method.

Figure 3.17 shows the density field $\rho(x, y)$ at 3 ms as δ_T and ν are varied. The results are presented on a grid so that fields in the same column have the same viscosity ν with decreasing diffuse interface thickness, while fields in the same row have the same diffuse-interface thickness δ_T with decreasing viscosity ν . A significant variation is observed in the small-scale features corresponding to the formation of the roll-up as δ_T is decreased, while no significant difference is observed as ν is decreased. Figure 3.18 continues the comparison by showing the mass fraction contours corresponding to the densities in Figure 3.17, further confirming that variations are observed as δ_T is decreased, but little variation as ν is decreased. In particular, as δ_T is decreased the roll-up appears at a later stage of the instability development. This is expected because if the instability development is measured with respect to the nondimensional time τ [Eq. (1.17)], then as the diffuse interface decreases, the growth reduction factor ψ (Sec. 4.2.2) also decreases, resulting in a larger value of τ for the same time.

Figure 3.19 shows the comparison of the vorticity field at 3 ms as ν and δ_T are varied. As δ_T is decreased, the vortex layer is thinner with more refined cores. In addition, as noted in the discussion of the mass fraction, the stage of the roll-up is more advanced as δ_T is decreased. For $\delta_T = 0.4$ cm, a core of the roll-up is barely visible. For $\delta_T = 0.3$ cm, the roll-up is beginning and for $\delta_T = 0.2$ cm, the roll-up is advanced. In addition, for $\delta_T = 0.4$ and 0.3 cm, no differences are visible in the layer as ν is decreased. However, for $\delta_T = 0.2$ cm, the layer becomes much thinner and concentrated as ν decreases. This is expected, as viscosity spreads the layer of vorticity. Such effects are more pronounced in the presence of a thin layer as opposed to a thicker layer.

Figure 3.20 shows a comparison of the densities at 5 ms when the roll-up develops. As δ_T is decreased, the details of the roll-up become sharper and the roll-up is more developed. For $\delta_T = 0.4$ and 0.3 cm, no visible effects are apparent as ν is decreased. For $\delta_T = 0.2$ cm, the roll-up is less diffuse for smaller values of ν . Figure 3.21 continues the comparison for the mass fraction contours. The results also confirm small variations as ν is decreased and larger variations as δ_T is increased. The contour corresponding to $\delta_T = 0.2$ cm and $\nu = 8 \times 10^{-4}$ cm²/ms shows the most structure within the roll-ups. As ν decreases, such structure is replaced by a large-scale round structure. This is a limitation of the mass fraction contours, as the fine-scale structure cannot be visualized effectively, although it was present in the density fields.

Figure 3.22 shows a comparison of the vorticity field at 5 ms. Variations are visible as both δ_T and ν are decreased. As δ_T is decreased, the cores become better defined and show additional

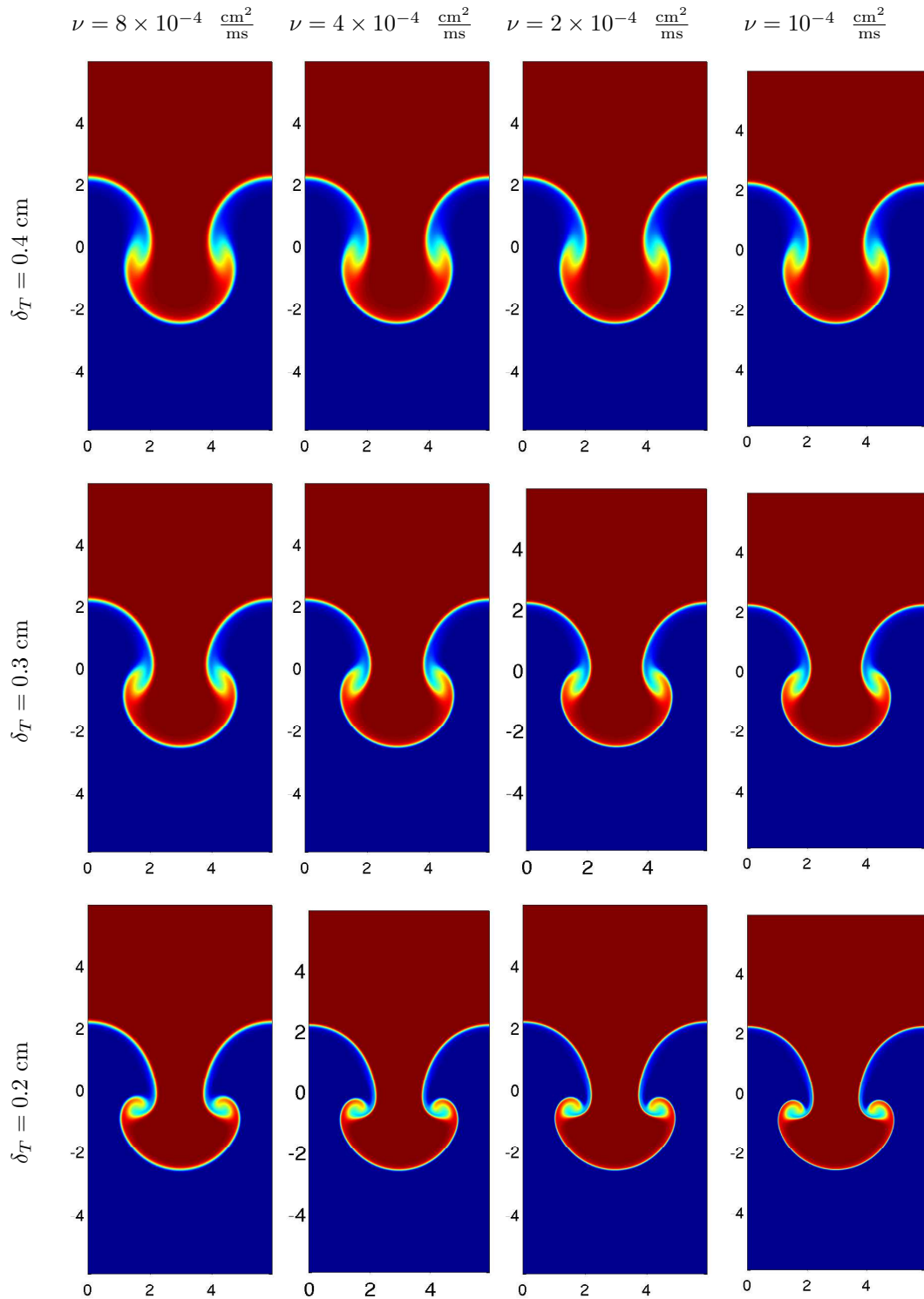


Figure 3.17. The density field $\rho(x, y)$ at 3 ms for different values of the diffuse-interface thickness δ_T and viscosity ν . The results were obtained with grid resolution 512×1024 using the VS method.

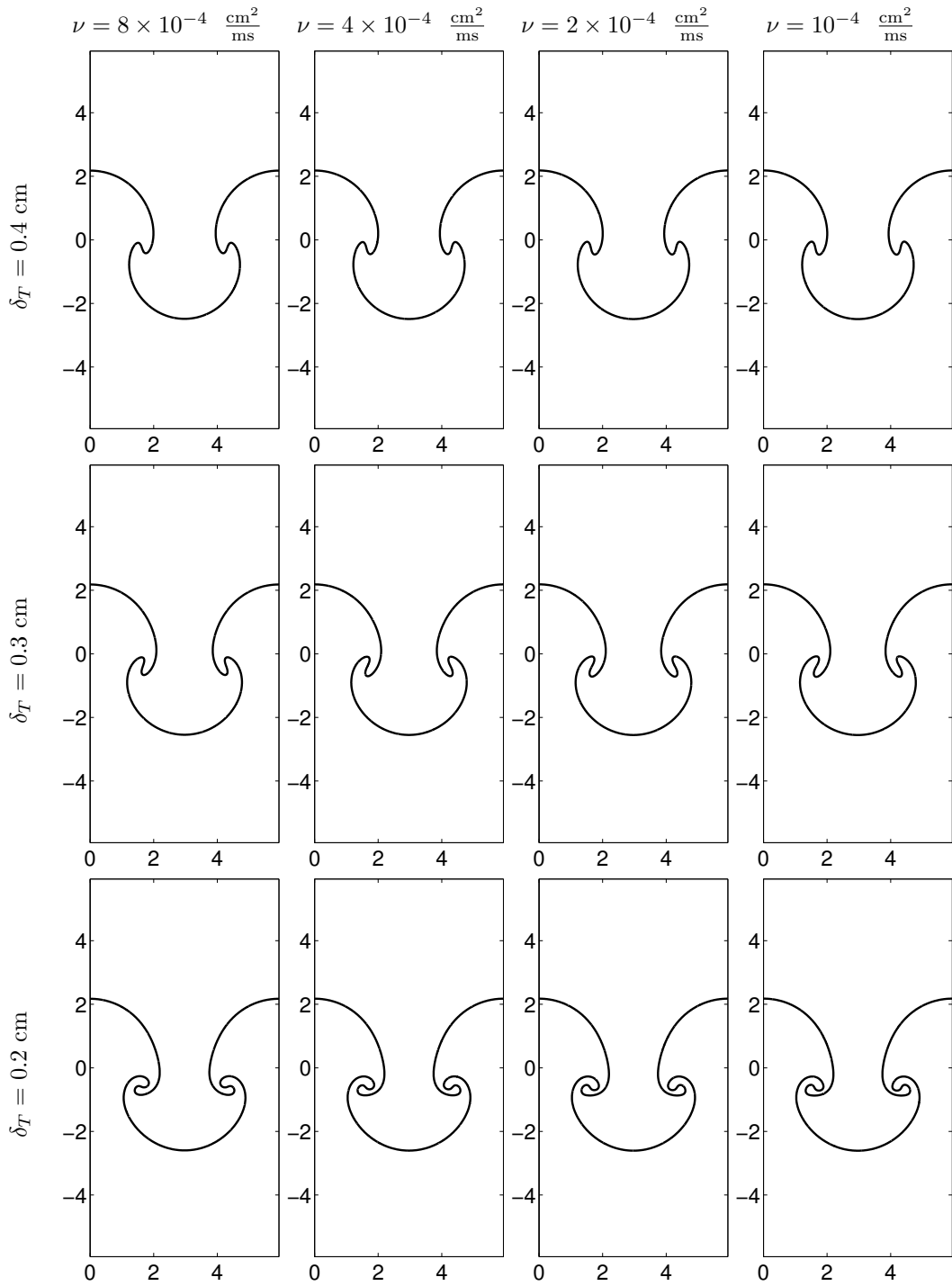


Figure 3.18. The mass fraction contour at 3 ms for different values of the diffuse-interface thickness δ_T and viscosity ν using the VS method.

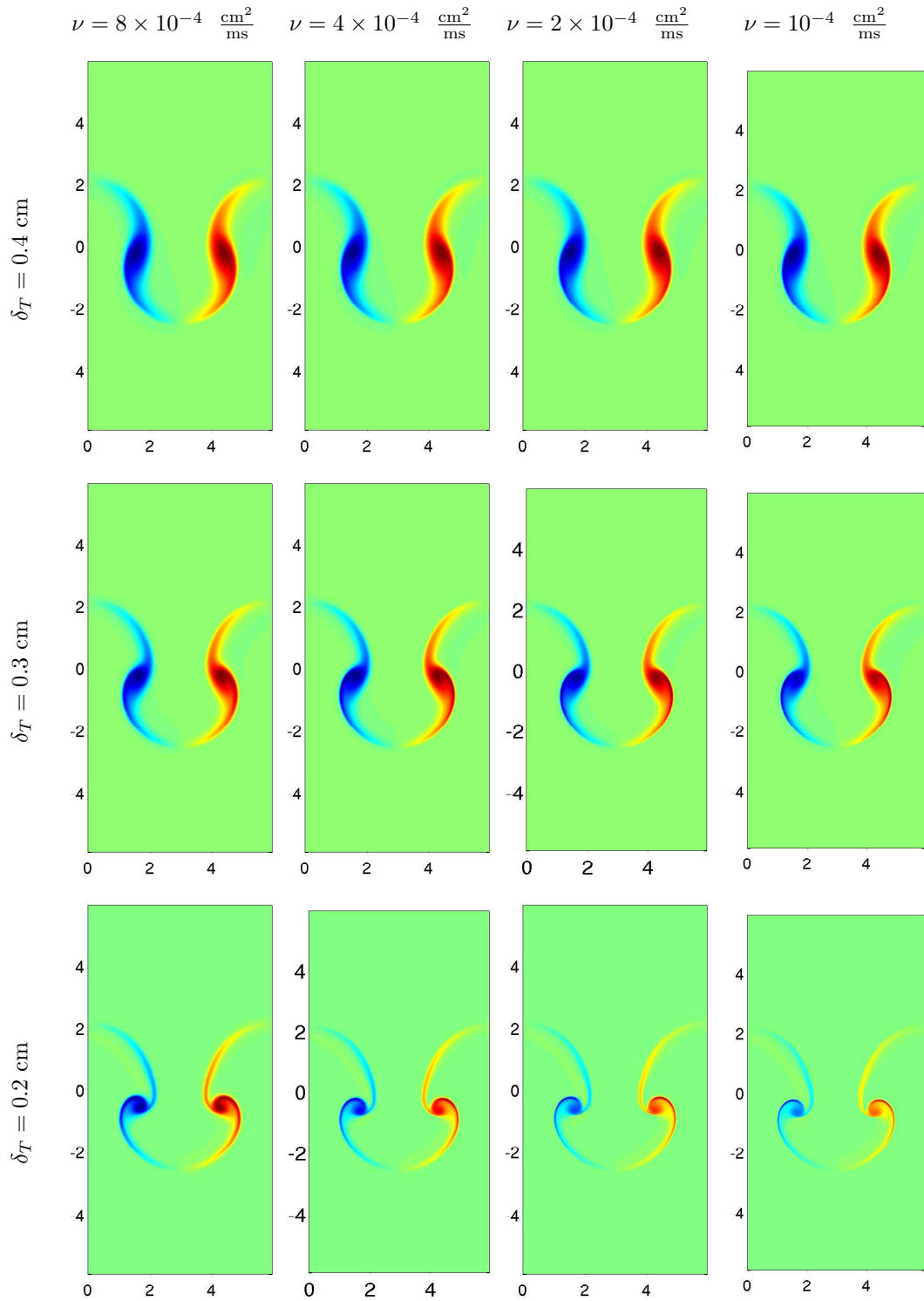


Figure 3.19. The vorticity field $\omega(x, y)$ at 3 ms for different values of the diffuse-interface thickness δ_T and viscosity ν using the VS method.

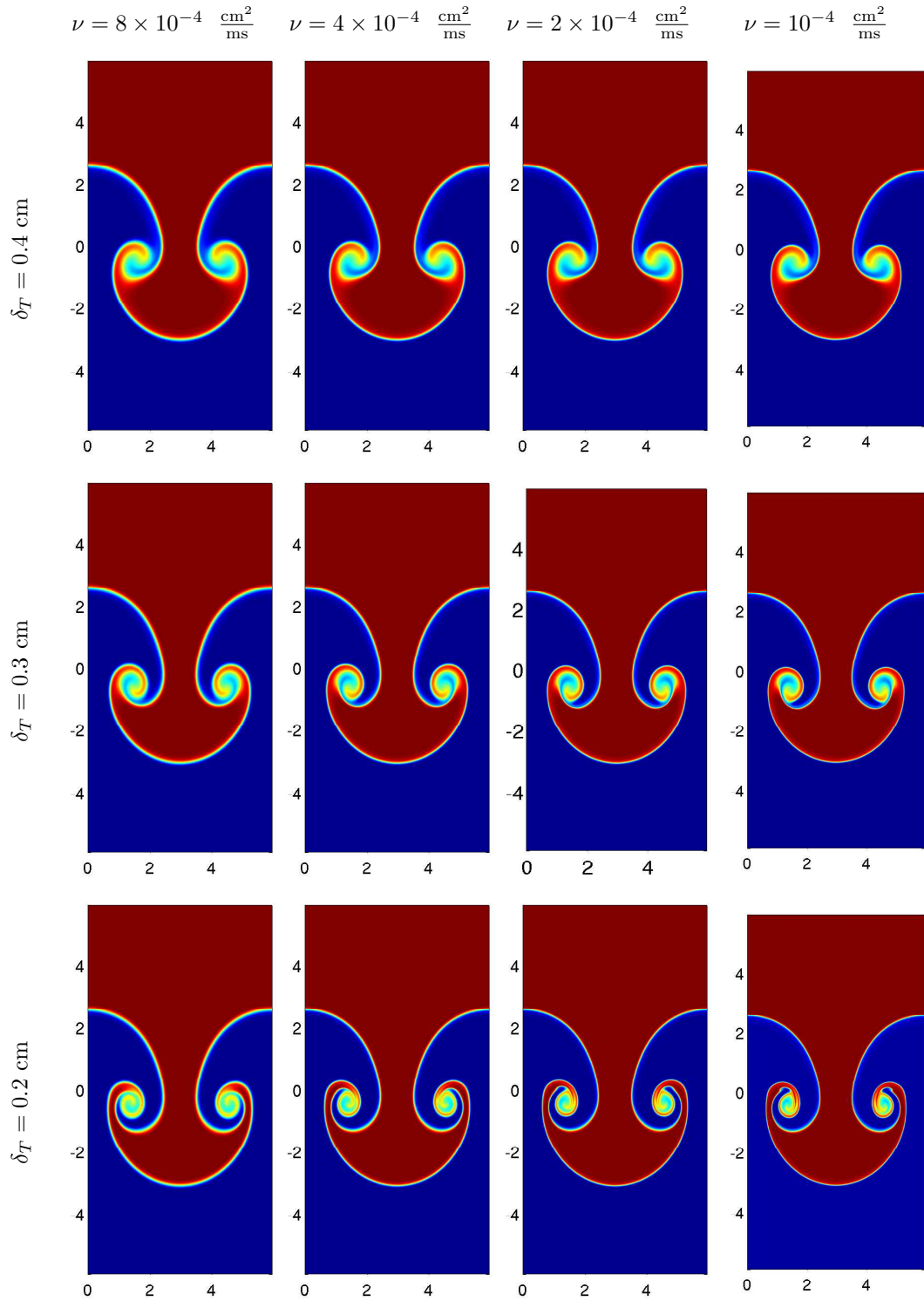


Figure 3.20. Same as Figure 3.17 but at 5 ms.

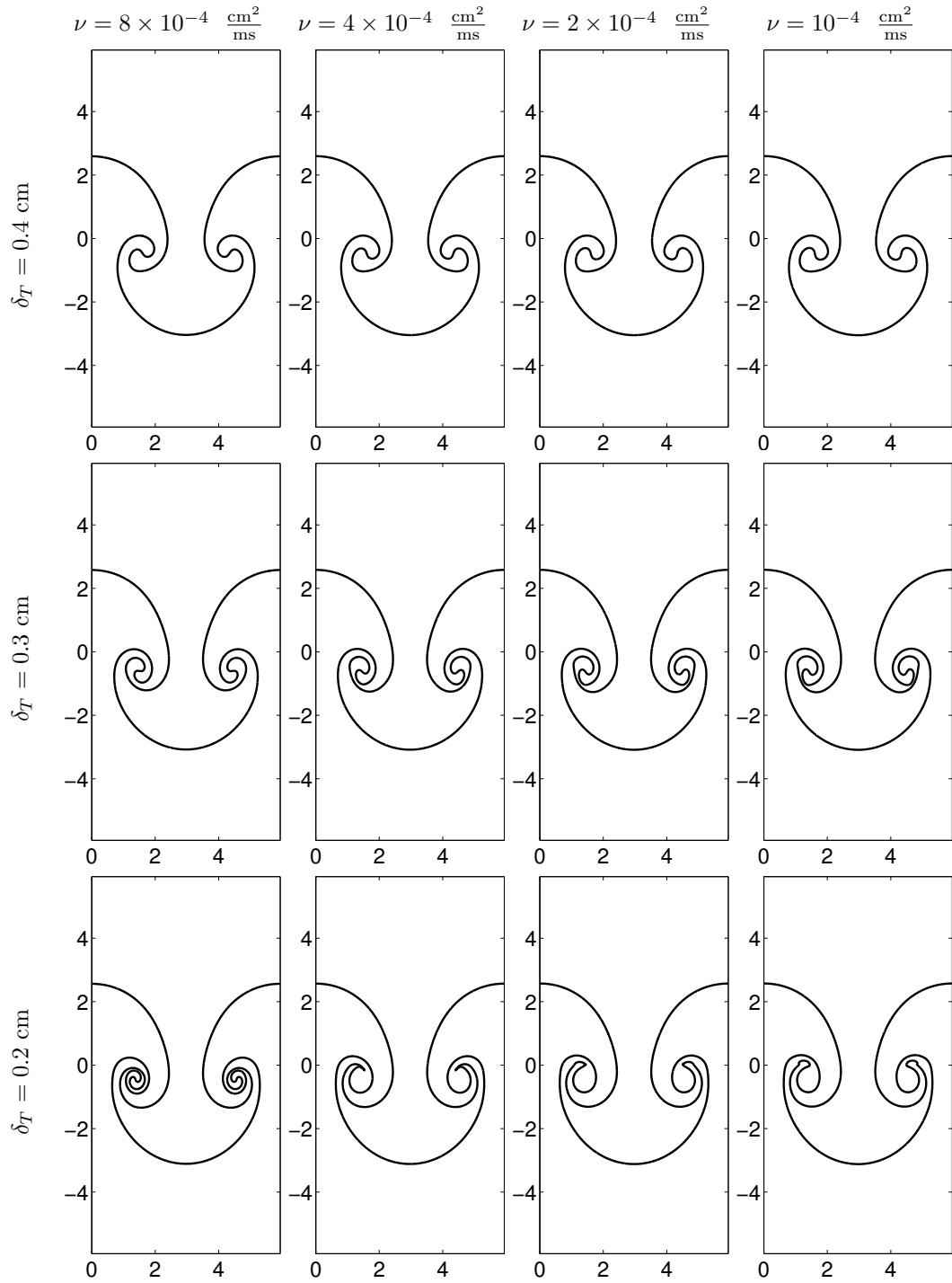


Figure 3.21. Same as Figure 3.18 but at 5 ms.

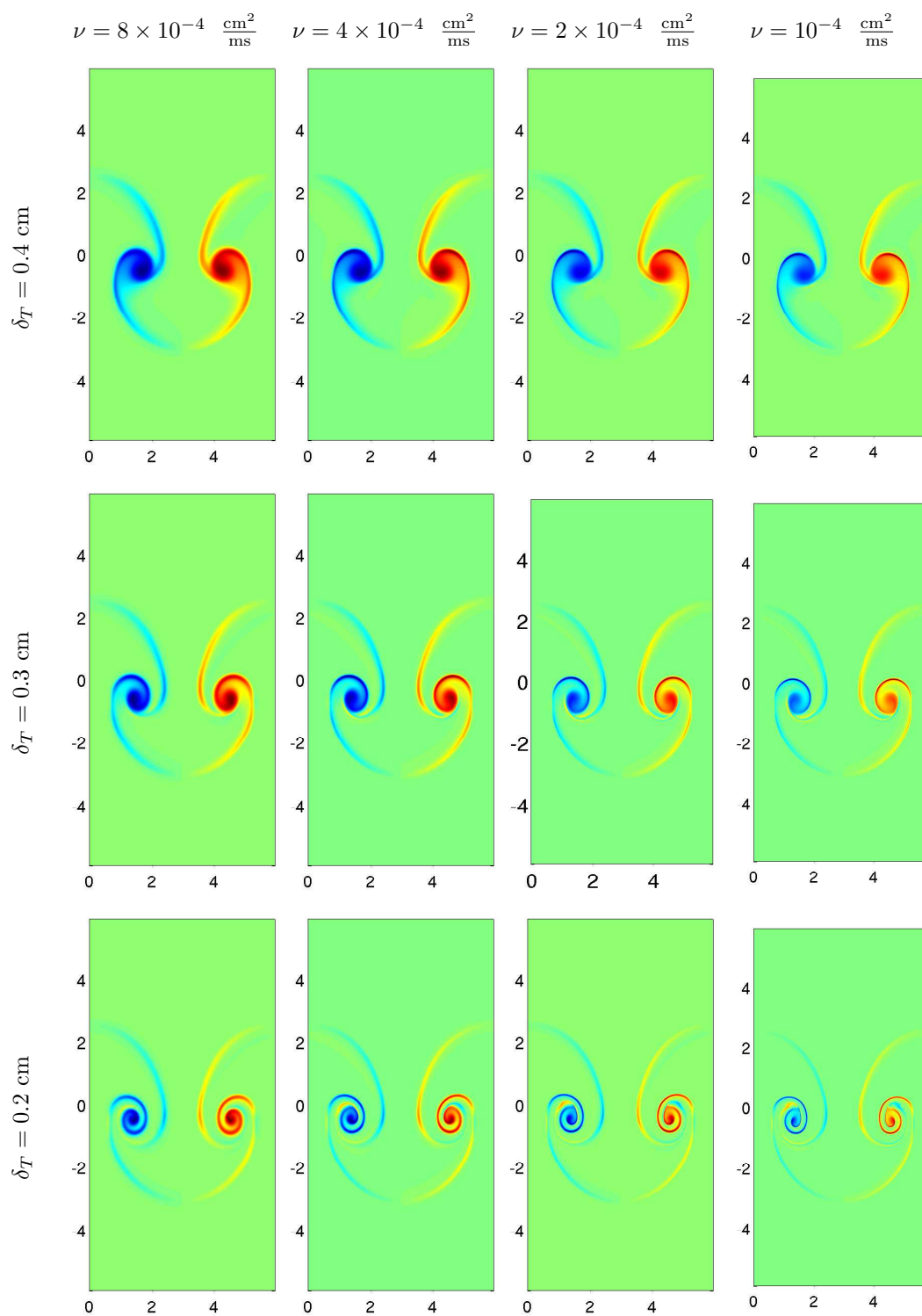


Figure 3.22. Same as Figure 3.19 but at 5 ms.

structure. For a fixed δ_T , as ν is decreased, the cores are stronger. For $\delta_T = 0.2$ cm and for decreasing ν , vorticity of opposite sign is observed within the cores, giving rise to a bi-layer.

Figure 3.23 shows a comparison of the density at 7 ms when the roll-up is fully developed. Significant differences are observed as δ_T decreases and smaller differences as ν decreases. In particular, the roll-ups for $\nu < 4 \times 10^{-4}$ cm²/ms are small, in contrast to more pronounced differences in roll-up structures observed when varying ν at earlier times.

Figure 3.24 continues with the comparison of the mass fraction contours. The results indicate differences in the small scale structure as the viscosity and diffuse-interface thickness are decreased.

Finally, Figure 3.25 shows a comparison of the vorticity field at 7 ms. As the viscosity is decreased, the structure of the roll-up and of the layer becomes more visible, showing tighter windings. For $\delta_T = 0.2$ cm, bi-layers of positive and negative vorticity are visible within the roll-ups.

3.2.2 Convergence study as the diffuse interface thickness is reduced

The results in the previous section were obtained for a grid resolution corresponding to $N_x = 512$. An important question arises as to whether the resolution chosen is sufficient to guarantee fourth-order point-wise convergence. In particular, as shown in Section 3.1.3, fourth-order convergence is expected at all times once sufficient resolution is provided. In order to demonstrate that the results are within the ball of fourth-order convergence, a grid resolution study is performed for the case of $\nu = 10^{-4}$ cm²/ms for different values of δ_T .

Figure 3.26 shows the time-evolution of the point-wise spatial convergence of the vorticity ω and density ρ as the grid is refined at 1, 3, 5, and 7 ms for $\delta_T = 0.4, 0.3,$ and 0.2 cm. For $\delta_T = 0.4$ cm, the results are fourth-order convergent at 1 ms for all grid resolutions. At 3 ms a deterioration of the convergence rate is observed corresponding to $N_x = 32, 64,$ and 128, as indicated by the second-order slope. For $N_x = 256$ and 512, fourth-order convergence is recovered, as indicated by the steepening profile. For 5 and 7 ms, fourth-order convergence is recovered only between $N_x = 256$ and $N_x = 512$. There is no error quoted at 7 ms for $N_x = 32$, as the simulation terminates before 7 ms due to oscillations. For $\delta_T = 0.3$ cm, a similar result applies. For 1 ms, fourth-order convergence is observed for all resolutions. At later times, a deterioration of the convergence properties is observed at coarser resolutions and fourth-order convergence is recovered between $N_x = 256$ and 512. For $\delta_T = 0.2$ cm, a similar result applies, except that the simulations corresponding to $N_x = 32$ and 64 terminate before 5 ms, and that corresponding to $N_x = 128$ before 7 ms. Only simulations with $N_x \geq 256$ give results up to 10 ms. Fourth-order convergence is recovered between $N_x = 256$ and 512.

The following convergence properties apply to the VS method. In general, all simulations exhibit fourth-order convergence at early times. At later times and for smaller values of the diffuse-interface thickness and viscosity, high order requires sufficient resolution to resolve all small-scale structures.

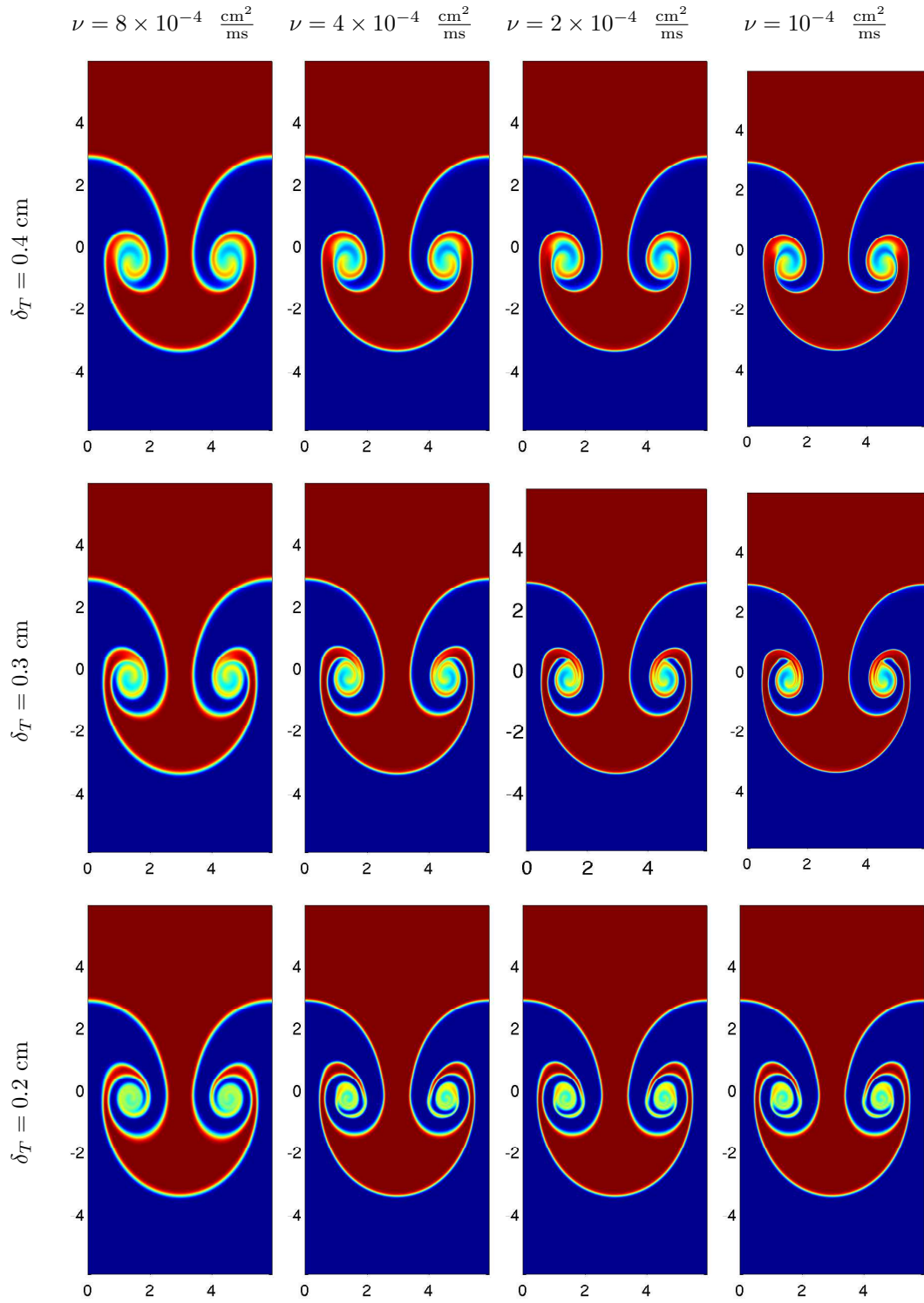


Figure 3.23. Same as Figure 3.17 but at 7 ms.

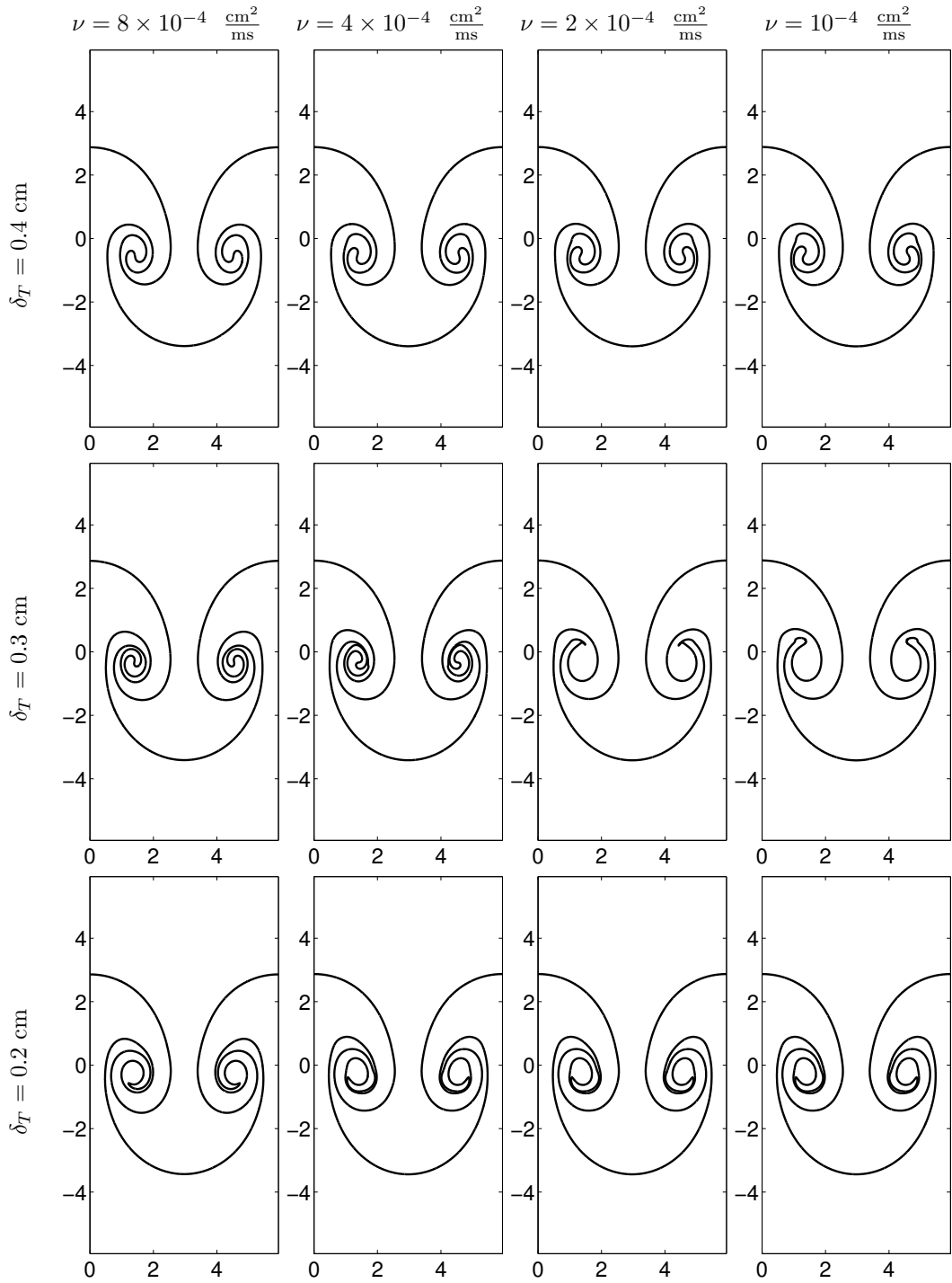


Figure 3.24. Same as Figure 3.18 but at 7 ms.

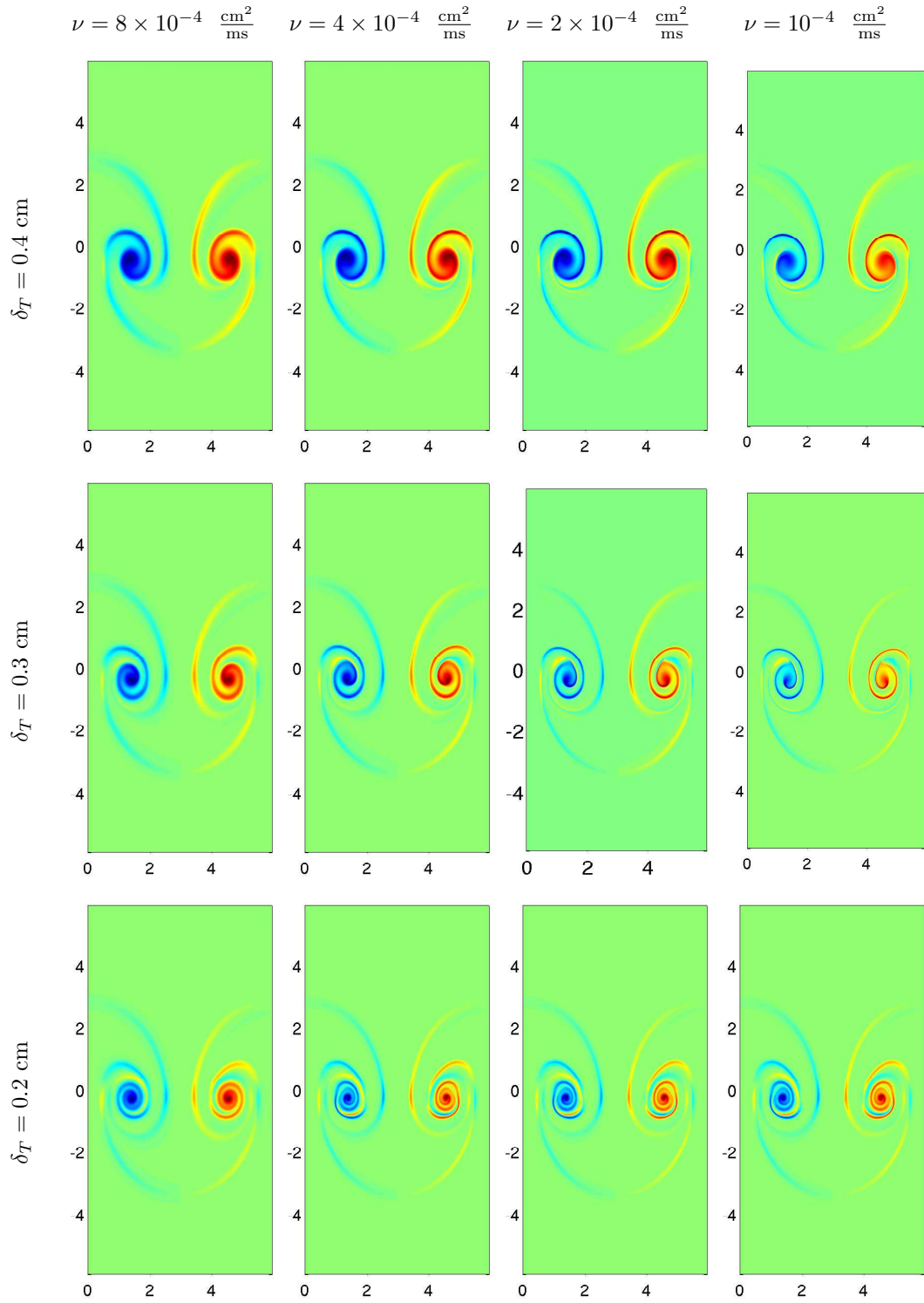


Figure 3.25. Same as Figure 3.19 but at 7 ms.

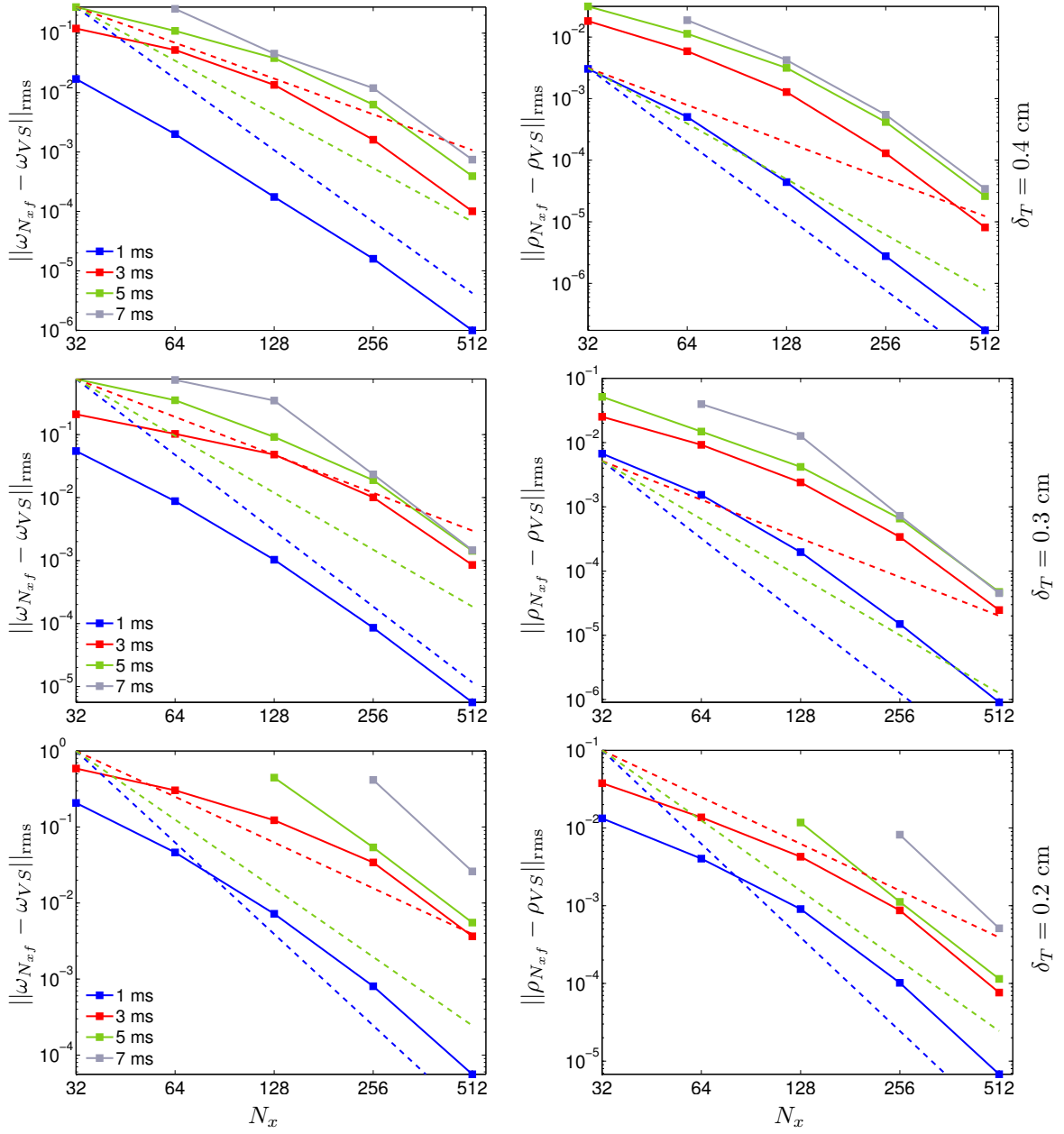


Figure 3.26. Time-evolution of the spatial convergence rate for the vorticity ω and density ρ when $\nu = 10^{-4}$ cm²/ms as the grid is refined for $\delta_T = 0.4, 0.3,$ and 0.2 cm at 1, 3, 5, and 7 ms. For the fine-grid simulation $N_{x,f} \times N_{y,f} = 1024 \times 2048$ when $N_x = 32, 64, 128, 256, 512$. The dashed red line represents N_x^{-2} , the green line N_x^{-3} , and the blue line N_x^{-4} , indicating, second-, third-, and fourth-order convergence.

When insufficient resolution is used, the method generates oscillations that degrade the solution. Even when sufficient resolution is used to prevent the formation of oscillations, the resolution may still not be sufficient to guarantee fourth-order convergence. In fact, as demonstrated here, regions with second- and third-order convergence are observed prior to full fourth-order convergence. The results also demonstrate that $N_x = 512$ is sufficient to guarantee that the results are in the region of fourth-order point-wise convergence.

3.2.3 Effects of viscosity and diffuse-interface thickness on the perturbation, bubble, and spike amplitudes, circulation, and Reynolds numbers

Presented here is a comparison of the perturbation, bubble, and spike amplitudes, circulation, and Reynolds numbers as the diffuse-interface thickness δ_T and viscosity ν are varied. The following conventions are used. Each simulation is assigned a distinctive color and line style as explained in Table 3.5. A series of three figures is shown for each quantity. In the top figure, results for all cases are presented together. In the middle figure, results are shown for a fixed $\delta_T = 0.3$ cm as the viscosity is varied. In the bottom figure, results are shown for a fixed $\nu = 2 \times 10^{-4}$ cm²/ms as δ_T is varied. This allows a more precise quantification of the effects of each parameter.

Figure 3.27 shows a comparison of the perturbation amplitude $a(t)$ as δ_T and ν are varied. No significant variation is observed in the amplitude as these parameters are varied. The reason for this is that the heavier fluid pushes onto the lighter fluid creating similar layer thicknesses as the instability develops. Differences emerge in the small-scale roll-up structure (Sec. 3.2.1) but these differences do not affect the amplitudes.

Figure 3.28 continues the comparison for the bubble and spike amplitudes $a_b(t)$ and $a_s(t)$, respectively. No significant variation is observed in the bubble and spike as ν is varied. Some variation is observed in the initial bubble amplitude as δ_T is varied. This initial difference decreases rapidly and is no longer visible at late times. By contrast, the spike amplitude shows no such variation at the initial time, but instead at intermediate times. No variation is observed at late times.

Figure 3.29 shows a comparison of the circulation $\Gamma(t)$ as δ_T and ν are varied. The circulation shows variation, developing at intermediate times and becoming more pronounced at later times. The variation is due to changes in δ_T , as indicated by the fact that results are grouped by color. In particular, smaller δ_T lead to larger Γ . Similarly, smaller ν lead to larger Γ , but by a smaller amount than changing the diffuse interface thickness.

Also shown in Figure 3.29 is a comparison of the circulation Reynolds number [113]

$$Re_\Gamma(t) \equiv \frac{\Gamma(t)}{\nu}. \quad (3.6)$$

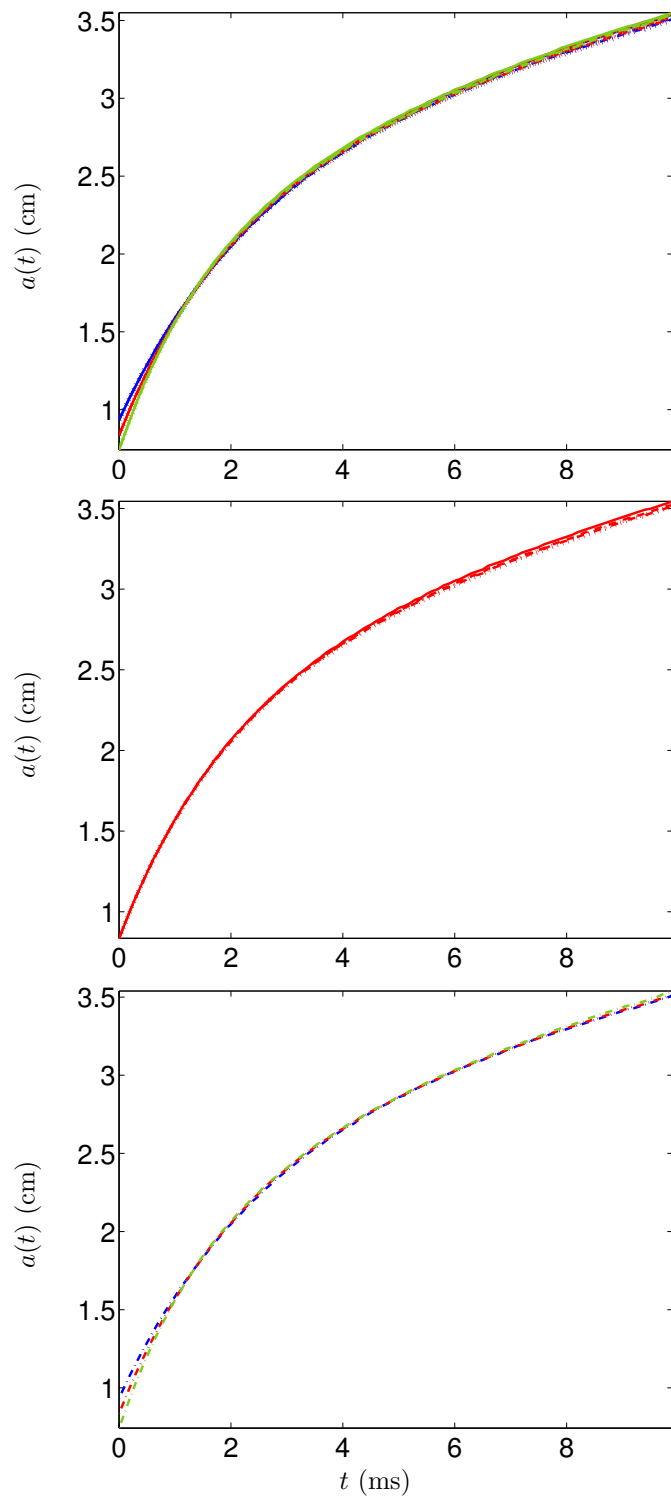


Figure 3.27. Comparison of the perturbation amplitude $a(t)$ when the viscosity ν and diffuse-interface interface thickness δ_T are varied (top). Comparison when ν is changed keeping $\delta_T = 0.3$ cm fixed (middle). Comparison when δ_T is changed keeping $\nu = 2 \times 10^{-4}$ cm²/ms fixed (bottom). Quantities obtained using $\delta_T = 0.4, 0.3,$ and 0.2 cm are shown in blue, red, and green, respectively; quantities obtained using $\nu = 8 \times 10^{-4}, 4 \times 10^{-4}, 2 \times 10^{-4},$ and 10^{-4} (cm²/ms) are shown using a solid, dashed, dash-dot, and dotted lines respectively.

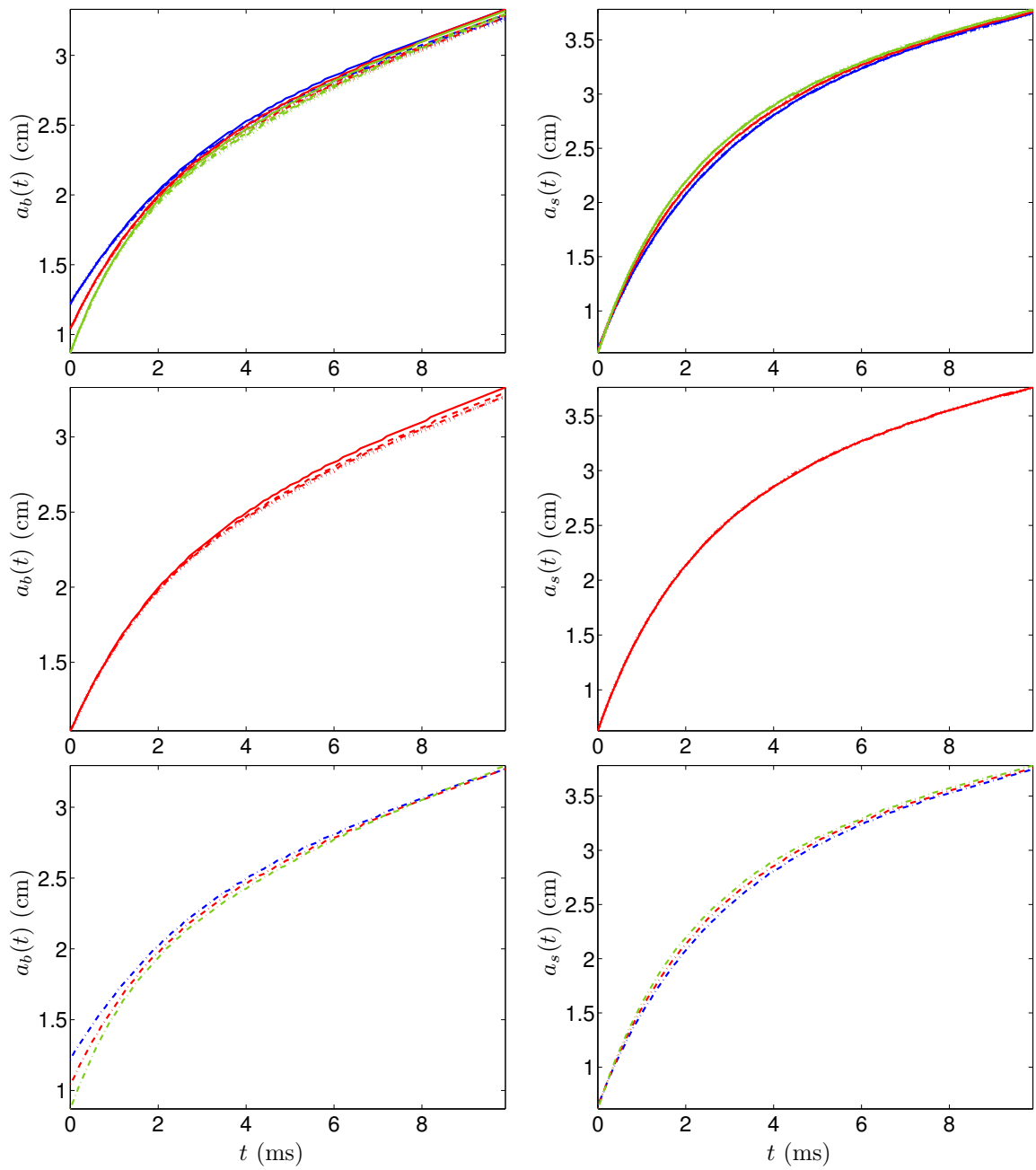


Figure 3.28. Comparison of the bubble and spike amplitudes $a_b(t)$ and $a_s(t)$ when the viscosity ν and diffuse-interface interface thickness δ_T are varied (top). Comparison when ν is changed keeping $\delta_T = 0.3$ cm fixed (middle). Comparison when δ_T is changed keeping $\nu = 2 \times 10^{-4}$ cm²/ms fixed (bottom). See Figure 3.27 for legend.

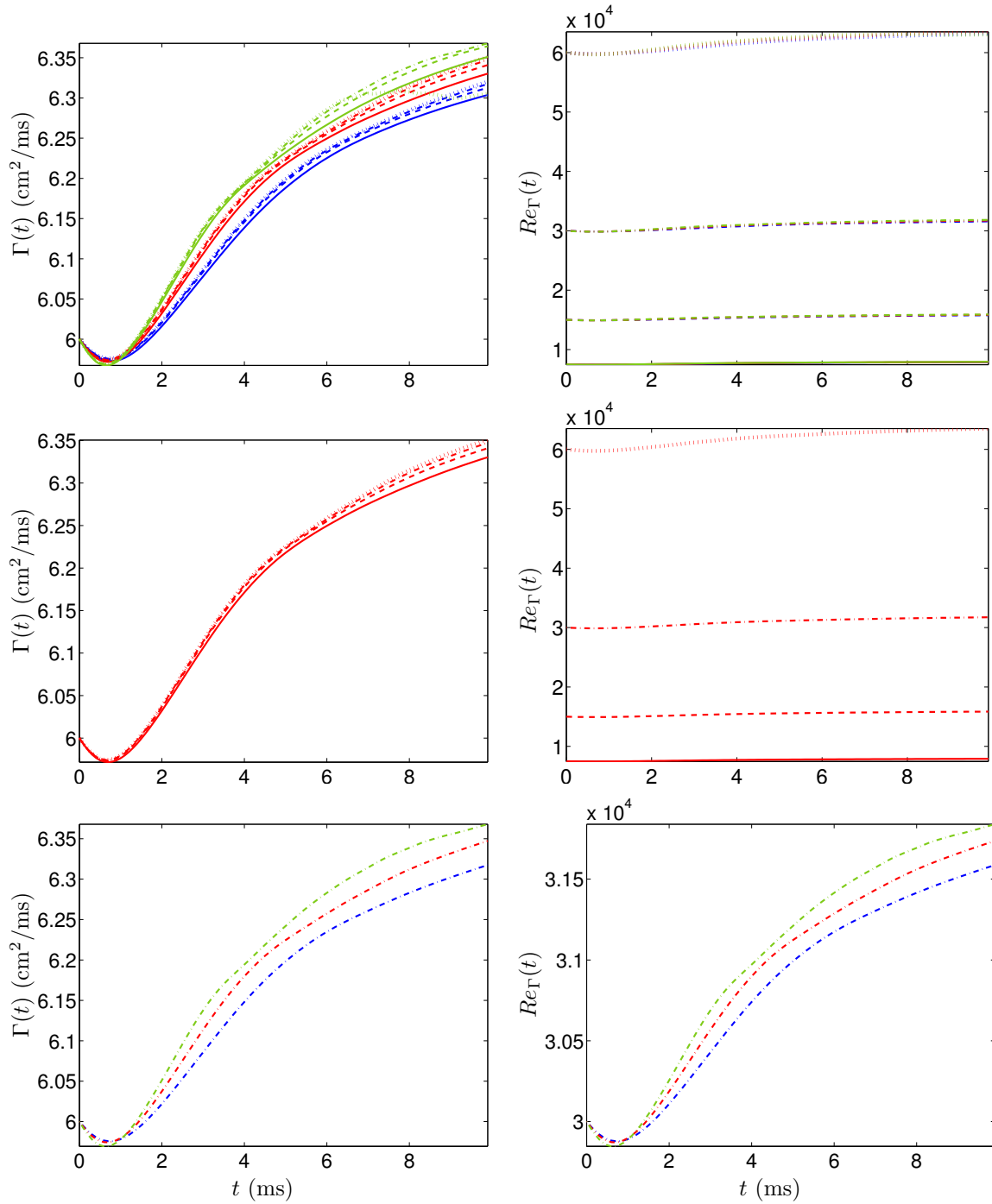


Figure 3.29. Comparison of the circulation $\Gamma(t)$ and Reynolds number $Re_\Gamma(t)$ when the viscosity ν and diffuse-interface thickness δ_T are varied (top). Comparison when ν is changed keeping $\delta_T = 0.3$ cm fixed (middle). Comparison when δ_T is changed keeping $\nu = 2 \times 10^{-4}$ cm^2/ms fixed (bottom). See Figure 3.27 for legend.

As the values of Γ are very similar for different values of ν , Re_Γ groups the results based on the viscosity. Some differences are also observed as δ_T is decreased, but such differences are smaller than when ν is changed.

A perturbation Reynolds number can also be defined based from the width [Eq. (3.4)] and the viscosity [28]

$$Re_h(t) \equiv \frac{h(t)}{\nu} \frac{dh(t)}{dt}, \quad (3.7)$$

where the results for different values of δ_T and ν are shown in Figure 3.30. The Reynolds numbers are clustered based on the viscosity and show some differences at early times with results for smaller δ_T having a larger peak. In fact, a smaller δ_T indicates slightly larger values of dh/dt ; Re_h and Re_Γ have similar magnitudes of $O(10^4)$.

Finally, another definition of the Reynolds number is [107, 77]

$$Re_{\Delta x}(t) \equiv \left[\frac{h(t)}{\Delta x} \right]^{4/3}, \quad (3.8)$$

where Δx is the grid spacing. Figure 3.30 shows the Reynolds number based on this definition. As all results are computed on the same grid corresponding to $N_x = 512$, the curves show a qualitative agreement similar to that of $a(t)$ (Fig. 3.27); $Re_{\Delta x}$ is slightly smaller than Re_Γ and Re_h .

The average fractional deviation Δ [Eq. (3.5)] between the results corresponding to $\delta_T = 0.2$ cm and $\nu = 10^{-4}$ cm²/ms is shown in Table 3.6. The results show that as ν and δ_T are decreased, the average fractional deviations for the perturbation, bubble, and spike amplitudes and the circulation decrease.

In summary, the singularity associated with the evolution of a vortex sheet (Sec. 2.2.1) was resolved here by thickening the sheet to obtain a vortex layer. Convergence of the thickened solution to the Biot-Savart velocity was demonstrated (Sec. 2.2.2). A VS method based on the third-order semi-implicit Adams-Bashforth backward differentiation (AB/BDI3) scheme was constructed (Sec. 2.3). The use of this scheme gave third-order in time and fourth-order in space convergent results for both $A = 0$ and $A = 0.4$. Similar results are expected for larger values of A . For the thin vortex sheet, a regularization corresponding to enlarging the cores of the vortex markers (in the Lagrangian- γ scheme of Sec. 2.1.2) or a regularization provided by the grid (in the VIC method of Sec. 2.1.3) are adopted. By contrast, in the VS method, an explicit thickening of the sheet based on the diffuse-interface thickness δ_T is adopted. Without viscosity, the evolution of the interface showed the formation of steep gradients that introduce oscillations (Sec. 3.1.1). To prevent the formation of such oscillations, viscosity and mass diffusivity were introduced (Secs. 3.1.2 and 3.1.3) keeping $Sc = \nu/D = 1$, and fourth-order accuracy is obtained.

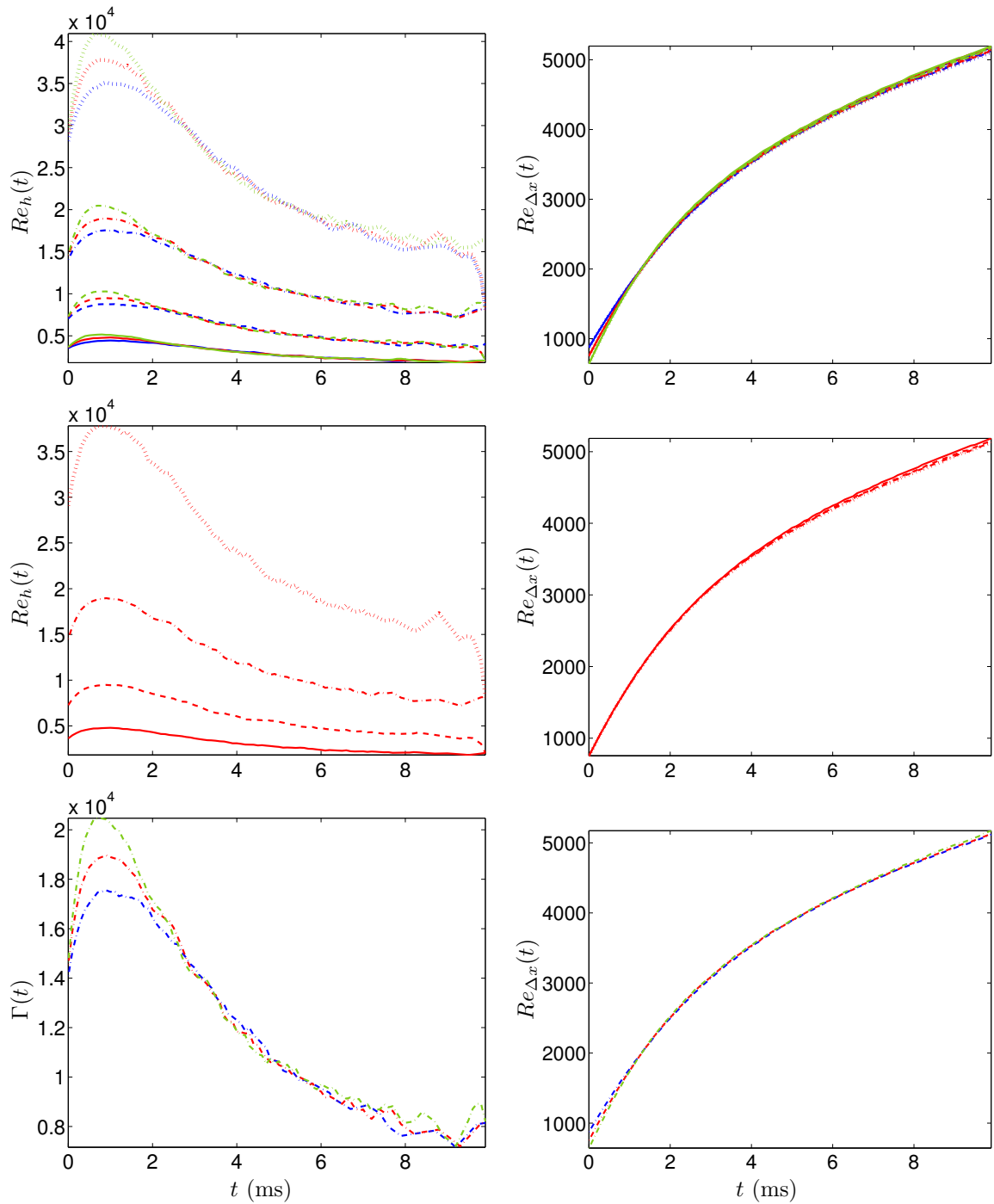


Figure 3.30. Comparison of the Reynolds numbers $Re_h(t)$ and $Re_{\Delta x}(t)$ when the viscosity ν and diffuse-interface interface thickness δ_T are varied (top). Comparison when ν is changed keeping $\delta_T = 0.3$ cm fixed (middle). Comparison when δ_T is changed keeping $\nu = 2 \times 10^{-4}$ cm²/ms fixed (bottom). See Figure 3.27 for legend.

$\Delta a(t)$ (%)	$\nu = 8 \times 10^{-4} \frac{\text{cm}^2}{\text{ms}}$	$\nu = 4 \times 10^{-4} \frac{\text{cm}^2}{\text{ms}}$	$\nu = 2 \times 10^{-4} \frac{\text{cm}^2}{\text{ms}}$	$\nu = 10^{-4} \frac{\text{cm}^2}{\text{ms}}$
$\delta_T = 0.4$ cm	1.22	0.85	0.71	0.62
$\delta_T = 0.3$ cm	0.87	0.47	0.3	0.21
$\delta_T = 0.2$ cm	0.61	0.22	0.08	0

$\Delta a_b(t)$ (%)	$\nu = 8 \times 10^{-4} \frac{\text{cm}^2}{\text{ms}}$	$\nu = 4 \times 10^{-4} \frac{\text{cm}^2}{\text{ms}}$	$\nu = 2 \times 10^{-4} \frac{\text{cm}^2}{\text{ms}}$	$\nu = 10^{-4} \frac{\text{cm}^2}{\text{ms}}$
$\delta_T = 0.4$ cm	5.39	4.54	4.23	4.02
$\delta_T = 0.3$ cm	3.23	2.39	2	1.79
$\delta_T = 0.2$ cm	1.44	0.58	0.2	0

$\Delta a_s(t)$ (%)	$\nu = 8 \times 10^{-4} \frac{\text{cm}^2}{\text{ms}}$	$\nu = 4 \times 10^{-4} \frac{\text{cm}^2}{\text{ms}}$	$\nu = 2 \times 10^{-4} \frac{\text{cm}^2}{\text{ms}}$	$\nu = 10^{-4} \frac{\text{cm}^2}{\text{ms}}$
$\delta_T = 0.4$ cm	2.7	2.67	2.66	2.65
$\delta_T = 0.3$ cm	1.37	1.34	1.32	1.31
$\delta_T = 0.2$ cm	0.1	0.08	0.03	0

$\Delta \Gamma(t)$ (%)	$\nu = 8 \times 10^{-4} \frac{\text{cm}^2}{\text{ms}}$	$\nu = 4 \times 10^{-4} \frac{\text{cm}^2}{\text{ms}}$	$\nu = 2 \times 10^{-4} \frac{\text{cm}^2}{\text{ms}}$	$\nu = 10^{-4} \frac{\text{cm}^2}{\text{ms}}$
$\delta_T = 0.4$ cm	5.9	5	4.6	4.4
$\delta_T = 0.3$ cm	2.5	1.5	1	0.08
$\delta_T = 0.2$ cm	0.19	0.13	0.1	0

Table 3.6. Average fractional deviations for the perturbation amplitude $a(t)$, bubble and spike amplitudes, $a_b(t)$ and $a_s(t)$, and circulation $\Gamma(t)$ as the viscosity ν and diffuse-interface thickness δ_T are varied.

Chapter 4

Investigation of the Two-Dimensional Single-Mode Richtmyer-Meshkov Instability

Presented here are two-dimensional simulations and analysis of the single-mode Richtmyer-Meshkov instability performed using the formally high-order accurate weighted essentially non-oscillatory (WENO) shock-capturing method and the vorticity-streamfunction (VS) method, including comparisons to the Lagrangian and vortex-in-cell (VIC) methods. The simulations are performed on a model of the Mach 1.3 experiment of Jacobs and Krivets [62] (Sec. 4.2.1) to provide an element of validation to the results. The WENO method is a shock-capturing method based on discretizing the compressible Euler equations of gas dynamics. As such, an *ab initio* simulation is performed, with a shock launched in the air(acetone) mixture interacting with the diffuse sinusoidal interface. By contrast, the VS simulation begins with the vorticity deposited on the interface by the shock and is incompressible. A comparison of results from these two methods also provides an element of further validation of the VS method developed here and provides a point of contact between the compressible and incompressible approaches for simulating the Richtmyer-Meshkov instability, using two different numerical methods.

This chapter is organized as follows. A description of the WENO method for the compressible simulations of the single-mode Richtmyer-Meshkov instability is presented in Section 4.1. Initial conditions for the WENO and VS simulations of the Mach 1.3 air(acetone)/SF₆ Jacobs and Krivets [62] experiment are discussed in Section 4.2. A comparison of results obtained from the WENO method using fifth- and ninth-order flux reconstruction is shown in Section 4.3. The dynamics of the instability evolution, including a comparison of the density fields from the WENO and VS simulations with the experimental PLIF images, are shown in Section 4.4. A comparison of the perturbation, bubble, and spike amplitudes from the WENO and VS methods with the experimental data points and with the predictions of amplitude growth models is presented in Section 4.5. A comparison

of the perturbation, bubble, and spike amplitudes and circulation for additional smaller and larger values of the Mach number is presented in Section 4.6. An investigation of reshock using the WENO method, including a comparison of the amplitude following reshock to the predictions of reshock models, is presented in Section 4.7. Finally, the results of an Atwood number study performed using the VS method with comparisons to the Lagrangian and VIC methods are presented in Section 4.8.

4.1 The weighted essentially non-oscillatory (WENO) method

The weighted essentially non-oscillatory (WENO) method is a shock-capturing scheme used in the investigation of the Richtmyer-Meshkov instability [78] and more generally of complex flows with shocks. A brief discussion of the development of the method, including its benefits for simulating this instability are discussed in Section 4.1.1. A brief description of the algorithmic implementation used here is also included in Section 4.1.2.

4.1.1 Literature survey

The WENO scheme belongs to a class of semi-discrete methods (method of lines) developed for the solution of hyperbolic conservation laws. In semi-discrete methods, the equations are discretized only in space, leaving the equations continuous in time. The semi-discrete approach is useful in developing methods with order of accuracy greater than two, as high-order flux reconstructions can be coupled with high-order time-stepping schemes for the system of ordinary differential equations [82, 83]. Methods of first reconstructing the spatial flux and then evolving the solution in time are called *reconstruction-evolution methods* [49]. The earliest of these is the Godunov method [41], which reconstructs the flux based on the average, and is therefore only first-order accurate. A second-order accurate approximation is obtained when a piecewise-linear approximation is used, as in the *monotone upwind schemes for scalar conservation laws* (MUSCL) proposed by Van Leer [143, 144]. Colella and Woodward [26] used piecewise-quadratic approximations in the *piecewise-parabolic method* (PPM). Harten and Osher [50], proposed a uniformly high-order accurate non-oscillatory method (UNO). This method is the same as the Van Leer MUSCL method except that the slopes in the piecewise-linear reconstruction are formed using the essentially non-oscillatory (ENO) reconstruction. Harten et al. [49, 50] proposed a reconstruction-evolution method based on the reconstruction via the primitive function combined with the ENO adaptive stencil high-order polynomial reconstruction. In this method, the stencil yielding the least oscillation is selected by choosing the point that gives the smallest divided-difference for a given choice of points for the polynomial reconstruction. Large values of the divided-differences indicate that a jump discontinuity is being crossed, which introduces large oscillations in the polynomial and considerably lowers the overall accuracy of the numerical solution. By avoiding such points, the ENO method achieves

uniformly high-order accuracy in smooth flow regions and minimizes oscillations.

Despite their success, ENO schemes have several drawbacks. For example, the stencil based on cell averages can be very sensitive to small round-off errors, which can yield two different stencils for small errors. Furthermore, ENO schemes are based on complex logical statements that are not efficiently parallelizable. To overcome these drawbacks, Liu, Osher, and Chan [88] developed the *cell-averaged WENO method*. In this method, a convex combination of *all* possible stencils is formed, instead of choosing a single stencil among several possible stencils. Each stencil is assigned a weight that determines its relative contribution to the computed numerical flux. The weights are assigned so that stencils crossing discontinuities are given nearly zero weight, while stencils that are formed from points in smoother regions are given similar weights. Such schemes are easily parallelized. Another advantage of the WENO method is that the resulting flux is smoother than the flux obtained from the ENO method, and this property can be used to prove the convergence of the method for one-dimensional scalar conservation laws.

Jiang and Shu [63] proposed significant improvements to the WENO method, including a *flux-averaged WENO* formulation and a new method to measure the smoothness of the stencils. When WENO reconstruction is performed over a smooth region and all the r stencils and $r - 1$ points are weighted equally, a method of formal order $2r - 1$ is obtained (a significant improvement over the $r + 1$ order of the Liu, Osher, and Chan formulation). This implementation of the WENO method is used in this investigation with fifth- and ninth-order reconstruction. Balsara and Shu [12] later combined the WENO reconstruction with the monotonicity-preserving bounds of Suresh and Huynh [138] to obtain high-order monotonicity preserving WENO (MPWENO) schemes. WENO methods have been used in simulations of complex flows with shocks [90, 131] and more recently in the investigation of the Richtmyer-Meshkov instability [78, 129, 77].

Approximating discontinuous solutions of hyperbolic conservation laws using high-order methods yields only first-order accuracy in general [89, 108]. In the case of a scalar law, the characteristics point into the shock. As a result, first-order errors are confined to a region near the shock and errors $O(\Delta x^p)$ are obtained in regions away from the shock when a scheme of order p is used. However, in the case of systems of conservation laws, multiple families of characteristics intersect the shock. As a result, the large error near the shock propagates into the entire post-shock region, so that even formally high-order methods give no better than first-order convergence, as demonstrated by Engquist and Sjögreen [36].

The reason for using high-order methods in flows with shocks, even if only first-order accuracy is realized in the post-shock region, is that high-order accuracy is desired for the propagation of high-frequency low-amplitude waves and small-scale structures present in a Richtmyer-Meshkov unstable mixing layer [21]. Furthermore, the nonlinearity of the WENO method removes the generation of spurious oscillations (usually associated with linear central-difference schemes), making the method

stable [21]. Recently, Gottlieb et al. [43] recovered third-order (design) accuracy in a post-shock region by applying the Gegenbauer postprocessing method to a fifth-order WENO simulation of the steady-state converging-diverging nozzle. This confirms an argument by Lax [79] that for a nonlinear system, more high-order information is retained by a high resolution scheme (such as the WENO method) and that this high-order information can (in principle) be recovered by suitable post-processing. In addition, it was shown earlier [77] that higher-order WENO methods have less numerical dissipation than lower-order methods and were more computationally advantageous than increasing the grid resolution for the simulation of the Richtmyer-Meshkov instability. Here, it is shown that increasing the grid resolution leads to second-order accurate convergence of the perturbation, bubble, and spike amplitudes and circulation (Sec. 4.3) for both fifth- and ninth-order WENO flux reconstructions.

Additional information on WENO schemes can be found in Shu [132]. Information on the stability analysis techniques used in the development of the WENO method can be found in Laney [74] and Leveque [82, 83].

4.1.2 Overview of the WENO method

The numerical simulations of the reshocked Richtmyer-Meshkov instability were performed using the characteristic projection-based, finite-difference WENO shock-capturing method using fifth- and ninth-order flux reconstruction [63, 12]. The parallel code used was developed as part of a collaboration between the Lawrence Livermore National Laboratory and Brown University [30]. A methods-of-lines approach to discretize the compressible Euler equations is adopted. The Euler equations are augmented by an additional equation for the conservation of mass fraction m (of the heavier gas):

$$\frac{\partial}{\partial t} \begin{bmatrix} \rho \\ \rho u \\ \rho v \\ \rho e \\ \rho m \end{bmatrix} + \frac{\partial}{\partial x} \begin{bmatrix} \rho u \\ \rho u^2 + p \\ \rho u v \\ (\rho e + p) u \\ \rho m u \end{bmatrix} + \frac{\partial}{\partial y} \begin{bmatrix} \rho v \\ \rho u v \\ \rho v^2 + p \\ (\rho e + p) v \\ \rho m v \end{bmatrix} = 0 \quad (4.1)$$

in two dimensions.

In the WENO method, the one-dimensional scalar conservation law

$$\frac{\partial u(x, t)}{\partial t} + \frac{\partial f(u)}{\partial x} = 0 \quad (4.2)$$

is discretized using a finite-difference approximation on a uniform grid discretized by x_i :

$$\frac{du_i(t)}{dt} = -\frac{1}{\Delta x} \left(\hat{f}_{i+\frac{1}{2}} - \hat{f}_{i-\frac{1}{2}} \right), \quad (4.3)$$

where $\widehat{f}_{i\pm\frac{1}{2}}$ are the numerical fluxes and $\Delta x = x_{i+1} - x_i$ is the uniform grid spacing. The WENO algorithm reconstructs the fluxes at the mid-points between cells $\widehat{f}_{i\pm\frac{1}{2}}$ based on the values at the center of the cells \widehat{f}_i .

Before applying the WENO reconstruction, an upwinding direction is established using local Lax-Friedrichs flux-splitting

$$\widehat{f}^\pm(u) = \frac{f(u) \pm \alpha u}{2}, \quad \alpha = \max_u \left| \frac{\partial f(u)}{\partial u} \right|. \quad (4.4)$$

Next the WENO reconstruction is applied to determine $\widehat{f}_{i\pm\frac{1}{2}}^+$ based on the point values of \widehat{f}_i . The main idea of the WENO method is to use a polynomial of degree k for the reconstruction, built on stencils containing $k+1$ points. For the $\widehat{f}_{i+\frac{1}{2}}^+$ reconstruction, the stencils must contain the point x_i , so that k reconstructions are formed. Next, the reconstructions are nonlinearly weighted

$$\widehat{f}_{i+\frac{1}{2}}^+ = \sum_{r=0}^{k-1} w_r \widehat{f}_{i+\frac{1}{2}}^{(r)+}, \quad w_r = \frac{\alpha_r}{\sum_{s=0}^{k-1} \alpha_s}, \quad (4.5)$$

where the α_r in the construction of the weights w_r are given by

$$\alpha_r = \frac{d_r}{(\epsilon + \beta_r)^2}, \quad \beta_r = \sum_{\ell=1}^{k-1} \int_{x_{i-\frac{1}{2}}}^{x_{i+\frac{1}{2}}} (\Delta x)^{2\ell-1} \left[\frac{\partial^\ell p_r(x)}{\partial x^\ell} \right]^2 dx, \quad (4.6)$$

d_r are the optimal weights [132], $p_r(x)$ are the interpolating polynomials, and $\epsilon = 10^{-6}$ is a small number. The construction of the weights achieves two goals:

1. in the presence of a discontinuity, the stencil that crosses the discontinuity is given an effectively zero weight, enforcing the ENO property of solutions to hyperbolic conservation laws;
2. in smooth regions, the information from the $2k-1$ points is efficiently used to give a $(2k-1)$ -th order accurate solution.

A similar reconstruction is performed for $\widehat{f}_{i+\frac{1}{2}}^-$. Finally, the flux entering the finite-difference formula [Eq. (4.3)] is

$$\widehat{f}_{i+\frac{1}{2}} = \widehat{f}_{i+\frac{1}{2}}^+ + \widehat{f}_{i+\frac{1}{2}}^-. \quad (4.7)$$

In the present simulations, a single value for the adiabatic exponent γ is specified: a multiple γ formulation introduces non-physical pressure oscillations near the material interfaces in conservative shock-capturing schemes for the multi-component fluid equations [65, 66, 1, 2]. Nonetheless, WENO schemes have been developed for two-gamma formulations [90, 58].

The system of ordinary differential equations from the spatial discretization

$$\frac{du}{dt} = L(u, t) \quad (4.8)$$

are integrated in time using a third-order total-variation-diminishing (TVD) Runge-Kutta method [133]

$$\begin{aligned} u^{(1)} &= u^n + \Delta t L(u^n), \\ u^{(2)} &= \frac{3}{4} u^n + \frac{1}{4} u^{(1)} + \frac{1}{4} \Delta t L(u^{(1)}), \\ u^{n+1} &= \frac{1}{3} u^n + \frac{2}{3} u^{(2)} + \frac{2}{3} \Delta t L(u^{(2)}), \end{aligned} \tag{4.9}$$

where Δt is the timestep. These methods were developed because ordinary Runge-Kutta methods are only linearly stable and do not guarantee convergence in the presence of shocks or other discontinuities. Moreover, the stability analysis is usually performed for fixed stencils and does not apply to ENO and WENO methods that have adaptive stencils. By contrast, the TVD property ensures stability of the numerical scheme [48]. In addition, a TVD scheme ensures that large oscillations are not introduced at shocks and contact surfaces in the numerical solution.

4.2 Initial and boundary conditions

The initial and boundary conditions used for the simulations of a model of the Mach 1.3 air(acetone) and SF₆ Jacobs and Krivets experiment (Sec. 4.2.1) are discussed here. For the WENO compressible simulations, only a single value of the adiabatic exponent can be specified. As the experiment contains gases with different values of the adiabatic exponent, the value of a mixture of 50% air(acetone) and 50% SF₆ is adopted in the *mix initial conditions* (Sec. 4.2.2). The VS and vortex methods begin the simulations immediately following the passage of the shock. As a result, the vorticity deposited on the interface by the shock in the WENO method is compared to predictions from linear instability theory and the Samtaney-Zabusky circulation-deposition model (Sec. 4.2.3). For the VS and for the Lagrangian and vortex-in-cell (VIC) methods, the initial conditions from linear instability theory are used to specify the initial vorticity (Sec. 4.2.4).

4.2.1 Late-time Mach 1.3 air(acetone)/SF₆ Richtmyer-Meshkov instability experiment of Jacobs and Krivets

Here, the WENO and VS methods are applied to a two-dimensional model of a Richtmyer-Meshkov shock tube experiment of Jacobs and Krivets [62]. Jacobs and Krivets modified the vertical shock tube previously used in the investigation of Collins and Jacobs [27] and in Jones and Jacobs [64] to include a longer driver section, allowing a stronger shock with Mach number $Ma = 1.3$ to be launched. The test section had a 8.9 cm square cross section and a length of 75 cm. A membraneless initial condition was created as follows: a mixture of air and acetone vapor [denoted air(acetone)] in the

sequel], and sulfur hexafluoride (SF_6) gas flowed towards each other, exiting from small slits located at the entrance of the test section. This generated a stable surface at the entrance of the test section. An oscillation imposed on the shock tube formed standing sinusoidal waves. This technique created a well-defined, slightly diffused initial condition. By contrast, the use of membranes gives sharp initial conditions, but their effects on the development of the instability are not fully understood.

Previously, using membraneless sinusoidal initial conditions and shocks with $Ma = 1.1$ and 1.2 , Collins and Jacobs [27] reported excellent agreement between their experimental measurements of the amplitude growth and the prediction of the Sadot et al. [114] nonlinear model. However, the late-time development of the instability was limited by the arrival of the transmitted shock during the reshock phase. The higher Mach number $Ma = 1.3$ allowed the investigation of “late-time” effects, with the instability developing more rapidly for the higher Mach number. Rescaling time, the instability development reached larger values of τ [Eq. (1.17)] due to the larger $[u]$. In addition to the $\lambda = 5.9$ cm experiment, Jacobs and Krivets also considered $\lambda = 3.6$ cm, resulting in larger values of k , allowing the investigation of even later-time effects. Only the $\lambda = 5.9$ cm experiment is considered here.

4.2.2 Mix and upstream initial conditions for the WENO method

In a previous investigation [78], the upstream conditions were matched so that the adiabatic exponent corresponding to the air(acetone) mixture was used. In the present thesis, both the upstream conditions and new *mix* initial conditions are adopted, where the adiabatic exponent corresponding to a 50% mixture of air(acetone) and SF_6 by volume is used.

The WENO code requires the specification of the following initial conditions:

1. physical properties of gases, including the densities ρ_r (r is fluid index), molecular weights M_r , adiabatic exponent γ , specific heat at constant pressure c_p , and specific heat at constant volume c_v ;
2. initial perturbation characteristics, including the preshock amplitude a_0^- , the wavelength λ , and the diffusion thickness δ_T , where the thickness function (multiplying the density) is

$$S(x, y) = \begin{cases} 1 & d \leq 0 \\ \exp(-\alpha |d|^8) & 0 < d < 1 \\ 0 & d \geq 1 \end{cases} \quad (4.10)$$

with $d = [x + \eta(y) + \delta_T - x]/(2\delta_T)$ and $\alpha = -\ln \beta$ (β is machine zero);

3. additional quantities, including the lengths of the domain L_x and L_y (and L_z in three dimensions), the shock Mach number, and the temperature ahead of the shock T_1 , and;

	air	acetone vapor	air(acetone)	SF ₆
M (g/mol)	28.95	58.08	34.76	146.05
ρ (g/cm ³)	1.202×10^{-3}	1.804×10^{-3}	1.3525×10^{-3}	5.494×10^{-3}
γ	1.4	1.1246	1.2776	1.093
R_g [erg/(g K)]	2.872011×10^6	1.431551×10^6	2.391681×10^6	5.692894×10^5
c_p [erg/(g K)]	1.005204×10^7	1.292076×10^7	1.100727×10^7	6.690681×10^6
c_v [erg/(g K)]	7.180028×10^8	1.148921×10^7	8.615586×10^6	6.121392×10^6
μ [g/(cm s)]	1.85×10^{-4}	7.56×10^{-5}	1.564×10^{-4}	1.61×10^{-4}
ν (cm ² /s)	1.539×10^{-1}	4.19×10^{-2}	1.157×10^{-1}	2.93×10^{-2}

Table 4.1. The physical properties of air, acetone vapor, SF₆, and air(acetone) mixture, including the molecular weight M , the density ρ , the adiabatic exponent γ , the particular gas constant R_g , the heat capacity at constant volume c_v , the heat capacity at constant pressure c_p , the dynamic viscosity μ , and the kinematic viscosity ν . The properties of air, acetone vapor, and SF₆ were obtained from the NIST Chemistry Webbook [87] at a temperature of $T_1 = 296$ K.

- numerical parameters, including the number of grid points per direction N_x and N_y (and N_z in three dimensions).

Other properties, including the initial pressure and energy are computed based on the density, temperature, and the particular gas constant $R_g = R_u/M$, where $R_u = 8.3143 \times 10^7$ erg/(mol K) is the universal gas constant. The pressure is then matched across the interface by adjusting the temperature of the gas T_2 [75].

The simulations were performed using the following boundary conditions:

- free-stream conditions at the entrance of the test section;
- reflecting boundary condition at the end of the test section, so that reshock occurs;
- periodic in the y direction (and in the z direction for three-dimensional simulations).

Table 4.1 shows the physical properties of air, acetone vapor, the air(acetone) mixture, and SF₆.

The physical properties of the air(acetone) mixture are obtained using the thermodynamic properties of a mixture [118]. The mixture is composed of 75% air and 25% acetone vapor by volume [27], so that the total density of the air(acetone) mixture is

$$\rho_{aa} = 0.75 \rho_{air} + 0.25 \rho_{ac}, \quad (4.11)$$

the air *mass fraction* and *mole fraction* are

$$m_{air} = \frac{0.75 \rho_{air}}{\rho_{aa}}, \quad X_{air} = \frac{m_{air} M_{ac}}{(1 - m_{air}) M_{air} + m_{air} M_{ac}}, \quad (4.12)$$

where M_r are the molecular weights. The heat capacity at constant pressure and the heat capacity at constant volume for the mixture are obtained by weighting the heat capacities of the components

by the mass fraction. Their ratio gives the adiabatic exponent of the mixture. The dynamic viscosity of the air(acetone) mixture is obtained using [140]

$$\mu_{aa} = \frac{X_{air} \mu_{air} \sqrt{M_{air}} + X_{ac} \mu_{ac} \sqrt{M_{ac}}}{X_{air} \sqrt{M_{air}} + X_{ac} \sqrt{M_{ac}}}. \quad (4.13)$$

In the present investigation, two different strategies are adopted to specify γ .

1. In the *mix initial conditions*, the adiabatic exponent corresponding to a mixture of 50% air(acetone) and 50% SF₆ by volume is adopted, resulting in $\gamma = 1.1405$. In order to match the initial growth rate v_0 [Eq. (1.16)] of the experiment, the *incident shock Mach number* is slightly increased to $Ma_i = 1.313$.
2. In the *upstream initial conditions*, the adiabatic exponent $\gamma = 1.2776$ of the air(acetone) mixture is used. With these initial conditions, the initial Mach number is that of the experiment $Ma_i = 1.292$, as now the velocity of the shock between the experiment and the simulations is matched. This is the reason these initial conditions are called “upstream”, as the conditions prior to the refraction process are all matched.

Normal shock refraction theory [75] is used to determine the jump in interface velocity $[u]$ and the post-shock Atwood number A^+ . These values are used to compute the initial growth rate v_0 [Eq. (1.16)] and to adjust the incident shock Mach number for the mix initial conditions. The post-shock initial perturbation amplitude and post-shock diffuse-interface thickness are

$$a_0^+ = \eta_{comp} a_0^-, \quad \delta_T^+ = \eta_{comp} \delta_T^-, \quad (4.14)$$

where

$$\eta_{comp} \equiv 1 - \frac{[u]}{u_{shock}} \quad (4.15)$$

is the *compression factor* [103].

Table 4.2 gives the properties of the air(acetone) mixture and of the SF₆ gas used in the present simulations when $\gamma_1 = \gamma_2 = 1.1405$ (mix initial conditions), and when $\gamma_1 = \gamma_2 = 1.2776$ (upstream initial conditions). When a different γ is selected, the gas constant R_g is the same, but the heat capacity at constant volume c_v is modified. In the upstream initial conditions, the physical properties of the air(acetone) mixture are exact.

Table 4.3 compares the flow properties as reported by Jacobs and Krivets [62] (*experimental initial conditions*) with values obtained from one-dimensional shock refraction theory. The *two-gas initial conditions* values are obtained using the adiabatic exponents $\gamma_1 = 1.2776$ for the air(acetone) mixture and $\gamma_2 = 1.093$ for SF₆. The *incident shock Mach number* is that of the experiment with $Ma_i = 1.292$. Also shown are the mix and upstream initial conditions. A comparison of the

Mix initial conditions		
	air(acetone)	SF ₆
γ	1.1405	1.1405
R_g [erg/(g K)]	2.391682×10^6	5.692894×10^5
c_p [erg/(g K)]	1.941408×10^7	4.621112×10^6
c_v [erg/(g K)]	1.70224×10^7	4.051823×10^6

Upstream initial conditions		
	air(acetone)	SF ₆
γ	1.2776	1.2776
R_g [erg/(g K)]	2.391682×10^6	5.692894×10^5
c_p [erg/(g K)]	1.100855×10^7	2.620044×10^6
c_v [erg/(g K)]	8.61659×10^6	2.050754×10^6

Table 4.2. The gas constant R , heat capacity at constant pressure c_p , and heat capacity at constant volume c_v for the air(acetone) mixture and SF₆ gas when $\gamma_1 = \gamma_2 = 1.1405$ for a mixture of 50% air(acetone) and 50% SF₆ by volume (*mix initial conditions*); and when $\gamma_1 = \gamma_2 = 1.2776$ of the air(acetone) mixture is used (*upstream initial conditions*).

experimental initial conditions with the two-gas initial conditions shows a $\approx 4.5\%$ difference in the initial perturbation growth rate v_0 [Eq. (1.16)] and a $\approx 14.1\%$ difference in the time of reshock $t_{reshock}$. These differences are due to the diffuse interface and can be quantified by the *growth reduction factor* ψ [34], which is a function of δ_T and A satisfying the boundary value problem

$$\frac{d}{dx} \left(\rho \frac{df}{dx} \right) = \left(\rho - \frac{\psi}{kA} \frac{d\rho}{dx} \right) k^2 f, \quad (4.16)$$

where the eigenfunction satisfies $f \rightarrow 0$ as $x \rightarrow \pm\infty$. This equation was solved numerically [78] assuming a density profile

$$\rho = \rho_1 + \frac{\rho_2 - \rho_1}{2} \left[1 + \operatorname{erf} \left(\frac{\sqrt{\pi} y}{\delta_T} \right) \right]. \quad (4.17)$$

Thus, in the comparisons of the simulation amplitude data to the predictions of the models (Sec 4.5), the amplitude growth rates are adjusted to account for the diffuse interface by the rescaling

$$\frac{da}{dt} \longrightarrow \frac{1}{\psi} \frac{da}{dt}. \quad (4.18)$$

Table 4.4 includes the parameters used in the single-mode sinusoidal perturbation in two dimensions [Eq. (1.1)]. Also included are additional physical parameters, including the shock Mach number $Ma = 1.313$ (used for the mix initial conditions), and the temperature in the region ahead of the shock T_1 . The table also includes the simulation parameters. The location of the left boundary for L_x and L_y may appear arbitrary. The reason for this choice is that the code places the mesh point at the center of the cell. Therefore, the selection of the limits corresponds to the first grid

	Experimental initial conditions		Two-gas initial conditions	
Ma_i	1.292 ± 0.006		1.292	
$u_{shock,i}$ (cm/s)	38858		38858	
$[u]$ (cm/s)	9260 ± 200		9477.3	
v_0 (cm/s)	1338.76		1403.9	
Ma_r	1.077		1.077	
$u_{shock,r}$ (cm/s)	34516		32203	
Ma_t	1.422		1.422	
$u_{shock,t}$ (cm/s)	19625		19625	
$t_{reshock}$ (ms)	6.00		5.15	
η_{comp}	–		0.756	
	Pre-shock	Post-shock	Pre-shock	Post-shock
a_0 (cm)	0.29	0.215	0.29	0.219
δ_T (cm)	0.5	–	0.5	0.378
A	0.605	0.635	0.605	0.6344
ψ	1.17	1.131	1.182	1.131

	Mix initial conditions		Upstream initial conditions	
Ma_i	1.313		1.292	
$u_{shock,i}$ (cm/s)	37311		38858	
$[u]$ (cm/s)	9770		9110	
v_0 (cm/s)	1336.8		1299.1	
Ma_r	1.092		1.084	
$u_{shock,r}$ (cm/s)	32203		34741	
Ma_t	1.437		1.406	
$u_{shock,t}$ (cm/s)	20265		20986	
$t_{reshock}$ (ms)	5.00		4.98	
η_{comp}	0.738		0.766	
	Pre-shock	Post-shock	Pre-shock	Post-shock
a_0 (cm)	0.29	0.214	0.29	0.222
δ_T (cm)	0.5	0.369	0.5	0.383
A	0.605	0.604	0.605	0.603
ψ	1.182	1.133	1.182	1.38

Table 4.3. Comparison of the flow properties, including initial, reflected, and transmitted shock Mach numbers, Ma_i , Ma_r , and Ma_t , respectively, shock velocities $u_{shock,i}$, $u_{shock,r}$, and $u_{shock,t}$, respectively, interface velocity $[u]$, initial interface growth v_0 , and pre- and post-shock initial amplitudes a_0^- and a_0^+ , the pre- and post-shock diffuse-interface thickness δ_T^- and δ_T^+ , pre- and post-shock Atwood numbers A^+ , and A^- , and pre- and post-shock growth reduction factor ψ^+ and ψ^- , when the initial conditions of Jacobs and Krivets are adopted in one-dimensional refraction theory. The results in the experiments of Jacobs and Krivets (top, left) are compared with the results obtained using one-dimensional refraction theory when $\gamma_1 = 1.2776$ of air(acetone) and $\gamma_2 = 1.093$ of SF₆ are used, corresponding to the *two-gas initial conditions* (top, right); when a single value of the adiabatic exponent $\gamma_1 = \gamma_2 = 1.1405$ of a mixture of 50% air(acetone) and 50% SF₆ by volume is used, corresponding to the *mix initial conditions* (bottom, left), and; when a single value of the adiabatic exponent $\gamma_1 = \gamma_2 = 1.2776$ of the air(acetone) mixture is used, corresponding to the *upstream initial conditions* (bottom, right).

Initial interface perturbation		
a_0^- (cm)	0.29	
λ (cm)	5.9	
k (cm ⁻¹)	1.064947	

Physical parameters		
Ma	1.313 (mix) 1.292 (upstream)	
T_1 (K)	296	

Numerical parameters		
128/ λ	x	y
N	1683	129
L (cm)	[-3.0232, 75.0216]	[-0.0232, 5.9624]
h (cm)	0.0464	0.0464
256/ λ	x	y
N	3364	257
L (cm)	[-3.0116, 75.01]	[-0.0116, 5.9508]
h (cm)	0.0232	0.0232
512/ λ	x	y
N	6726	513
L (cm)	[-3.0058, 75.0042]	[-0.0058, 5.9334]
h (cm)	0.0116	0.0116
1024/ λ	x	y
N	13450	1025
L (cm)	[-3.0029, 75.0013]	[-0.0029, 5.9363]
h (cm)	0.0058	0.0058

Table 4.4. Initial interface perturbation properties, including the pre-shock amplitude a_0^- , wavelength λ , and wavenumber k ; additional initial physical parameters, including the shock Mach number Ma for the mix and upstream initial conditions, and the temperature T_1 ahead of the shock, and; numerical parameters, including the number of grid points N , grid separation h , and domain size for the longitudinal L_x , and transverse (periodic) direction L_y , used in the two-dimensional simulations. The numerical parameters are based on 128, 256, 512, and 1024 points per initial perturbation wavelength λ . For three-dimensional simulations in Chapter 5, the values for the periodic z direction are the same as the values for the periodic y dimension.

point at -3 cm for L_x and at 0 cm for L_y . The right side limit is obtained by multiplying the number of grid points N by the mesh separation h . This ensures that, as the mesh spacing is halved and the number of mesh points is increased, the grid points overlap.

4.2.3 Baroclinic circulation deposition on the interface and comparison to the predictions of models

The circulation deposited on the interface by the shock constitutes the principal driving mechanism for the evolution of the Richtmyer-Meshkov instability. The circulation on the sinusoidal interface

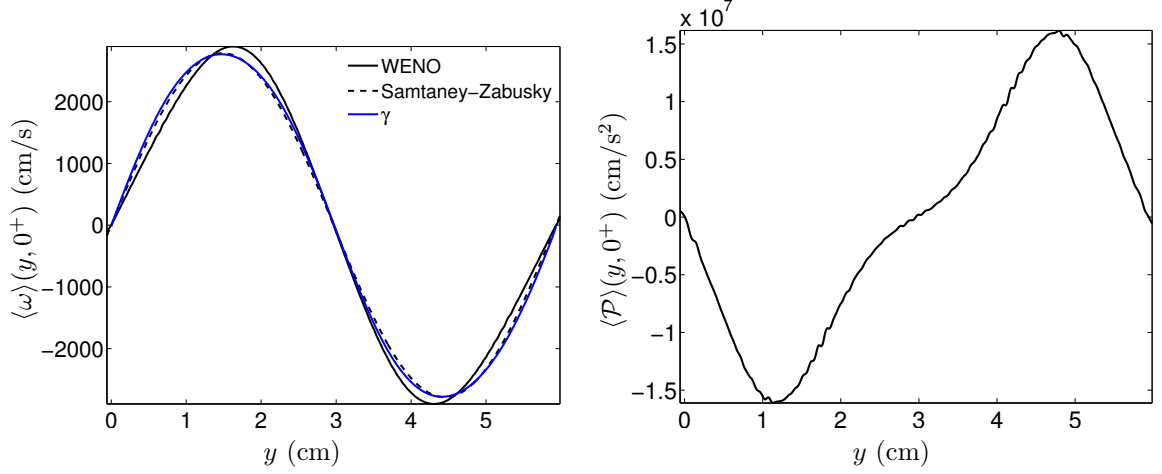


Figure 4.1. The initial deposition of circulation on the interface $\langle \omega \rangle(y, 0^+)$ from the incident shock at time $t = 0^+$ from the WENO simulation (solid black line), together with the predictions of the Samtaney-Zabusky model (dashed line) and linear instability theory (solid blue line) (left). The initial baroclinic vorticity production $\langle \mathcal{P} \rangle(y, 0^+)$ is also shown (right).

can be quantified by [127, 128]

$$\langle \omega \rangle(y, 0^+) \equiv \int_{-\infty}^{\infty} \omega(x, y, 0^+) dx, \quad (4.19)$$

which can be compared to the prediction of analytical models.

1. In the *Samtaney-Zabusky model* [128] the circulation is

$$\langle \omega \rangle(y, 0^+) = \Gamma'_1 a_0 k \sin(ky), \quad (4.20)$$

where

$$\Gamma'_1 = \frac{c_1}{Ma_s} \left[\frac{1}{\gamma_2 - 1} \frac{1 - \psi(p_4/p_2)}{\eta \gamma_1 / \gamma_2} - \frac{1 - \psi(p_5/p_3) \psi(p_3/p_1)}{\gamma_1 - 1} \right], \quad (4.21)$$

$p_1 = p_2$ is the initial pressure ahead of the incident shock, p_3 is the pressure behind the incident shock, $p_4 = p_5$ is the pressure behind the reflected and transmitted shocks, η is the initial density ratio, c_1 is the initial sound speed, and the ratio of sound speed across the incident, reflected and transmitted shocks is given by $\sqrt{\psi(p_3/p_1)}$, $\sqrt{\psi(p_5/p_3)}$ and $\sqrt{\psi(p_4/p_2)}$, respectively, where $\psi(r) \equiv r(1 + \mu r)/(\mu + r)$ and $\mu \equiv (\gamma + 1)/(\gamma - 1)$.

2. In the *linear instability model*, the vortex dipole and initial circulations are

$$\mu(e, 0^+) = 2v_0 \cos[kx(e, 0^+)] \cosh[ky(e, 0^+)], \quad \gamma(e, 0^+) = \frac{\partial \mu(e, 0^+)}{\partial e}, \quad (4.22)$$

where v_0 [Eq. (1.16)] is the initial instability growth rate.

The values of Γ'_1 , $\max[\gamma]$, and $\max[\langle\omega\rangle]$ are shown in Table 4.10 together with a comparison of values from the mix and upstream initial conditions. Figure 4.1 shows the initial circulation deposited by the shock $\langle\omega\rangle(y, 0^+)$ from the WENO simulation, together with the prediction of the Samtaney-Zabusky model [Eq. (4.20)] and the linear instability model [Eq. (4.22)]. The Samtaney-Zabusky model and the linear model give virtually identical predictions (0.6% difference). However, the models underpredict the simulation results by $\approx 4.3\%$. The difference between the numerical and model predictions can be attributed to the fact that the circulation is computed at 0.06 ms. As a result, the initial circulation deposited on the interface has evolved, increasing in value in the proximity of the bubble and spikes.

The average of the baroclinic vorticity production term on the interface $\langle\mathcal{P}\rangle$ is also shown in Figure 4.1. The coarse- and fine-grid simulations give virtually identical results (1.4% difference). The shape of the curve is a skewed sinusoid. This effect can also be attributed to the evolution of this term on the interface, following the passage of the shock. The term could not have been computed at an earlier time, while the shock was crossing the interface.

4.2.4 Initial conditions for the vorticity-streamfunction, Lagrangian, and vortex-in-cell methods

Simulations of the Richtmyer-Meshkov instability performed using the VS, the Lagrangian, and the vortex-in-cell (VIC) methods begin following the passage of the shock. The shocked interface is represented by a thin vortex sheet discretized by vortex markers in the Lagrangian and VIC methods, and by a vortex layer on a Cartesian grid in the VS method.

In the Lagrangian representation (Lagrangian- γ and VIC methods), the shocked interface is represented by a sinusoidal vortex sheet discretized using N equally-spaced vortex markers located at $[x_n, \eta(x_n)]$ [$\eta(x)$ is given by Eq. (1.1)]. In the present simulations $N = 256$ markers are used. For the VIC method, an auxiliary Cartesian grid is introduced. This grid is specified over the rectangle $[0, L_x] \times [-L_{\text{bot}}, L_{\text{top}}]$ and has uniform grid spacing $h = \Delta x = \Delta y$ with $N_x \times N_y$ grid points. In the present simulations, a rectangular grid of dimension $[0, 5.94] \times [-11.88, 11.88]$ is specified with $N_x \times N_y = 32 \times 128$.

The vorticity deposited by the shock on the interface constitutes the initial condition for the Lagrangian representation. In Section 4.2.3 it was shown that the deposition of circulation on the interface by the shock can be adequately characterized by the Samtaney-Zabusky circulation deposition model [Eq. (4.20)] or by linear instability theory [Eq. (4.22)]. Adopted in the present study is the linear instability theory, because it has a direct physical interpretation [v_0 corresponds to the instability growth rate of Eq. (1.16)]. The initial values and parameters used for the Lagrangian and the VIC simulations are summarized in Table 4.5.

Initial perturbation and vortex sheet properties		
	Atwood number study	Jacobs and Krivets
A	–	0.604
a_0 (cm)	0.594	0.214
λ (cm)	5.94	5.94
k (cm ⁻¹)	1.064947	1.064947
v_0 (cm/ms)	1.5	1.33876

Lagrangian methods	
N	256
δ	0.15
Δt (ms)	0.001

VIC method		
N	256	
Δt (ms)	0.005	
	x	y
N	32	256
L (cm)	[0, 5.94]	[-23.76, 23.76]
h (cm)	0.185625	0.185625

VS method		
N	1024	
CFL	0.3	
δ_T (cm)	0.2	
ν (cm ² /ms)	10^{-4}	
\mathcal{D} (cm ² /ms)	10^{-4}	
	x	y
N	256	1024
L (cm)	[0, 5.94]	[-11.88, 11.88]
h (cm)	2.3203125×10^{-2}	2.3203125×10^{-2}

Table 4.5. Initial perturbation and vortex sheet properties for the VS and vortex simulations, including the initial sheet amplitude a_0 , the wavelength λ , the wavenumber k , and the initial growth rate v_0 for the Atwood number study and for the comparison with the experiment of Jacobs and Krivets with $A = 0.604$. Also shown are the properties of the Lagrangian method, including the number of markers N , the regularization parameter δ , and the time step Δt , the properties of the VIC method, including the dimension of the Cartesian grid, and the number of grid points, and grid spacing $h = \Delta x = \Delta y$, and; the properties of the VS method, including the CFL number, thickness of the layer δ_T , and the viscosity and mass diffusivity ν and \mathcal{D} , respectively.

	$N_x = 128$	$N_x = 256$	$N_x = 384$	$N_x = 512$	$N_x = 768$
Ninth-order	WENO9-128 (dashed light blue)	WENO9-256 (solid light blue)	WENO9-384 (dash-dot blue)	WENO9-512 (dashed blue)	WENO9-768 (solid blue)
Fifth-order	WENO5-128 (dashed light red)	WENO5-256 (solid light red)	WENO5-384 (dash-dot red)	WENO5-512 (dashed red)	WENO5-768 (solid red)

Table 4.6. Keys used to denote simulations with different order of WENO flux reconstruction and grid resolution. The number after the dash is the number of grid points per initial perturbation wavelength λ .

$\max[\langle\omega\rangle(y, 0^+)] \frac{\text{cm}}{\text{s}}$	$N_x = 128$	$N_x = 256$	$N_x = 384$	$N_x = 512$	$N_x = 768$
ninth-order	2925.567	2918.665	2924.82	2909.141	2928.68
fifth-order	2954.307	2887.19	2887.12	2874.68	2872.3

$\max[\langle\mathcal{P}\rangle(y, 0^+)] \frac{\text{cm}}{\text{s}^2}$	$N_x = 128$	$N_x = 256$	$N_x = 384$	$N_x = 512$	$N_x = 768$
ninth-order	1.6875×10^7	1.6542×10^7	1.6415×10^7	1.6313×10^7	1.6512×10^7
fifth-order	1.5814×10^7	1.6087×10^7	1.6301×10^7	1.6416×10^7	1.6594×10^7

Table 4.7. Comparison of the initial circulation deposition $\max[\langle\omega\rangle(y, 0^+)]$ and baroclinic production $\max[\langle\mathcal{P}\rangle(y, 0^+)]$ from the fifth- and ninth-order simulations for different grid resolutions.

For the VS method, the initial vorticity on the Cartesian grid is specified using the Gaussian interpolant [Eq. (3.1)] and the initial density using a hyperbolic tangent [Eq. (3.2)]. A summary of the numerical parameters used for the vortex methods is presented in Table 4.5.

4.3 Comparison of fifth- and ninth-order WENO simulations for different grid resolutions

Presented here is a comparison of the effects of order of WENO reconstruction and grid resolution on the instability evolution, including the density, vorticity, and baroclinic vorticity production fields (Sec. 4.3.1) and on the perturbation, bubble, and spike amplitudes (Sec. 4.3.2).

4.3.1 Comparison of the instability evolution and fields

Simulations are performed for grid resolutions corresponding to $N_x = 128, 256, 384, 512,$ and 768 points per initial perturbation wavelength using the mix initial conditions (Sec. 4.2.2) and fifth- and ninth-order WENO reconstruction. The keys used to denote the simulations performed here is presented in Table 4.6.

Figure 4.2 shows a comparison of the initial circulation deposition $\langle\omega\rangle(y, 0^+)$ [Eq. (4.19)] for the fifth- and ninth-order simulations at different grid resolutions. All of the simulations have the same deposition of vorticity on the interface. This is further seen by comparing $\max[\langle\omega\rangle(y, 0^+)]$

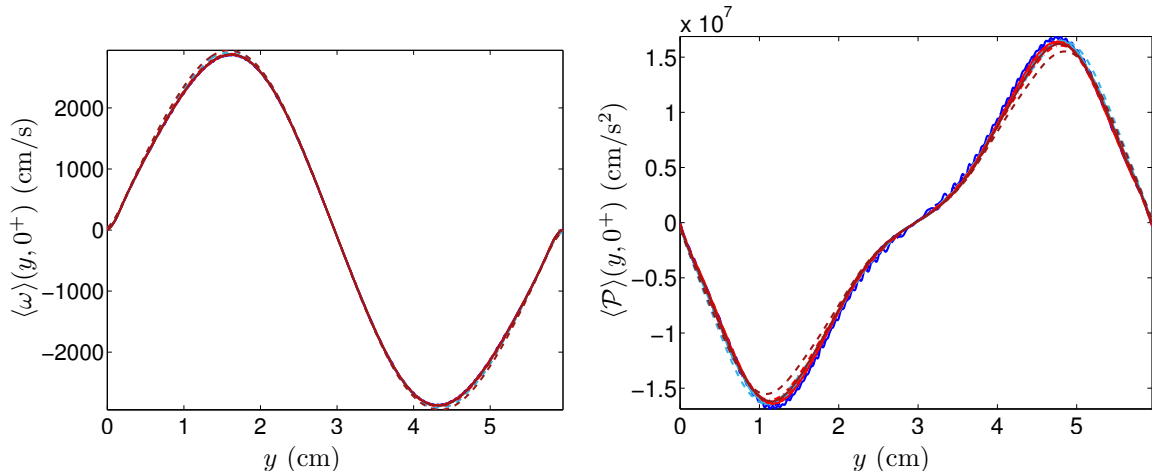


Figure 4.2. Comparison of the initial circulation deposition $\langle \omega \rangle(y, 0^+)$ and baroclinic production $\langle \mathcal{P} \rangle(y, 0^+)$ from the fifth- and ninth-order WENO simulations at different grid resolutions. See Table 4.6 for the legend.

in Table 4.7. Also shown in the figure is a comparison of the baroclinic vorticity production field $\langle \mathcal{P} \rangle(y, 0^+)$, demonstrating very good agreement between the simulations with different orders and grid resolutions. A comparison of $\max[\langle \mathcal{P} \rangle(y, 0^+)]$ in Table 4.7 also quantitatively confirms this finding.

Figure 4.3 shows a comparison of the density field and mass fraction contour at 5.26 ms for the different simulations. As the resolution is increased, additional fine-scale structure becomes evident in the roll-ups. In particular, such fragmentation has impacted and deformed the stem of the perturbation in the WENO9-512 and WENO9-768 simulations. The mass fraction contours also reveal that starting from the WENO5-384 and WENO9-256 simulations, symmetry is broken with the spike and bubble sides yielding different results. The additional structure in the cores of the roll-ups can be explained by the fact that different resolutions and different orders of reconstruction correspond to different values of the implicit numerical viscosity [77]. In particular, as the order and resolution increase, the implicit numerical dissipation decreases.

Figure 4.4 shows a comparison of the vorticity $\omega(x, y)$ and baroclinic vorticity production $\mathcal{P}(x, y)$ fields. As the resolution and orders are increased, the vorticity cores become smaller, more compact, and surrounded by more fine-scale, disordered structure. The baroclinic vorticity production field is active in the roll-ups. In addition, the ninth-order results show more disordered structure than the fifth-order results. Despite the differences in the fields, a comparison of the mass fraction contours in Figure 4.5 shows agreement in the bubble amplitudes and in the width of the stem and large-scale spike roll-up dynamics.

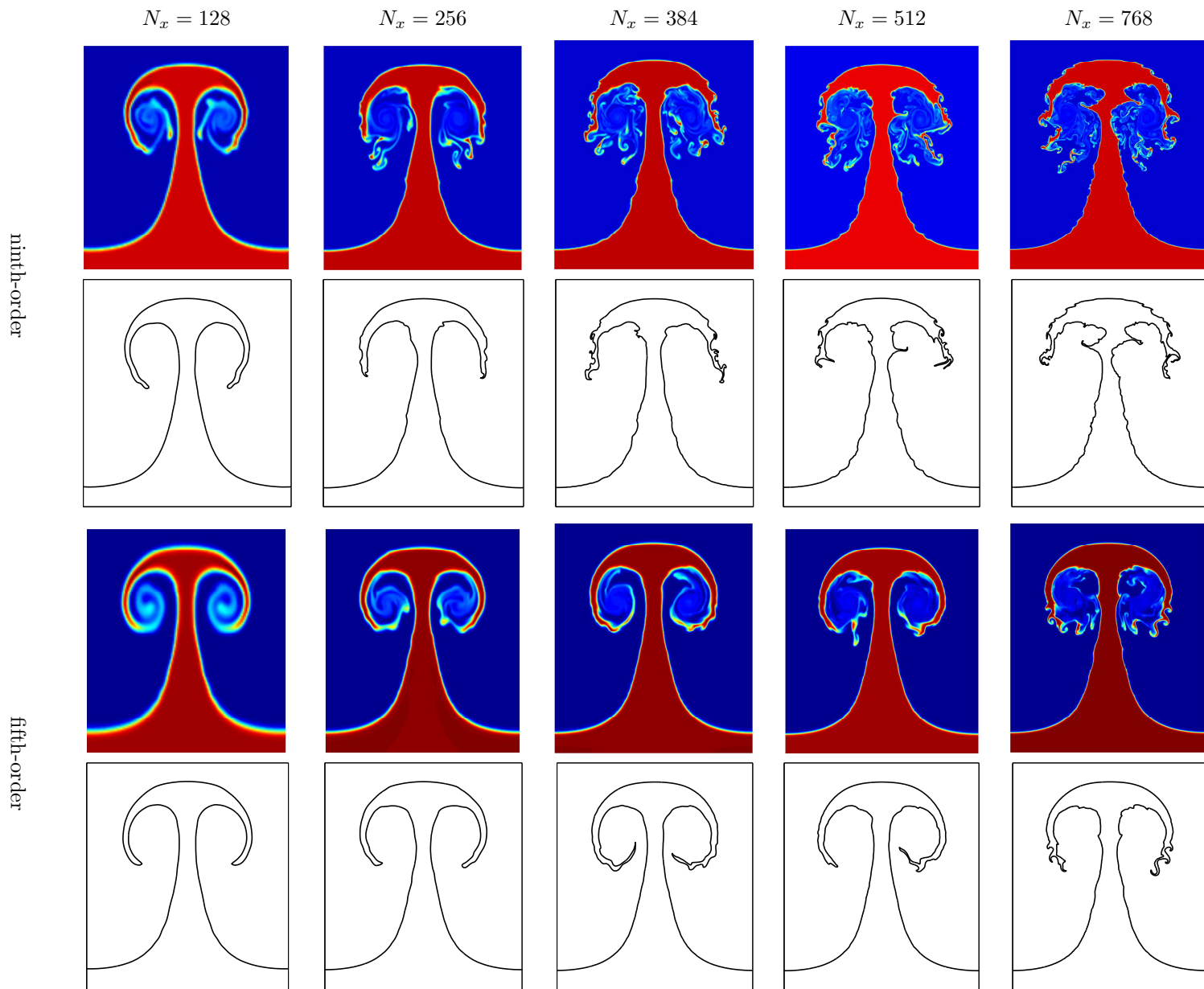


Figure 4.3. Comparison of the density fields and mass fraction contours at 5.26 ms from the fifth- and ninth-order WENO simulations using different grid resolutions.

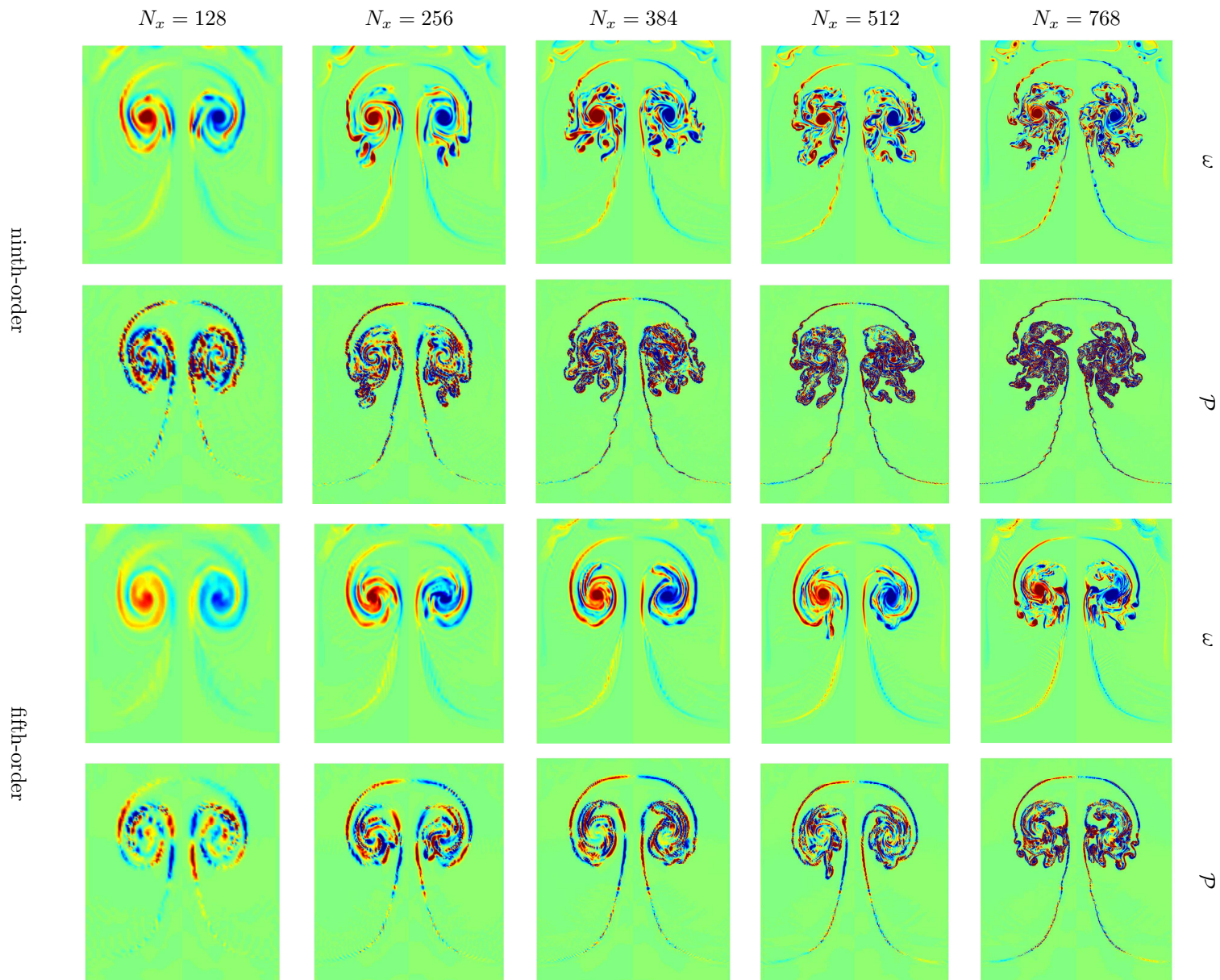


Figure 4.4. Comparison of the vorticity $\omega(x, y)$ and baroclinic vorticity production $\mathcal{P}(x, y)$ fields at 5.26 ms from the fifth- and ninth-order WENO simulations using different grid resolutions.

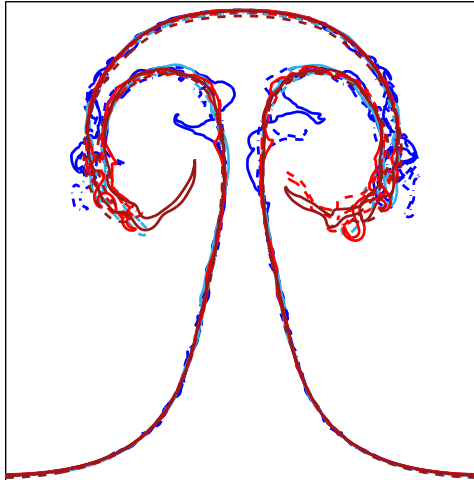


Figure 4.5. Comparison of the mass fraction contours as the order and resolution are varied. See Table 4.6 for the legend.

4.3.2 Comparison of the perturbation, bubble, and spike amplitudes, circulation, and Reynolds number

Presented here is a comparison of the perturbation, bubble, and spike amplitudes, circulation and Reynolds number for different orders and grid resolutions.

The perturbation amplitude is computed from the mole fraction X as follows. From the mass-fraction m_2 of the SF_6 gas [evolved in the Euler equations (4.1)], determine the *mole fraction*

$$X = \frac{m_2 M_1}{(1 - m_2) M_2 + m_2 M_1}, \quad (4.23)$$

where M_r are the molecular weights of fluid r (Table 4.4). Spatially averaging the mole fraction in the periodic y -direction [or the periodic (y, z) -plane in three dimensions] gives

$$\bar{X}(x, t) = \frac{1}{L_y} \int_0^{L_y} X(x, y, t) dy, \quad (4.24)$$

where L_y is the width of the domain in the spanwise direction. The spike and bubble locations, $\ell_s(t)$ and $\ell_b(t)$, are defined as the x position where $\bar{X} \geq \epsilon$ and $\bar{X} \leq 1 - \epsilon$, respectively, with $\epsilon = 0.01$. Therefore, the *perturbation width* and *amplitude* are

$$h(t) = \ell_b(t) - \ell_s(t), \quad a(t) = \frac{h(t)}{2}. \quad (4.25)$$

To determine the bubble and spike amplitudes, a numerical simulation without an initial perturbation (but otherwise identical) was performed to obtain the position of the interface ℓ_{int} , so that

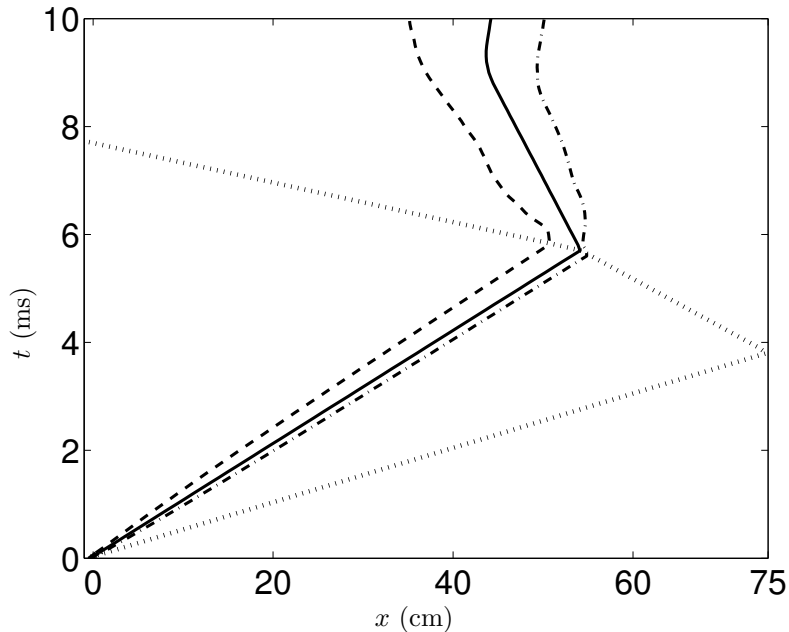


Figure 4.6. The x - t diagram showing the position of the interface $\ell_{\text{int}}(t)$ (solid line), shock (dotted line), and bubble and spike locations $\ell_b(t)$ and $\ell_s(t)$ (dash-dot and dashed lines, respectively). The horizontal distance between the spike and the bubble location is the perturbation width $h(t)$.

$$a_b(t) = \ell_b(t) - \ell_{\text{int}}(t), \quad a_s(t) = \ell_{\text{int}}(t) - \ell_s(t). \quad (4.26)$$

Figure 4.6 shows the x - t diagram from the WENO9-256 simulation. The locations of the bubble $\ell_b(t)$ and of the spike $\ell_s(t)$ are shown using the dash-dot and the dashed lines, respectively. The interface location is also shown using a solid line. The horizontal distance between the spike and bubble is the perturbation width $h(t)$, and half of this distance is the perturbation amplitude $a(t)$. Reshock occurs at ≈ 5.65 ms, when the shock wave refracts at the evolving interface, generating a transmitted shock in the air(acetone) and a reflected rarefaction wave returning back into the SF_6 . The transmitted shock following reshock moves faster than the incident shock, as indicated by the change in the slope, corresponding to a slow-fast refraction [55]. Following reshock, the interface is compressed (as indicated by the kink in the bubble and spike locations) and moves away from the end wall of the test section. The reflected rarefaction wave returning back into the SF_6 is not shown in the x - t diagram. However, this rarefaction reflects from the end wall of the test section and interacts with the interface at ≈ 8.5 ms, causing an expansion of the interface (as shown from the position of the bubble and spikes) and causing the interface to move towards the end wall. The interaction with the reflected rarefaction causes a compression wave to return back into the SF_6 , and a series of wave interactions follows until the interface eventually comes to rest in the shock tube test section.

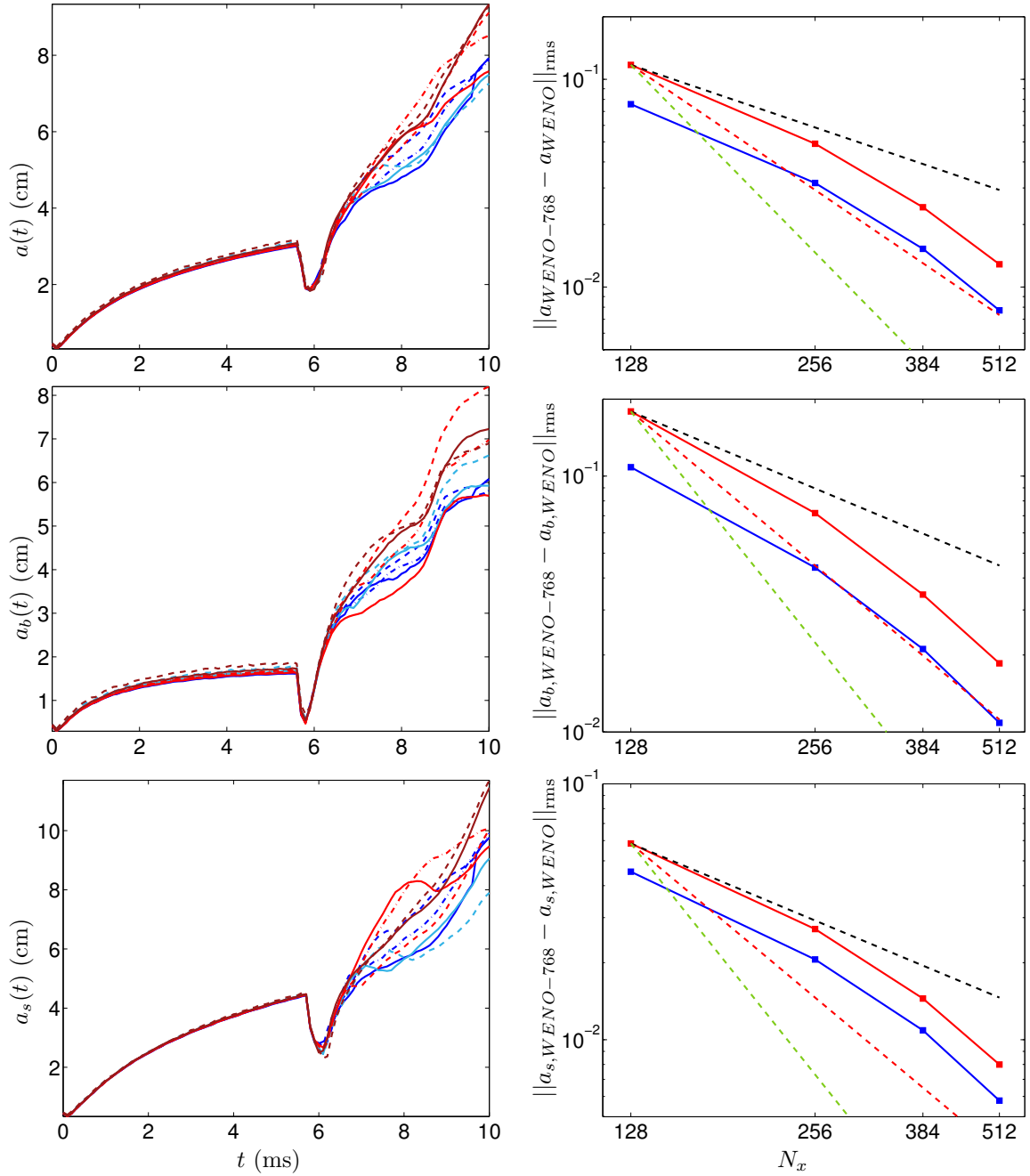


Figure 4.7. Comparison of the time-evolution of the perturbation, bubble, and spike amplitudes $a(t)$, $a_b(t)$, and $a_s(t)$, respectively, as the grid is refined and the order of flux reconstruction is varied (left). Also shown is the rms-norm of the difference between results obtained on the $N_x = 768$ grid and results obtained on coarser grids for the WENO5 (red) and WENO9 (blue) simulations. The dashed black line indicates N_x^{-1} , the dashed red line N_x^{-2} , and the dashed green line N_x^{-3} . See Table 4.6 for the legend.

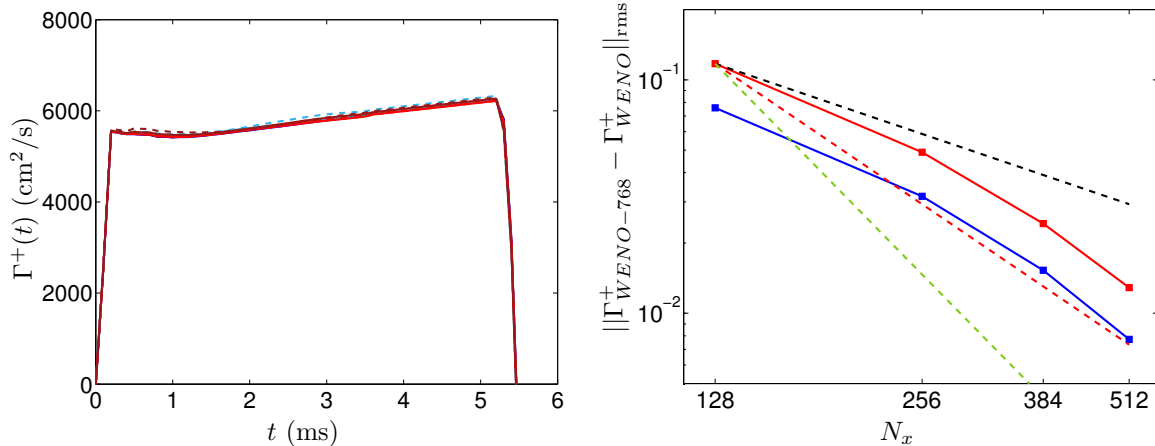


Figure 4.8. Comparison of the time-evolution of the positive circulation $\Gamma^+(t)$ before reshock as the grid is refined and the order of reconstruction is varied (left). Also shown is the rms-norm of the difference between results obtained on the $N_x = 768$ grid and those on coarser grids for the WENO5 (red) and WENO9 (blue) simulations. See Table 4.6 for the legend.

Figure 4.7 shows a comparison of the perturbation, bubble, and spike amplitudes, $a(t)$, $a_b(t)$, and $a_s(t)$, respectively, from the fifth- and ninth-order simulations at different grid resolutions. All of the simulations are in agreement prior to reshock and for short times following reshock. Following reshock, no clear agreement is observed. Also shown is the norm of the difference between results obtained on the $N_x = 768$ grid and those on the coarser grids, indicating second-order convergence in the amplitudes, despite the differences in the fields (Figs. 4.3 and 4.4).

Figure 4.8 shows a comparison of the circulation for the fifth- and ninth-order WENO simulations at different grid resolutions. The results indicate good agreement between the simulations. Also shown is the norm of the difference between the circulation on the $N_x = 768$ grid and those on the coarser grids. The results indicate second-order convergence similar to the amplitudes (Fig. 4.7). The average fractional deviation Δ [Eq. (4.40)] between results obtained from the WENO9-768 simulation and the other simulations is shown in Table 4.8.

Finally, shown in Figure 4.9 is the Reynolds number $Re_{\Delta x}(t)$ [Eq. (3.8)] for the simulations. As the value depends on Δx , simulations at the same grid resolutions give similar values of $Re_{\Delta x}(t)$. As the value also depends on $h(t)$, $Re_{\Delta x}(t)$ increases following the passage of the shock, decreases at reshock and then rapidly increases at late times.

4.4 Dynamics of the instability evolution

Simulations of the Jacobs and Krivets [62] $Ma = 1.3$ air(acetone)/ SF_6 shock tube experiment (Sec. 4.2.1) are performed using the fifth- and ninth-order WENO method and the VS method. First the density fields from the WENO and VS simulations are compared to the experimental PLIF

$\Delta a(t)$ (%)	$N_x = 128$	$N_x = 256$	$N_x = 384$	$N_x = 512$	$N_x = 768$
ninth-order	4.134	1.48	0.7324	0.357	0
fifth-order	7.01	2.96	1.611	0.997	0.419

$\Delta a_b(t)$ (%)	$N_x = 128$	$N_x = 256$	$N_x = 384$	$N_x = 512$	$N_x = 768$
ninth-order	8.47	3.129	1.43	0.75	0
fifth-order	15.17	6.25	3.413	2.131	0.876

$\Delta a_s(t)$ (%)	$N_x = 128$	$N_x = 256$	$N_x = 384$	$N_x = 512$	$N_x = 768$
ninth-order	1.944	0.667	0.405	0.176	0
fifth-order	2.871	1.35	0.728	0.461	0.205

$\Delta \Gamma^+(t)$ (%)	$N_x = 128$	$N_x = 256$	$N_x = 384$	$N_x = 512$	$N_x = 768$
ninth-order	2.25	1.411	0.695	0.424	0
fifth-order	1.49	0.787	0.436	0.287	0.24

Table 4.8. Average fractional deviation Δ from the WENO9-768 results as the order and grid resolution are varied for the perturbation amplitude $a(t)$, bubble and spike amplitudes $a_b(t)$ and $a_s(t)$, respectively, and the positive circulation $\Gamma^+(t)$.

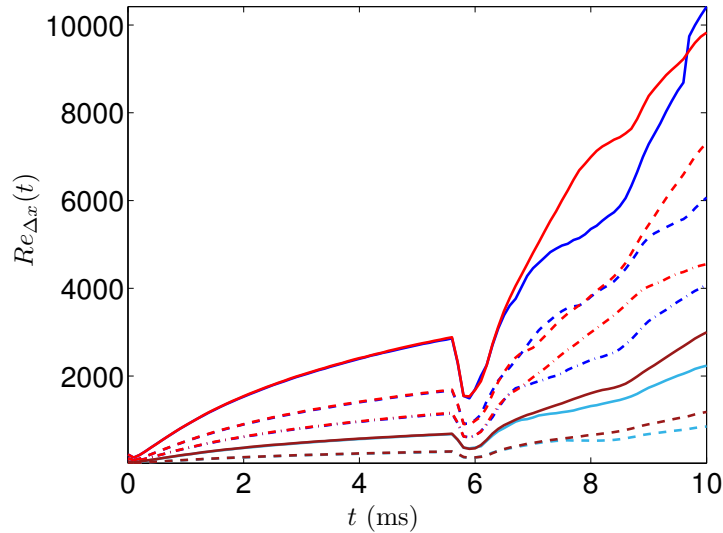


Figure 4.9. Comparison of the numerical Reynolds numbers $Re_{\Delta x}(t)$ for the fifth- and ninth-order simulations at different resolutions. See Table 4.6 for the legend.

images (Sec. 4.4.1). In addition, the mass fraction contour from these simulations is compared. The vorticity and baroclinic vorticity production fields from the WENO5, WENO9, and VS methods are also compared (Sec. 4.4.2). The vorticity can be interpolated onto the mass fraction contour to give the vortex sheet strength on the interface.

4.4.1 Comparison of density fields to experimental PLIF images

Figure 4.10 shows a comparison of the density fields from the fifth- and ninth-order WENO and VS simulations with the PLIF images from the experiments of Jacobs and Krivets. The VS simulation does not capture reshock or small-scale features, but captures the main large-scale features of the instability evolution. At 3.06 ms, the VS method captures the beginning of the roll-up, but the roll-up from the experiment appears more developed, while the roll-up of the WENO simulation shows additional small-scale structure. This is also observed at 5.26 ms, where the VS simulation captures the roll-up, but not the small-scale structure. Overall, the VS method captures the larger spike stem of the instability evolution and the wider roll-up region.

Figure 4.11 continues the comparison showing the mass fraction contours from the fifth- and ninth-order WENO and VS simulations. At 1.16 ms, all methods give a similar characterization of the bubble and spike initial growth. At 3.06 ms, differences are already visible in the structure of the roll-up. The WENO method supports a well-developed roll-up, the VS method shows the beginnings of a roll-up, and the Lagrangian method shows an earlier stage of the roll-up. At 5.26 ms, the differences are more pronounced. The WENO method shows a fully-developed roll-up with fragmentation, which is not captured by the contour but was visible in the density [Fig. 4.10]. The VS method shows a fully-developed roll-up and captures the internal fragmented structure of the WENO method with a large lump structure.

4.4.2 Visualization of the vorticity and baroclinic vorticity production fields

Figure 4.12 shows a comparison of the vorticity field $\omega(x, y)$ and baroclinic vorticity production field $\mathcal{P}(x, y)$ from the fifth- and ninth-order WENO and VS simulations. At 0.06 ms, all methods give a similar representation of the vorticity field, with one layer of positive and negative vorticity deposited by the shock. The vorticity from the VS and WENO methods have similar widths, further indicating that the VS approach of thickening the vortex sheet best models the diffuse interface of the Jacobs and Krivets experiments and the diffuse interface of the WENO simulations. The initial baroclinic vorticity production is different across the VS and WENO methods, but shows similar trends with the reduction of vorticity near the bubble tip and the increase of vorticity near the spike tip. At 1.16 ms, the vorticity across the methods appears similar, with a stronger

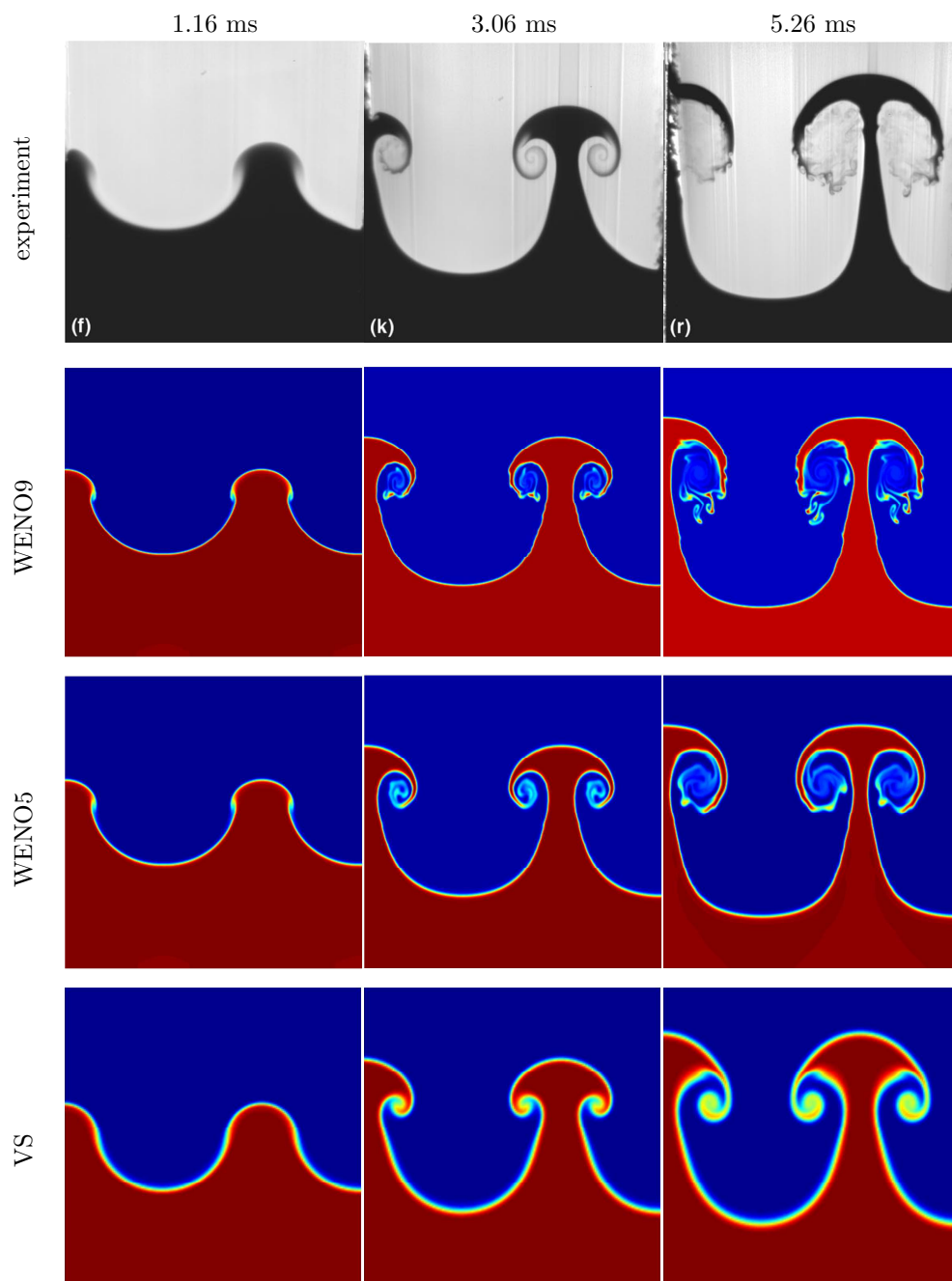


Figure 4.10. Comparison of the corrected PLIF images from the Jacobs and Krivets experiment with the density fields $\rho(x, y)$ from the ninth- and fifth-order WENO simulations at a resolution of 512 points per wavelength and the density field $\rho(x, y)$ from the VS simulation at 1.16, 3.06, and 5.26 ms. The experimental images are taken from Figure 5 of Jacobs and Krivets [62] (reprinted with permission of the American Institute of Physics).

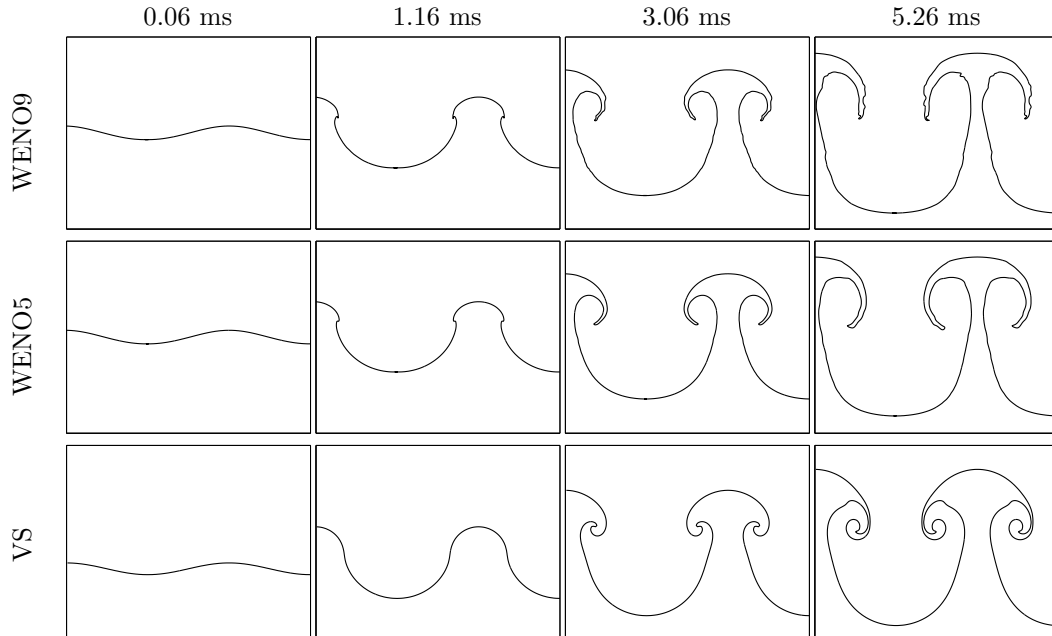


Figure 4.11. Comparison of the mass fraction contour from the ninth- and fifth-order WENO simulations and the VS simulation at 0.06, 1.16, 3.06, and 5.26 ms.

concentration of vorticity corresponding to the roll-up region. The baroclinic vorticity production is also similar across the WENO and VS methods as more generation occurs near the spike tip. At 3.06 ms, there are differences between the WENO and VS vorticities. The WENO simulation shows fragmentation surrounding the main rotating core, produced by the secondary vortex accelerated vorticity deposition (VAVD), which is related to baroclinic vorticity production. This is not captured in the VS simulations due to the coarser grid used and the regularizing effects of viscosity. The baroclinic vorticity production also exhibits differences. In the WENO simulation, most of the production is centered near the cores and along the interface. In the VS simulations, most of the production is centered near the core and spike roll-up regions. The differences may be due to compressibility effects in the WENO method. Similar observations apply to the vorticity and baroclinic vorticity production at late times (5.26 ms).

Figure 4.13 shows a comparison of the vortex sheet strength $\gamma(e, t)$ on the mass fraction contour for the WENO and VS simulations. The initial circulation deposition at 0.06 ms is captured very well by all of the methods. At 1.16 ms, the vortex sheet strength of the WENO simulation is steeper than that of the VS simulation, due to the earlier formation of the roll-up in the WENO method. At 3.06 ms, the WENO simulation shows oscillatory regions, due to oscillations in the mass fraction contour (Fig. 4.11). However, the overall structure is very similar across all methods. At 5.26 ms, the oscillations in the WENO method are more pronounced; however, the structure is in agreement across the methods. Overall, there is good agreement in the vortex sheet strength.

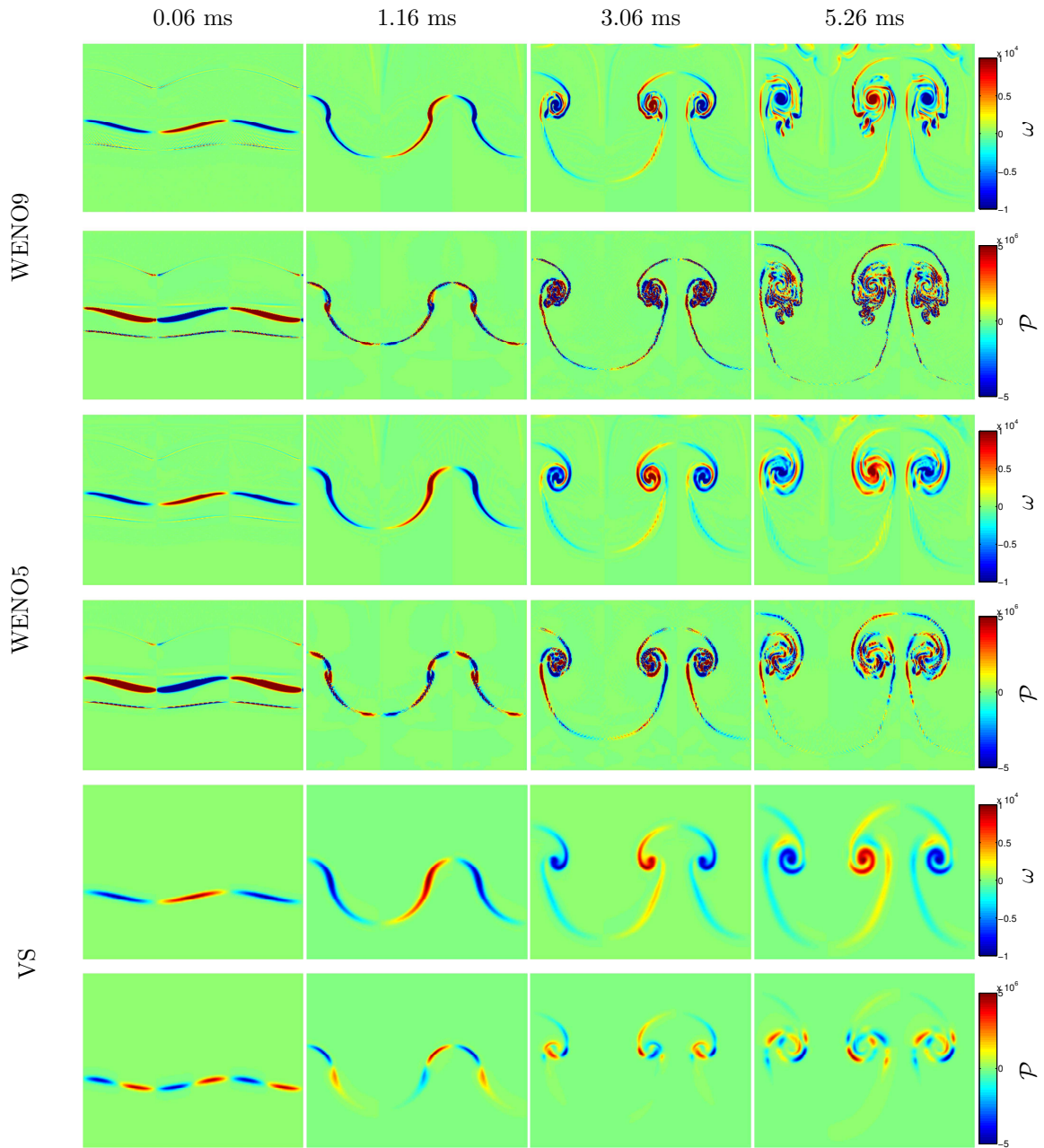


Figure 4.12. Comparison of the vorticity fields $\omega(x, y)$ and the baroclinic vorticity production fields $\mathcal{P}(x, y)$ from the ninth- and fifth-order WENO simulation and the VS simulation at 0.06, 1.16, 3.06, and 5.26 ms.

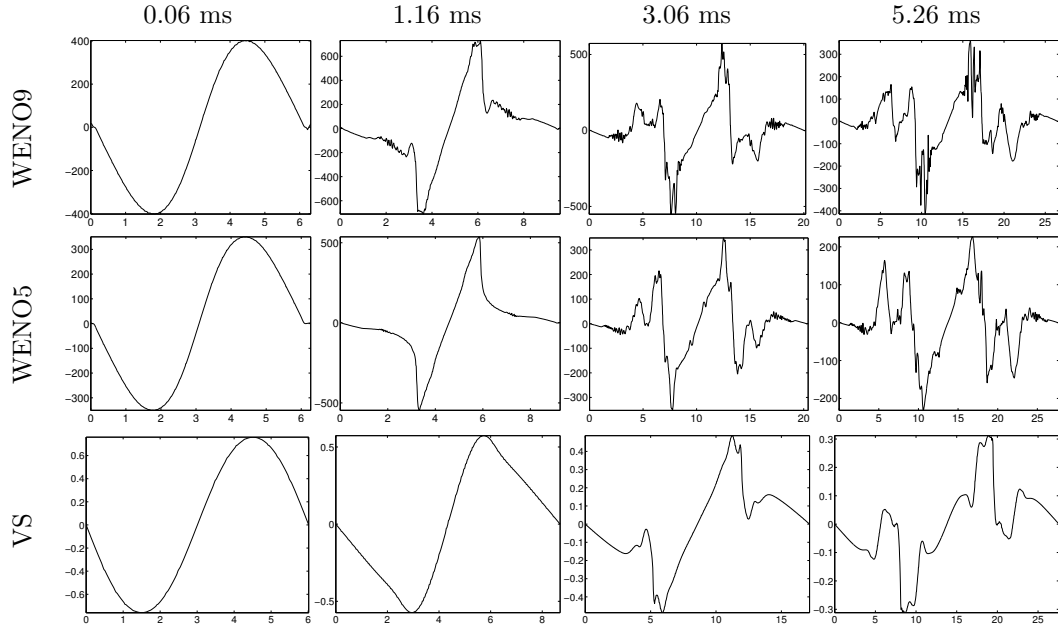


Figure 4.13. Comparison of the vortex sheet strength $\gamma(e, t)$ on the mass fraction contour from the fifth- and ninth-order WENO and VS simulations at 0.06, 1.16, 3.06, and 5.26 ms.

Figure 4.14 shows a comparison of the interface position $z(e)$, vortex-sheet strength $\gamma(e)$, and horizontal and vertical components of the velocity, $u(e)$ and $v(e)$, respectively, from the WENO and VS simulations. The interface position at 0.06 ms shows very good agreement following reshock, confirming that the growth reduction formula [Eq. (4.15)] is appropriate for determining the post-shock amplitude. The VS and WENO methods show agreement in the vortex-sheet strength. In the VS method, the value is due to the Gaussian thickening [Eq. (2.26)] to assign the vorticity on the grid. As the Gaussian is a smoothing interpolant, it is expected that the vortex sheet strength is reduced. For the WENO method, the initial diffuse thickness of the interface also corresponds to reduced values of the vortex sheet strength on the mass fraction contour. The horizontal velocity from the WENO method is larger at 0.06 ms than that from the VS method, due to the difficulty of computing the horizontal velocity in the small layer immediately behind the shock. The vertical velocity $v(e)$ is in close agreement. The vertical velocity of the WENO method may be smaller due to the difficulty of computing its value at such early times. At 1.16 ms, the interface evolution is very similar across all methods. The WENO method shows the formation of roll-ups, which are also apparent in the vortex sheet strength $\gamma(e)$. The VS and WENO methods have comparable values for the vortex sheet strength. The horizontal and vertical velocity are also in qualitative and quantitative agreement. The WENO method shows additional oscillations due to the formation of the roll-ups. Such oscillations are also present in the VS method as the roll-up develops. At 3.06 ms, the methods show similar large-scale bubble and spike dynamics, but different roll-up dynamics.

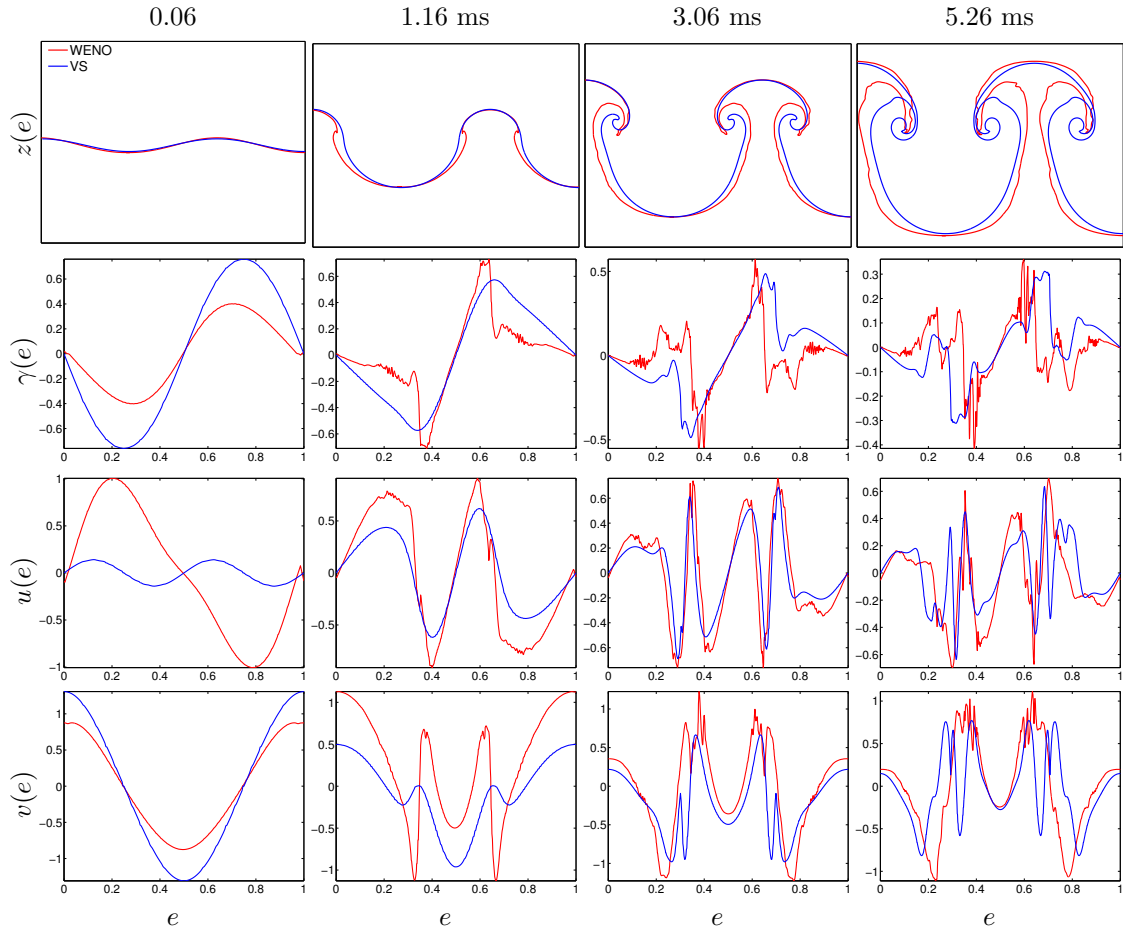


Figure 4.14. Comparison of the interface position $z(e)$, vortex-sheet strength $\gamma(e)$, and horizontal and vertical components of the velocity, $u(e)$ and $v(e)$, respectively, from the ninth-order WENO (red) and VS (blue) simulations at 0.06, 1.16, 3.06, and 5.26 ms.

This is expected as the roll-ups differ across the methods. The circulation also shows that the WENO and VS methods are in agreement. The horizontal and vertical components of the velocity are similar across all methods, with slightly reduced values in the vertical component of the Lagrangian method due to the different stages of the roll-up. At 5.26 ms, the large-scale bubble and spike amplitudes and velocities are similar. The WENO method shows a flatter bubble and spike tip. The structure of the roll-up indicates that the WENO method has a thinner stem than the vortex methods, all of which have very similar stem widths.

These results show that the interface dynamics and vortex sheet strength of the WENO and VS methods are in qualitative and quantitative agreement, as both methods have diffuse interfaces on a Cartesian grid. The large-scale bubble and spike amplitudes and velocities are quantitatively and qualitatively similar across the methods.

4.5 Comparison of the perturbation, bubble, and spike amplitudes with experimental data and to the predictions of amplitude growth models

Presented here is a comparison of the perturbation, bubble, and spike amplitudes from the WENO and VS simulations together with the experimental data points of Jacobs and Krivets and the predictions of amplitude growth models. A brief review of the models (Sec. 4.5.1) is followed by a comparison of the amplitudes with the experimental data of Jacobs and Krivets and with the predictions of these models (Sec. 4.5.2). The circulation and Reynolds numbers from the simulations are also compared. Finally, a comparison of the mix and upstream initial conditions for the WENO simulations is presented (Sec. 4.5.3).

4.5.1 Literature survey on Richtmyer-Meshkov instability growth models

Since the work of Richtmyer [121], many models have been proposed to predict the perturbation amplitude. In earlier work [78, 76], the models were grouped according to their fundamental physical assumptions: (1) *impulsive models* based on representing the shock as an instantaneous δ -function acceleration (Sec. 4.5.1.1); (2) *perturbation models*, based on the asymptotic expansion of the linear perturbation equations; (3) *empirical models* based on using data from experiments (or simulations) to determine model parameters (Sec. 4.5.1.2), and; (4) *potential flow models* based on representing the flow above and below the vortex sheet as incompressible and irrotational (Sec. 4.5.1.3).

4.5.1.1 Impulsive and linear models

The first linear model predicting the growth of an impulsively accelerated single-mode perturbation is due to Richtmyer [121]. Richtmyer modified earlier work by Taylor [139] on the growth of a single-mode perturbation when a dense fluid is continuously accelerated into a lighter fluid (the Rayleigh-Taylor instability), by replacing the constant gravitational acceleration g with an impulsive acceleration $[u] \delta(t)$, where $[u]$ is the change in velocity at the interface, following shock refraction.

Meyer and Blewett [97] performed two-dimensional Lagrangian simulations of the single-mode Richtmyer-Meshkov instability and computed growth rates corresponding to a shock propagating from a light to a heavy and from a heavy to a light gas. They found that improved agreement between simulation results and model predictions was obtained by averaging the pre- and post-shock amplitudes in the Richtmyer model. In general, the prediction of Meyer and Blewett is best for a reflected rarefaction wave.

Fraley [39] analytically solved the linearized perturbation equations for a reflected shock wave. The complete set of linearized, compressible perturbation equations was first considered by Richt-

myer [121], who solved them numerically. Fraley reconsidered the perturbation equations for a single-mode initial perturbation and solved the equations using Laplace transform techniques in time. Mikaelian [104] later recognized this solution as the most accurate for the linear growth.

Vandenboomgaerde, Mügler, and Gauthier [146] replaced the impulsive acceleration, post-shock Atwood number, and post-shock amplitude with linearly time-varying values from pre- to post-shock quantities. This is a good approximation for both a reflected shock wave and a reflected rarefaction wave, provided the incident shock is not too strong.

The impulsive model has also been extended to the case of diffuse initial interfaces. Duff, Harlow, and Hirt [34] heuristically proposed that the growth rate for a diffused initial interface subject to the Rayleigh-Taylor instability is reduced by a constant *growth reduction* factor. Mikaelian [102] extended this to the Richtmyer-Meshkov instability, obtaining results by considering both the initial density profile of Duff, Harlow, and Hirt, and a density profile used by Saffman and Meiron [125]. The resulting equations were later solved using an N -layer matrix method [98, 99] and a moment method [100]. Brouillette and Sturtevant [19] used the procedure of Mikaelian [102] to compute the growth reduction factor for a slightly different density profile. The growth reduction factor was used to obtain better agreement between the model predictions and the experimental results of Collins and Jacobs [27].

A different type of linear model was proposed by Wouchuk and Nishihara [150] for both a reflected rarefaction and a reflected shock wave. In this model, the impulsive growth due to the localized deposition of vorticity at shock refraction is corrected by the interaction with pressure perturbations from the transmitted shock and the reflected shock fronts. Typically, these pressure perturbations slow down the growth rate, causing in some cases full cancellation or “freeze-out” [104]. This new definition of linear growth encompasses a wider class of instabilities than the impulsive models and is used by Velikovich et al. [147] to define a class of *Richtmyer-Meshkov-like* instabilities.

4.5.1.2 Perturbation and empirical models

Zhang and Sohn [156] developed a model for the growth rate of a two-dimensional Richtmyer-Meshkov unstable interface, valid for compressible fluids from early to late times for a reflected shock (light-to-heavy transition). The dynamics of the initially-perturbed interface are modeled using the linear, compressible flow equations for early times and using the nonlinear, incompressible flow equations for later times. Under appropriate kinematic and Bernoulli boundary conditions, a perturbation solution ansatz yields differential equations for the functions. Solving these equations at the location of the bubbles and spikes gives the amplitude and growth rate of the bubbles and spikes. The radius of convergence of the series solution is extended via Padé approximants.

Vandenboomgaerde, Gauthier, and Mügler [145] proposed a simplified version of the perturbation expansion of Zhang and Sohn [156]. They noted that an accurate perturbation series can be obtained

by retaining only the terms with the largest unbounded part of the Zhang-Sohn solution. As only the high-order terms in the series are retained, this shifts the problem from integrating to solving an algebraic system of equations. As a result, series of much higher order are obtained. The radius of convergence of these series is also extended using Padé approximants.

Matsuoka, Nishihara, and Fukuda [91] proposed a new formulation of the kinematic boundary conditions in the perturbation expansion of the Zhang-Sohn potential flow to account for stretching at the interface. The perturbation expansion yields different expansions for the bubble and spike.

The Sadot et al. [114] empirical model for the Richtmyer-Meshkov instability is based on fits to experimental data and on asymptotic growth laws. The model was presented in the context of providing a single formula that could capture the initial linear growth and the later nonlinear growth of both the bubble and spike. This model was extensively tested against experimental data, and excellent agreement was found for both the bubble and spike growth.

4.5.1.3 Potential models

The first potential model is due to Layzer [80], who derived analytic solutions for the flow of an ideal, incompressible fluid contained in the upper half of a vertical tube falling under the action of gravity. For inviscid fluids initially at rest, the velocity field can be described by a scalar potential in two and three dimensions satisfying the Laplace and Bernoulli equations and additional kinematic boundary conditions. An ansatz for the solution yields a system of differential equations that gives the amplitude of the Rayleigh-Taylor bubble via integration.

Hecht, Alon, and Shvarts [52] extended the Layzer model to the Richtmyer-Meshkov instability. The two-dimensional equations for the potential ϕ were modified so that $g = 0$, and an initial velocity perturbation $v_b^{RM}(0)$ equal to the change in velocity after the shock was introduced.

Mikaelian [105] extended the Layzer model to the case when $a_b(0) \neq 0$ for both the Rayleigh-Taylor and Richtmyer-Meshkov instabilities. Equations for the bubble velocity in the Rayleigh-Taylor and Richtmyer-Meshkov instabilities were derived in two- and three-dimensional geometries.

Zhang [155] extended the Layzer model to determine the spike velocity for both the Richtmyer-Meshkov and Rayleigh-Taylor instabilities in two and three dimensions. Expressions for the spike and bubble velocity were determined by assuming that the interface is locally parabolic.

Goncharov [42] extended the two-dimensional Layzer model to the case of $A \neq 1$ for both the Rayleigh-Taylor and Richtmyer-Meshkov instabilities. Sohn [134] also extended the Layzer model to fluids with arbitrary density ratios. The approach differs from that of Goncharov in the use of a simpler form for the potential functions from Layzer [80].

Mikaelian [106] presented explicit expressions for the evolution of the bubble amplitude in single-mode Rayleigh-Taylor and Richtmyer-Meshkov instabilities in two and three dimensions. The main idea was to combine the amplitudes from the linear regime with the analytic nonlinear amplitudes

obtained from the Layzer potential theory.

Motivated by the desire to develop a simple model to understand the penetration of bubbles in the Rayleigh-Taylor instability, Zufiria [158] augmented the Layzer model for $A = 1$ to account for bubbles that change in size. This was accomplished by modeling bubbles with source flows. Zufiria then generalized the model for the case of multiple bubbles, where the potential was given by the superposition of the potential from different bubbles. Simulations showed that smaller bubbles have smaller velocity, and therefore were overcome by other larger bubbles. The larger bubbles therefore grew even larger, while the smaller bubbles shrank and were left behind in a process called *bubble competition*. Sohn and Zhang [137, 135] extended the Zufiria model to the Richtmyer-Meshkov instability for $A = 1$ and later extended both the Rayleigh-Taylor and Richtmyer-Meshkov instability to arbitrary Atwood numbers.

4.5.2 Comparison of amplitudes to experimental data and to the predictions of amplitude growth models

Presented here is a comparison of the perturbation, bubble, and spike amplitudes from the ninth-order WENO and VS simulations using 512 points per initial perturbation wavelength with the experimental data points of Jacobs and Krivets and the predictions of amplitude growth models.

Figure 4.15 shows a comparison of the perturbation amplitude $a(t)$ from the ninth-order WENO and VS simulations with the experimental data points. The VS and vortex simulations do not capture reshock at ≈ 5.65 ms. The results show good agreement between the simulation results and the experimental data points. At early times, the WENO and VS amplitudes are in close agreement. At later times before reshock, the VS amplitudes are slightly smaller than the WENO amplitudes, and the Lagrangian results are in-between. Also shown in Figure 4.15 is a comparison of the bubble and spike amplitudes from the simulations. The VS simulation slightly underpredicts the spike amplitude and overpredicts the bubble amplitude. The Lagrangian simulation also slightly underpredicts the spike amplitudes at all times and overpredicts the bubble amplitude at late times.

When comparing the simulation data to the predictions of the models, the amplitude growth rate is adjusted to account for the diffuse interface by including the growth reduction factor [Eq. (4.18)]. Shown in Figure 4.16 is a comparison of the perturbation amplitude from the WENO and VS simulations with the experimental data points and the predictions of the linear Richtmyer model [121] [Eq. (1.16)], the nonlinear Zhang-Sohn series model [156]

$$\frac{da}{dt} = v_0 \left\{ 1 - k^2 v_0 t a_0^+ + \left[(A^+)^2 - \frac{1}{2} \right] k^2 v_0^2 t^2 \right\}, \quad (4.27)$$

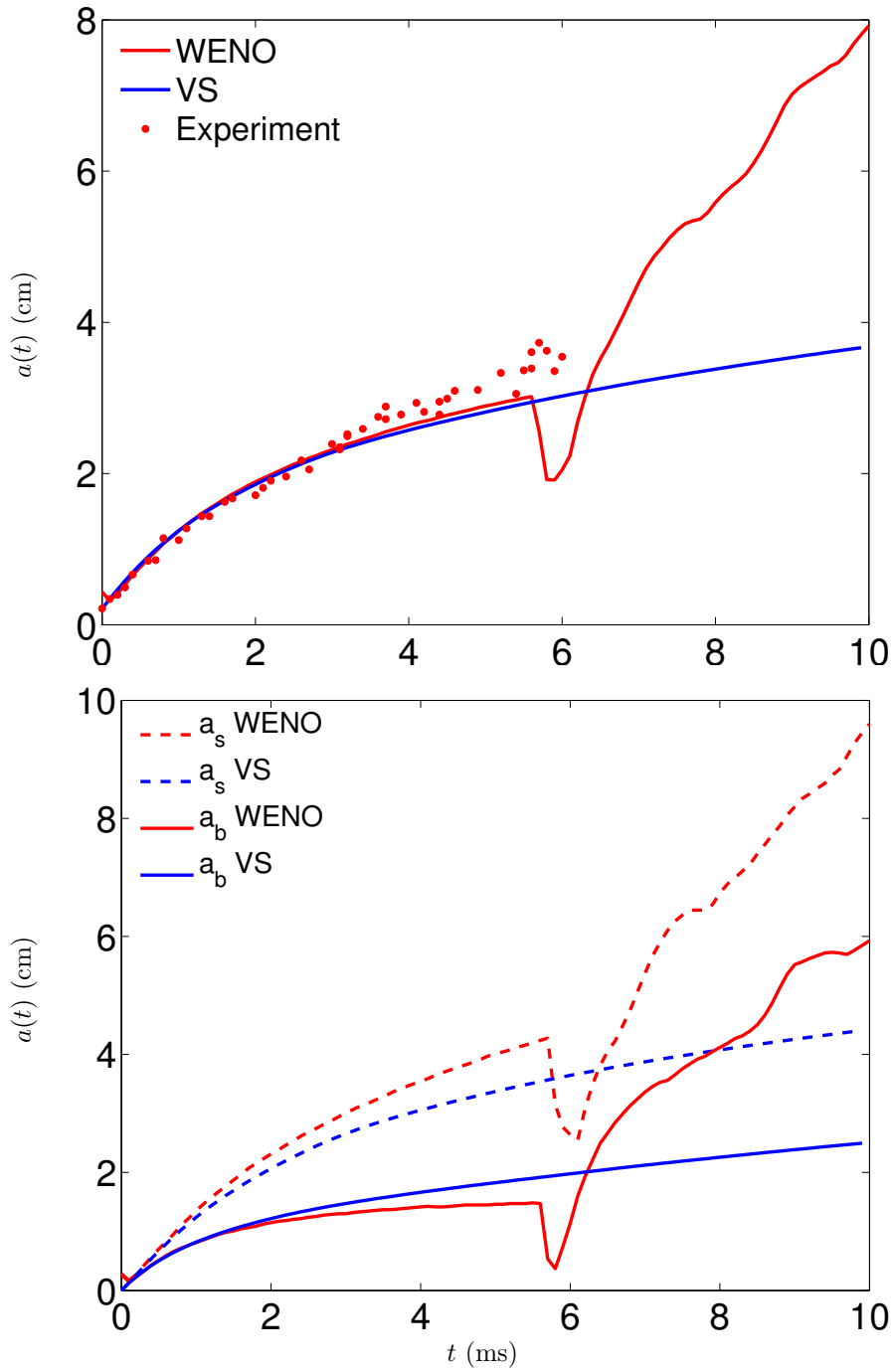


Figure 4.15. Comparison of the perturbation amplitude $a(t)$ from the WENO and VS methods with the experimental data points (top). Also shown is a comparison of the bubble and spike amplitudes $a_b(t)$ and $a_s(t)$, respectively, from the simulations (bottom).

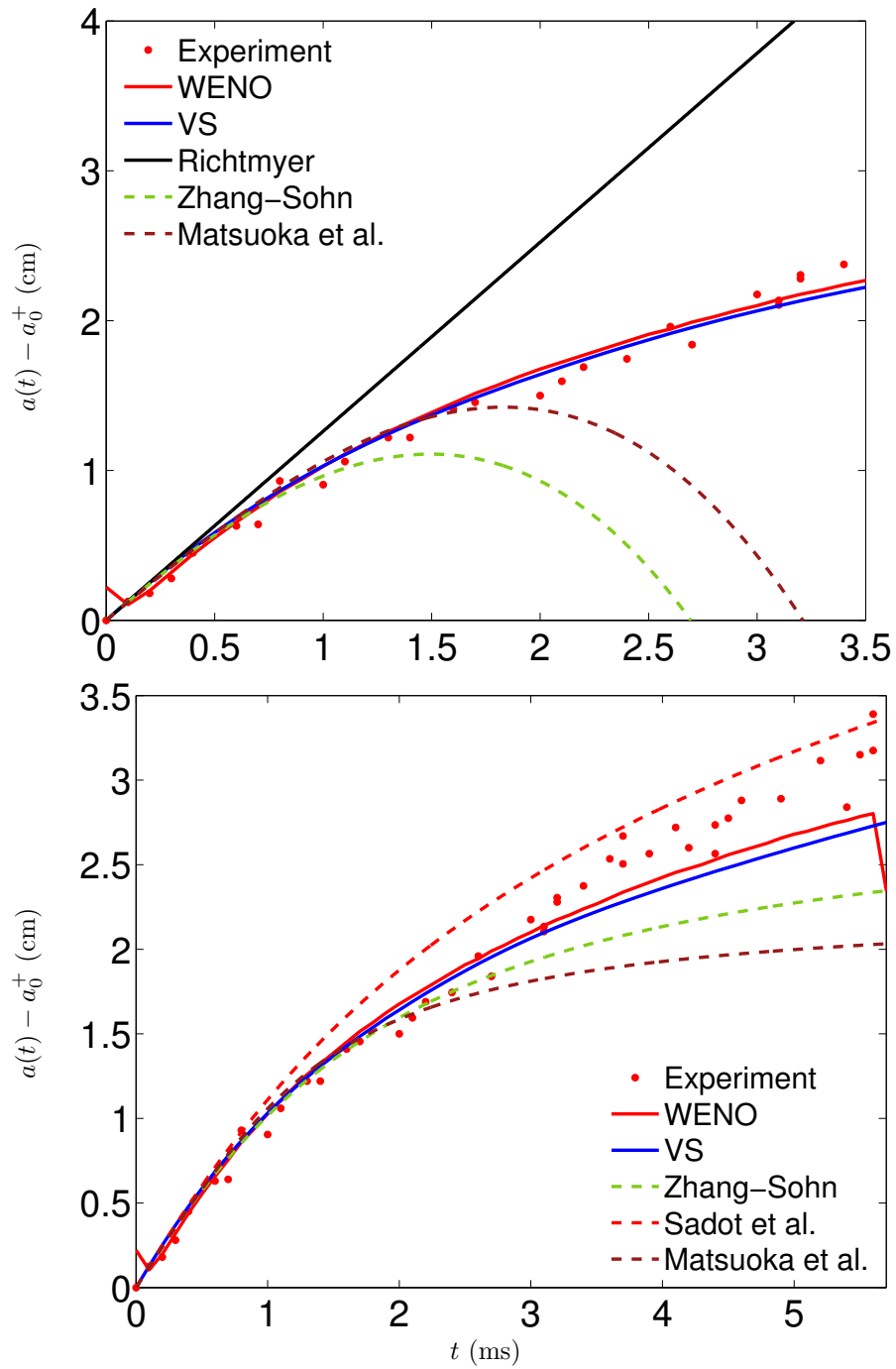


Figure 4.16. The perturbation amplitude $a(t) - a_0^+$ versus time t from the WENO and VS methods and the experimental data points, together with the predictions of the linear and nonlinear models.

and the Matsuoka et al. series model [91], obtained by averaging the bubble and spike velocities

$$\begin{aligned} \frac{\partial a_{b,s}}{\partial \tau} &= \left[\mp (A^+)^2 \pm \frac{1}{2} \right] \tau^2 + \left[\mp 2 (A^+)^2 k a_0^+ + A^+ \pm k a_0^+ \right] \tau \\ &+ \left[\mp 2 (A^+)^2 \pm \frac{3}{2} \right] (k a_0^+)^2 + \frac{k a_0^+ A^+}{2} \mp 1, \end{aligned} \quad (4.28)$$

where τ is the rescaled time [Eq. (1.17)] and the upper (+ or -) and lower (- or +) sign in \pm or \mp denotes the bubble and spike, respectively. The Richtmyer model only captures the initial growth of the interface. The series models capture the initial linear and weakly-nonlinear growth before diverging. Also shown in Figure 4.16 is a comparison of the perturbation amplitude, together with the experimental data points and the predictions of the nonlinear Zhang-Sohn Padé model

$$\frac{da}{dt} = \frac{v_0}{1 + k^2 v_0 a_0^+ t + \max \left[0, (k a_0^+)^2 - (A^+)^2 + \frac{1}{2} \right] k^2 v_0^2 t^2}, \quad (4.29)$$

the nonlinear Sadot et al. model [114], obtained by averaging the bubble and spike velocities

$$\frac{da_b}{dt} = \frac{v_0 (1 + k v_0 t)}{1 + (1 + A^+) k v_0 t + \frac{1}{2\pi C} k^2 v_0^2 t^2}, \quad (4.30)$$

$$\frac{da_s}{dt} = \frac{v_0 (1 + k v_0 t)}{1 + (1 - A^+) k v_0 t + \frac{1 - A^+}{1 + A^+} \frac{1}{2\pi C} k^2 v_0^2 t^2}, \quad (4.31)$$

where $C = 1/(3\pi)$ for $A^+ \geq 0.5$ and $C = 1/(2\pi)$ otherwise, and the nonlinear Matsuoka et al. Padé model [91], obtained by averaging the bubble and spike velocities

$$\frac{\partial a_{b,s}}{\partial \tau} = \frac{f_{\pm}^3}{\left\{ f_{\pm} \left[(A^+)^2 - \frac{1}{2} \right] + g_{\pm}^2 \right\} \tau^2 - f_{\pm} g_{\pm} \tau + f_{\pm}^2}, \quad (4.32)$$

where $f_{\pm} \equiv \mp \left[2 (A^+)^2 - 3/2 \right] (k a_0^+)^2 + A^+ k a_0^+ / 2 \mp 1$ and $g_{\pm} \equiv \mp 2 (A^+)^2 k a_0^+ + A^+ \pm k a_0^+$. The Sadot et al. model overpredicts the perturbation amplitude, while the Zhang-Sohn and Matsuoka et al. models underpredict. The Zhang-Sohn model gives the best overall agreement with the data.

Shown in the first row of Figure 4.17 is a comparison of the WENO and VS bubble amplitudes, together with the predictions of the Zhang-Sohn model [156]

$$\frac{da_b}{dt} = -\frac{da}{dt} + \frac{A^+ k v_0^2}{1 + 2 k^2 a_0^+ v_0 t + 4 k^2 v_0^2 \left[(a_0^+)^2 k^2 + \frac{1 - (A^+)^2}{3} \right] t^2}, \quad (4.33)$$

the Sadot et al model [114] [Eq. (4.30)], the Matsuoka et al. model [91] [Eq. (4.32)], and the

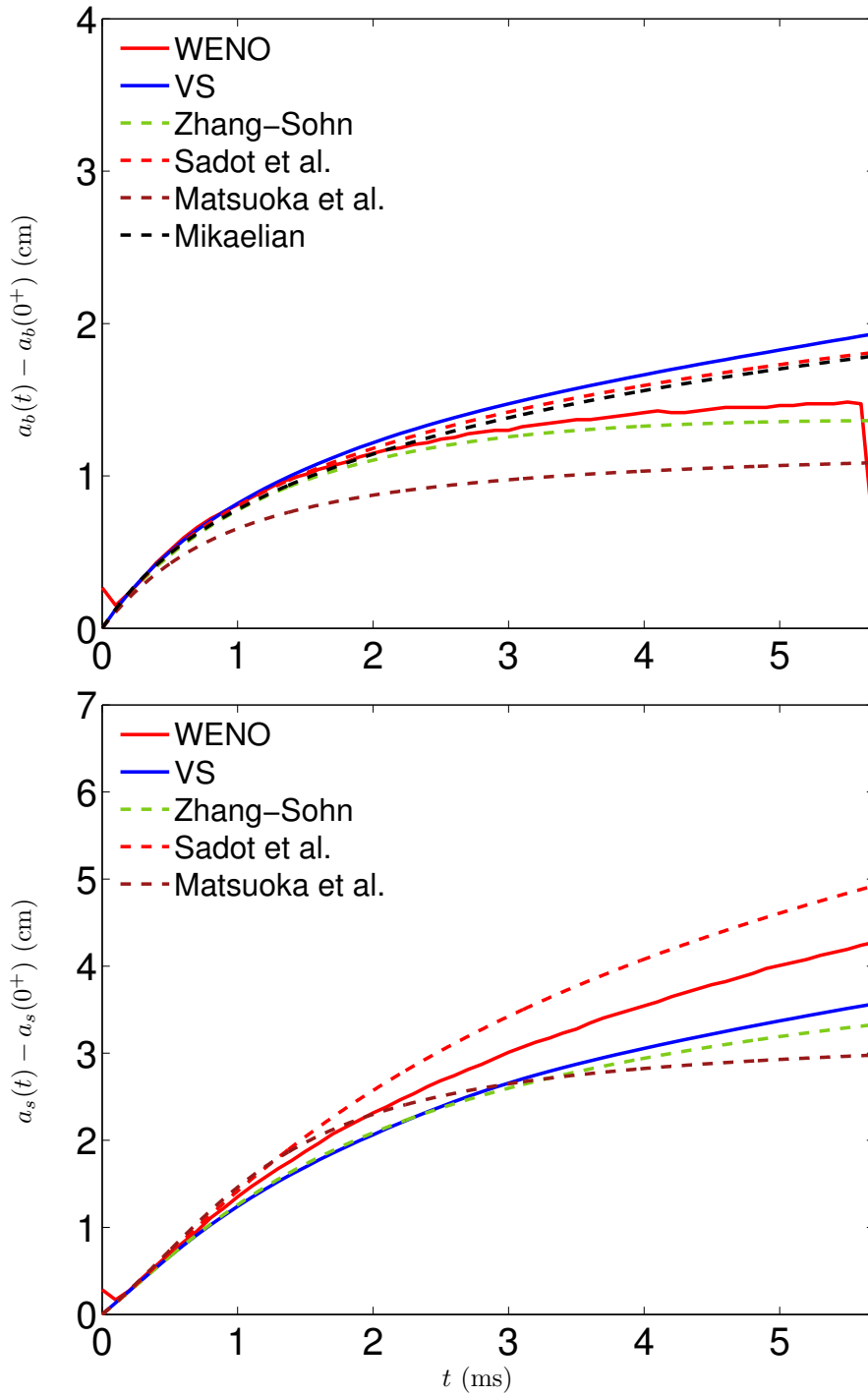


Figure 4.17. Comparison of the WENO and VS bubble and spike amplitudes $a_b(t)$ and $a_s(t)$ with the predictions of the Zhang-Sohn, Sadot et al., Matsuoka et al., and Mikaelian models.

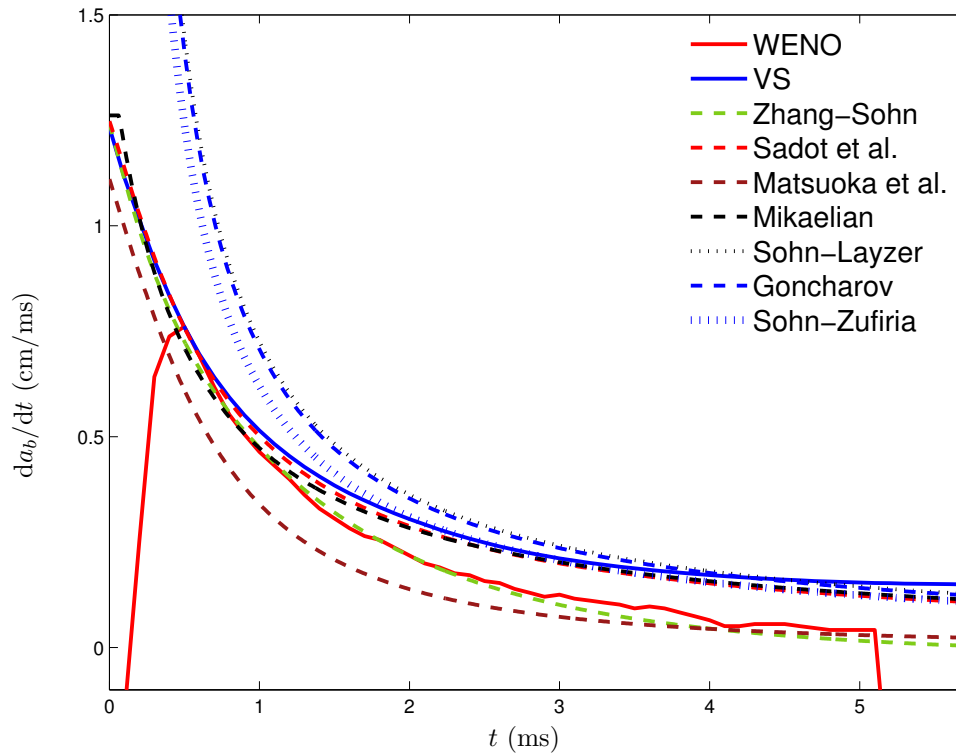


Figure 4.18. Comparison of the WENO and VS bubble velocity $da_b(t)/dt$ with the predictions of the Zhang-Sohn, Sadot et al., Matsuoka et al., Mikaelian, Sohn-Layzer, Goncharov, and Sohn-Zufiria models.

Mikaelian model [106]

$$a_b(t) = \begin{cases} a_0^+ (1 + k [u] A^+ t) & \text{for } t < t^*, \\ \frac{1}{3k} + \frac{3+A^+}{3(1+A^+)k} \ln \left[1 + \frac{3k v_{b,0} (1+A^+)}{3+A^+} (t - t^*) \right] & \text{for } t > t^*, \end{cases} \quad (4.34)$$

where the transition time is $t^* = [1/(3k a_0^+) - 1]/(k A^+ [u])$. The VS bubble amplitude is in best agreement with the prediction of the Sadot et al. and Mikaelian models. The WENO bubble amplitude is in best agreement with the Zhang-Sohn prediction.

Figure 4.18 shows the bubble amplitude growth from the simulations together with the corresponding predictions from the models. In addition, also shown are the asymptotic bubble velocities from the Sohn-Layzer model [134]

$$\frac{da_b}{dt} \longrightarrow \frac{2}{(2+A)kt}, \quad (4.35)$$

the Goncharov model [42]

$$\frac{da_b}{dt} \longrightarrow \frac{3+A}{3(1+A)kt}, \quad (4.36)$$

	WENO	VS
	Δ_{sim}	Δ_{sim}
Experiment	6.35	7.63
Zhang-Sohn Padé (all)	3.22	2.59
Zhang-Sohn Padé (bubble)	1.7	6.24
Zhang-Sohn Padé (spike)	5.31	2.75
Matsuoka et al. Padé (all)	6.02	4.19
Matsuoka et al. Padé (bubble)	13.31	21.65
Matsuoka et al. Padé (spike)	8.86	13.17
Sadot et al. (all)	8.26	9.38
Sadot et al. (bubble)	5.18	1.18
Sadot et al. (spike)	9.8	14.9
Mikaelian (bubble)	3.13	2.3

Table 4.9. Average fractional deviations Δ_{exp} between the experimental amplitude $a_{\text{exp}}(t)$ and the amplitude from the WENO and VS simulations a_{sim} and the predictions from nonlinear models $a_{\text{mod}}(t)$ obtained using the mix initial conditions, respectively. Also shown is the average fractional deviation Δ_{sim} between the simulation amplitude $a_{\text{sim}}(t)$, and the amplitude from the nonlinear models $a_{\text{mod}}(t)$.

and the Sohn-Zufiria model [137, 135]

$$\frac{da_b}{dt} \rightarrow \left[\frac{A+3}{3(1+A)} - \frac{1}{\zeta(A)} + \frac{2A}{3(1+A)\zeta(A)^2} \right] \frac{1}{kt}, \quad (4.37)$$

where $\zeta(A)$ is the root of the cubic polynomial $(3-A)\zeta^3 - (21+9A)\zeta^2 + (3+15A)\zeta - 4A = 0$. The asymptotic bubble velocity from the vortex simulations is larger than that from the WENO simulation. The WENO asymptotic bubble velocity is best captured by the Zhang-Sohn and Matsuoka et al. models. All other models shows asymptotic agreement with the vortex simulations. Also shown in Figure 4.17 is a comparison of the WENO and VS spike amplitude together with the predictions from the Zhang-Sohn model [156]

$$\frac{da_s}{dt} = \frac{da}{dt} + \frac{A^+ k v_0^2}{1 + 2k^2 a_0^+ v_0 t + 4k^2 v_0^2 \left[(a_0^+)^2 k^2 + \frac{1-(A^+)^2}{3} \right] t^2}, \quad (4.38)$$

the Sadot et al. model [114] [Eq. (4.31)], and the Matsuoka et al. model [91] [Eq. (4.32)]. The VS amplitudes are in excellent agreement with the predictions of the Zhang-Sohn model. The WENO amplitudes are best captured by the Sadot et al. and Zhang-Sohn models.

To make the agreement between the perturbation amplitude and the experimental data points more quantitative, the *average fractional deviation* [62, 78]

$$\Delta_{\text{exp}} = \frac{1}{N} \sum_{i=1}^N \frac{|a_{\text{mod}}(t_i) - a_{\text{exp}}(t_i)|}{a_{\text{exp}}(t_i)} \quad (4.39)$$

is shown in Table 4.9 under the row ‘‘Experiment’’. All of the simulations capture the experimental

	Mix initial conditions		Upstream initial conditions	
$\Gamma'_1 a_0^+$ (cm/s)	2784.881		2791.2	
$\max(\gamma)$ (cm/s)	2768.647		2690.566	
Γ'_1 (1/s)	12952.936		12572.973	
	Coarse-grid	Fine-grid	Coarse-grid	Fine-grid
$\max[\langle\omega\rangle(y, 0^+)]$ (cm/s)	2918.665	2908.141	2708.698	2705.33
$\max[\langle\mathcal{P}\rangle(y, 0^+)]$ (cm/s ²)	1.65417×10^7	1.63127×10^7	8.49831×10^6	8.23361×10^6

Table 4.10. Comparison of the initial circulation deposition $\max[\langle\omega\rangle(y, 0^+)]$ from the WENO simulations using mix and upstream initial conditions with the predictions of the Samtaney-Zabusky model $\Gamma'_1 a_0^+$ and the prediction from linear instability theory $\max(\gamma)$. Also shown is $\max[\langle\mathcal{P}\rangle(y, 0^+)]$, which measures the initial circulation deposition on the interface.

data points very well. The best agreement is given by the WENO simulation followed by the VS simulation. Also shown in Table 4.9 is the average fractional deviation between the WENO and VS simulation, and the nonlinear model predictions,

$$\Delta_{\text{sim}} = \frac{1}{N} \sum_{i=1}^N \frac{|a_{\text{mod}}(t_i) - a_{\text{sim}}(t_i)|}{a_{\text{sim}}(t_i)}. \quad (4.40)$$

The perturbation amplitude and bubble and spike amplitudes from the WENO simulations are best captured by the Zhang-Sohn Padé model. The perturbation and bubble amplitudes from the VS simulation are best captured by the Zhang-Sohn model, while the bubble amplitude is best captured by the Sadot et al. model.

4.5.3 Comparison of the mix and upstream initial conditions for the WENO method

Presented here is a comparison when the mix and upstream initial conditions are used in the WENO simulations. Visualizations for the upstream initial conditions are not shown as they are very similar to the visualizations for the mix initial conditions.

The baroclinic circulation deposition [Eq. (4.19)] from the simulations using the upstream and mix initial conditions are compared. Figure 4.21 shows $\langle\omega\rangle(y, 0^+)$ from the simulations together with the predictions of the Samtaney-Zabusky model [Eq. (4.20)] and the linear model [Eq. (4.22)]. As shown in Table 4.10, $\max[\langle\omega\rangle]$ is $\approx 7\%$ larger in the mix initial conditions case than in the upstream initial conditions case. The predictions of the Samtaney-Zabusky model (as measured by $\Gamma'_1 a_0^+$) are very similar for both initial conditions ($\approx 0.2\%$ difference). Similarly, the linear instability predictions for both initial conditions, $\max(\gamma)$ are also very similar ($\approx 2\%$ difference). The slightly larger value for the mix initial conditions can be attributed to the larger shock Mach number compared to the initial shock Mach number for the upstream initial conditions. The shape

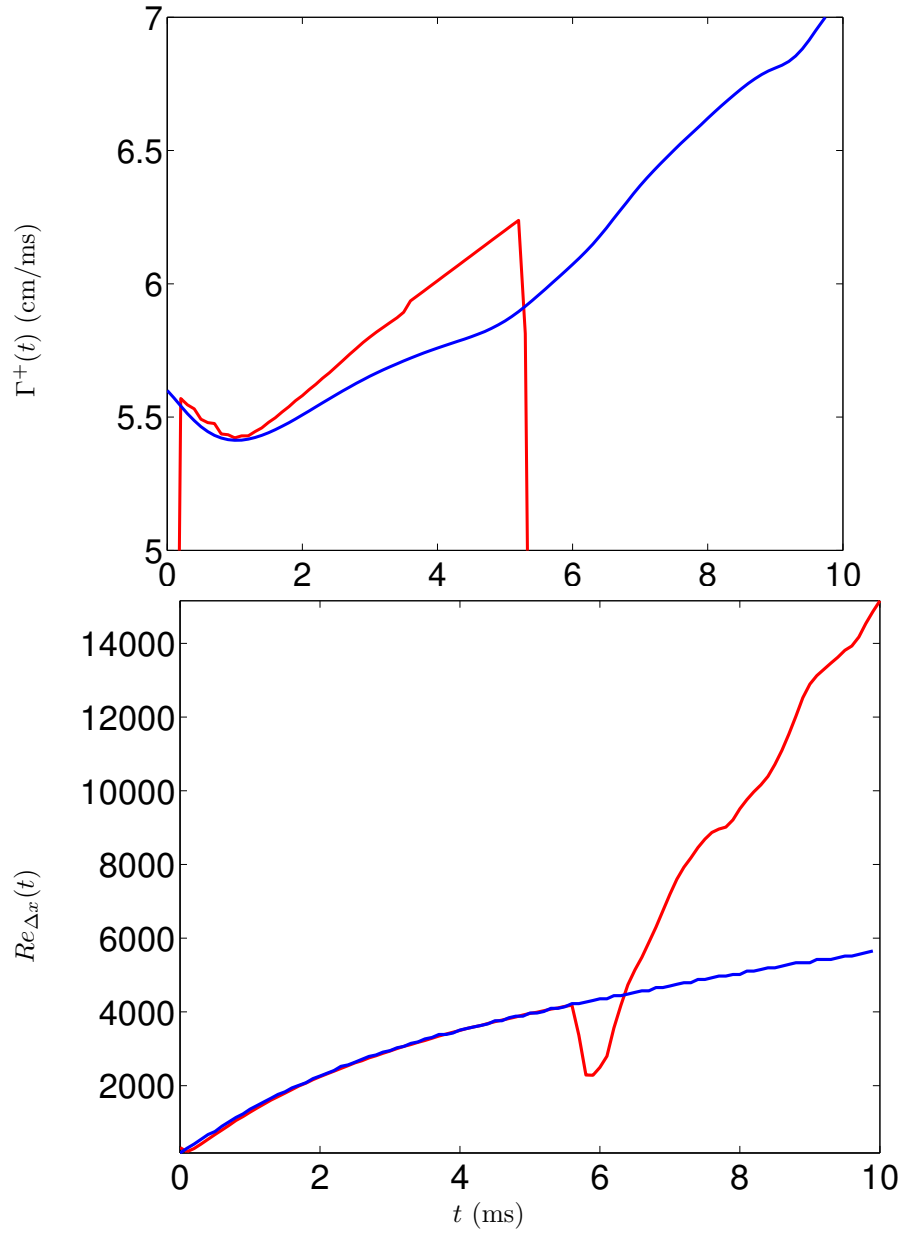


Figure 4.19. Comparison of the circulation $\Gamma^+(t)$ and Reynolds number $Re_{\Delta x}(t)$ from the WENO (red) and VS (blue) simulations.

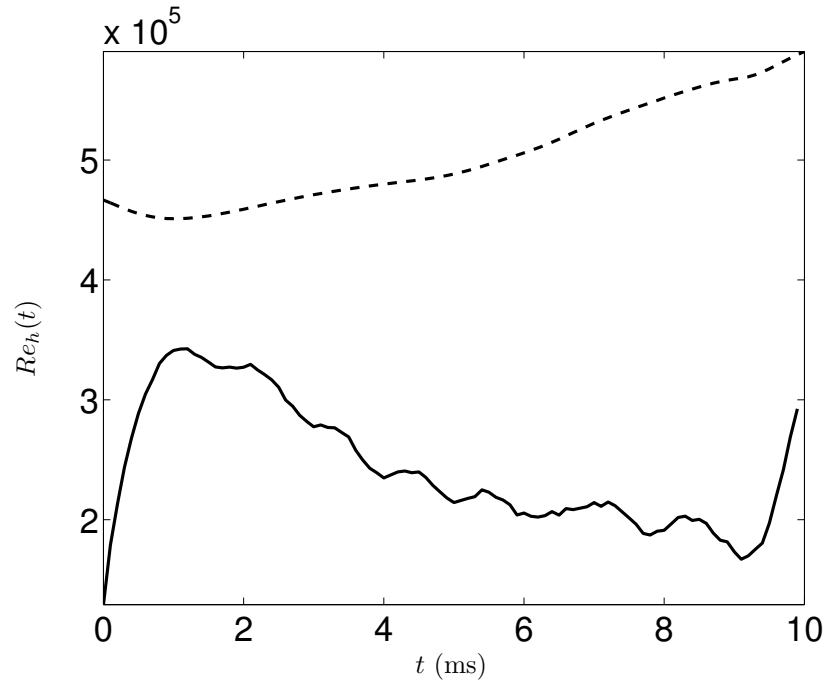


Figure 4.20. Comparison of the Reynolds number $Re_h(t)$ (solid black) and $Re_T(t)$ (dashed line) from the VS simulation.

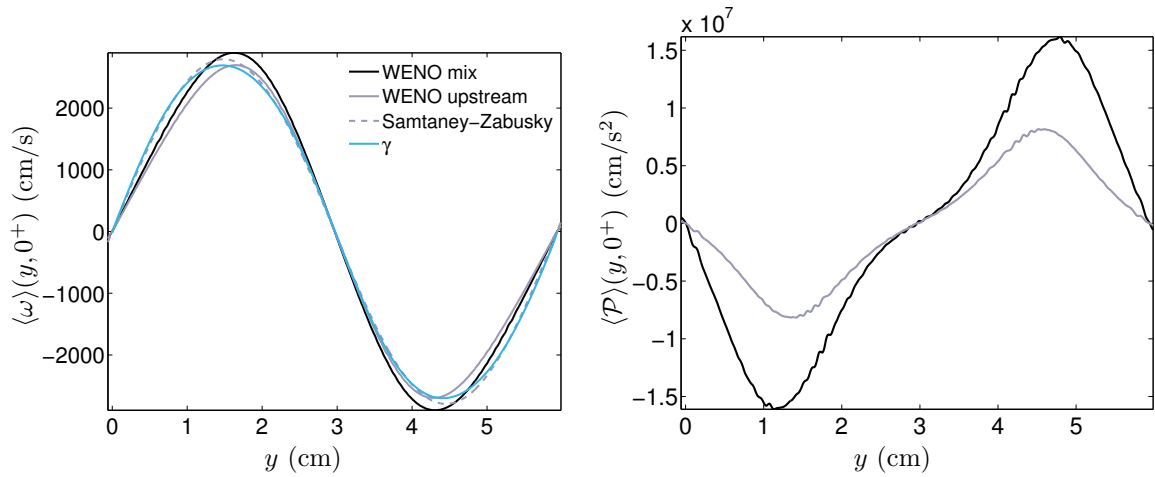


Figure 4.21. The initial deposition of circulation on the interface $\langle \omega \rangle(y, 0^+)$ from the incident shock at time 0^+ from the WENO simulation using mix initial conditions (solid black line) and upstream initial conditions (solid gray line), together with the predictions of the Samtaney-Zabusky and linear instability models. The initial baroclinic vorticity production $\langle \mathcal{P} \rangle(y, 0^+)$ on the interface is also shown (right).

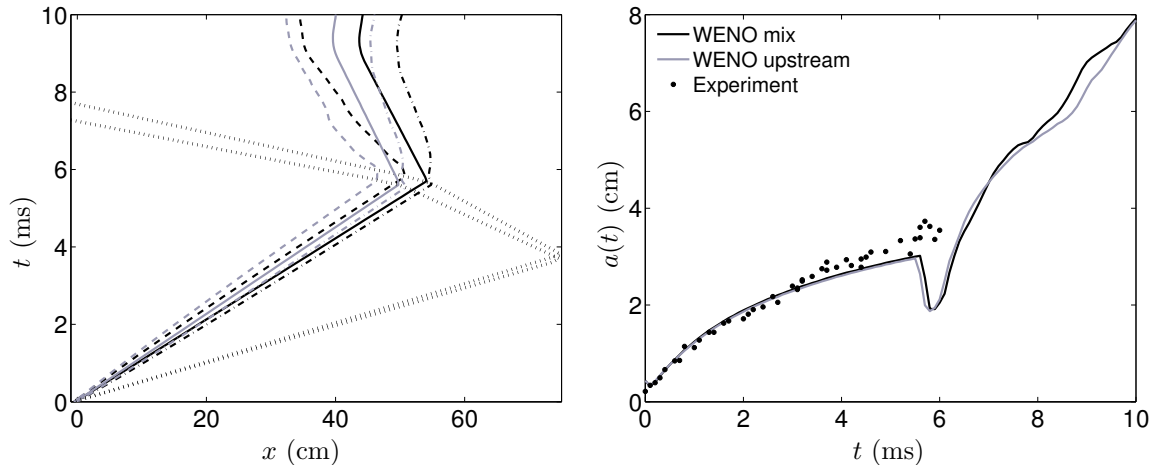


Figure 4.22. Comparison of the the $x-t$ diagram (left) and perturbation amplitude $a(t)$ (right) for the mix (black) and the upstream (gray) initial conditions.

of the circulation deposition also shows a slight skewness, when compared to the predictions of the models. As mentioned in Section 4.2.3, this is due to the evolution of the circulation on the interface following the passage of the shock. The comparison of the maximum baroclinic vorticity production, $\max \langle \mathcal{P} \rangle (y, 0^+)$, shows that the mix initial conditions value is approximately twice that for the upstream initial conditions value; the larger value for the former can be attributed to the larger shock Mach number.

A comparison of the $x-t$ diagram from the mix and upstream initial conditions is shown in Figure 4.22. As discussed in Section 4.2.2, the mix and upstream initial conditions predict different wave and interface velocities, as indicated by the different slopes of the transmitted shock, interface position $\ell_{\text{int}}(t)$, and bubble and spike positions $\ell_b(t)$ and $\ell_s(t)$. However, reshock occurs at the same time. Furthermore, the perturbation amplitude $a(t)$ is the same.

To better quantify the agreement between the experimental data points and the amplitudes from the WENO simulations with the upstream and mix initial conditions, the average fractional deviation Δ_{exp} [Eq. (4.39)] is shown in Table 4.11. The upstream and mix initial conditions are both very close to the experimental data points (a difference of $\approx 4.2\%$). In addition, the predictions of the amplitude growth models are also computed using the model parameters from the upstream initial conditions and compared to the simulation amplitude. The agreement is quantified using the average fractional deviation Δ_{sim} [Eq. (4.40)] shown in Table 4.11. The mix and upstream initial conditions give very similar results, with the Sadot et al. model yielding the best agreement, followed by the Vandenboomgaerde et al., Zhang-Sohn, and Matsuoka et al. model. The values for Δ_{sim} are similar to those from the mix initial conditions case.

In summary, the perturbation, bubble, and spike amplitudes from the upstream initial conditions

	Mix		Upstream	
	initial conditions	initial conditions	initial conditions	initial conditions
	Δ_{exp}	Δ_{sim}	Δ_{exp}	Δ_{sim}
Experiment	—	6.35	—	6.63
Zhang-Sohn Padé (all)	17.7	3.8	17.72	3.72
Zhang-Sohn Padé (bubble)	—	1.7	—	2.12
Zhang-Sohn Padé (spike)	—	5.31	—	4.8
Matsuoka et al. Padé (all)	27.23	6.52	27.25	6.19
Matsuoka et al. Padé (bubble)	—	13.85	—	15.64
Matsuoka et al. Padé (spike)	—	10.89	—	11.43
Sadot et al. (all)	10.52	11.37	10.7	12.49
Sadot et al. (bubble)	—	7.33	—	6.14
Sadot et al. (spike)	—	13.38	—	15.7
Mikaelian (bubble)	—	4.76	—	2.43

Table 4.11. Average fractional deviations Δ_{exp} between the experimental amplitude $a_{\text{exp}}(t)$ and the amplitude from the nonlinear models $a_{\text{mod}}(t)$ obtained using the upstream and mix initial conditions. Also shown is the average fractional deviations Δ_{sim} between the simulation amplitudes and the predictions of the Zhang-Sohn, Matsuoka et al., Sadot et al., and Mikaelian models.

simulation are in quantitative agreement with the results from the mix initial conditions simulation. As a result, the choice of consistent initial conditions has little effect on the agreement with data and on the predictions of the nonlinear models.

4.6 Comparison of WENO and vorticity-streamfunction simulations for different Mach numbers

To further understand the differences in bubble and spike amplitudes between the WENO and VS simulations, the perturbation, bubble, and spike amplitudes and circulation from the WENO and VS methods are compared as the Mach number is varied. Simulations are performed using the mix initial conditions (Sec. 4.2.2) by modifying the incident shock Mach number to $Ma = 1.05, 1.15,$ and 1.45 . The shock speeds, initial growth rates, post-shock amplitudes and Atwood numbers used to initialize the VS simulations are shown in Table 4.12. The results in the present study are also compared to the $Ma = 1.31$ results of Section 4.5.

Figure 4.23 shows a comparison of the perturbation amplitude $a(t)$ from the WENO and VS simulations as the Mach number is varied. First, reshock occurs at earlier times as the Mach number increases, as the transmitted shock and interface both travel at a faster speed (Table 4.12). For $Ma = 1.05$ the amplitudes are very similar. As the Mach number is increased, the agreement between the WENO and VS amplitudes decreases. Also shown is a comparison of the bubble amplitude $a_b(t)$ as the Mach number is increased. The WENO and VS amplitudes are in excellent agreement for $Ma = 1.05$. For $Ma = 1.15$ the VS amplitude is slightly larger. The VS amplitudes

	$Ma = 1.05$		$Ma = 1.15$	
$u_{shock,i}$ (cm/s)	29837		32679	
$[u]$ (cm/s)	1719		4946	
v_0 (cm/s)	301		779.58	
Ma_r	1.016		1.047	
$u_{shock,r}$ (cm/s)	29069		30313	
Ma_t	1.067		1.205	
$u_{shock,t}$ (cm/s)	15049		16992	
$t_{reshock}$ (ms)	8.9		6.8	
η_{comp}	0.942		0.849	
	Pre-shock	Post-shock	Pre-shock	Post-shock
a_0 (cm)	0.29	0.273	0.29	0.246
δ_T (cm)	0.5	0.471	0.5	0.424
A	0.605	0.605	0.605	0.605
ψ	1.182	1.152	1.182	1.152

	$Ma = 1.31$		$Ma = 1.45$	
$u_{shock,i}$ (cm/s)	37311		41204	
$[u]$ (cm/s)	9770		13543	
v_0 (cm/s)	1336.8		1679.7	
Ma_r	1.092		1.126	
$u_{shock,r}$ (cm/s)	32203		33695	
Ma_t	1.437		1.639	
$u_{shock,t}$ (cm/s)	20265		23100	
$t_{reshock}$ (ms)	5		4.1	
η_{comp}	0.738		0.671	
	Pre-shock	Post-shock	Pre-shock	Post-shock
a_0 (cm)	0.29	0.214	0.29	0.195
δ_T (cm)	0.5	0.369	0.5	0.336
A	0.605	0.604	0.605	0.601
ψ	1.182	1.133	1.182	1.19

Table 4.12. Comparison of the flow properties, including initial, reflected, and transmitted shock Mach numbers, Ma_i , Ma_r , and Ma_t , respectively, shock velocities $u_{shock,i}$, $u_{shock,r}$, and $u_{shock,t}$, respectively, interface velocity $[u]$, initial interface growth v_0 , and pre- and post-shock initial amplitudes a_0^- and a_0^+ , the pre- and post-shock diffuse-interface thickness δ_T^- and δ_T^+ , pre- and post-shock Atwood numbers A^+ , and A^- , and pre- and post-shock growth reduction factor ψ^+ and ψ^- , for $Ma = 1.05, 1.15, 1.31, \text{ and } 1.45$.

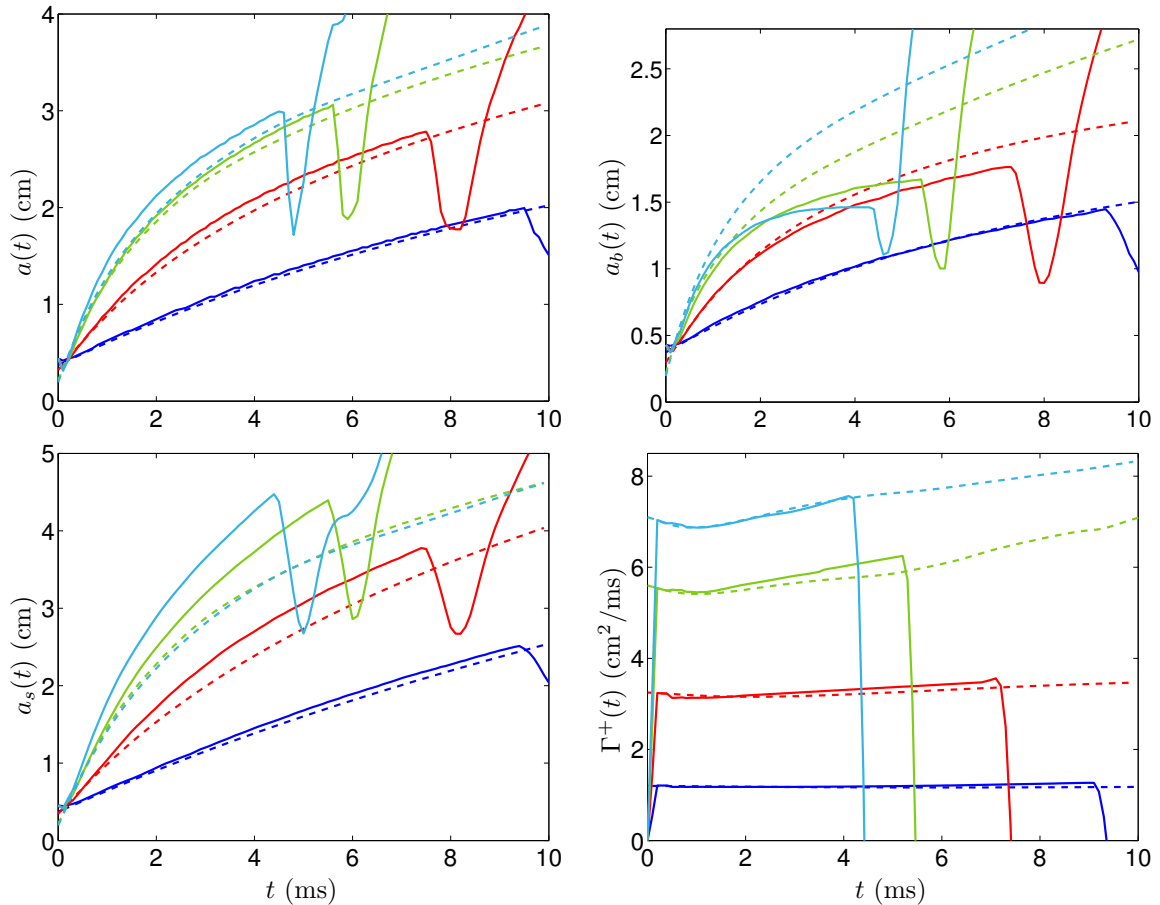


Figure 4.23. Comparison of the perturbation, bubble, and spike amplitudes $a(t)$, $a_b(t)$, $a_s(t)$, and circulation $\Gamma^+(t)$ from the WENO (solid line) and VS (dashed line) simulations for $Ma = 1.05$ (blue), 1.15 (red), 1.31 (green), and 1.45 (light blue).

are much larger than the WENO amplitudes for $Ma = 1.31$ and 1.45. In addition, the bubble amplitude from the $Ma = 1.45$ simulation is smaller than that from the $Ma = 1.31$ simulation. This can be explained by the Wouchuk-Nishihara vorticity deposition model [150]. Following shock refraction and the instantaneous deposition of vorticity on the interface, the transmitted shock is super-stable (*i.e.* its perturbation decreases in time as $t^{-3/2}$ [40]). As the shock stabilizes, pressure perturbations are generated, which interact with the layer causing a decrease in the bubble growth. Also shown in the figure is a comparison of the spike amplitude $a_s(t)$. The spike amplitudes from the WENO and VS simulations are in close agreement for $Ma = 1.05$. As the Mach number increases, the WENO simulation gives a larger spike amplitude. Also shown in Figure 4.23 is a comparison of the circulation $\Gamma^+(t)$. In general, the WENO and VS circulations are in good agreement up to reshock. The average fractional deviation Δ between the WENO and VS results is shown in Table 4.13, confirming the good agreement for $Ma = 1.05$ and the progressively larger differences as the Mach number is increased.

	$Ma = 1.05$	$Ma = 1.15$	$Ma = 1.31$	$Ma = 1.45$
$\Delta a(t)$ (%)	2.34	3.37	4.85	7.83
$\Delta a_b(t)$ (%)	0.82	2.59	7.63	21.19
$\Delta a_s(t)$ (%)	0.89	4.25	8.5	21.95
$\Delta \Gamma^+(t)$ (%)	1.04	2.35	3.05	3.03

Table 4.13. The average fractional deviation Δ between the perturbation, bubble, and spike amplitudes $a(t)$, $a_b(t)$, $a_s(t)$, and circulation $\Gamma^+(t)$ from the WENO and VS simulations for $Ma_i = 1.05$, 1.15, 1.31, and 1.45.

4.7 Investigation of reshock using the WENO method

Following the initial shock refraction at 0 ms, the transmitted shock reflects from the end wall of the shock tube and interacts with the evolving mixing layer in a process called *reshock* at ≈ 5.65 ms. Reshock imparts additional energy into the mixing layer, contributing to the formation of additional complex disordered structures. Reshock is of fundamental interest [129] and occurred in the experiments of Collins and Jacobs [27] and Jacobs and Krivets [62]. Investigated here are the dynamics of reshock (Sec. 4.7.1), including a visualization of the complex wave interactions. The mixing layer width is also compared to the predictions of reshock models (Sec. 4.7.2).

4.7.1 Dynamics of the reshock process

Figure 4.24 shows the time-evolution of the density and simulated density Schlieren fields during reshock at time intervals of 0.1 ms (and later 0.2 ms) from 5.6 to 7 ms. Simulated density Schlieren images are used to visualize the detailed wave structure present during reshock. The density Schlieren shown is [90]

$$\Phi(x, y, t) = \exp \left[-\alpha(m) \frac{|\nabla\rho|}{\max|\nabla\rho|} \right], \quad \alpha(m) = \begin{cases} 20 & \text{if } m > m^*, \\ 100 & \text{if } m < m^*, \end{cases} \quad (4.41)$$

where m is the mass fraction of SF_6 and $m^* = 0.25$.

Figure 4.24 shows the arrival of the reflected shock at 5.6 ms, the reflected shock refracting at the interface at 5.7 ms and at 5.8 ms, and the beginning of the inversion process at 5.9 ms, where bubbles transform into spikes and vice versa. As reshock is a refraction from a heavier fluid (SF_6) into a lighter fluid [air(acetone)], a transmitted shock enters the air(acetone) and a reflected rarefaction wave returns back into the SF_6 . The transmitted shock is highly curved, following the interaction with the bubble at 5.7 ms, and also generates a complex system of waves as it passes through the roll-ups at 5.8 and 5.9 ms. The reason for the inversion is the deposition of vorticity of opposite sign on the interface that drives the formation of rolls-up in the opposite direction. The simulated density Schlieren not only provides a sharp visualization of the system of reflected and transmitted waves

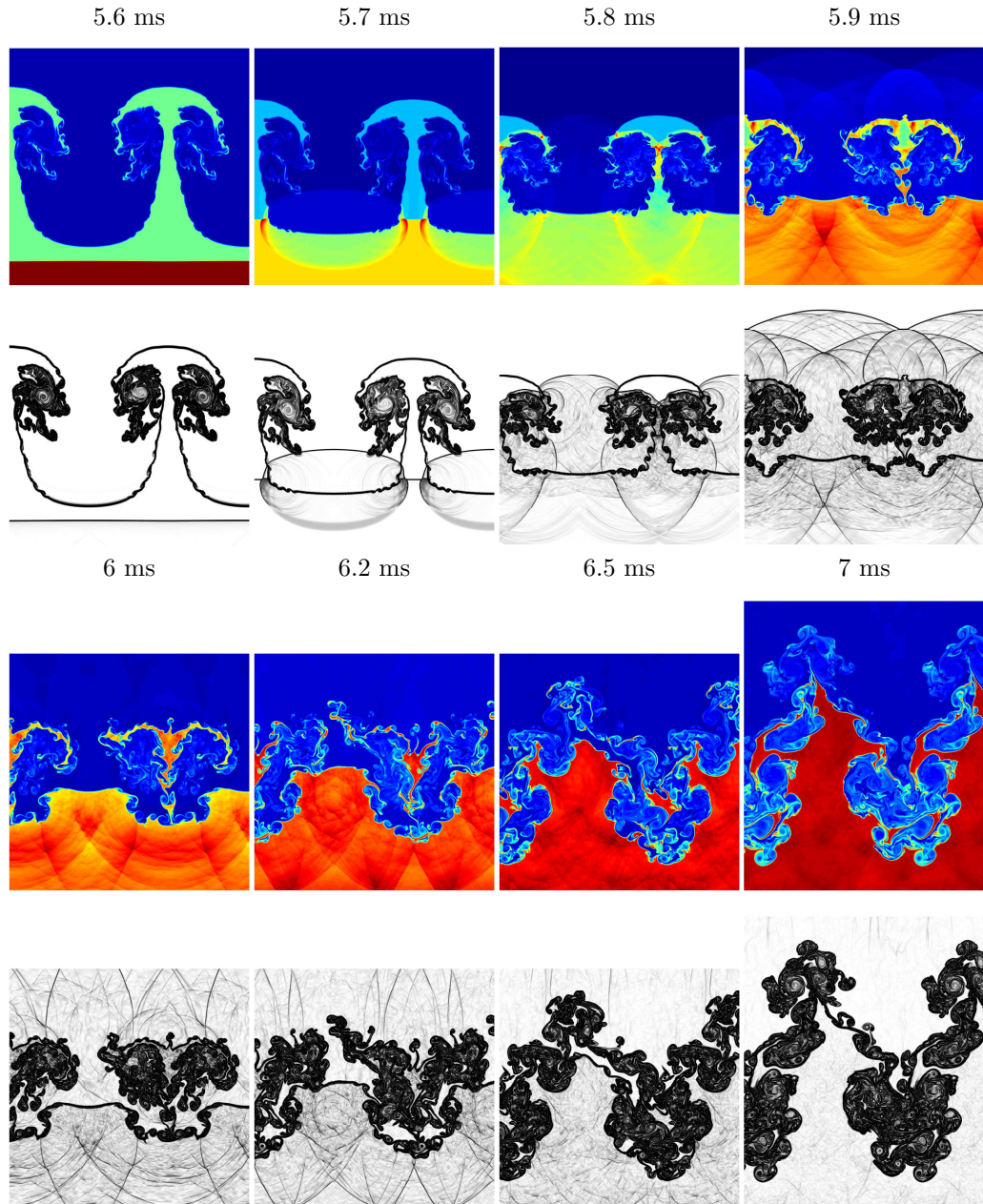


Figure 4.24. Time-evolution of the density and simulated density Schlieren fields from the WENO9-512 simulation illustrating the reshock process at 5.6, 5.7, 5.8, 5.9, 6, 6.2, 6.5, and 7 ms.

generated during reshock, but also of the fine-scale mixing within the roll-ups and, more generally, within the mixing layer. In particular, prior to reshock, the cores of the roll-up contain well-mixed complex regions. During reshock, these regions are compressed by the passage of the shock. At late times, large spikes of SF_6 develop. Near the large spike, a finely-mixed complex layer is observed, which are the remnants of the spike prior to reshock. The creation of small disordered structures breaks symmetry [129], leading to the formation of complex structures at late times.

Figure 4.25 shows the time-evolution of the vorticity $\omega(x, y)$ and baroclinic vorticity production field $\mathcal{P}(x, y)$ at the same times as in Figure 4.24. Immediately prior to reshock (5.6 ms), strong rotating cores develop, together with the vortex bilayers that contribute to the formation of the irregular structures within the roll-ups. At 5.7 ms, vorticity of opposite sign is deposited by the shock on the interface and drives the inversion process at 5.8 and 5.9 ms. The vorticity deposited by the shock is eight times more intense than the vorticity present inside the roll-ups. As a result, at 5.7 ms the vorticity inside the roll-ups appears much smaller. By contrast, the baroclinic vorticity production experiences a ten-fold increase at reshock, and the baroclinic production inside the roll-ups is almost not apparent at 5.7 ms. Following the passage of the transmitted shock, the baroclinic vorticity production forms strong positive and negative cores around the roll-up, contributing to the further fragmentation and increased mixing within the layer, as shown by the simulated density Schlieren. The baroclinic vorticity production also contributes to the formation of strong vortex bilayers. As a result, the layers of negative (or positive) vorticity present immediately following the passage of the shock at 5.9 ms on the surface of the spike are replaced by a disordered set of alternating layers of positive and negative vorticity at 6 ms. Following 6 ms, the inversion process forms a strong spike that penetrates into the mixing layer, forming a region of finely-mixed material corresponding to the presence of the spike and a region of unmixed SF_6 (associated with the formation of the new spike). The presence of the numerous vortex bilayers in the region previously occupied by the spike may facilitate the penetration of the spike, which instead has a strong region of positive and negative vorticity which acts as a “vortex projectile”. This may also elucidate why spikes penetrate deeply into the mixing layer at 6.3 and 6.5 ms. At late times, larger-scale structures form due to the inverse energy cascade [129], particularly in the coarse-grid simulations.

Finally, Figure 4.26 shows the density, vorticity, and baroclinic vorticity production fields at late times following reshock. Both simulations produce complex structures at late times. A dominant spike is present, and finely-mixed fluid is present between the structures. The vorticity shows the formation of localized strong cores of positive and negative vorticity. The baroclinic vorticity production shows fragmentation and activity that occurs at the boundaries of the large-scale structure and in between the separation region.

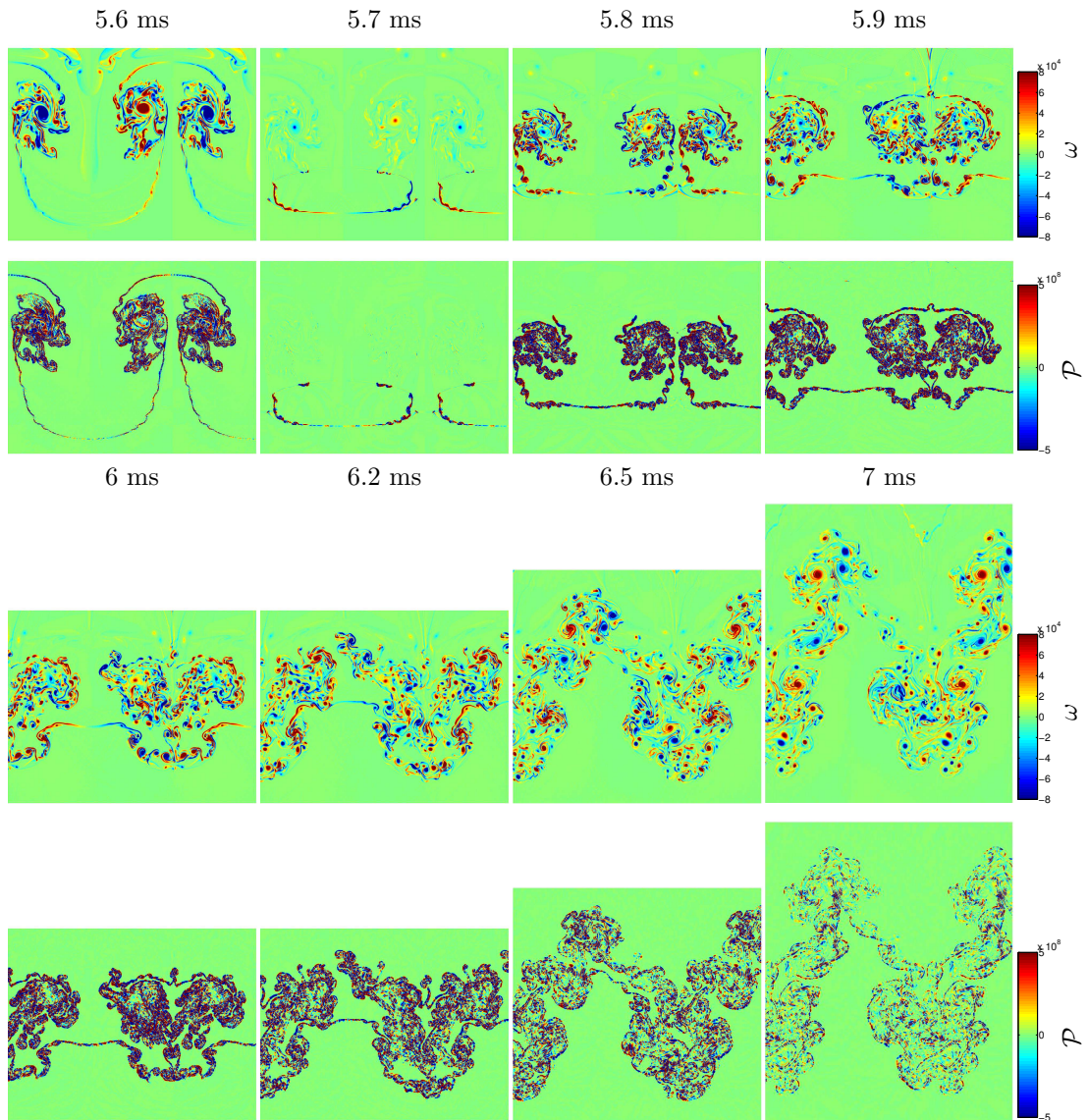
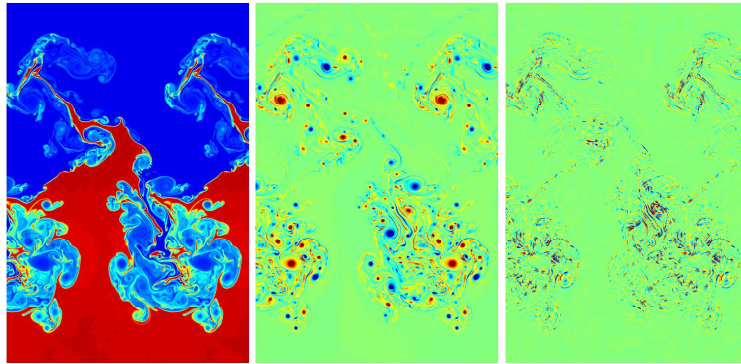


Figure 4.25. Time-evolution of the vorticity $\omega(x, y)$ and baroclinic vorticity production $\mathcal{P}(x, y)$ fields from the WENO9-512 simulation during reshock at 5.6, 5.7, 5.8, 5.9, 6, 6.2, 6.5, and 7 ms.

8 ms



10 ms

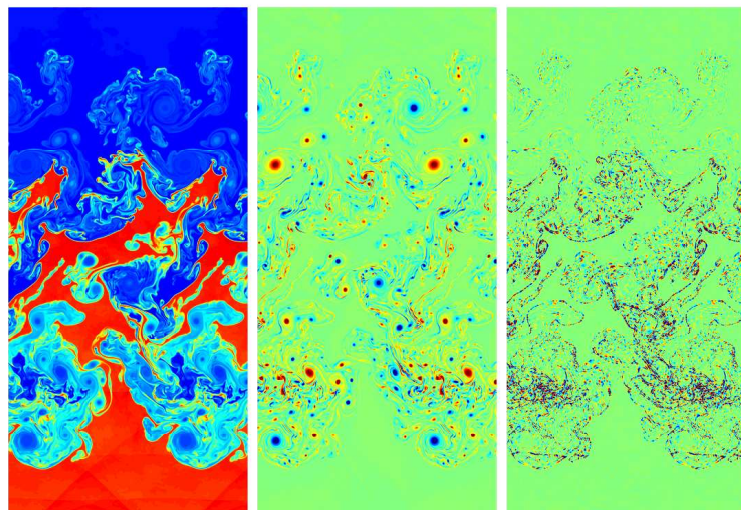
 ρ ω \mathcal{P}

Figure 4.26. Time-evolution of the density $\rho(x, y)$, vorticity $\omega(x, y)$, and baroclinic vorticity production $\mathcal{P}(x, y)$ fields from the WENO9-512 simulation at 8 and 10 ms.

4.7.2 Comparison of the mixing layer amplitude to the predictions of reshock models

Here, the mixing layer amplitude from the WENO9-512 simulation is compared to the predictions of reshock models.

A linear power-law model for the mixing layer width following reshock was developed by Mikaelian [101] developed the linear power-law model

$$a(t) = 0.14 [u]_1 A_1^+ t, \quad (4.42)$$

where A_1^+ is the post-reshock Atwood number, based on the experimental results of Read [120] and Youngs [153] for the width of a Rayleigh-Taylor mixing layer.

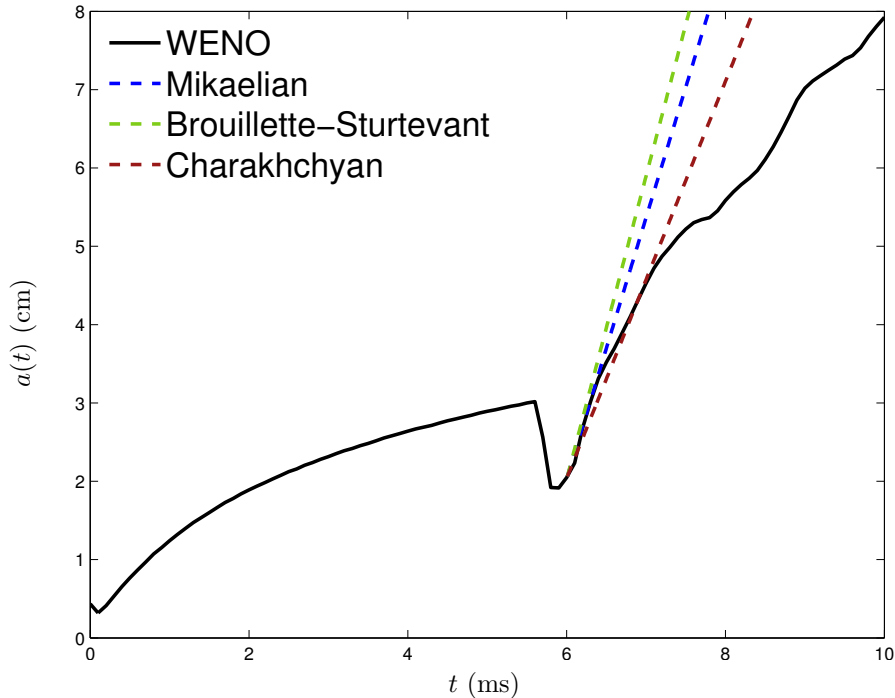


Figure 4.27. The mixing layer amplitude $a(t)$ versus time t from the WENO9-512 simulation together with the predictions of the linear models following reshock.

Brouillette and Sturtevant [18] performed shock tube experiments to assess the effects of a thick, diffuse interface on the growth of the Richtmyer-Meshkov instability. The growth

$$\frac{da}{dt} = k [u] A^+ a_0^+ + k [u]_1 A_1^+ a_1^+, \quad (4.43)$$

where the 1 subscript indicates values following reshock, was obtained by empirically generalizing the Richtmyer model.

Charakhch'yan [22] assumed that reshock is much weaker than the initial incident wave and occurs during the nonlinear phase, to obtain

$$\frac{da}{dt} = v_0 - 1.25 \Delta u_1 A^+, \quad (4.44)$$

which does not depend on the initial amplitude and on the change in Atwood number at reshock.

Figure 4.27 shows the mixing layer amplitude and the predictions of the Mikaelian, Brouillette-Sturtevant, and Charakhch'yan reshock models. These models predict linear growth (Table 4.14). The Brouillette-Sturtevant model predicts the largest growth rate, followed by the Mikaelian and the Charakhch'yan models. The models are intended to apply immediately after reshock (≈ 5.77 ms) until the arrival of the reflected rarefaction wave at ≈ 7 ms. The models are in agreement with

	$\frac{da}{dt}$ (cm/ms)	$k \frac{da}{d\tau}$
Richtmyer	1337.29	1
Mikaelian	3334.21	2.49326
Brouillette-Sturtevant	3870.64	2.89438
Charakhch'yan	2534	1.89487

Table 4.14. The growth rate da/dt and the normalized growth rate $k da/d\tau$ for the Richtmyer model before reshock for the mix initial conditions. Also shown is the growth rate and the normalized growth rates from the Mikaelian, Brouillette-Sturtevant, and Charakhch'yan reshock models.

the simulation data. The growth rates da/dt and the normalized growth rates $k da/d\tau$ are also shown in Table 4.14.

4.8 Atwood number study using the vorticity-streamfunction method and comparison to the Lagrangian and vortex-in-cell methods

In the limit of small diffuse-interface thickness δ_T , the evolution of the vortex layer should be similar to the evolution of a vortex sheet. Presented here is a comparison of simulations performed using the VS method to simulations performed using the Lagrangian vortex method (Lagrangian- γ) and the vortex-in-cell method based on the iterative-time-step formulation (VIC-ITS) for $A = 0, 0.2, 0.4, 0.6, \text{ and } 0.8$. For $A = 1$, the Lagrangian simulations are performed with the methods based on the vortex sheet strength (Lagrangian- γ) and vortex dipole (Lagrangian- μ), which use principal values to remove the singularity [9]. The effects of the Atwood number on the evolution of the instability are compared across the methods through a visualization of common quantities (Sec. 4.8.1), and the perturbation amplitude (Sec. 4.8.2).

4.8.1 Comparison of instability evolution from the Lagrangian, vortex-in-cell, and vorticity-streamfunction methods

Presented here is a visualization of the initial growth of the instability, including the formation of roll-ups at 0, 1, 2, 3, 4, and 5 ms for quantities from the three simulations. These times are chosen because in most shock tube experiments, the evolution of the single-mode instability is limited by the arrival of reshock. In addition, many features of interest to the investigation of the instability are already present at 5 ms. For the VS and VIC simulations, the vorticity is compared on the Cartesian grid. The density field of the VS simulation is also visualized. From the density field, the mass fraction contour is computed and compared to the interface of the Lagrangian and VIC simulations. In addition, field quantities can be *interpolated* onto the VS mass fraction contour with

the same procedure used to interpolate field quantities onto vortex markers in the VIC simulation. This allows a direct comparison of quantities on the interface across all simulations.

Figure 4.28 shows a visualization of the instability evolution for $A = 0$ at 1 ms intervals. The first and second rows show the interface evolution from the Lagrangian- γ and VIC simulations, the third row shows the mass fraction contour from the VS simulation, and the fourth row shows the time-evolution of the mass fraction field (for $A = 0$, the density is constant across the interface). The $A = 0$ case represents the evolution of a vortex sheet with a sinusoidal initial distribution of vorticity. As a result, the vorticity evolves and advects under its own velocity field. In the VS method this corresponds to zero baroclinic vorticity production, since the density is uniform. First, all three simulations provide similar characterizations of the evolution of the interface. The instability develops with the formation of a “bubble” and “spike”. In the Richtmyer-Meshkov instability “bubble” refers to the lighter fluid “rising” into the heavier fluid, and “spike” refers to the heavier fluid penetrating into the lighter fluid. For $A = 0$, the densities are the same, so that the bubbles and spikes have similar amplitudes. At 2 ms, the spike and bubble form roll-ups. The VS simulation shows a more pronounced roll-up compared to the Lagrangian and VIC simulations. The VS method represents the evolution of a diffused layer of vorticity, which is a qualitatively different problem from the evolution of a thin vortex sheet in the other methods. As a result, the VS simulation exhibits differences when compared to the other simulations. After 3 ms, additional finer-scale structure develops in the roll-up. The Lagrangian- γ simulation has the most structure in the roll-up, followed by the VS and VIC simulations.

Figure 4.29 shows the evolution of the vorticity from the VS and VIC simulations. The initial vorticity follows the sinusoidal distribution at 0 ms and has positive and negative signs on different parts of the sinusoidal curve. The vorticity then rolls-up and forms strong cores by 5 ms. The VIC vorticity is thicker due to the coarser grid and has smaller magnitude than that from the VS simulation. Both simulations are based on an initial vortex marker representation of the interface with markers carrying the same circulation. As a result, the vorticity field on the Cartesian grid is a function of the thickness of the hyperbolic tangent diffusion layer in the VS method, and a function of the Cartesian grid spacing in the VIC method. The evolution of the vorticity is similar across the two simulations. Between 1 and 3 ms, the vorticity from the VIC simulation increases in magnitude. Shown in the third, fourth, and fifth row is the vortex sheet strength $\gamma(e)$ from the Lagrangian- γ and VIC simulations, and the circulation interpolated back onto the contour from the VS simulation. At 0 ms, the circulation from the three simulations has the same shape, but the circulation of the VS simulation has smaller magnitude because the diffuse vorticity is interpolated back onto the contour resulting in an overall smaller circulation. As time evolves, the circulation develops spikes, corresponding to the roll-ups where the circulation is concentrated. The circulations for the Lagrangian and VIC simulations are very similar, while the circulation for the VS simulation

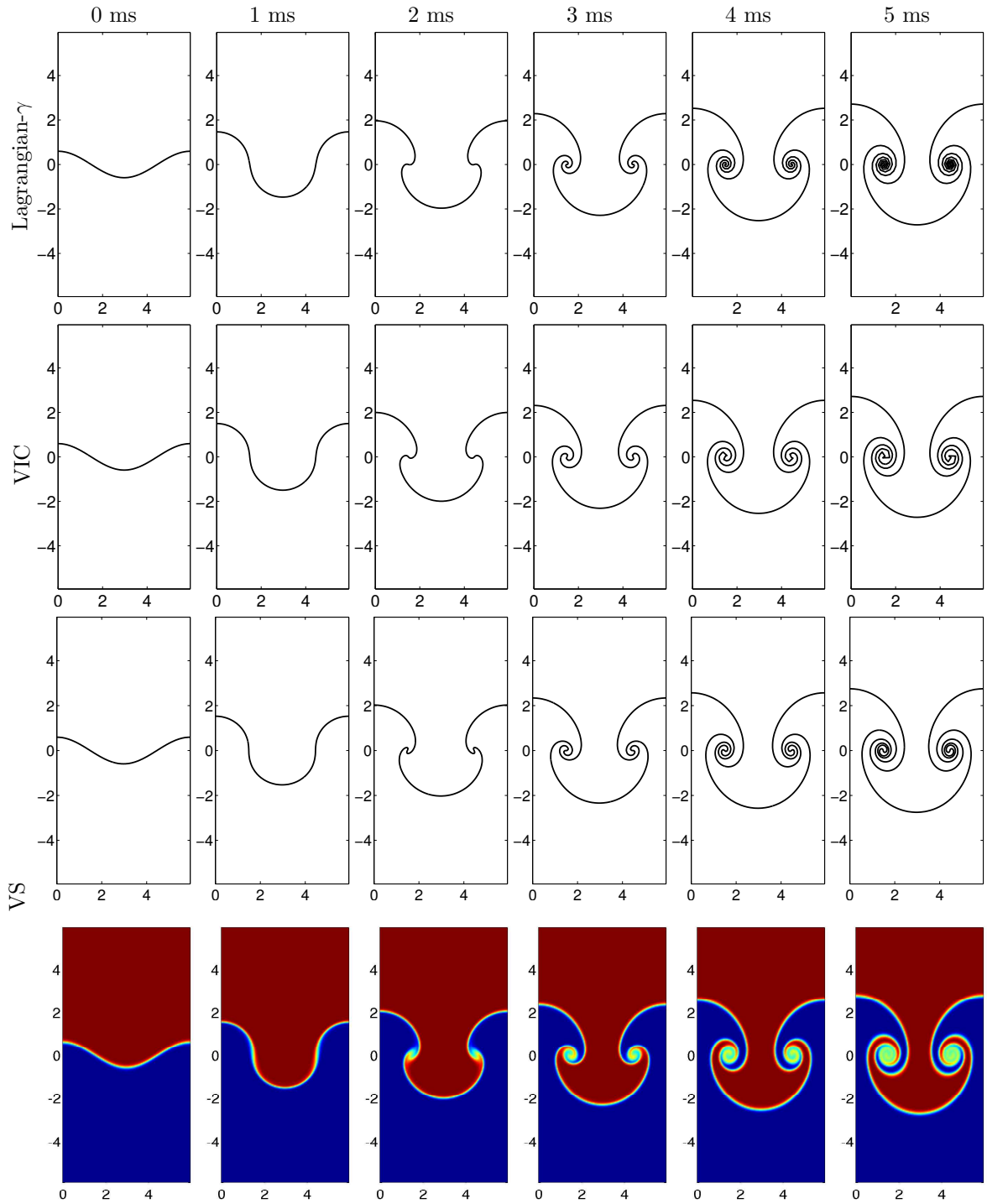


Figure 4.28. Time-evolution of the interface for the Richtmyer-Meshkov instability when $A = 0$ at 0, 1, 2, 3, 4, and 5 ms using the Lagrangian- γ method with $N = 256$ markers and $\delta = 0.15$, the VIC method with grid resolution $N_x \times N_y = 32 \times 128$ and $N = 256$ vortex markers, and of the mass fraction contour corresponding to $m_1 = 1/2$ from the VS method with grid resolution $N_x \times N_y = 128 \times 512$. Also shown is the evolution of the mass fraction field $m(x, y)$ from the VS method.

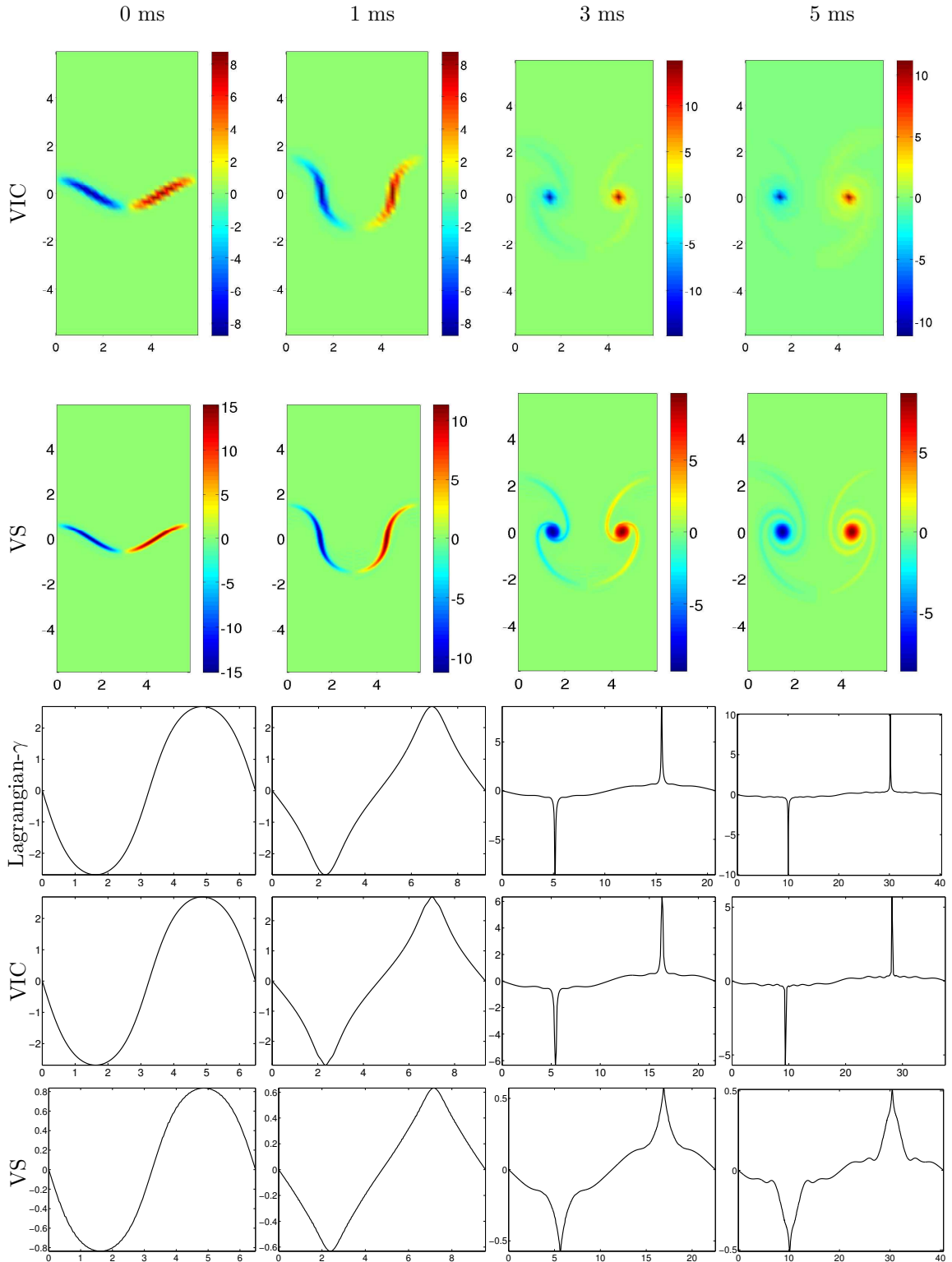


Figure 4.29. Time-evolution of the vorticity field $\omega(x,y)$ for the Richtmyer-Meshkov instability when $A = 0$ at 0, 1, 3, and 5 ms using the VS method and the VIC method with grid resolution $N_x \times N_y = 32 \times 128$ and $N = 256$ vortex markers and the VS method with a grid resolution $N_x \times N_y = 128 \times 512$ (top two rows). Also shown is the circulation on the interface $\gamma(e)$ at 0, 1, 3, and 5 ms for the VIC, VS, and Lagrangian- γ methods with $N = 256$ markers and $\delta = 0.15$ (bottom three rows).

is wider. The width in the VS simulation is due to the diffusion of the layer and the use of viscosity which tends to thicken the strong spiked cores. The circulation is plotted as a function of the arclength s , so that the length of the horizontal axis represents the length of the interface. At 5 ms, the Lagrangian- γ and VS simulations have similar lengths, while the VIC simulation has slightly smaller length. As the interface length is caused by the structure in the roll-up, this confirms that more structure is captured using the Lagrangian and VS methods and slightly less is captured using the VIC method.

Figure 4.30 shows a comparison of the instability evolution for $A = 0.4$ for the Lagrangian, VIC, and VS simulations at intervals of 1 ms until 5 ms. Shown for the VS simulation are the density field and the mass fraction contour. For $A > 0$, the baroclinic vorticity production term is activated and contributes to the vorticity evolution. In the Lagrangian and VIC methods, this effect is captured by the coupled system of integral equations describing the evolution of the circulation on the interface. When $A > 0$, a distinctive bubble rises in the heavier fluid and a spike penetrates into the lighter fluid. In addition, an asymmetry develops between the bubble and spike amplitude. The roll-ups of the VIC and VS simulations are nearly identical. The roll-up in the VS simulation exhibits more structure.

Figure 4.31 shows the time-evolution of the vorticity field $\omega(x, y)$ for the VS and VIC simulations and of the circulation on the interface for the three simulations for $A = 0.4$. Comparing these results with those for $A = 0$ (Fig. 4.29) shows that the cores during the roll-up phase at 3 and 5 ms are wider. This is evident from the smaller values in the vorticity field in the VIC simulation at 3 and 5 ms, which indicate that the vorticity is assigned to multiple cells. This phenomenon is also visible in the wider peaks in the circulation $\gamma(e)$ at 3 and 5 ms. The width of the peaks in the VS simulation is not affected, as this method has viscosity which spreads the cores. However, the results show more structure in the area surrounding the cores. This additional structure is also visible in the Lagrangian and VS simulations.

Figure 4.32 continues the comparison of the instability evolution across the methods for $A = 0.6$. Comparing the interface evolution with the results for $A = 0.4$ in Figure 4.30 shows that the stem of the instability becomes longer. In addition, the spike roll-up structure appears different across all simulations at 5 ms. Both the Lagrangian and VIC simulations show a lump structure at the tip of the roll-up region. The VIC simulation also shows a wider spike compared with the Lagrangian simulation and the region between the beginning of the roll-up and the lump structure is thinner. By contrast, the VS simulation does not show such a lump structure and the spike roll-up is longer in extent.

Figure 4.33 shows a comparison of the vorticity field evolution $\omega(x, y)$ for the VIC and VS simulations when $A = 0.6$. Comparing with the results for $A = 0.4$ in Figure 4.31 at 1 ms shows the formation of a vortex lump close to the spike, which accelerates the growth of the spike. A

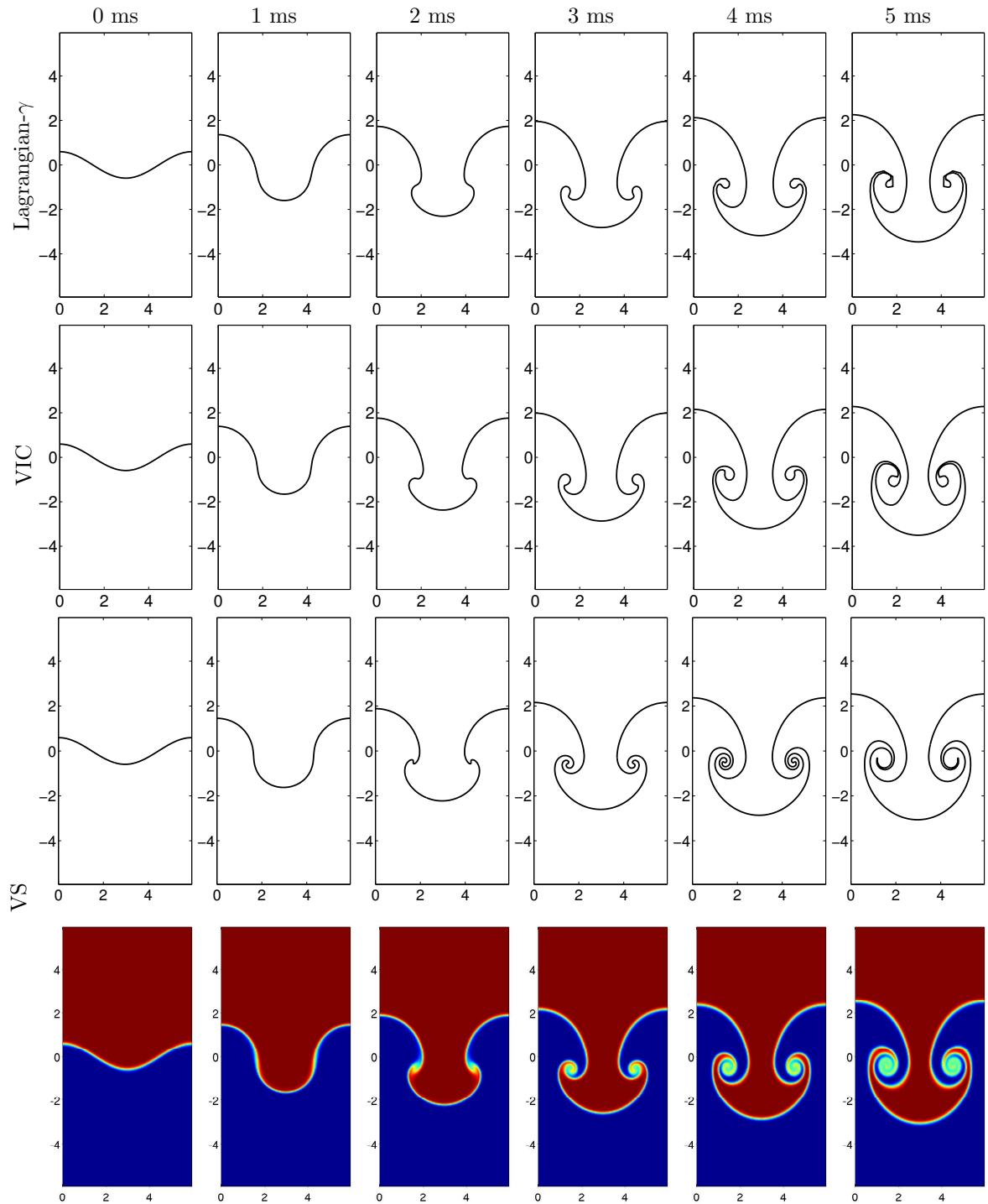
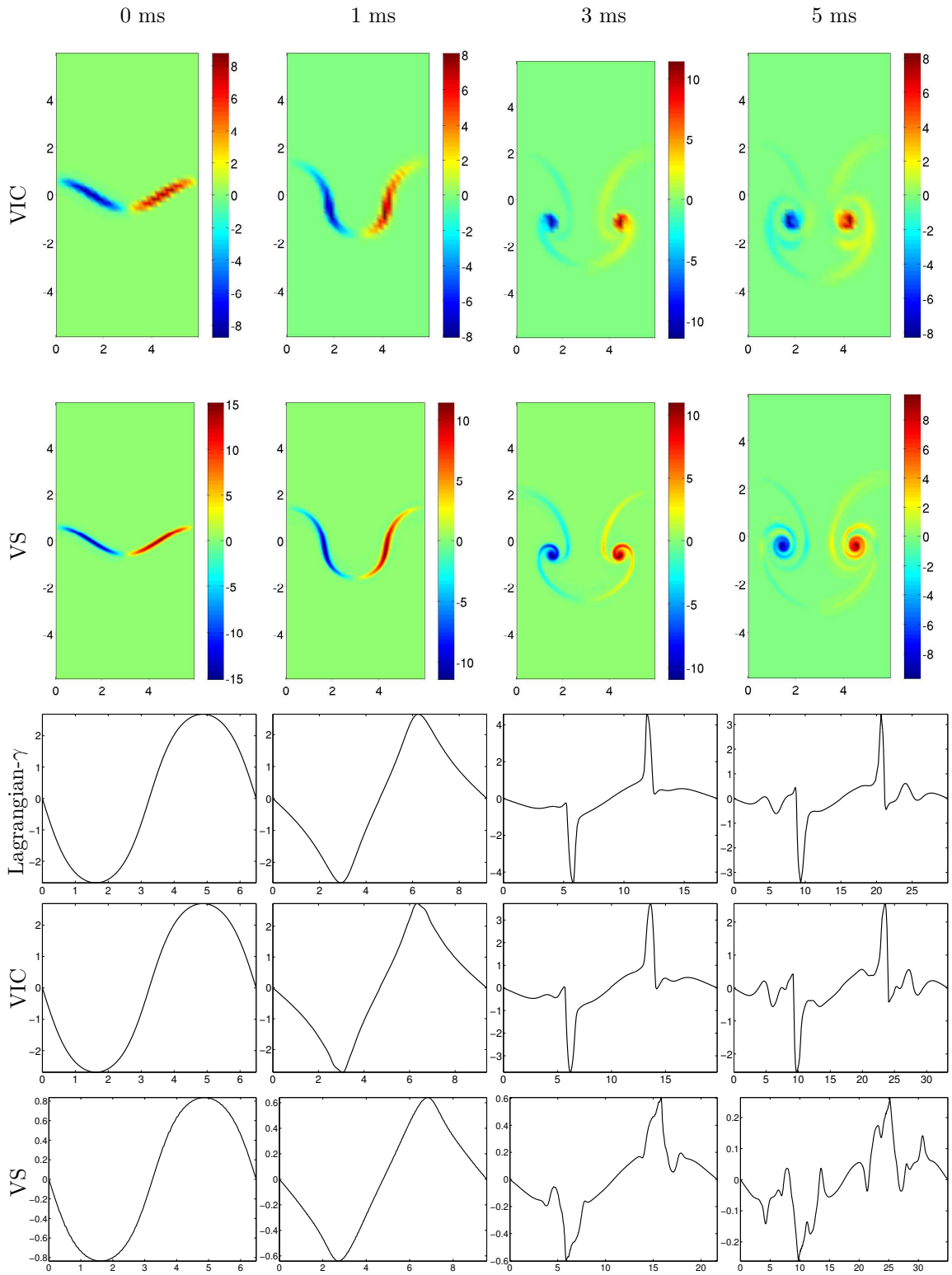
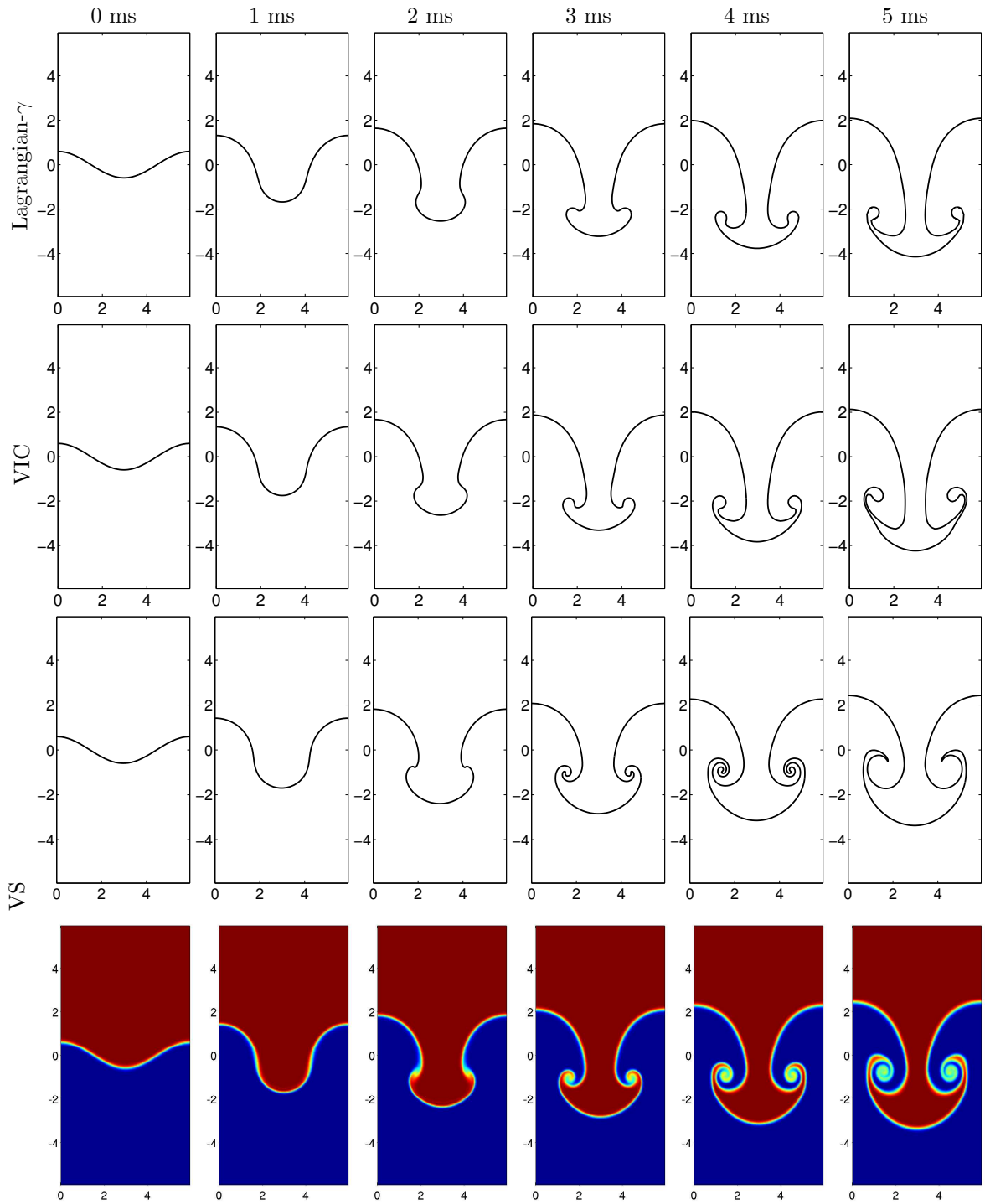
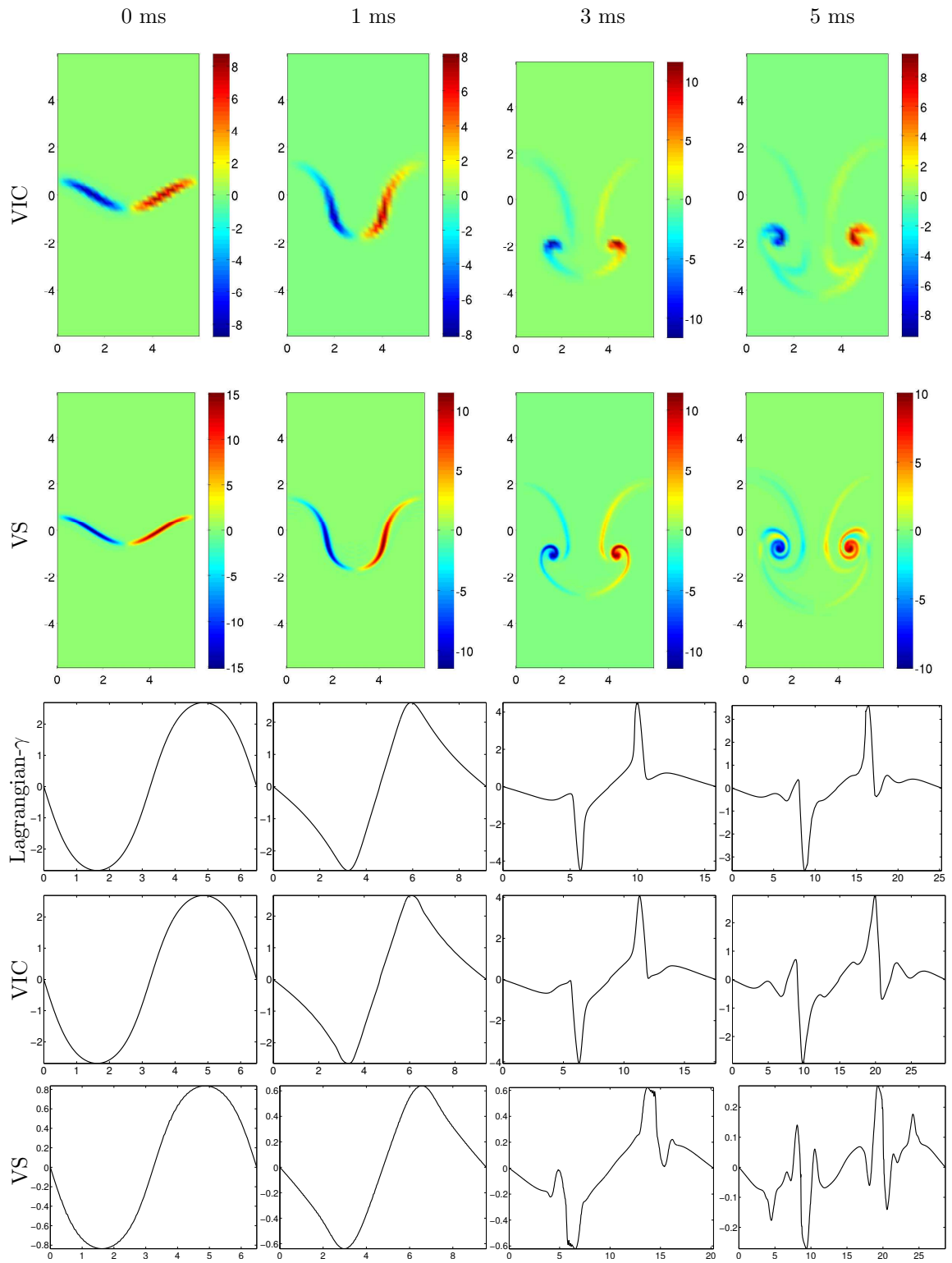


Figure 4.30. Same as Figure 4.28 but for $A = 0.4$.

Figure 4.31. Same as Figure 4.29 but for $A = 0.4$.

Figure 4.32. Same as Figure 4.28 but for $A = 0.6$.

Figure 4.33. Same as Figure 4.29 but for $A = 0.6$.

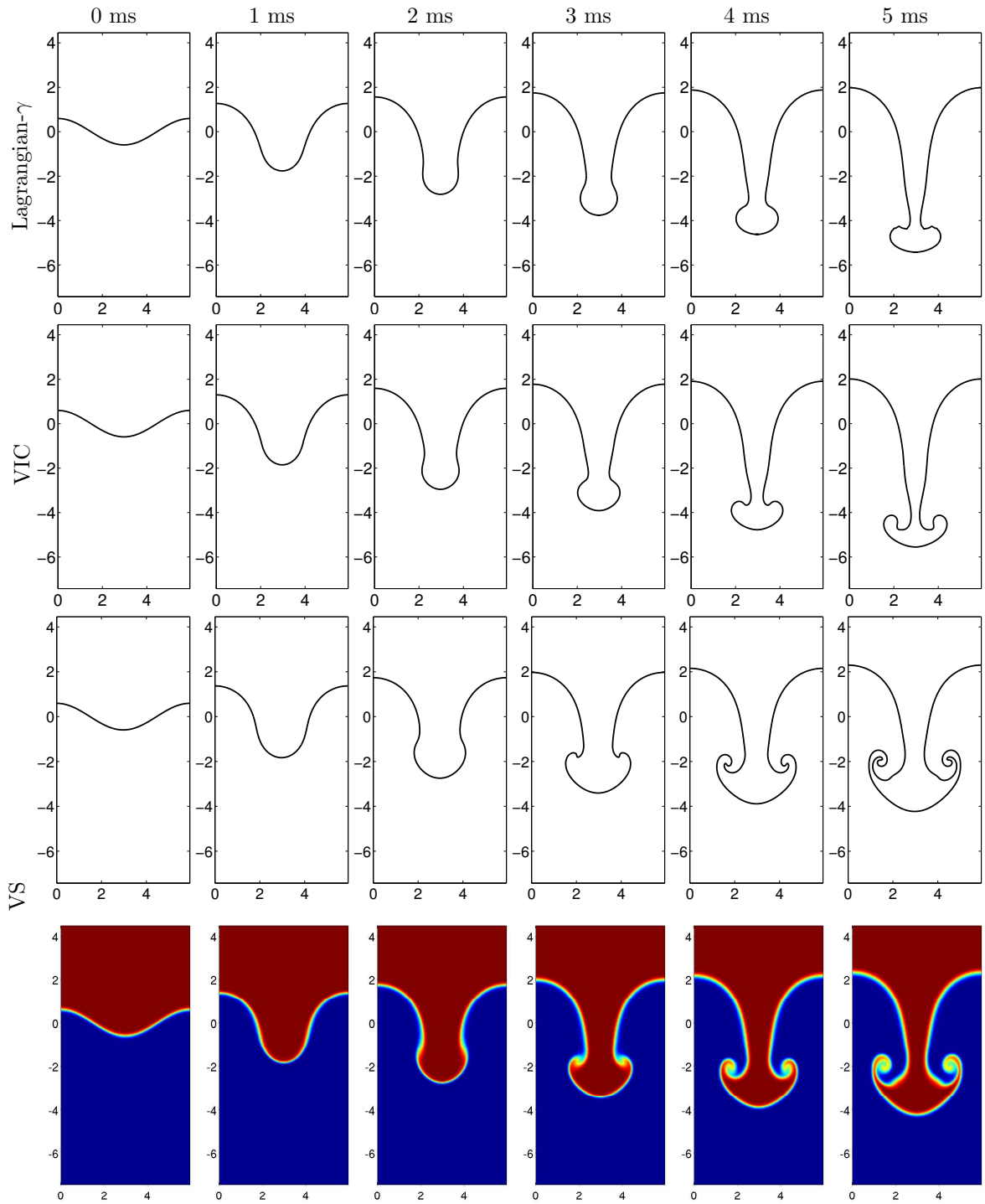
similar pattern is observed in the VS simulation. At 3 and 5 ms, the roll-up of the spike is marked by the formation of strong cores. The VS simulation shows a region of positive vorticity above the negative core and a region of negative vorticity above the positive core at 5 ms. This is the *vortex bilayer* [115] contributing to the formation of the secondary instability in the WENO simulations and in the experiments of Jacobs and Krivets [62]. Also shown in the figure is a comparison of the vortex sheet evolution $\gamma(e)$ across the simulations. The vortex sheet evolution shows the formation of the spikes and cores in the Lagrangian and VIC simulations. The circulation does not contain any spike or region of high frequency, as these occur in the inner core of the roll-up. However, under the Lagrangian and VIC simulations, the inner core is not resolved but represented by a lump. The VS simulation shows a similar representation for the vortex sheet evolution along the mass fraction contour.

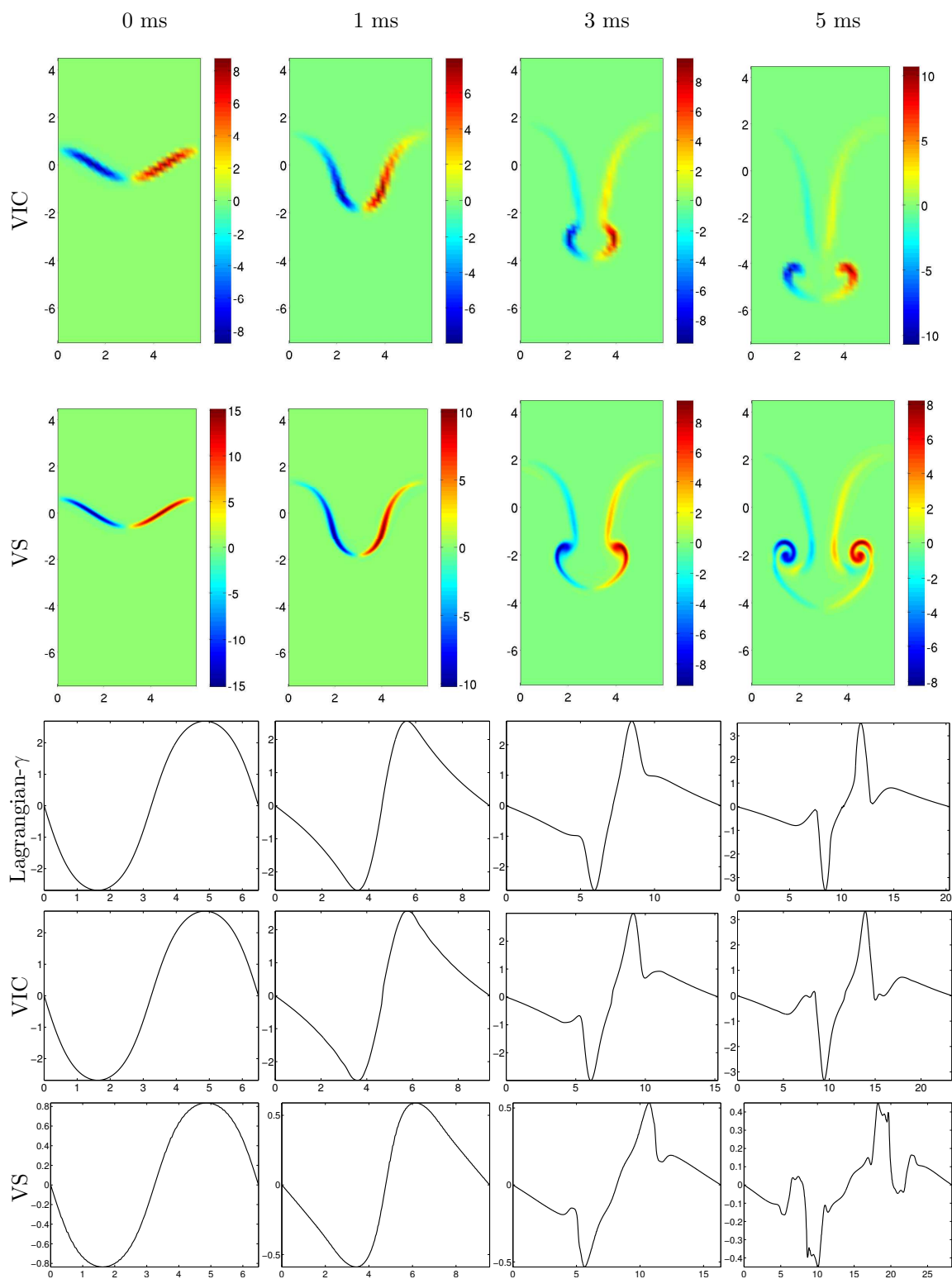
Figure 4.34 continues the comparison of the instability evolution for the three simulations when $A = 0.8$. As the Atwood number increases, the spike amplitude increases significantly. In addition, differences are observed in the roll-up structure between the simulations at 5 ms. The VIC simulation shows a more evolved roll-up compared with the Lagrangian simulation.

Figure 4.35 shows the vorticity field $\omega(x, y)$ for the VIC and VS simulations when $A = 0.8$. As the Atwood number increases, more vorticity accumulates close to the spike, contributing to its rapid growth. A similar trend was already visible for $A = 0.6$ in Figure 4.33. The vorticity then begins to form rotating cores at 3 ms and more developed cores at 5 ms. Also shown is a comparison of the vortex sheet strength $\gamma(e)$ for the three simulations, showing the formation of the roll-ups and then the formation of the rotating cores. The cores are not formed at 3 ms, so that the vorticity does not show sharp peaks, as for smaller values of the Atwood number.

Figure 4.36 shows the time-evolution of the instability when $A = 1$, which corresponds to a fluid falling into a vacuum. As a result, the instability is not expected to develop roll-up singularities. Shown are Lagrangian simulations obtained using the vortex sheet strength formulation (Lagrangian- γ) and the vortex dipole formulation (Lagrangian- μ). These formulations do not contain the blob regularizations of the $A < 1$ Lagrangian- γ simulations. Instead, principal value integrals are used to remove the singularity. The VIC simulation shows the formation of a lumped, droplet-like, flat spike front. This droplet was also observed in the simulation of the Richtmyer-Meshkov instability of Zufiria [159]. Zufiria [160] performed a linear instability analysis of the VIC algorithm and attributed the formation of this structure to the effects of an equivalent numerical surface tension.

Figure 4.37 shows the time-evolution of the vorticity field $\omega(x, y)$ for the VIC simulation when $A = 1$. The results indicate a concentration of the vorticity on the tip of the spike without the formation of roll-ups. Also shown is the vortex sheet strength $\gamma(e)$ on the interface for the Lagrangian- γ , Lagrangian- μ , and VIC simulations. The Lagrangian- γ and Lagrangian- μ circulations are in close agreement and exhibit the formation of a steep profile at 3 ms, due to the concentration of vorticity

Figure 4.34. Same as Figure 4.28 but for $A = 0.8$.

Figure 4.35. Same as Figure 4.29 but for $A = 0.8$.

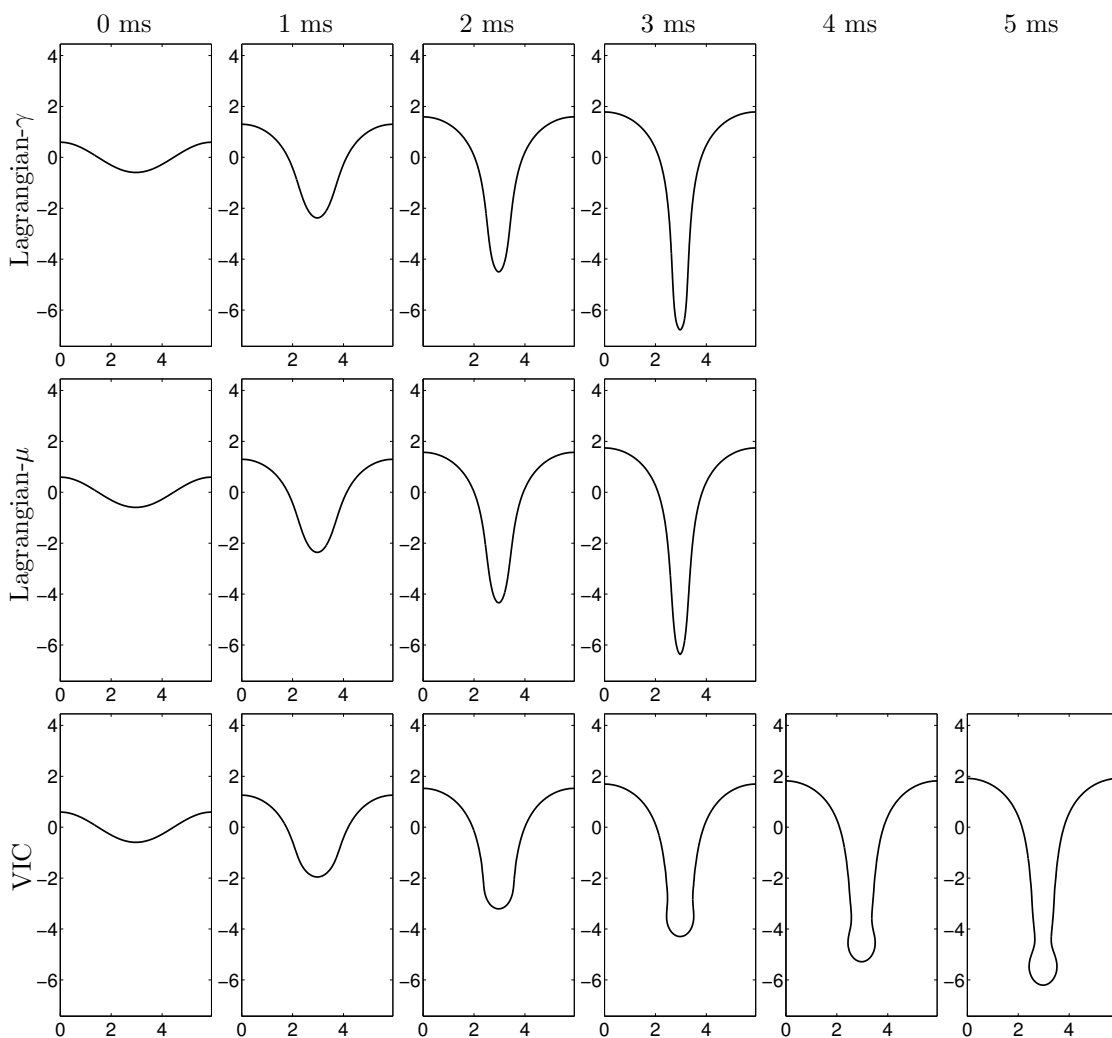


Figure 4.36. Time-evolution of the interface for the Richtmyer-Meshkov instability when $A = 1$ at 0, 1, 2, 3, 4, and 5 ms using the Lagrangian- γ and Lagrangian- μ methods with $N = 256$ markers (these simulations only converge for $t < 3.4$ ms, so that visualizations at late times are not shown), and the VIC method with grid resolution $N_x \times N_y = 32 \times 128$ and $N = 256$ vortex markers.

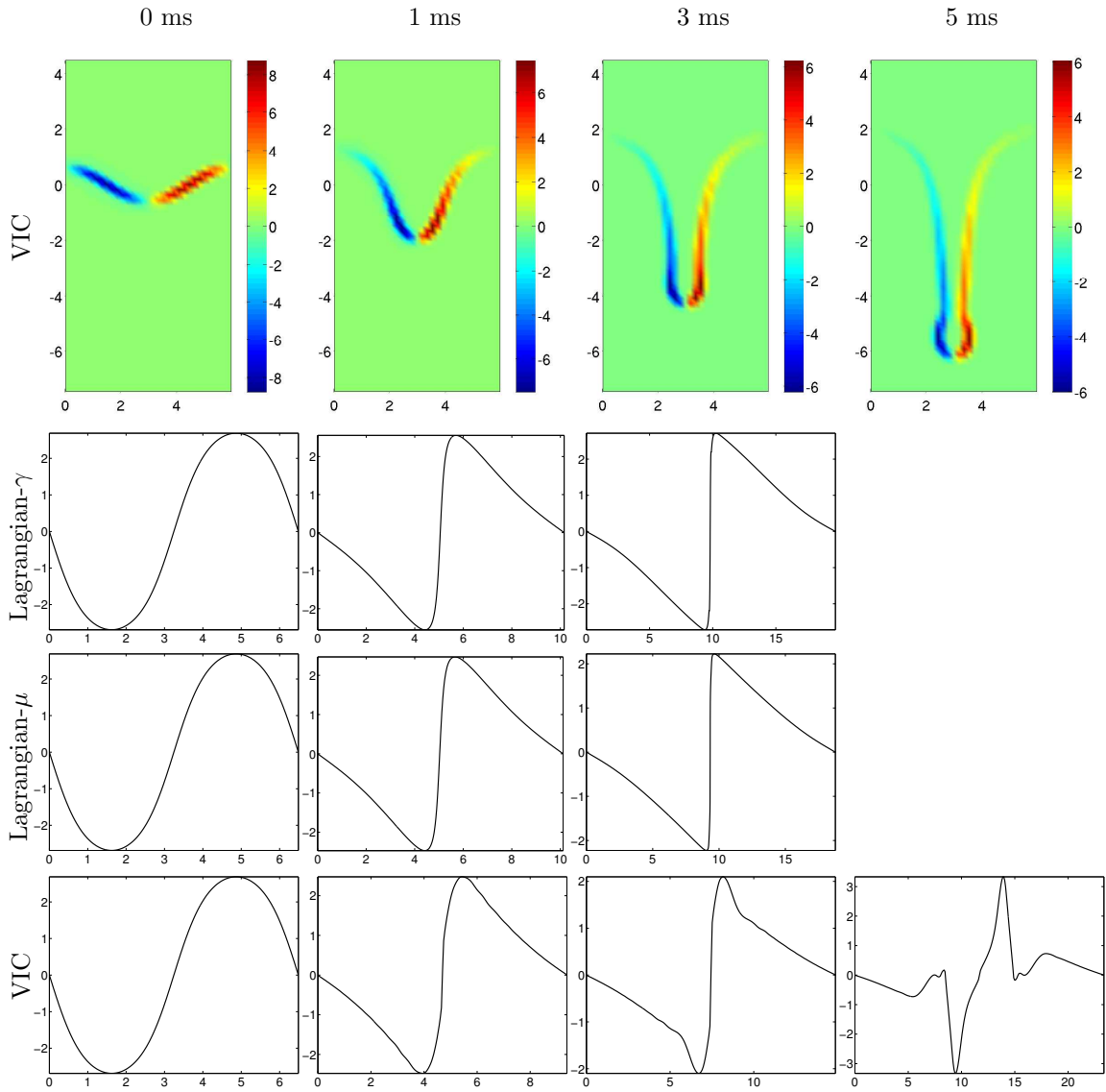


Figure 4.37. Time-evolution of the vorticity field $\omega(x, y)$ for the Richtmyer-Meshkov instability when $A = 1$ at 0, 1, 2, 3, 4, and 5 ms using the VIC method with grid resolution $N_x \times N_y = 32 \times 128$ and $N = 256$ vortex markers. Also shown is the circulation on the interface $\gamma(e)$ at 0, 1, 3, and 5 ms for the VIC, Lagrangian- γ , and Lagrangian- μ methods with $N = 256$ markers.

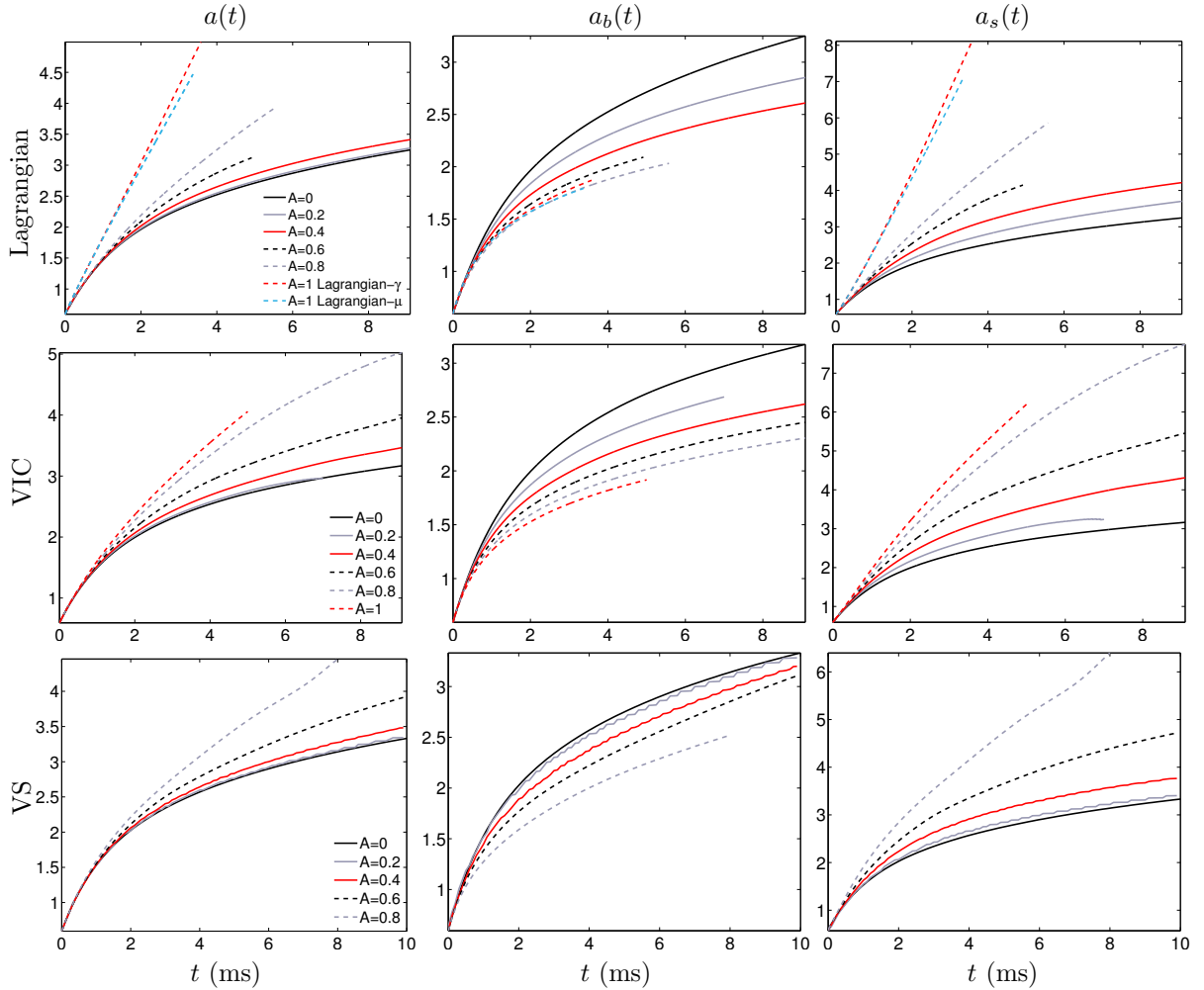


Figure 4.38. Comparison of the perturbation amplitude $a(t)$, bubble amplitude $a_b(t)$, and spike amplitude $a_s(t)$ for $A = 0, 0.2, 0.4, 0.6, 0.8,$ and 1 from the Lagrangian, VIC, and VS methods.

of opposite sign on the tip of the spike. By contrast, $\gamma(e)$ from the VIC simulation does not show the formation of a very steep profile at 3 ms, but shows a wider rounded tip. This is due to the formation of the droplet-like feature.

4.8.2 Comparison of the perturbation, bubble, and spike amplitudes to the predictions of amplitude growth models

Presented here is a quantitative comparison of the perturbation, bubble, and spike amplitudes from the Lagrangian, VIC, and VS simulations of the Richtmyer-Meshkov instability for $A = 0, 0.2, 0.4, 0.6, 0.8,$ and 1 with the predictions of amplitude growth models.

Shown in the first row of Figure 4.38 is a comparison of the perturbation amplitude $a(t)$, bubble amplitude $a_b(t)$, and spike amplitude $a_s(t)$ from the Lagrangian simulations for $A = 0, 0.2, 0.4, 0.6,$

0.8, and 1. For $A = 1$, both the Lagrangian simulations using the vortex sheet strength formulation (Lagrangian- γ) and the simulations using the vortex dipole formulation (Lagrangian- μ) are shown. As A increases, the perturbation amplitude increases. By contrast, the bubble amplitude decreases with increasing A . The spike amplitude increases as A increases. For $A = 1$, the spike amplitude increases very rapidly, corresponding to the case of a Richtmyer-Meshkov instability in a vacuum. The smaller amplitude for the bubble and the larger amplitude for the spike as a function of increasing Atwood number can be understood in terms of vorticity dynamics. In fact, as shown from the VS simulation, the baroclinic vorticity production reduces the vorticity of the bubble and increases the vorticity of the spike. As A increases, the simulations terminate at earlier times. In particular, the $A = 1$ simulations end at 3.6 ms.

Shown in the second row of the figure is the comparison of the amplitudes from the VIC simulations. The results are qualitatively similar to those from the Lagrangian simulations. For $A = 1$, the perturbation and spike amplitudes do not show the same growth as in the Lagrangian simulations. The smaller growth is due to the physical interpretation of the effects of the Cartesian grid in the VIC algorithm, which can be related to the effects of surface tension [160], thus reducing the growth of the instability.

Shown in the third row of the figure is the comparison of the perturbation, bubble, and spike amplitudes from the VS simulations. The results are qualitatively similar to the results from the VIC and Lagrangian simulations. For all Atwood numbers (except $A = 1$), the perturbation amplitude is computed to 10 ms and beyond, highlighting one of the key advantages of this formulation. Comparing the bubble and spike amplitude as a function of A shows that in the VS simulation the bubble has a larger growth and the spike has a smaller growth than the Lagrangian and VIC results. This is expected, as the VS simulation represents the evolution of a thickened vortex layer, while the Lagrangian and VIC simulations represent the evolution of a thin vortex sheet.

Figures 4.39 and 4.40 show a comparison of the perturbation amplitude from the Lagrangian, VIC, and VS simulations with the predictions of the nonlinear Zhang-Sohn Padé model [156] [Eq. (4.29)], the nonlinear Sadot et al. model [114] [Eqs. (4.30) and (4.31)] and the nonlinear Matsuoka et al. Padé model [91] [Eq. (4.32)]. The comparison of the results from the Lagrangian, VIC, and VS simulations provides an element of cross-validation. The three simulations are obtained using different numerical and modeling approaches to capture the effects of the instability, so that the general agreement of the simulations provides confidence in the results. Analyzing the differences between the simulation results is also essential to understand the robustness of the numerical methods or to evaluate the modeling assumptions underlying the simulations. Comparison of the simulation amplitudes with the predictions of the linear Richtmyer model and with the nonlinear series models provides understanding on the range of validity of these models. Vortex methods can reach nonlinear stages of the instability development not accessible via analytical models. For $A = 0$

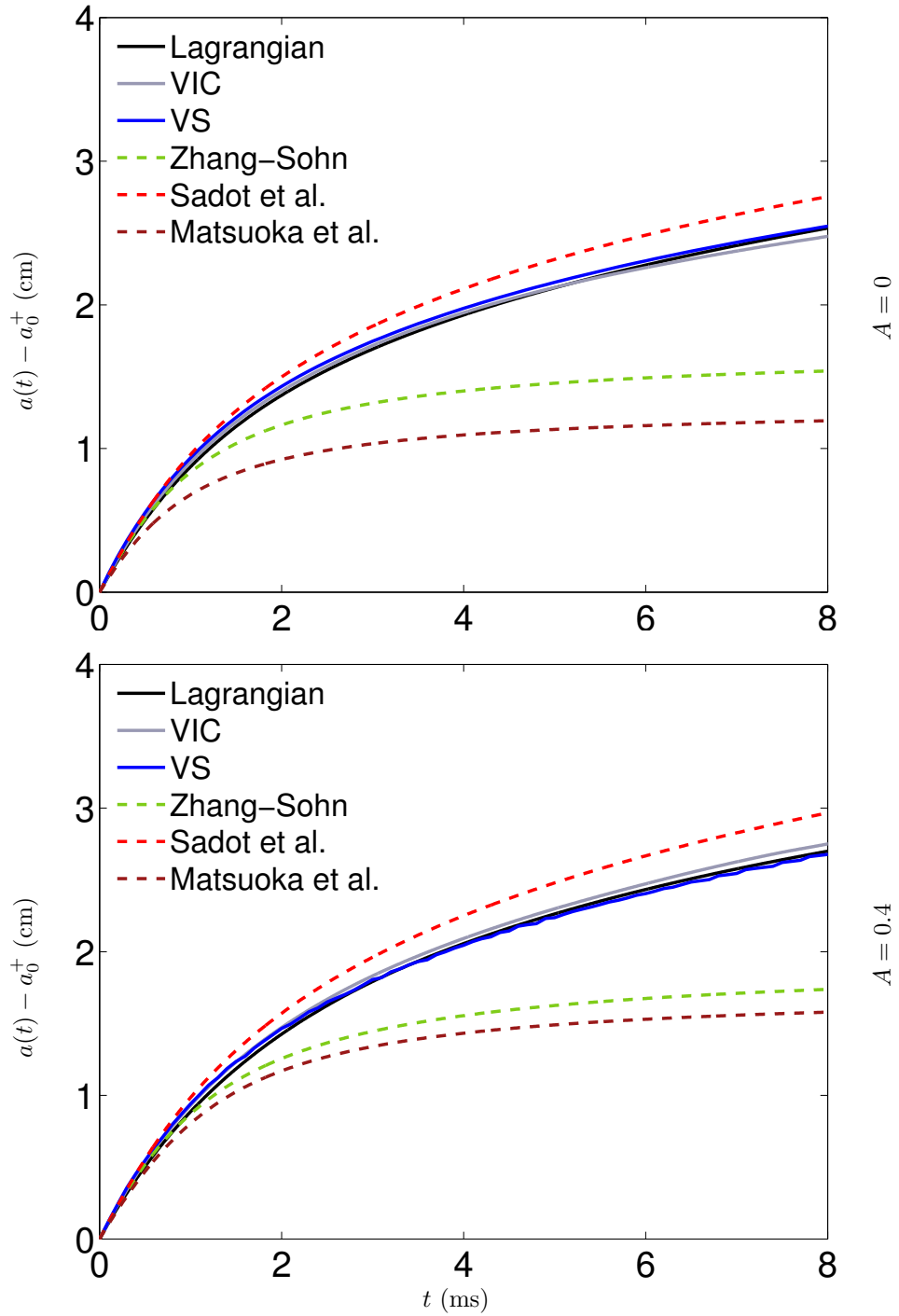


Figure 4.39. The perturbation amplitude $a(t) - a_0^+$ from the Lagrangian- γ , VIC, and VS simulations with the predictions of the nonlinear models for $A = 0$ and 0.4.

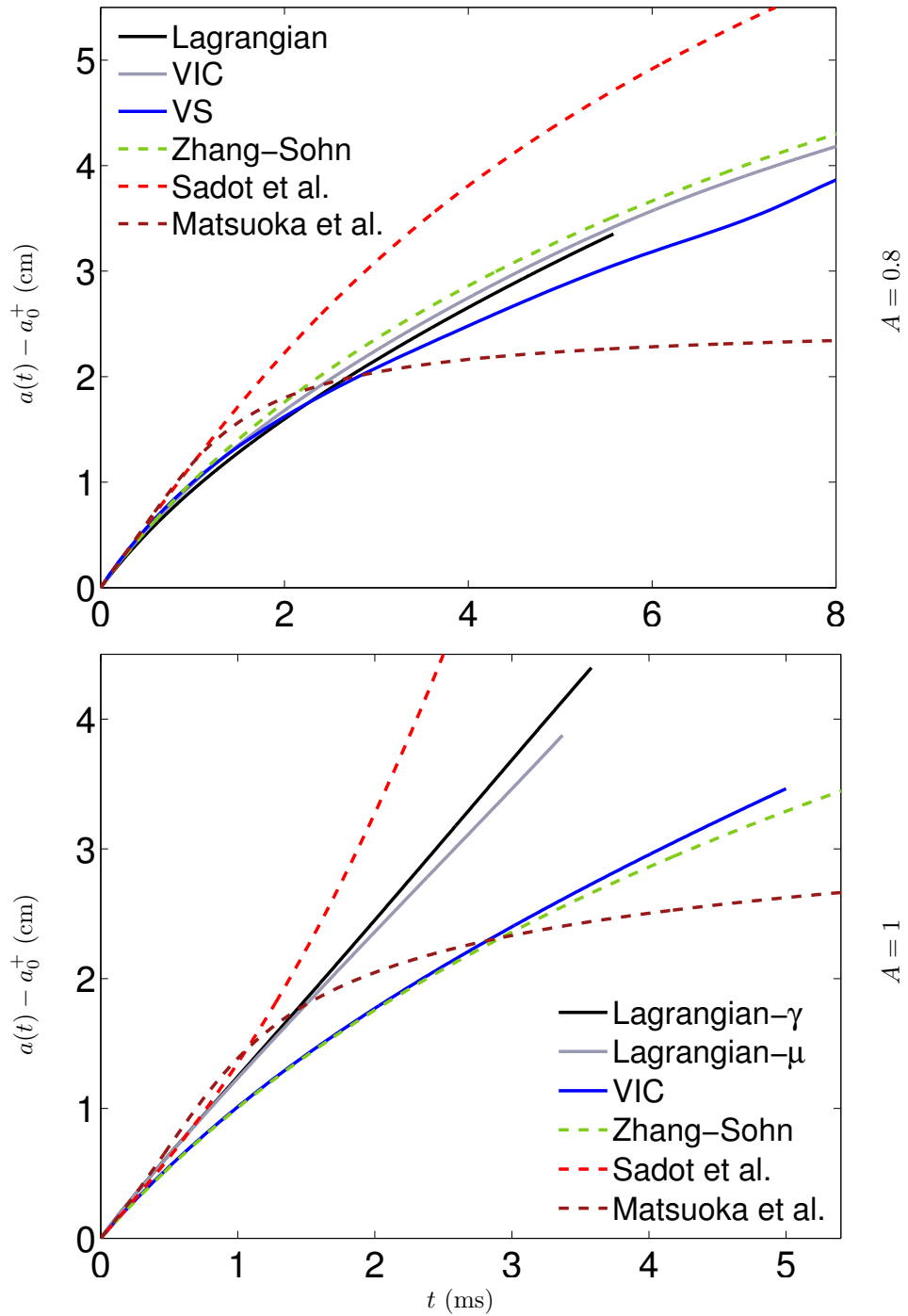


Figure 4.40. Same as Figure 4.39 but with $A = 0.8$ and 1.

all three simulation amplitudes are in very close agreement. The comparison of the amplitudes to the prediction of the nonlinear models extended via Padé approximants or to semi-analytical models assesses the robustness and predictive capability of the models as a function of the Atwood number. The results for $A = 0$ in Figure 4.39 show that the Sadot et al. model slightly overpredicts the simulation amplitudes but is in best overall agreement. By contrast, the Zhang-Sohn and Matsuoka et al. models underpredict the perturbation amplitude from the simulations. The simulation amplitudes for $A = 0.4$ also show excellent agreement. The amplitudes for $A = 0.4$ show a similar behavior, with the Sadot et al. model overpredicting the simulation amplitudes. The Matsuoka et al. model is closer to the prediction of the Zhang-Sohn model, but both models underpredict the simulation amplitudes. For $A = 0.8$ in Figure 4.40, the simulation amplitudes begin to show differences. The VIC simulation gives the largest amplitude followed by the Lagrangian and VS simulations. The Lagrangian and VIC amplitudes are in close agreement until ≈ 5 ms when the Lagrangian amplitudes are no longer available. The VS amplitudes underpredict the VIC amplitudes at late times. The Sadot et al. model overpredicts, while the Matsuoka et al. and Zhang-Sohn models underpredict. The Lagrangian- γ and VIC simulation amplitudes for $A = 1$ are in good agreement, while the VIC amplitude underpredicts. The Zhang-Sohn model is in good agreement with the VIC amplitude, while the Sadot et al. and Matsuoka et al. models are in agreement with the Lagrangian simulations at early times, and over-predict later.

Figures 4.41 and 4.43 compare the bubble amplitude from the three simulations with the predictions of the Zhang-Sohn model [156] [Eq. (4.33)], the Sadot et al model [114] [Eq. (4.30)], the Matsuoka et al. model [Eq. (4.32)], and the Mikaelian model [Eq. (4.34)]. Shown in Figures 4.42 and 4.44 is the bubble amplitude growth from the simulations together with the corresponding model predictions. In addition, the asymptotic bubble velocities from the Sohn-Layzer model [Eq. (4.35)], the Goncharov model [Eq. (4.36)], and the Sohn-Zufiria model [Eq. (4.37)] are also shown. The amplitudes for $A = 0$ indicate good agreement between the bubble amplitudes from the three simulations. The Sadot et al. and Mikaelian models are in best agreement with the amplitude, with the first slightly overpredicting, and the second slightly underpredicting. As in the case of the perturbation amplitude in Figure 4.39, the Matsuoka et al. and Zhang-Sohn models underpredict the simulation amplitudes. The growth in Figure 4.42 shows that all three simulations give similar predictions for the growth at all times. The Sadot et al. model shows the best agreement at all times, while the Mikaelian model slightly underpredicts at early times. The potential models are all in excellent agreement with the asymptotic bubble velocity. The Matsuoka et al. and Zhang-Sohn models underpredict the asymptotic growth. For $A = 0.4$, the VS simulation gives a larger bubble amplitude compared with the bubble amplitude from the Lagrangian and VIC simulations. The Sadot et al. model is in excellent agreement with the amplitude and the Mikaelian model is also very close. The Matsuoka et al. and Zhang-Sohn models underpredict the simulation results. The

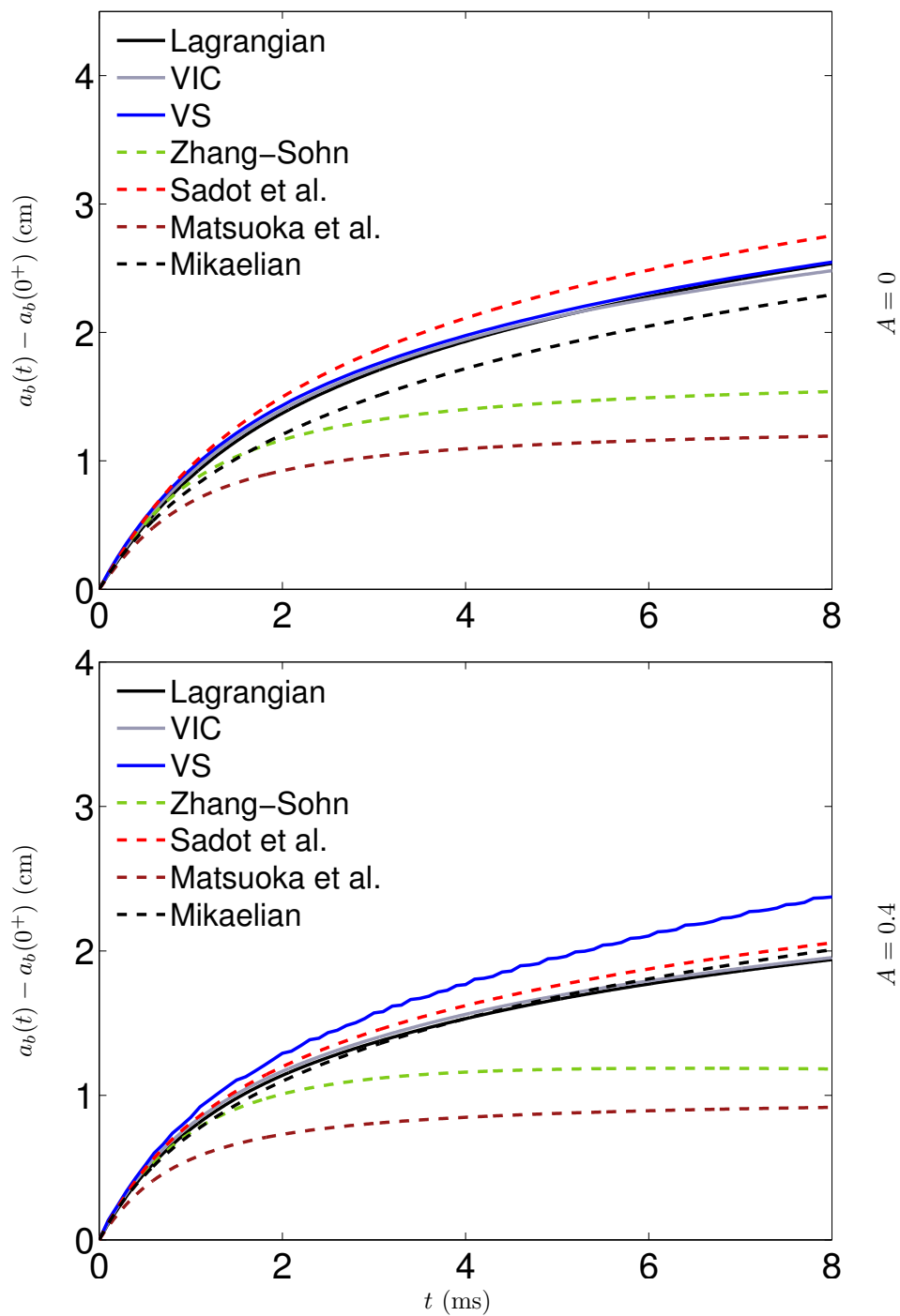


Figure 4.41. The bubble amplitude $a_b(t) - a_b(0^+)$ from the Lagrangian- γ , VIC, and VS simulations with the predictions of the nonlinear models for $A = 0$ and 0.4.

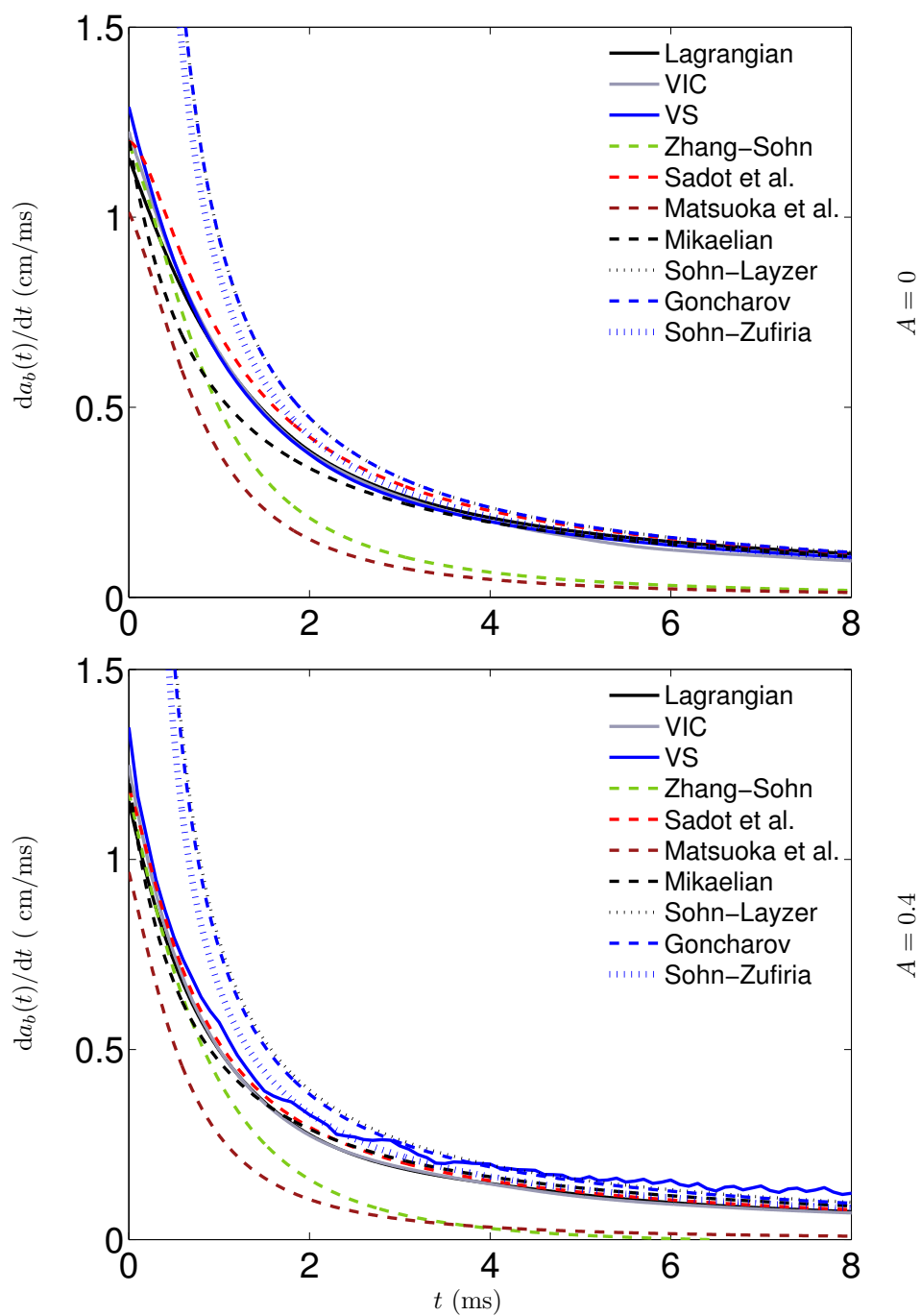


Figure 4.42. The bubble growth $da_b(t)/dt$ from the Lagrangian- γ , VIC, and VS simulations with the predictions of the nonlinear models for $A = 0$ and 0.4.

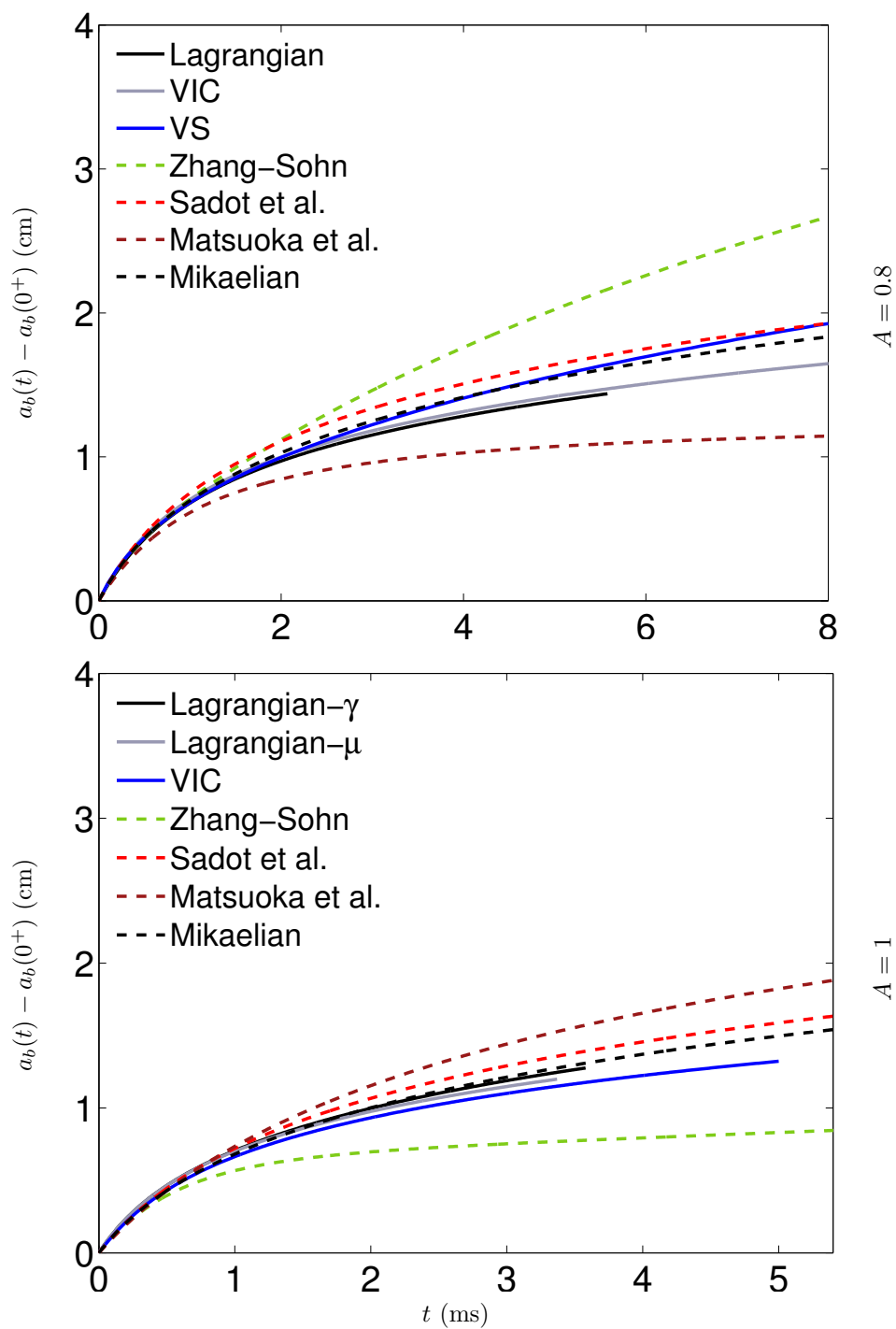


Figure 4.43. Same as Figure 4.41 but for $A = 0.8$ and 1.

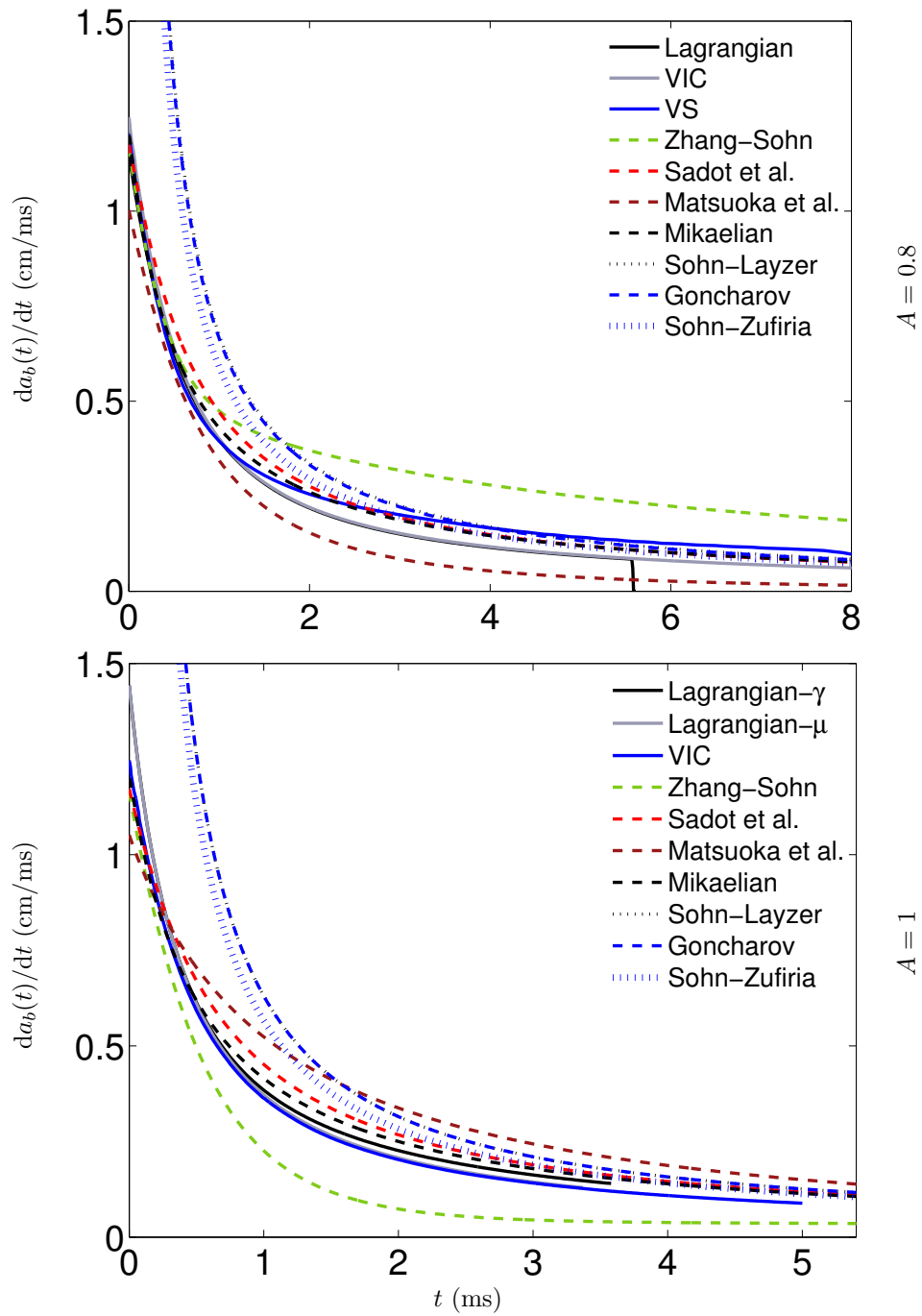


Figure 4.44. Same as Figure 4.42 but for $A = 0.8$ and 1.

asymptotic bubble velocities from the simulations show excellent agreement. The Sadot et al. and Mikaelian models now capture the bubble velocity at all times. The asymptotic bubble velocity is also captured by the potential models. The Matsuoka et al. and Zhang-Sohn models underpredict the simulation results. The amplitudes for $A = 0.8$ show that the Lagrangian and VIC amplitudes are in good agreement up to ≈ 5 ms when only the VIC results are available. The VS simulation gives bubble amplitudes larger than the Lagrangian and VIC amplitudes at late-to-intermediate times. However, the VS simulation is now in good agreement with the predictions of the Mikaelian and Sadot et al. models. The Zhang-Sohn model overpredicts the simulation amplitudes, while the Matsuoka et al. model underpredicts the amplitudes. The bubble velocity shows that the predictions of the nonlinear Sadot et al. and Mikaelian models and the potential models fall between the VIC and VS bubble velocities. The amplitudes for $A = 1$ show that the Lagrangian- γ and Lagrangian- μ bubble amplitudes are close and slightly larger than the bubble amplitude from the VIC simulation. The Mikaelian model is in best agreement with the Lagrangian amplitude.

Figures 4.45 and 4.46 show the spike amplitudes from the three simulations with the predictions of the Zhang-Sohn model [Eq. (4.38)], the Sadot et al. model [Eq. (4.31)], and the Matsuoka et al. model [Eq. (4.32)]. For $A = 0$ in Figure 4.45, the three simulations give similar spike amplitudes. The Sadot et al. model is in best agreement with the simulation data, while the Zhang-Sohn and Matsuoka et al. models underpredict. The spike velocities from the simulations are also in excellent agreement and are best predicted by the Sadot et al. model. For $A = 0.4$, the spike amplitude from the Lagrangian and VIC simulations are in excellent agreement. The VS spike amplitude is slightly lower. The spike amplitudes from the VIC and Lagrangian simulations are in excellent agreement with the predictions of the Sadot et al. model. The Matsuoka et al. and Zhang-Sohn models underpredict the simulation results. The spike amplitude for $A = 0.8$ in Figure 4.46 shows that the VS simulation gives spike amplitudes that are larger than the VIC amplitudes. The Zhang-Sohn model is in best agreement with the simulation amplitudes, while the Sadot et al. model overpredicts and the Matsuoka et al. model underpredicts the amplitudes. The spike amplitude for $A = 1$ shows that the Lagrangian- γ simulation has the largest value followed closely by the Lagrangian- μ simulation, and are in best agreement at early times with the Sadot et al. and Matsuoka et al. models. The amplitude from the VIC simulation is smaller and in best agreement with the Zhang-Sohn model. The comparison between the amplitudes from the three simulations and the predictions of the models can be made more quantitative by computing the average fractional deviations Δ_{sim} [Eq. (4.40)]. The results for $A = 0, 0.2, \text{ and } 0.4$ and for $0.6, 0.8, \text{ and } 1$ are shown in Tables 4.15 and 4.16, respectively.

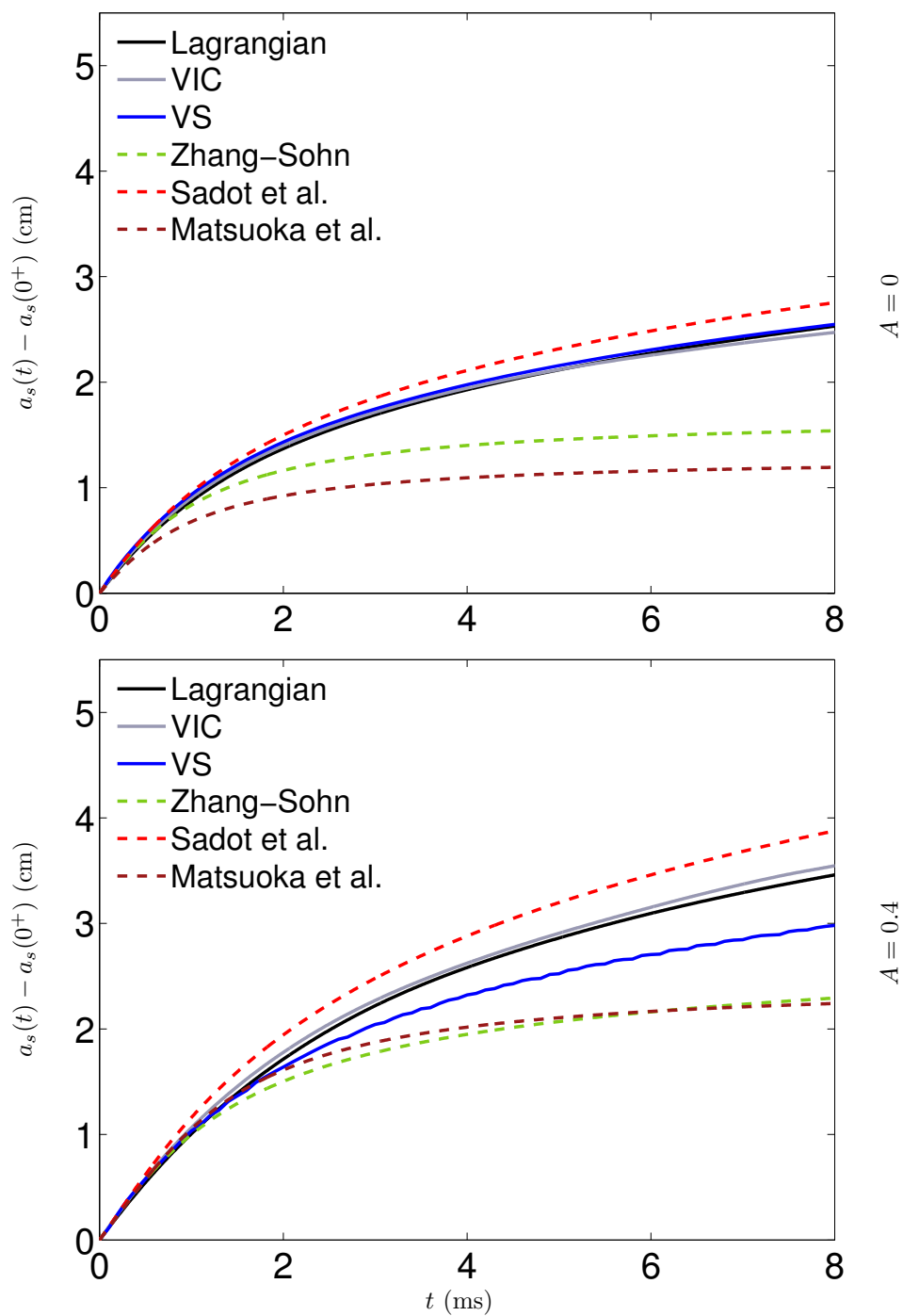


Figure 4.45. The spike amplitude $a_s(t) - a_s(0^+)$ from the Lagrangian- γ , VIC, and VS simulations with the predictions of the nonlinear models for $A = 0$ and 0.4.

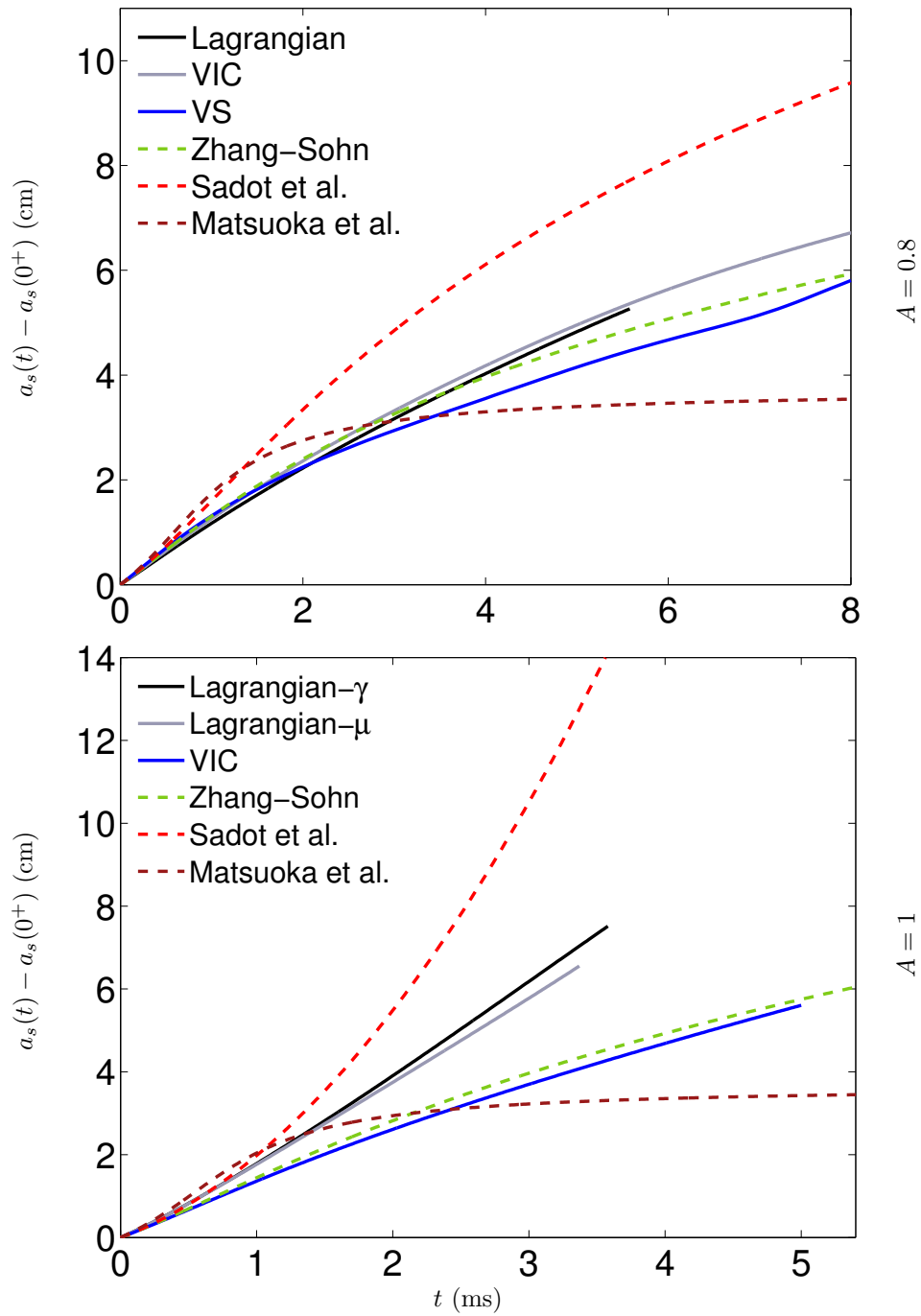


Figure 4.46. Same as Figure 4.45 but with $A = 0.8$ and 1.

	Lagrangian- γ	VIC	VS
$A = 0$			
	Δ_{sim}	Δ_{sim}	Δ_{sim}
Zhang-Sohn Padé (all)	12.89	15.09	16.95
Zhang-Sohn Padé (bubble)	12.92	15.12	16.94
Zhang-Sohn Padé (spike)	12.86	15.06	16.96
Matsuoka et al. Padé (all)	38.81	42.6	42.16
Matsuoka et al. Padé (bubble)	31.40	34.99	35.38
Matsuoka et al. Padé (spike)	31.31	34.92	35.40
Sadot et al. (all)	8.30	5.64	3.94
Sadot et al. (bubble)	8.27	5.62	3.95
Sadot et al. (spike)	8.32	5.66	3.94
Mikaelian (bubble)	11.05	14.07	15.83
$A = 0.2$			
	Δ_{sim}	Δ_{sim}	Δ_{sim}
Zhang-Sohn Padé (all)	12.28	15.31	16.66
Zhang-Sohn Padé (bubble)	12.07	15.13	19.27
Zhang-Sohn Padé (spike)	12.51	15.43	14.83
Matsuoka et al. Padé (all)	32.9	37.62	36.75
Matsuoka et al. Padé (bubble)	39.4	44.02	46.56
Matsuoka et al. Padé (spike)	16.25	20.7	19.21
Sadot et al. (all)	3.64	0.8	1.52
Sadot et al. (bubble)	2.05	1.48	5.48
Sadot et al. (spike)	5.06	1.39	3.08
Mikaelian (bubble)	7.2	10.7	14.41
$A = 0.4$			
	Δ_{sim}	Δ_{sim}	Δ_{sim}
Zhang-Sohn Padé (all)	10.09	13.09	12.25
Zhang-Sohn Padé (bubble)	9.45	12.53	19.16
Zhang-Sohn Padé (spike)	10.7	13.4	7.66
Matsuoka et al. Padé (all)	17.64	22.3	19.58
Matsuoka et al. Padé (bubble)	38.18	42.61	48.62
Matsuoka et al. Padé (spike)	6.91	5.34	3.87
Sadot et al. (all)	8.92	5.32	5.68
Sadot et al. (bubble)	5.1	2.20	4.17
Sadot et al. (spike)	11.48	7.44	11.95
Mikaelian (bubble)	3.32	6.59	12.74

Table 4.15. Average fractional deviations Δ_{sim} between the simulation amplitudes from the Lagrangian- γ , VIC, and VS methods $a_{\text{sim}}(t)$ and the amplitudes from the nonlinear models $a_{\text{mod}}(t)$ for $A = 0, 0.2$, and 0.4 .

	Lagrangian- γ	VIC	VS
$A = 0.6$			
	Δ_{sim}	Δ_{sim}	Δ_{sim}
Zhang-Sohn Padé (all)	5.61	7.79	5.44
Zhang-Sohn Padé (bubble)	3.33	6.25	12.54
Zhang-Sohn Padé (spike)	7.1	8.47	1.89
Matsuoka et al. Padé (all)	5.26	5.73	3.54
Matsuoka et al. Padé (bubble)	27.23	31.38	37.16
Matsuoka et al. Padé (spike)	17.31	12.79	17.59
Sadot et al. (all)	14.87	10.93	12.42
Sadot et al. (bubble)	7.84	5.05	1.11
Sadot et al. (spike)	18.55	14.04	19.03
Mikaelian (bubble)	1.46	3	8.93
$A = 0.8$			
	Δ_{sim}	Δ_{sim}	Δ_{sim}
Zhang-Sohn Padé (all)	7.86	3.37	6.02
Zhang-Sohn Padé (bubble)	9.49	8.42	8.6
Zhang-Sohn Padé (spike)	7.44	2.01	5.22
Matsuoka et al. Padé (all)	12.1	9.05	9.13
Matsuoka et al. Padé (bubble)	7.58	11.27	7.42
Matsuoka et al. Padé (spike)	24.35	19.57	20.19
Sadot et al. (all)	22.96	18.76	20.36
Sadot et al. (bubble)	10.25	7.48	8.91
Sadot et al. (spike)	27.82	23.07	24.16
Mikaelian (bubble)	4.31	2.9	2.90
$A = 1$			
	Δ_{sim}	Δ_{sim}	Δ_{sim}
Zhang-Sohn Padé (all)	33.31	29.53	1.1
Zhang-Sohn Padé (bubble)	34.87	32.62	25.88
Zhang-Sohn Padé (spike)	32.96	28.82	5.75
Matsuoka et al. Padé (all)	19.52	16.7	14.98
Matsuoka et al. Padé (bubble)	14.67	15.91	18
Matsuoka et al. Padé (spike)	28.89	25.52	21.63
Sadot et al. (all)	19.02	20.87	34.46
Sadot et al. (bubble)	6.08	7.47	9.62
Sadot et al. (spike)	21.42	23.36	40.02
Mikaelian (bubble)	3.55	4.57	5.08

Table 4.16. Same as Table 4.15 but for $A = 0.6$ and 0.8 . For $A = 1$ the average fractional deviation from the Lagrangian- γ , Lagrangian- μ , and VIC methods is shown.

Chapter 5

Investigation of the Three-Dimensional Single-Mode Richtmyer-Meshkov Instability

Presented here are three-dimensional simulations and analysis of the single-mode Richtmyer-Meshkov instability performed using the weighted essentially non-oscillatory (WENO) shock-capturing method and the vorticity-streamfunction (VS) method. The simulations are performed using the mix initial conditions with an initial perturbation [Eq. (1.20)] that constitutes the generalization in three dimensions of the two-dimensional perturbation [Eq. (1.1)]. The goal is to investigate the three-dimensional dynamics of the instability evolution, including the bubble and spike dynamics, and to compare the amplitudes to the predictions of the three-dimensional single-mode Zhang-Sohn model [157]. An analysis of the reshock dynamics is also performed using the WENO method. The VS simulations use the same initial conditions as the WENO simulations and are performed to evaluate how well the methods agree. An Atwood number study is also performed using the VS method to investigate the effects of this parameter on the instability evolution.

This chapter is organized as follows. Initial conditions for the WENO and VS methods are presented in Section 5.1. The dynamics of the instability evolution, including a comparison of the mass fraction and enstrophy isosurfaces is shown in Section 5.2. A comparison of the perturbation, bubble, and spike amplitudes for the WENO and VS methods with the predictions of amplitude growth models is shown in Section 5.3. An investigation of reshock in three dimensions using the WENO method is presented in Section 5.4. Finally, the results of an Atwood number study using the VS method are presented in Section 5.5.

5.1 Initial and boundary conditions

The initial and boundary conditions used for the simulations of the three-dimensional single-mode Richtmyer-Meshkov instability are discussed here. A generalization of the single-mode initial con-

dition is used in three dimensions. Two initial amplitudes are selected: an amplitude matching the two-dimensional value ($a_0^- = 0.29$ cm), and a reduced amplitude ($a_0^- = 0.205$ cm) such that the three-dimensional growth rate matches the two-dimensional value. The vorticity deposited on the interface by the shock is compared to the predictions from linear theory (Sec. 5.1.2). The linear theory is used to initialize the VS method in three dimensions (Sec. 5.1.3).

5.1.1 Initial conditions for the WENO method

The initial and boundary conditions for the simulations here are similar to those used for the two-dimensional simulations in Table 4.4, with the values for the periodic z direction the same as those for the periodic y direction: $L_z = L_y$, $h_z = h_y$, and $N_z = N_y$. The initial perturbation is given by Equation (1.20) and is the standard initial condition for single-mode Richtmyer-Meshkov instability in three dimensions. It was previously used in the quantitative study of three-dimensional Richtmyer-Meshkov instability by Zhang and Sohn [157] and in a comparison between two- and three-dimensional simulations by Li and Zhang [84].

As $k_y = k_x = k_{2D}$, the effective wavenumber for the three-dimensional perturbation is

$$k_{3D} = \sqrt{k_x^2 + k_y^2} \quad (5.1)$$

so that $k_{3D} = \sqrt{2} k_{2D}$. As a result, two values for the initial pre-shock amplitude a_0^- are considered:

1. $a_0^- = 0.205$ cm, where the pre-shock amplitude is reduced by $\sqrt{2}$ so that the corresponding initial growth v_0 [Eq. (1.16)] is the same as in the two dimensional simulations (Chapter 4), and;
2. $a_0^- = 0.29$ cm, where the pre-shock amplitude is the same as in the two-dimensional simulations. The corresponding v_0 is $\sqrt{2}$ larger than in the two-dimensional simulations.

A summary of these initial conditions, including a comparison to the two-dimensional (mix) initial conditions is presented in Table 5.1. The simulations were performed using the ninth-order WENO with a resolution of 128 points per initial perturbation wavelength. Symmetry boundary conditions were used in the transverse directions.

Figure 5.1 shows a comparison of the $x-t$ diagram for the three-dimensional simulations with $a_0^- = 0.205$ and 0.29 cm, including the bubble and spike position, unperturbed interface position, and the shock position. Prior to reshock, the spike position from the simulation with $a_0^- = 0.29$ cm is slightly behind that of the simulation with $a_0^- = 0.205$. The bubble positions are the same. The location of the shock and the time of reshock are the same. Following reshock, differences between the two simulations become even less pronounced. In particular, the positions for both the bubble and spike agree, even following the arrival of the reflected rarefaction at ≈ 8.5 ms.

	3D $a_0^- = 0.205$ cm initial conditions		3D $a_0^- = 0.29$ cm initial conditions		2D mix initial conditions	
k (cm $^{-1}$)	1.4976		1.4976		1.0590	
v_0 (cm/s)	1336.8		1891.2		1336.8	
	Pre-shock	Post-shock	Pre-shock	Post-shock	Pre-shock	Post-shock
a_0 (cm)	0.205	0.1513	0.29	0.214	0.29	0.214

Table 5.1. Initial conditions for the three-dimensional simulations and comparison to the initial conditions for the two-dimensional simulations with mix initial conditions.

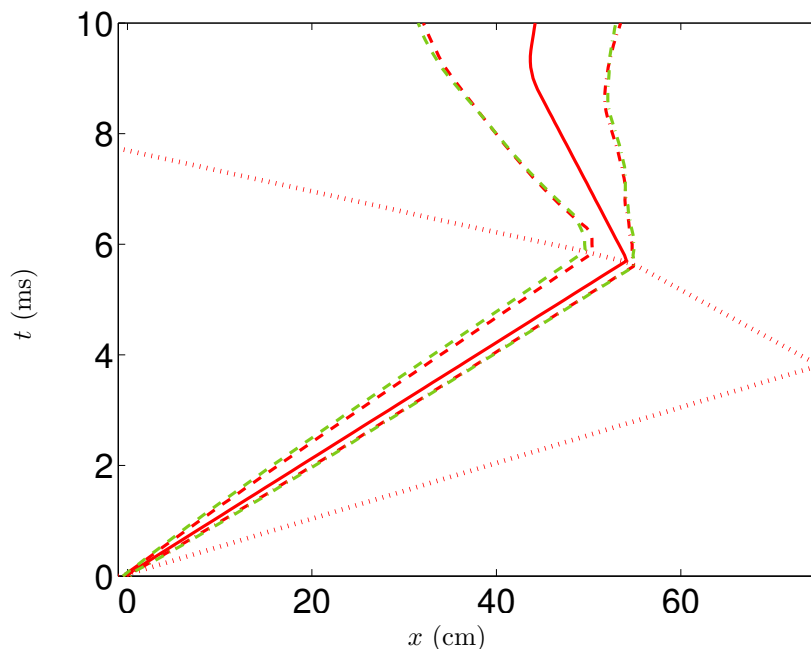


Figure 5.1. The x - t diagram showing the position of the interface $\ell_{\text{int}}(t)$ (solid line), shock (dotted line), and bubble and spike locations $\ell_b(t)$ and $\ell_s(t)$ (dash-dot and dashed lines, respectively) for the three-dimensional simulation with $a_0^- = 0.205$ cm (red) and $a_0^- = 0.29$ cm (green).

The WENO simulations were performed using a parallel Fortran 90 code on the uP computer at the Lawrence Livermore National Laboratory; each processor is an IBM POWER5 with 3 GB of memory per 4-CPU node and clock speed of 1.9 GHz. For each simulation, the number of nodes and the total number of processors is shown in Table 5.2. The CPU times required to advance the simulations from 0.4 ms to 0.5 ms are also shown in Table 5.2. Doubling the resolution constitutes an eight-fold increase in computational time. Changing the order constitutes a 50% increase in computational cost. These results are generally consistent with previous findings in two-dimensional simulations of the single-mode Richtmyer-Meshkov instability [77].

	2D-128	2D-256	2D-384	2D-512	2D-768	3D-128
Nodes	8	8	8	8	16	16
CPUs	64	64	64	64	128	128
Time steps	26,351	52,853	79,280	105,707	158,560	30,949

WENO 5						
Grid size	1688 × 134	3369 × 263	5050 × 391	6731 × 518	10093 × 774	1688 × 71 × 71
Total cells	226,192	886,047	1,974,550	3,486,658	7,811,982	8,509,208
CPU time (s)	20	156	516	1233	2127	720

WENO 9						
Grid size	1692 × 138	3373 × 267	5054 × 395	6735 × 522	10093 × 774	1692 × 75 × 75
Total cells	233,496	900,591	1,996,330	3,515,670	7,855,466	9,517,500
CPU time	32	261	803	2013	3254	1101

Table 5.2. Number of nodes, CPUs, and time steps for the WENO simulations. Also shown is the grid size, total number of cells, and CPU times for advancing the simulations by $\Delta t = 0.1$ ms for the WENO5 and WENO9 simulations.

5.1.2 Baroclinic circulation deposition on the interface and comparison to linear theory

The circulation on the sinusoidal interface is defined by adapting Equation (4.19) to three dimensions:

$$\langle \omega_i \rangle(y, z, t) = \int_{-\infty}^{\infty} \omega_i(x, y, z, t) dx \quad (5.2)$$

for the component $\omega_i(\mathbf{x}, t)$ of the vorticity vector. Equation (5.2) can be compared with the predictions of linear theory [47]. By analogy with two dimensions [Eq. (2.18)], define the vortex dipole in three dimensions

$$\mu(x, y) = 2 v_0 \cos(kx) \cos(ky), \quad (5.3)$$

so that the initial vortex sheet in three dimensions is [47]

$$\boldsymbol{\gamma}(x, y) = \frac{\frac{\partial \mu}{\partial y} \hat{\mathbf{i}} - \frac{\partial \mu}{\partial x} \hat{\mathbf{j}} + \left(\frac{\partial \eta}{\partial x} \frac{\partial \mu}{\partial y} - \frac{\partial \eta}{\partial y} \frac{\partial \mu}{\partial x} \right) \hat{\mathbf{k}}}{\sqrt{1 + \left(\frac{\partial \eta}{\partial x} \right)^2 + \left(\frac{\partial \eta}{\partial y} \right)^2}}. \quad (5.4)$$

For the present $\eta(x, y)$ [Eq. (1.20)] and $\mu(x, y)$ [Eq. (5.3)], it follows that $\gamma_3 \equiv 0$.

Figure 5.2 shows a visualization of the mass fraction and enstrophy isosurface at 0.06 ms (immediately following the passage of the shock) used to determine the circulation deposition [Eq. (5.2)]. The first row of the figure shows the *mass fraction isosurface* corresponding to $m_{\text{SF}_6} = 1/2$. “Front” denotes a view of the isosurface from the air(acetone) side; “back” denotes a view from the SF₆ side. The isosurfaces show the shocked initial sinusoidal interface. Also shown is the (x, y) -cross-section corresponding to the central value of the z -coordinate denoted z_{mid} . The cross-section shows the

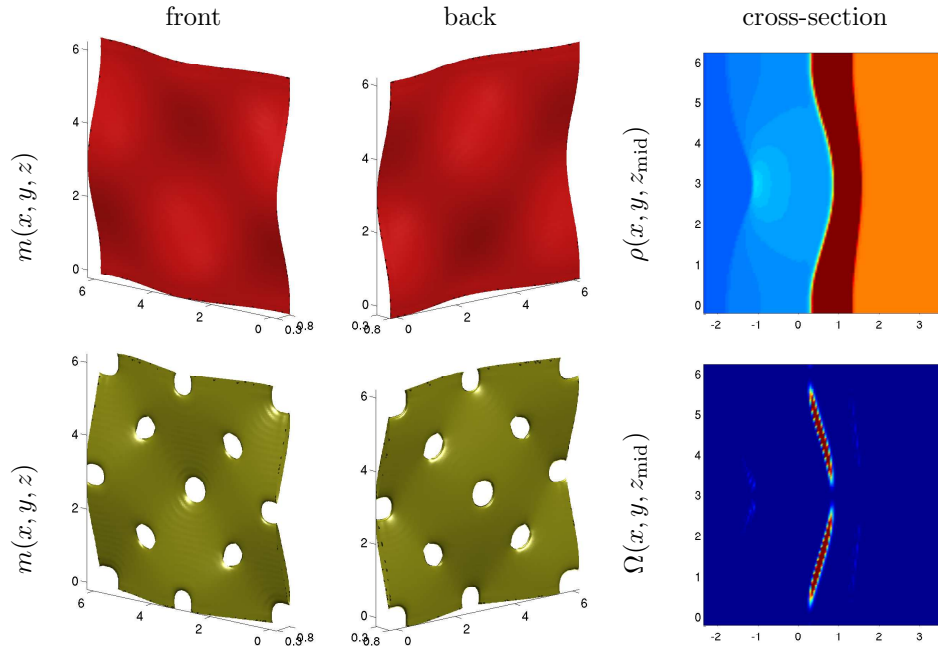


Figure 5.2. Visualization of the mass fraction isosurface corresponding to $m = 1/2$, the density cross-section at $z_{mid} = L_z/2$, the enstrophy isosurface $\Omega = 10^8 \text{ s}^{-2}$ at 0.06 ms, and the enstrophy cross-section at z_{mid} using the WENO method.

transmitted shock entering SF_6 , the reflected shock returning back into the air (acetone), and the compressed initial interface. Shown in the second row is the *enstrophy isosurface*, where

$$\Omega(x, y, z, t) = \frac{\omega_1^2 + \omega_2^2 + \omega_3^2}{2} \quad (5.5)$$

is the *enstrophy*. The isosurface is computed at a value corresponding to half the maximum and minimum enstrophy values. A uniform layer of enstrophy is deposited on the interface and white represents regions where $\Omega = 0$, corresponding to the tip of the bubble or the tip of the spike. An (x, y) -cross-section corresponding to z_{mid} shows the deposition of enstrophy on the interface and the zero values of the enstrophy corresponding to the tip and the bottom of the bubble. The enstrophy is expected to be zero in these regions, just as the vorticity is zero at the tip of the bubble and spike. In these regions the density and the pressure gradients are parallel, so that the baroclinic vorticity production vanishes.

Figure 5.3 shows a visualization of the initial baroclinic circulation deposition by the shock for the $a_0^- = 0.205 \text{ cm}$ initial condition. The first column shows $\langle \omega_1 \rangle(y, z, 0^+)$, $\langle \omega_2 \rangle(y, z, 0^+)$, and $\langle \omega_3 \rangle(y, z, 0^+)$ used to visualize the initial baroclinic circulation deposition on the interface by the shock and a visualization of the initial enstrophy on the interface $\langle \Omega \rangle(y, z, 0^+)$. The values of $\langle \omega_1 \rangle(y, z, 0^+)$ are much smaller than the values for the other components of the vorticity field,

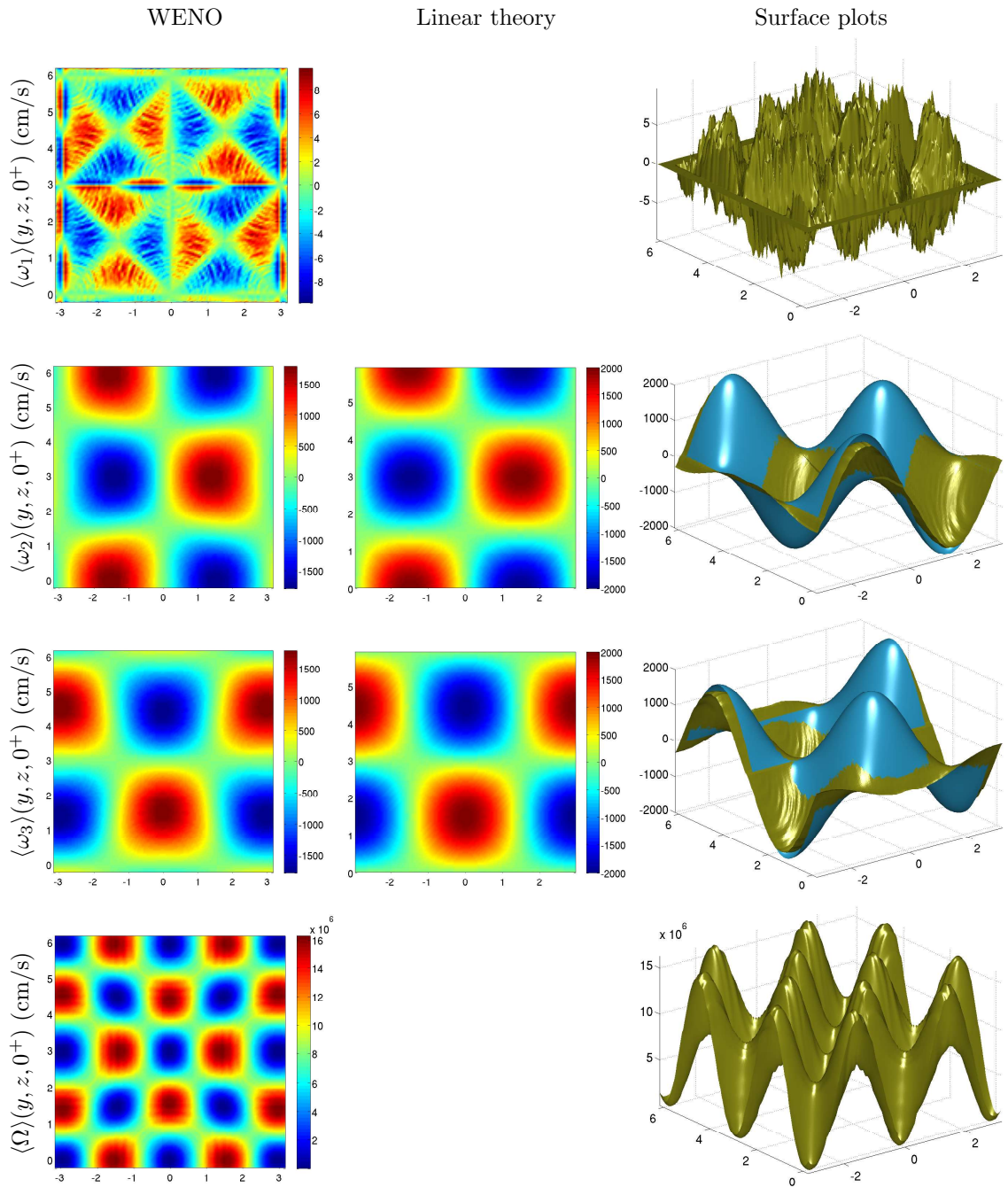


Figure 5.3. The initial deposition of circulation on the interface from the three-dimensional WENO simulation with $a_0^- = 0.205$ cm, as measured by the averaged components of the vorticity vector $\langle \omega_1 \rangle(y, z, 0^+)$, $\langle \omega_2 \rangle(y, z, 0^+)$, $\langle \omega_3 \rangle(y, z, 0^+)$, and the enstrophy $\langle \Omega \rangle(y, z, 0^+)$ from the incident shock at time 0^+ (left column) with the comparison from linear instability theory (center column). Also shown is the surface-plot comparison of the results from the simulation (green) with the results from linear instability theory (blue) (right column).

	3D $a_0^- = 0.205$ cm initial conditions		3D $a_0^- = 0.29$ cm initial conditions	
	WENO	Theory	WENO	Theory
$\max [\langle \omega_1 \rangle (y, z, 0^+)]$ (cm/s)	9.7698	0	20.8719	0
$\max [\langle \omega_2 \rangle (y, z, 0^+)]$ (cm/s)	1.7828×10^3	1.9525×10^3	2.5768×10^3	2.7623×10^3
$\max [\langle \omega_3 \rangle (y, z, 0^+)]$ (cm/s)	1.7835×10^3	1.9525×10^3	2.5765×10^3	2.7623×10^3
$\max [\langle \Omega \rangle (y, z, 0^+)]$ (cm/s ²)	1.6267×10^7	—	3.2774×10^7	—

Table 5.3. Comparison of the initial circulation deposition $\max [\langle \omega_1 \rangle (y, z, 0^+)]$, $\max [\langle \omega_2 \rangle (y, z, 0^+)]$, and $\max [\langle \omega_3 \rangle (y, z, 0^+)]$ from the three-dimensional WENO simulations with $a_0^- = 0.205$ and $a_0^- = 0.29$ cm together with the predictions of linear instability theory. Also shown is the baroclinic circulation deposition on the interface $\max [\langle \Omega \rangle (y, z, 0^+)]$.

indicating that it is negligible; $\langle \omega_2 \rangle (y, z, 0^+)$ and $\langle \omega_3 \rangle (y, z, 0^+)$ show the formation of alternating strong positive and negative vortices, as expected by the different misalignments of the density and pressure gradient vectors. Note that $\langle \omega_3 \rangle (y, z, 0^+)$ is the same as $\langle \omega_2 \rangle (y, z, 0^+)$, but rotated 90° clockwise. The second column shows the predictions for $\langle \omega_2 \rangle (y, z, 0^+)$ and $\langle \omega_3 \rangle (y, z, 0^+)$ from linear theory. Linear theory gives similar qualitative and quantitative predictions as those from the simulations. The only difference is that the maximum values are slightly larger in the linear prediction, and that the vortices are much rounder in the linear predictions. The discrepancy can be attributed to the fact that the simulation values are measured at 0.06 ms, so that the circulation deposited on the interface by the shock has evolved. The right column of the figure presents surface plot visualizations for the simulations (green) with a comparison to the predictions of linear theory (blue). The surface plots for $\langle \omega_1 \rangle (y, z, 0^+)$ show a disordered noisy structure. The surface plots of $\langle \omega_2 \rangle (y, z, 0^+)$ and $\langle \omega_3 \rangle (y, z, 0^+)$ show the formation of a sinusoid-like structure with the prediction of linear theory shown above the simulation in the peaks of the vortices and shown below in the case of the valleys. A visualization for the $a_0^- = 0.29$ cm initial condition yields similar results and is not shown.

A quantitative measure of the initial circulation deposition is obtained by comparing the maximum values from the WENO simulations with the predictions of linear theory. The results for the simulations with $a_0^- = 0.205$ and 0.29 cm are shown in Table 5.3, and indicate that linear theory overpredicts the simulation by 8.7% in the case of $a_0^- = 0.205$ cm and by 2.5% in the case of $a_0^- = 0.29$ cm. The WENO values for ω_3 and ω_2 also confirm that the simulations retain symmetry, as the difference is only 0.04%. The results also show that the simulation with $a_0^- = 0.29$ cm has initial circulations that are one third larger than those with $a_0^- = 0.205$ cm. The nonzero value of $\max [\langle \omega_1 \rangle (y, z, 0^+)]$ indicates an error of 1% between the simulations and theory. As the WENO values are taken at 0.06 ms, the baroclinic vorticity production has already modified the vorticity, which can be quantified as follows. The baroclinic vorticity production has magnitude $\mathcal{P}_1 \sim \times 10^7$ and $\mathcal{P}_2 \sim 10^9$ (in units of s⁻²) in the longitudinal and periodic directions, respectively.

For $\Delta t \sim 0.06$ ms, this corresponds to an increase in vorticity $\Delta \langle \omega_1 \rangle \sim \Delta t \mathcal{P}_1 \Delta x \sim 1$ (cm/s) and $\Delta \langle \omega_2 \rangle \sim \Delta t \mathcal{P}_2 \Delta x \sim 10^3$ (cm/s), which is consistent with the discrepancy between the WENO results and the predictions from linear instability theory.

5.1.3 Initial conditions for the vorticity-streamfunction method

Initial conditions for the three-dimensional VS method are adapted from the two-dimensional simulations (Sec. 4.2.4) and the three-dimensional initial conditions for the WENO method (Sec. 5.1.1). The initial perturbation is the three-dimensional product of sinusoids [Eq. (1.20)]. A Cartesian grid is specified over the domain $[0, L_x] \times [0, L_y] \times [L_{\text{bot}}, L_{\text{top}}]$, with uniform grid spacing $h = \Delta x = \Delta y = \Delta z$ and $N_x \times N_y \times N_z$ grid points. In the present simulations, the domain has dimensions $[0, 5.94] \times [0, 5.94] \times [-8.91, 5.94]$ with resolution $N_x \times N_y \times N_z = 80 \times 80 \times 200$ (Table 5.4).

A VS simulation of the Richtmyer-Meshkov instability begins immediately after the passage of the shock. As a result, the initial vorticity must be specified on the grid. To specify the initial vorticity, linear instability theory is used [Eqs. (5.3) and (5.4)]. Next, use $N = 4 N_x$ markers to discretize $[0, L_x]$ and $[0, L_y]$ to give x_i and y_j . Let $z_{n,m} = \eta(x_n, y_m)$ and

$$\Delta s_{m,n,1} = \frac{1}{2} \sqrt{(x_{m+1} - x_{m-1})^2 + (z_{m+1,n} - z_{m-1,n})^2}, \quad (5.6)$$

$$\Delta s_{m,n,2} = \frac{1}{2} \sqrt{(y_{n+1} - y_{n-1})^2 + (z_{m+1,n} - z_{m-1,n})^2}, \quad (5.7)$$

be the arclength along the x and y directions, respectively. The circulations on each of the $N \times N$ markers is

$$\Gamma_{m,n,1} = \gamma_1(x_m, y_n) \Delta s_{m,n,1} \Delta s_{m,n,2}, \quad \Gamma_{m,n,2} = \gamma_2(x_m, y_n) \Delta s_{m,n,1} \Delta s_{m,n,2}. \quad (5.8)$$

Assign Γ_1 and Γ_2 on the grid to obtain the initial vorticities

$$\omega_1(x_i, y_j, z_k) = \sum_{m,n} \frac{\Gamma_{m,n,1}}{h^3} L_{g,3D}(x_i - x_m, y_j - y_n, z_k - z_{m,n}, h, \delta_T), \quad (5.9)$$

$$\omega_2(x_i, y_j, z_k) = \sum_{m,n} \frac{\Gamma_{m,n,2}}{h^3} L_{g,3D}(x_i - x_m, y_j - y_n, z_k - z_{m,n}, h, \delta_T), \quad (5.10)$$

where the Gaussian in three dimensions is

$$L_{g,3D}(x, y, z, h, \delta_T) = \frac{h^3}{\pi^{3/2} \delta_T^3} \exp\left(-\frac{x^2 + y^2 + z^2}{\delta_T^2}\right). \quad (5.11)$$

Initial surface and vortex sheet properties		
	Atwood number study	WENO comparison
A	–	0.604
a_0 (cm)	0.42	0.151321
λ (cm)	5.94	5.94
k (cm ⁻¹)	1.064947	1.064947
v_0 (cm/ms)	1.5	1.33876

VS method		
	x and y	z
N	80	200
CFL	[0, 5.94]	[-8.91, 5.94]
δ_T (cm)		
ν (cm ² /ms)	7.425×10^{-2}	7.425×10^{-2}

Table 5.4. Initial surface and vortex sheet properties for the VS simulations of the Atwood number study and the comparison with the WENO method in three dimensions, including the initial amplitude a_0 , the wavelength λ , the wavenumber k , and the initial vortex sheet strength parameter v_0 . Also shown are the properties of the VS method, including the CFL number, thickness of the sheet δ_T , and the viscosity ν .

The initial density field is

$$\rho(x_i, y_j, z_k) = \frac{\rho_1 + \rho_2}{2} \left\{ 1 + A \tanh \left[\frac{z_j - a_0 \cos(k x_i) \cos(k y_j)}{\delta_T} \right] \right\}. \quad (5.12)$$

Figure 5.4 shows the mass fraction and enstrophy isosurfaces at 0 ms, corresponding to the initial conditions of the VS method. The mass fraction isosurface shows the sinusoidal interface [Eq. (1.20)]. The spike and bubble view refers to whether the spike or bubble are at the center of the visualization box. The enstrophy isosurface shows that the deposition of vorticity is largest in the regions between the tips of the bubble and spike and is smallest at the tips of the bubble and spike. This is expected as the density and pressure gradients are parallel at the tip of the bubble and are mis-aligned in-between.

5.2 Dynamics of the instability evolution

Presented here is a visualization of the time-evolution of the Richtmyer-Meshkov instability in three dimensions using the mass fraction and enstrophy isosurfaces. As the initial surface in three-dimensions [Eq. (1.20)] resembles an “egg carton” (Fig. 1.1), a distinctive “bubble” corresponding to the perturbation entering into the SF₆, and a distinctive “spike” corresponding to the perturbation entering into the air(acetone) can be identified. In addition, a “front side” corresponding

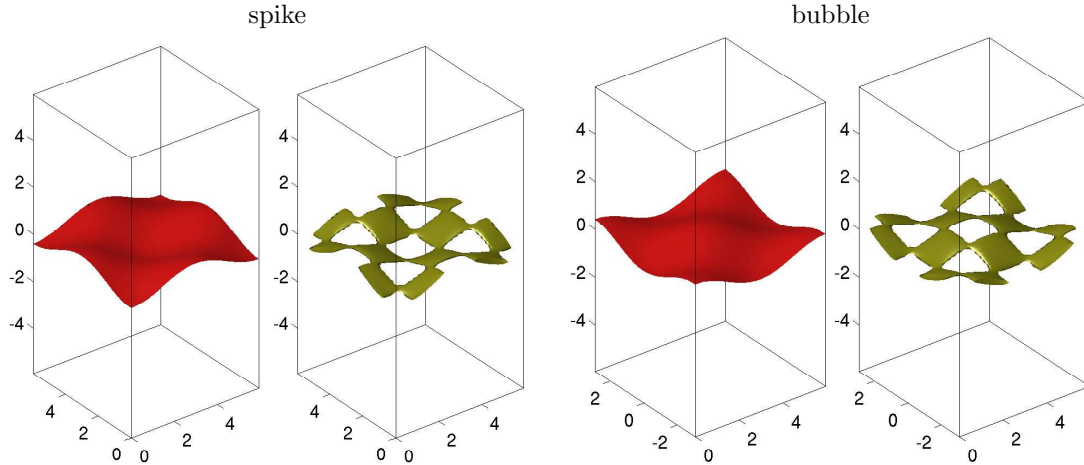


Figure 5.4. Visualization of the mass fraction isosurface corresponding to $m = 1/2$ and enstrophy isosurface corresponding to $\Omega = 10 \text{ ms}^{-2}$ at 0 ms from the VS simulation.

to a view from the air(acetone) side, and a “back side” corresponding to a view from the SF_6 side can be identified. The visualizations shown here are for the $a_0^- = 0.205 \text{ cm}$ initial conditions (the visualizations for $a_0^- = 0.29 \text{ cm}$ are expected to be very similar and are not shown).

Figures 5.5 and 5.6 show the time-evolution of the mass fraction isosurfaces illustrating the dynamics of the bubble and spike from the front [air(acetone)] side and the back (SF_6) side from the WENO and VS simulations. The initial shocked interface (Fig. 5.2 for the WENO and Fig. 5.4 for the VS simulations) shows the initial perturbation, including the bubble and the spike. The bubble front contains a quarter of the spike front corresponding to the sides on the quarters, which becomes more apparent at later times. Following the passage of the shock, bubbles of air(acetone) start rising into the heavier SF_6 and spikes of SF_6 start penetrating into the air(acetone). At 1.16 ms, a tube-like feature links the spike fronts at the separation between the bubbles and the spikes: this feature is the result of the initial conditions and the fact that in three dimensions two roll-ups are observed, one corresponding to the spike and one corresponding to the bubble. These tube-like features form the roll-up of the bubble and spike at 1.76 ms. On the front bubble, features appear at the corners due to the interaction of the bubble with adjacent bubbles, indicating the onset of the nonlinear interaction. As the instability develops further, the bubble and spike roll-up further. At 3 ms, the spike develops a further structure on the roll-up. This structure can be seen when visualizing the back of the spike, where corrugations form on the curved part of the spike. This structure is further evident at 4.5 ms when these additional structures can be seen on both the front and back of the spike, and develop a nearly star-shaped feature. At late times (5.6 ms) the roll-ups develop additional complex structure. The sides of the mass fraction isosurface offer a view of the roll-ups, which are similar to those in two-dimensional simulations.

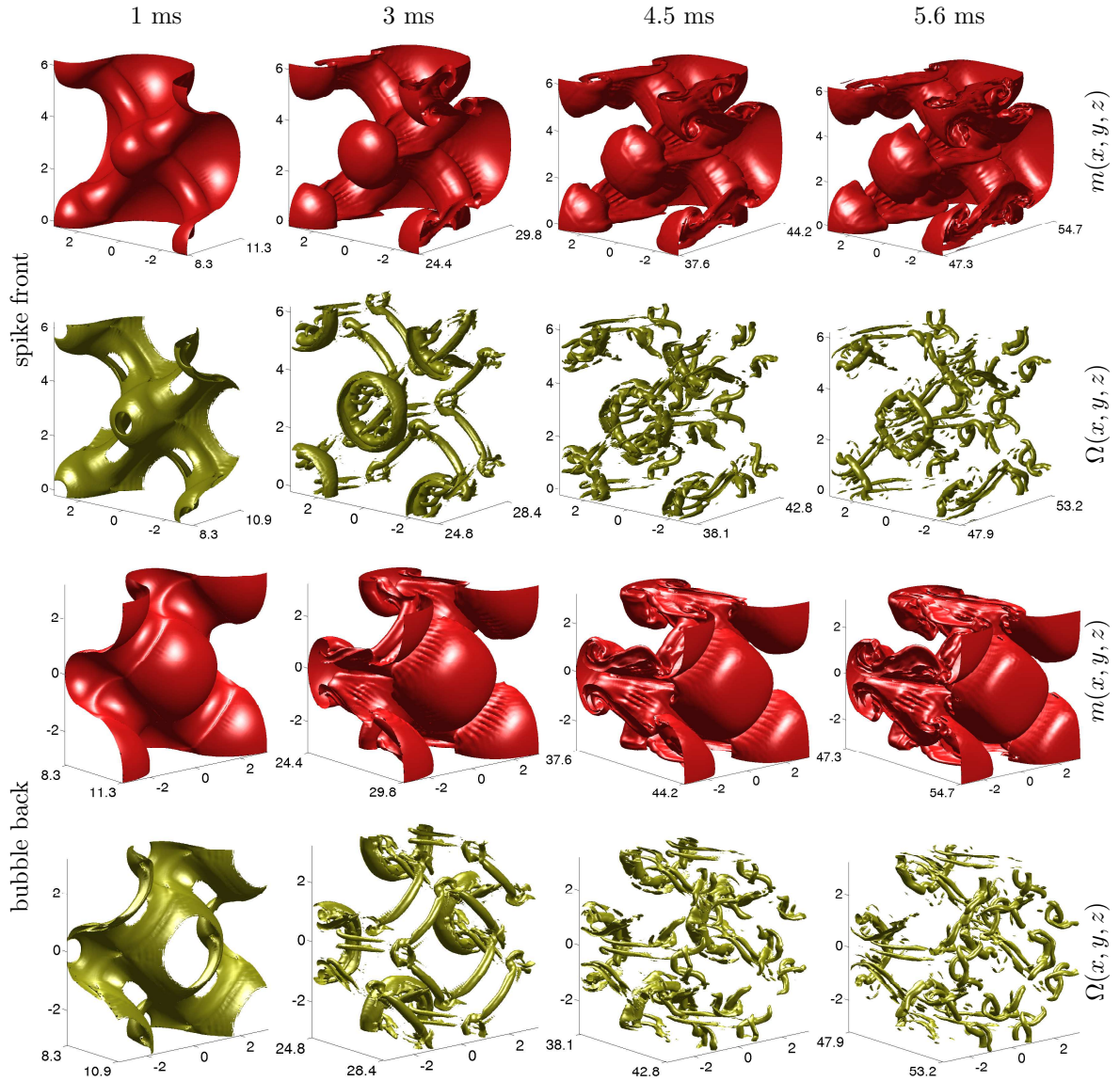


Figure 5.5. Time-evolution of the mass fraction isosurface $m_{SF_6} = 1/2$ and enstrophy isosurface $\Omega = 10^8 \text{ s}^{-2}$ for the single-mode Richtmyer-Meshkov instability at 1, 3, 4.5, and 5.6 ms from the WENO simulation. The spike side facing the air(acetone) (top two rows), and the bubble side facing SF_6 (bottom two rows) are shown.

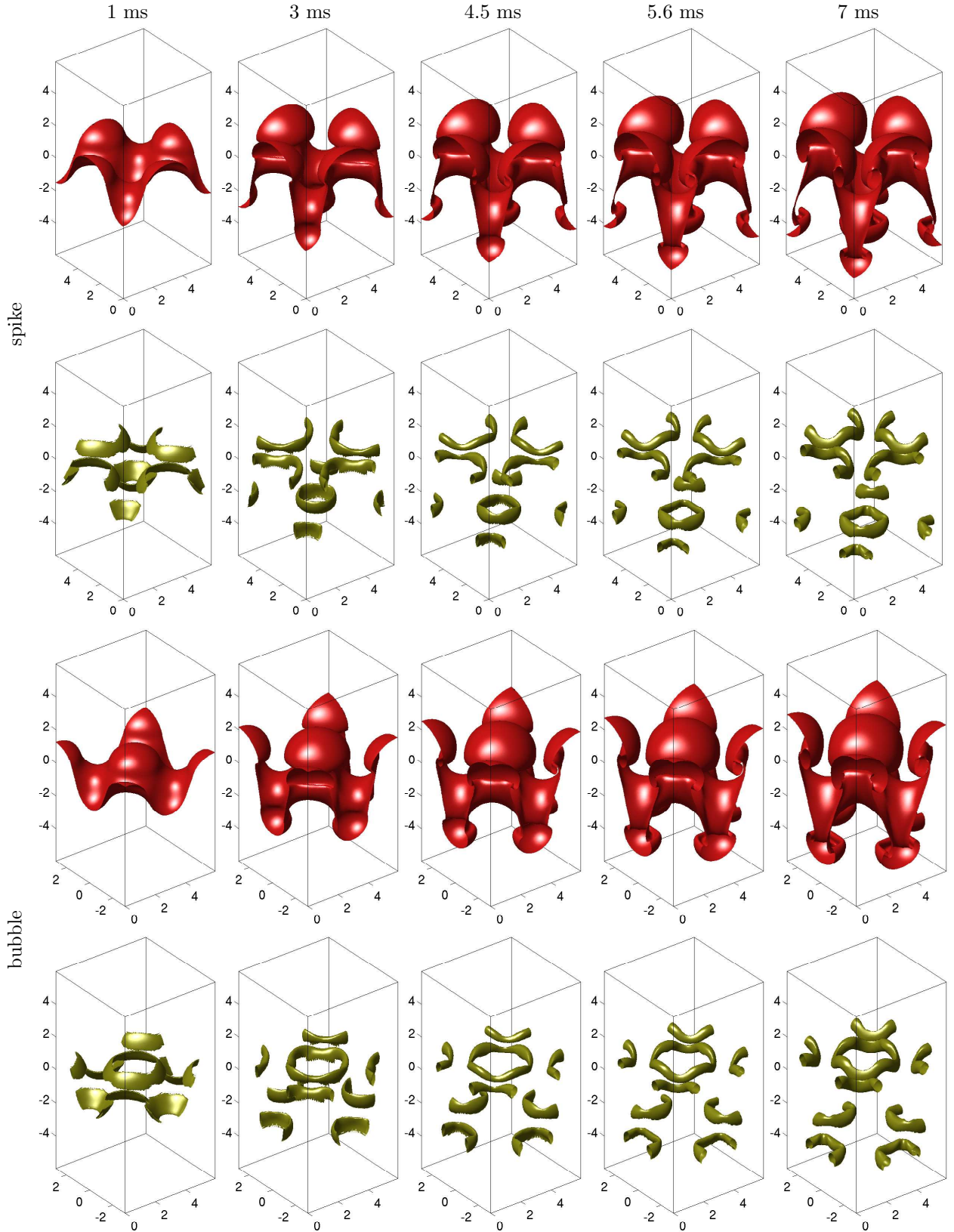


Figure 5.6. Time-evolution of the mass fraction isosurface $m_{SF_6} = 1/2$ and entropy isosurface $\Omega = 10^2 \text{ ms}^{-2}$ for the single-mode Richtmyer-Meshkov instability at 1, 3, 4.5, 5.6, and 7 ms from the VS simulation. The spike side facing the air(acetone) (top two rows), and the bubble side facing SF_6 (bottom two rows) are shown

Figures 5.5 and 5.6 also show the time-evolution of the enstrophy isosurfaces following the passage of the shock through 5.6 ms. The enstrophy [Eq. (5.5)] is used here to visualize the dynamics of the vorticity. Immediately following the passage of the shock at 0.06 ms in Fig. 5.5, a layer of vorticity is deposited on the interface due to the baroclinic vorticity production mechanism. At 1 ms, the enstrophy isosurfaces begin rolling up with bubbles of air(acetone) rising into the SF₆ and spikes of SF₆ penetrating into the air(acetone). At 3 ms, the enstrophy shows a toroidal tube-like structure indicating the formation of a rotating vortex corresponding to the spike. The bubble also shows a similar circular feature but it is larger. In the WENO simulation, the vortex tubes meet at corners forming a complex structure, responsible for the ripples in the mass fraction isosurface at 3 ms. In addition, the vortex tubes connecting the spike to the bubble divide, indicating that further roll-ups are occurring. The bubble also shows the formation of complex structures. At 4.5 ms, the vortex tubes connecting the bubble fragment. At later times, the spike still retains a major central core, while the bubble fragments further. The vortex tubes also become smaller with the formation of thinner and finer structures. This is the result of vortex stretching at the interface which causes the elongation of the vortex tubes (an effect absent in two dimensions).

5.3 Comparison of the perturbation, bubble, and spike amplitudes to the predictions of an amplitude growth model

Figure 5.7 shows a comparison of the perturbation amplitude $a(t)$ from the WENO and VS simulations with $a_0^- = 0.29$ and 0.205 cm. The three-dimensional simulations are in excellent agreement for both initial conditions up to reshock. Also shown is a comparison of the bubble and spike amplitudes, $a_b(t)$ and $a_s(t)$, respectively. The VS bubble amplitude is in good agreement with the WENO amplitude at early times. At intermediate times, it overpredicts the WENO amplitude. Similarly, the VS spike amplitude is in agreement with the WENO simulation at early times. At intermediate-to-late times, the spike amplitude is slightly smaller. Overall, the results show excellent agreement between the VS and WENO simulations.

Figures 5.8 and 5.9 show a comparison of the VS and WENO perturbation amplitudes with $a_0^- = 0.29$ and 0.205 cm and the predictions of the three-dimensional Zhang-Sohn model [157]

$$\frac{da}{dt} = \frac{v_0}{1 + \epsilon a_0^+ v_0 \lambda_1 t + \max[0, (k a_0^+)^2 \lambda_1^2 - \lambda_2] k^2 v_0^2 t^2}, \quad (5.13)$$

where $\lambda_1 = 0.08887 (A^+)^2 + 0.45567$ and $\lambda_2 = 0.39136 (A^+)^2 + 0.22784$. The Zhang-Sohn models agree with the simulations at early-to-intermediate times. At later times, the models underpredict the simulation amplitudes.

Figures 5.8 and 5.9 also show a comparison of $a_b(t) - a_b(0^+)$ from the WENO and VS simulations

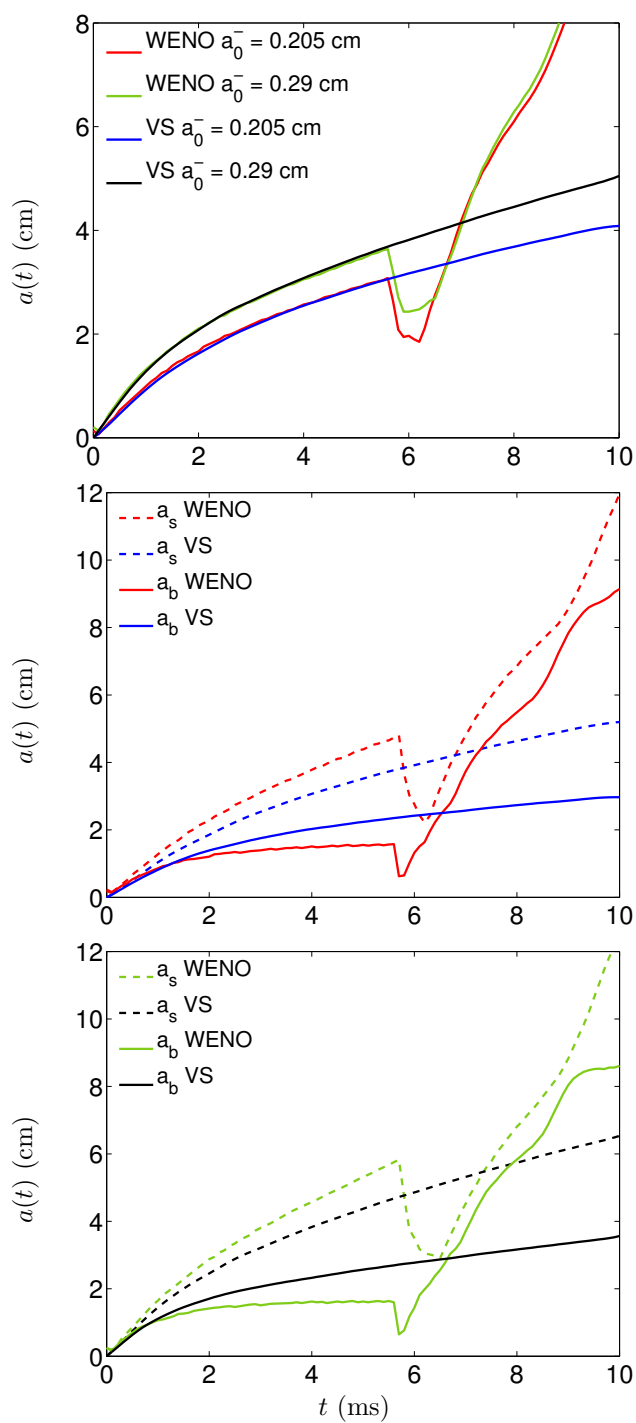


Figure 5.7. Comparison of the perturbation amplitude from the WENO and VS simulations with $a_0^- = 0.205$ and 0.29 cm (top). The bubble and spike amplitudes $a_b(t)$ and $a_s(t)$, respectively, for $a_0^- = 0.205$ cm (middle) and for $a_0^- = 0.29$ cm (bottom) are also shown.

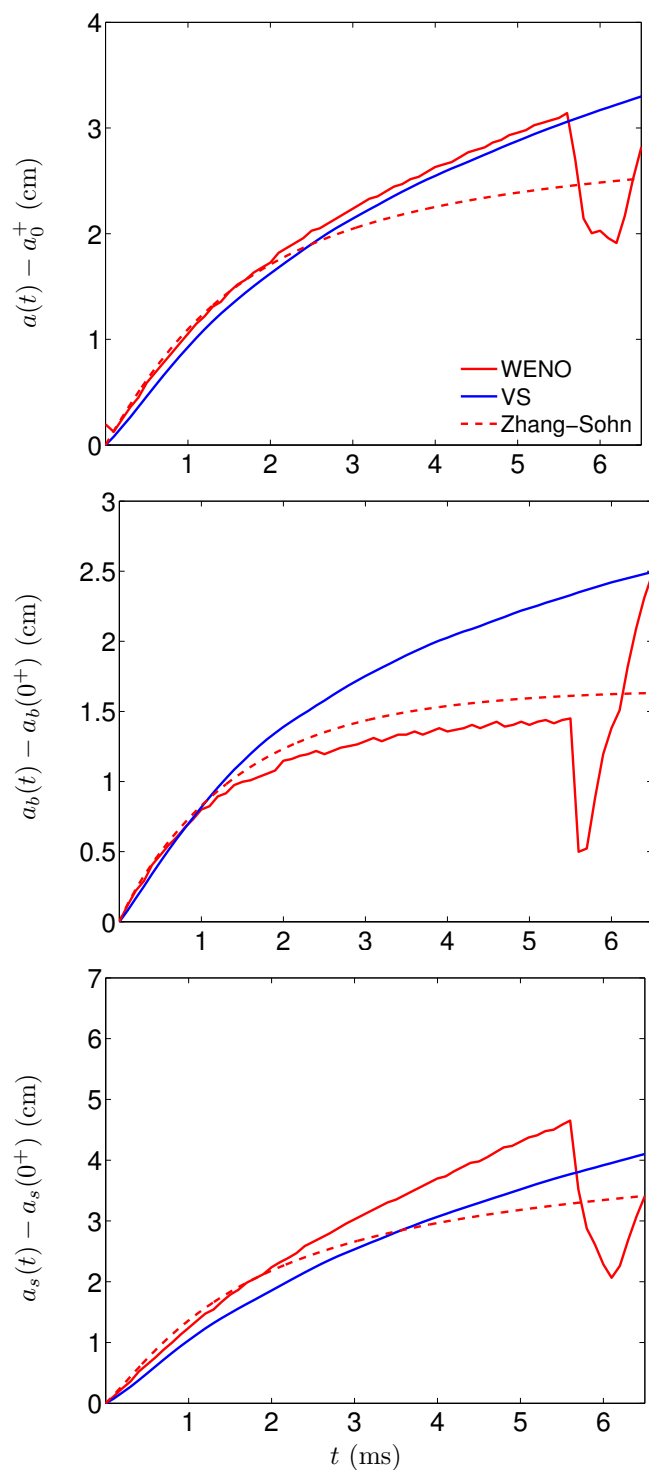


Figure 5.8. Comparison of the amplitudes $a(t) - a_0^+$, $a_b(t) - a_b(0^+)$, and $a_s(t) - a_s(0^+)$ from the WENO and VS simulations with $a_0^- = 0.205$ cm and the predictions of the Zhang-Sohn model.

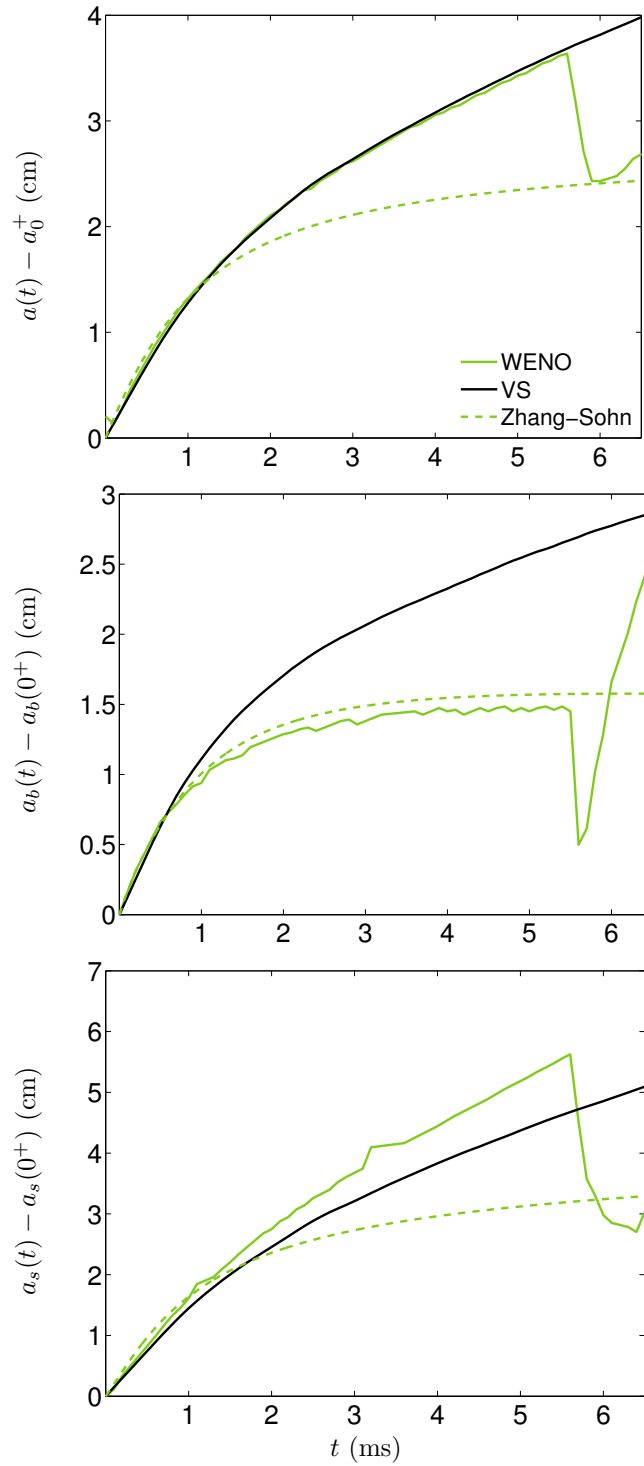


Figure 5.9. Same as Figure 5.8 but for simulations with $a_0^- = 0.29$ cm.

	VS $a_0^- = 0.205$ cm	VS $a_0^- = 0.29$ cm
	Δ_{sim}	Δ_{sim}
Zhang-Sohn Padé (all)	2.1	7.09
Zhang-Sohn Padé (bubble)	6.2	19.74
Zhang-Sohn Padé (spike)	3.75	12.68

	WENO $a_0^- = 0.205$ cm	WENO $a_0^- = 0.29$ cm
	Δ_{sim}	Δ_{sim}
VS	4.49	6.35
Zhang-Sohn Padé (all)	4.08	6.31
Zhang-Sohn Padé (bubble)	2.55	3.7
Zhang-Sohn Padé (spike)	7.96	8.31

Table 5.5. Average fractional deviation Δ_{sim} between the WENO and VS simulation amplitudes for $a_0^- = 0.205$ and 0.29 cm and the predictions of the Zhang-Sohn model.

with $a_0^- = 0.29$ and 0.205 cm with the predictions of the Zhang-Sohn model

$$\frac{da_b}{dt} = -\frac{da}{dt} + \frac{v_0^2 k \lambda_3 t}{1 + \frac{v_0 a_0^+ k^2 \lambda_4}{\lambda_3} + v_0^2 k^2 \left[\frac{(a_0^+)^2 k^2 \lambda_4^2}{\lambda_3^2} + \frac{\lambda_5}{\lambda_3} \right] t^2}, \quad (5.14)$$

where $\lambda_3 = 4.8482 (A^+)^3 + 1.8257 A^+$, $\lambda_4 = 0.32772 (A^+)^3 + 9.87594 A^+$, and $\lambda_5 = 0.02435 (A^+)^3 + 3.15422 A^+$. The predicted bubble amplitude agrees with the simulated bubble amplitudes at early times. At later times, the model underpredicts.

Also shown in Figures 5.8 and 5.9 is a comparison of $a_s(t) - a_s(0^+)$ from the simulations with the predictions of the Zhang-Sohn model

$$\frac{da_s}{dt} = \frac{da}{dt} + \frac{v_0^2 k \lambda_3 t}{1 + \frac{v_0 a_0^+ k^2 \lambda_4}{\lambda_3} + v_0^2 k^2 \left[\frac{(a_0^+)^2 k^2 \lambda_4^2}{\lambda_3^2} + \frac{\lambda_5}{\lambda_3} \right] t^2}. \quad (5.15)$$

The model predictions agree with the simulated spike amplitude at early times. At late times, the models underpredict. The agreement between the model predictions and the simulation amplitudes can be made more quantitative by computing the average fractional deviation Δ_{sim} [Eq. (4.40)] shown in Table 5.5.

5.4 Investigation of reshock using the WENO method

As in the two-dimensional investigation (Sec. 5.4), the transmitted shock reflects from the end wall of the shock tube and interacts with the evolving mixing layer during reshock at ≈ 5.65 ms. Investigated here are the dynamics of reshock (Sec. 5.4.1), including a visualization of the complex

wave interactions. The mixing layer amplitude is also compared to the predictions of reshock models (Sec. 5.4.2).

5.4.1 Dynamics of the reshock process

Figures 5.10–5.12 show the dynamics of the mass fraction isosurface, including the arrival of the shock wave (5.7 ms), the inversion process (5.8 and 5.9 ms), and the development of a complex mixing layer at late times (8 and 10 ms). At 5.7 ms, reshock is indicated by the compression of the bubble which now shows a flat tip. Following reshock, a transmitted shock enters the air(acetone) and a reflected rarefaction returns back into the SF_6 . The vorticity deposited by the reshock process induces an inversion process, where the bubble turns into a spike and vice versa. The inversion process at 5.8 and 5.9 ms shows the bubble returning back into the air(acetone). The spike is also compressed by the passage of the transmitted shock, causing the formation of additional complex structures in the roll-up. At 6 ms (Fig. 5.11), the mixing layer is compressed and shows the formation of complex structures. At 6.5 ms, the new spike generated by the inversion of the bubble forms. This spike grows at later times (7, 8, and 10 ms), as shown in Figure 5.12. This central spike is the only large-scale structure following reshock, and is similar to that in two-dimensional simulations (Fig. 4.24).

Figures 5.10–5.12 also show the time-evolution of the mass fraction isosurface during reshock. At 5.7 ms, reshock causes a significant deposition of vorticity on the interface, which is much larger than the existing vorticity on the interface. As a result, the enstrophy is largest at reshock and the isosurface only shows a structure corresponding to the reshocked surface. Furthermore, as the vorticity is generated by the misalignment of the density and pressure gradients, it attains its largest values near the curved parts of the bubble. This explains why the enstrophy isosurface is primarily observed along a strip on the side of the bubble. At 5.8 ms, the transmitted shock has interacted with the spike, causing deposition of vorticity in the region. At 5.9 ms, the vorticity begins fragmenting. This fragmentation continues with the formation of a dense, thick, tubular structure by 6 ms in Figure 5.11. This phenomenon is further observed at 6.2 and 6.5 ms. At later times, the mixing layer width grows, but the fragmentation of the vorticity persists, forming complex structure.

Figures 5.13 and 5.14 show the density cross-sections for the bubble and spike during reshock. At 5.7 ms, the transmitted shock enters the air(acetone) and a reflected rarefaction wave returns back into the SF_6 . The reflected rarefaction is clearly visible from the lighter red colors corresponding to the bubble position. The transmitted shock is weaker and is visible only when it interacts with the spike, where it leaves behind a dark red color. The transmitted shock is not seen in the air(acetone), as it is weak and does not significantly increase the density. The transmitted shock enters the spike at 5.8 ms and the interactions with the density structures cause the formation of a complex system of reflected and transmitted waves. At 5.9 ms, the transmitted shock has crossed the mixing layer

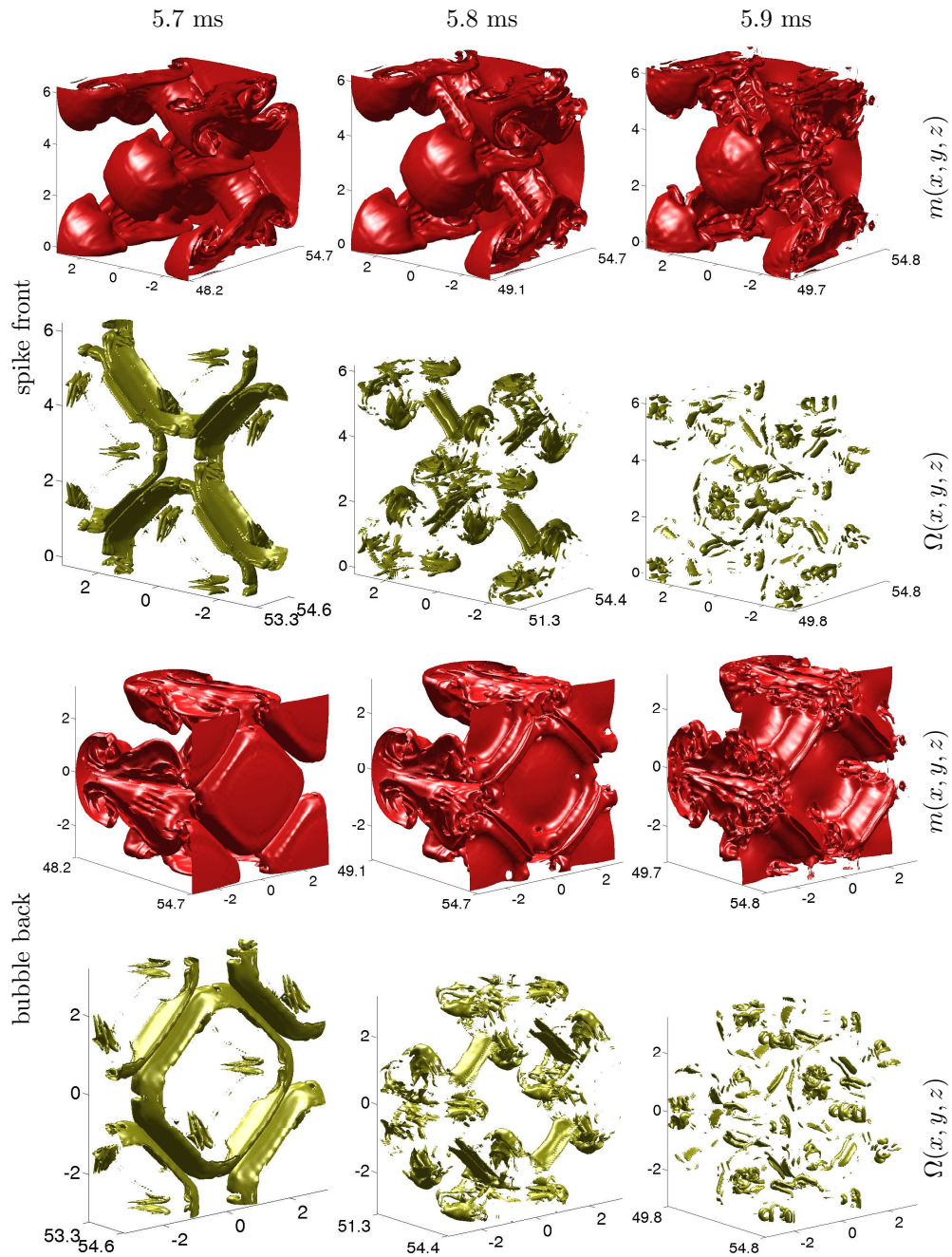


Figure 5.10. Time-evolution of the mass fraction isosurface $m_{SF_6} = 1/2$ and enstrophy isosurface $\Omega = 10^8 \text{ s}^{-2}$ at 5.7, 5.8, and 5.9 ms using the WENO method. The spike side facing the air(acetone) (top two rows) and the bubble side facing SF_6 (bottom two rows) are shown.

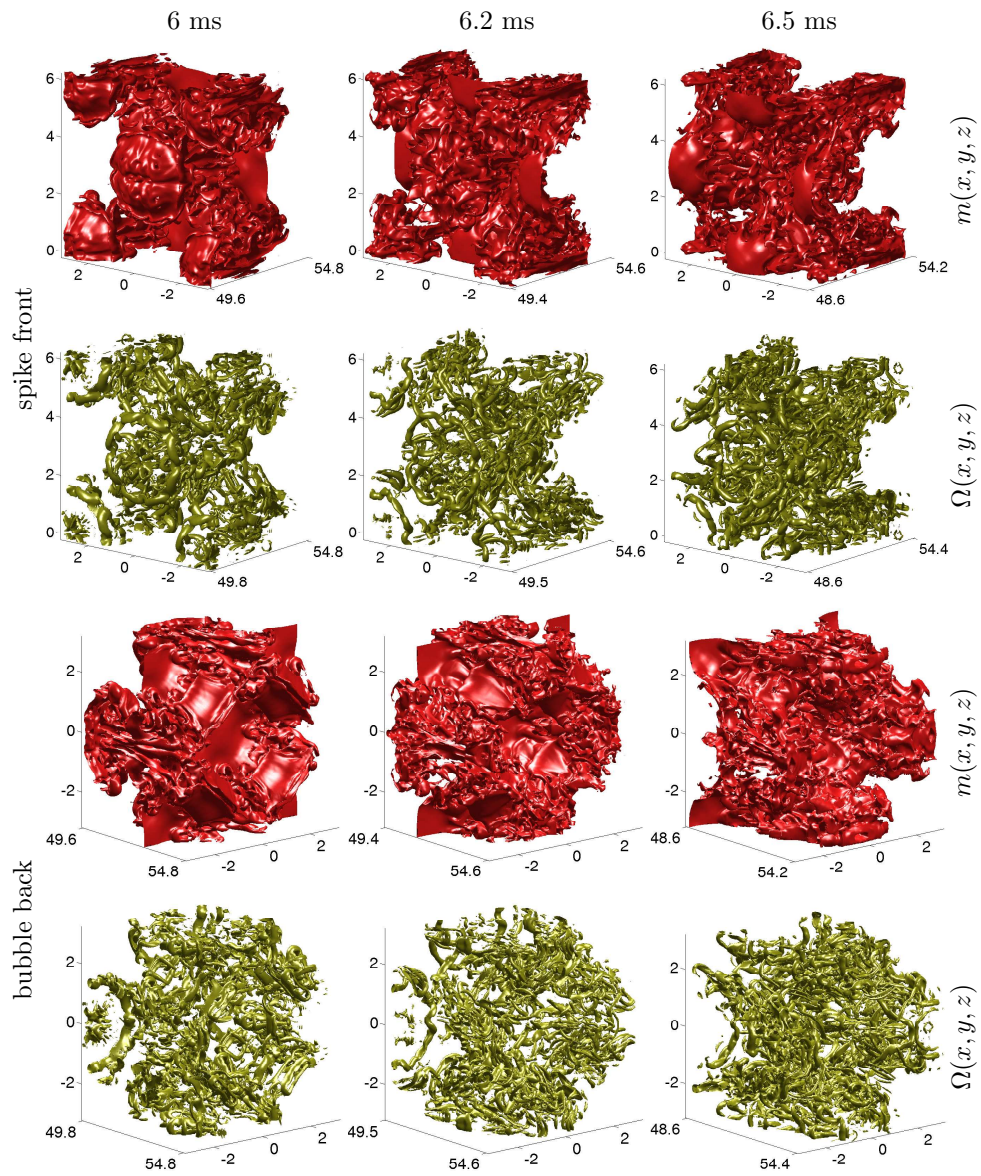


Figure 5.11. Same as Figure 5.10 but at 6, 6.2, and 6.5 ms.

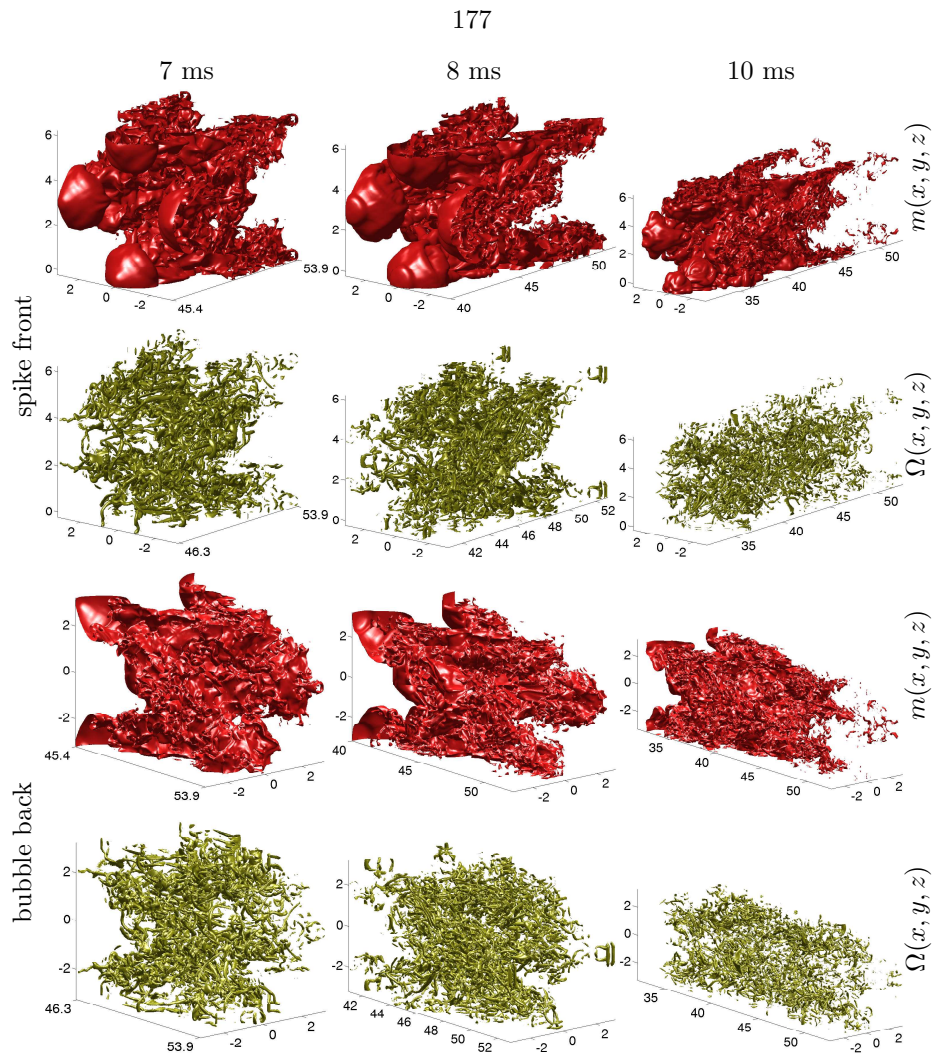


Figure 5.12. Same as Figure 5.10 but at 7, 8, and 10 ms.

and the inversion process begins. The visualizations at 6, 6.1, 6.3, and 6.5 ms show the inversion process, with the pre-shock spike thinning and the pre-shock bubble transforming into a strong spike. At 7 ms, this spike begins to roll-up as shown in Fig. 5.14. A reflected rarefaction wave further interacts with the mixing layer after 8 ms and causes the change in colors at 10 ms. Between the spikes, the density cross-sections reveal the formation of a well-mixed region. The formation of a well-mixed region between large-scale structures was also observed in two-dimensional simulations (Fig. 4.26). However, whereas the two-dimensional simulations show the formation of strong cores of vorticity, the enstrophy isosurface shows that the vorticity is fragmented and forms small, short, tubular structures in three dimensions.

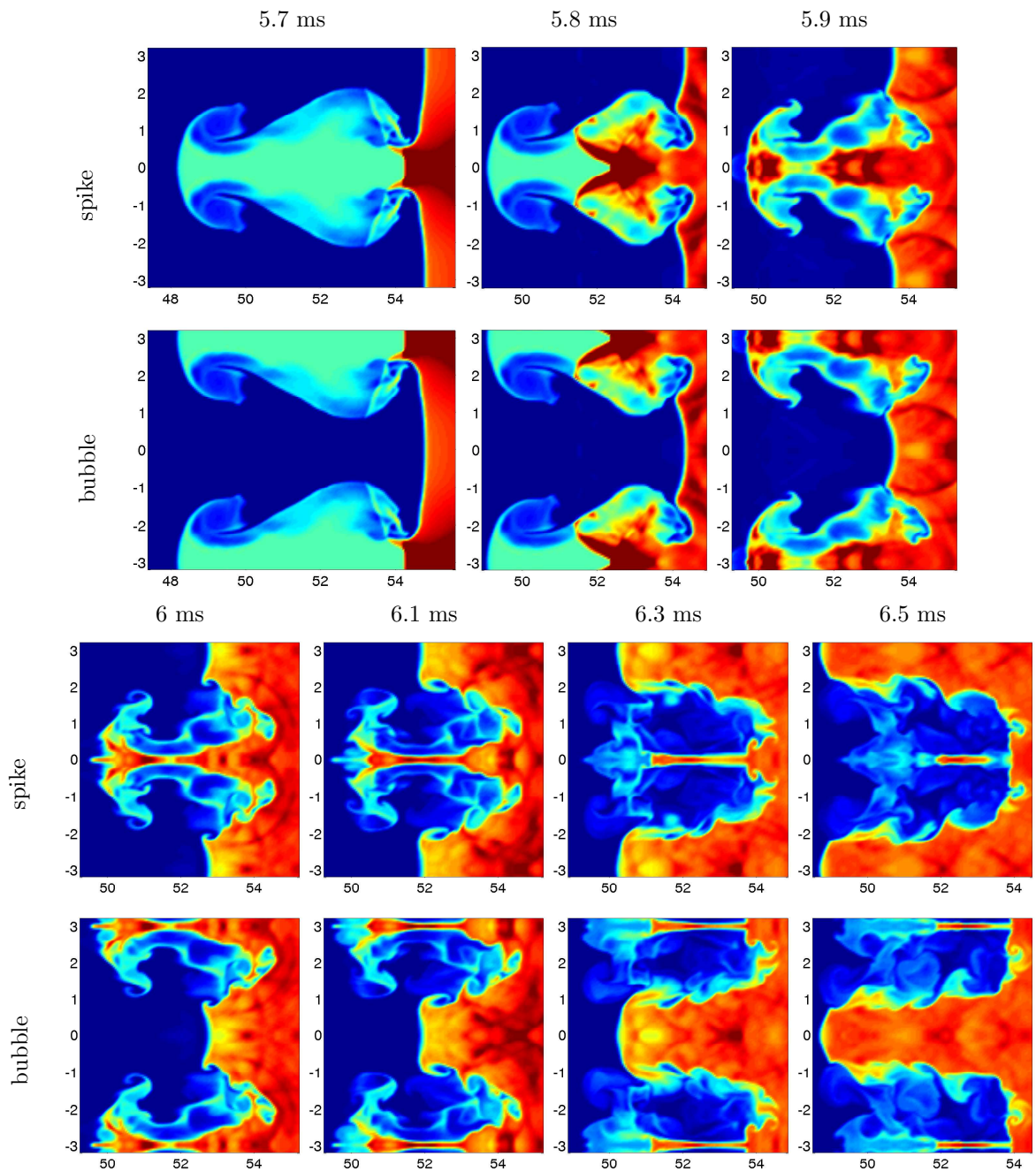


Figure 5.13. Time-evolution of the density in the (x, y) -plane at 5.7, 5.8, 5.9, 6, 6.1, 6.3, and 6.5 ms using the WENO method. Both the evolution of the spike (first and third row) and of the bubble (second and fourth row) are shown.

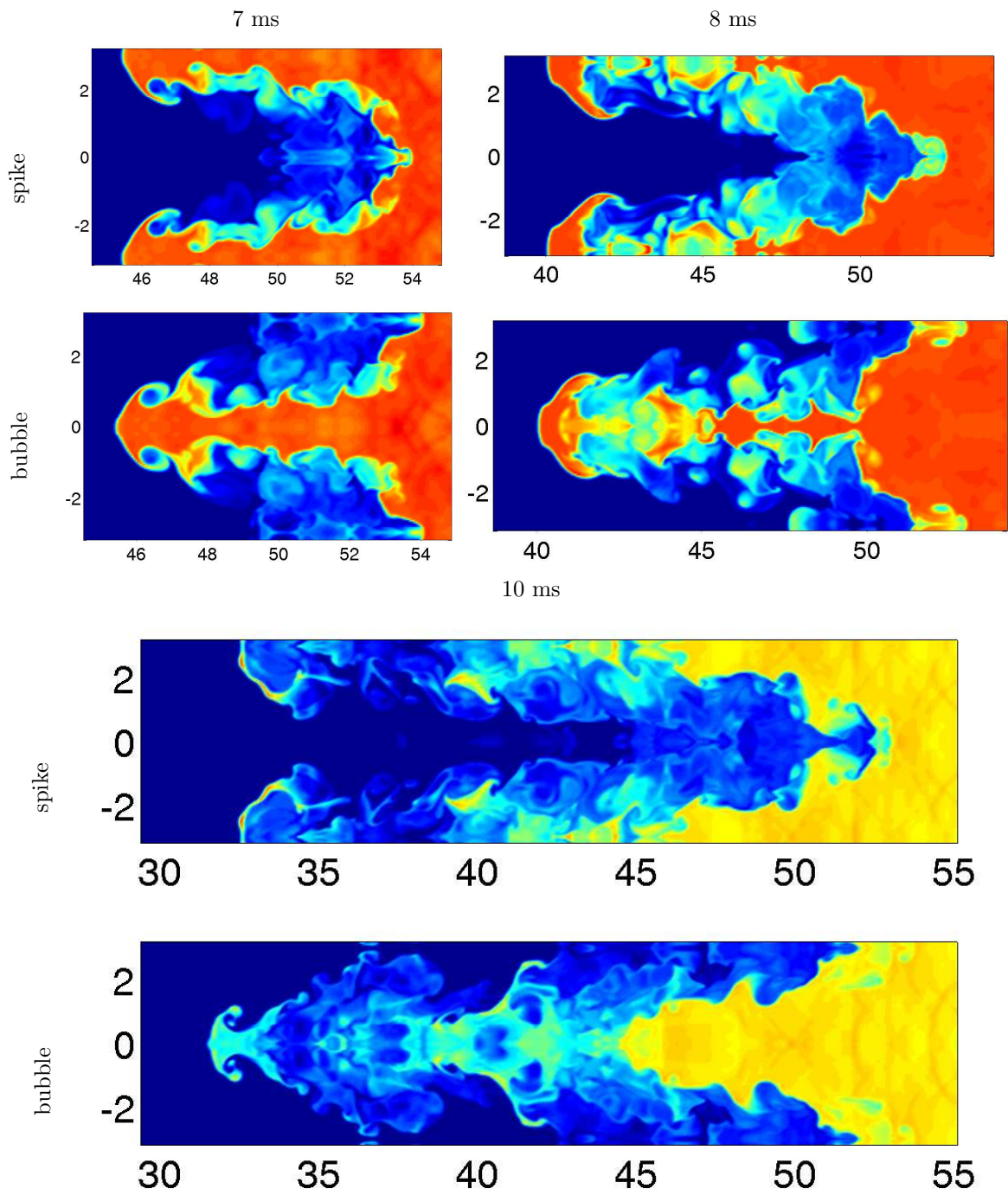


Figure 5.14. Same as Figure 5.13 but at 7, 8, and 10 ms.

	3D $a_0^- = 0.205$ cm initial conditions		3D $a_0^- = 0.29$ cm initial conditions	
	$\frac{da}{dt}$ ($\frac{\text{cm}}{\text{ms}}$)	$k \frac{da}{d\tau}$	$\frac{da}{dt}$ ($\frac{\text{cm}}{\text{ms}}$)	$k \frac{da}{d\tau}$
Richtmyer	1337.29	1	1891.22	1
Mikaelian	3334.21	2.49326	3334.21	1.763
Brouillette-Sturtevant	3070.64	2.29616	4341.63	2.29568
Charakhch'yan	2534	1.89488	3641.42	1.92521

Table 5.6. The growth rate da/dt and the normalized growth rate $k da/d\tau$ for the Richtmyer model before reshock for the three-dimensional WENO simulations with $a_0^- = 0.205$ and 0.29 cm. Also shown are the growth rates and the normalized growth rates for the Mikaelian, Brouillette-Sturtevant, and the Charakhch'yan reshock models.

5.4.2 Comparison of the mixing layer amplitude to the predictions of reshock models

Here, the mixing layer amplitude after reshock is compared to the prediction of reshock models. As the models for the mixing layer amplitude are linear, the growth rate can be computed in dimensional and rescaled units (Table 5.6).

Figure 5.15 shows a comparison of the mixing layer amplitude from the three-dimensional WENO simulations with $a_0^- = 0.205$ and 0.29 cm, together with the prediction of the Mikaelian reshock model [Eq. (4.42)], the Brouillette-Sturtevant model [Eq. (4.43)], and the Charakhch'yan model [Eq. (4.44)]. The Mikaelian model depends only on the post-reshock Atwood number A_1^+ , which has the same value in all simulations. As a result, only a single curve is plotted. This model overpredicts the numerical results. By contrast, the Brouillette-Sturtevant reshock model yields a different prediction for each simulation. The prediction corresponding to the three-dimensional simulation with $a_0^- = 0.205$ cm has the smallest value, followed by the model corresponding to the three-dimensional simulation with $a_0^- = 0.29$ cm (30% larger), as shown in Table 5.6. The Charakhch'yan model depends on the post-reshock Atwood number A_1^+ and the mixing layer growth rate v_0 , so that two curves are plotted, corresponding to the simulations with $a_0^- = 0.205$ and 0.29 cm. This model has the smallest prediction for the simulation with $a_0^- = 0.205$ cm, and the prediction for the three-dimensional simulation with $a_0^- = 0.29$ cm is 30% larger. In conclusion, the Mikaelian reshock model is in best agreement with the simulation results, as the mixing layer amplitude following reshock does not depend on the pre-shock amplitude.

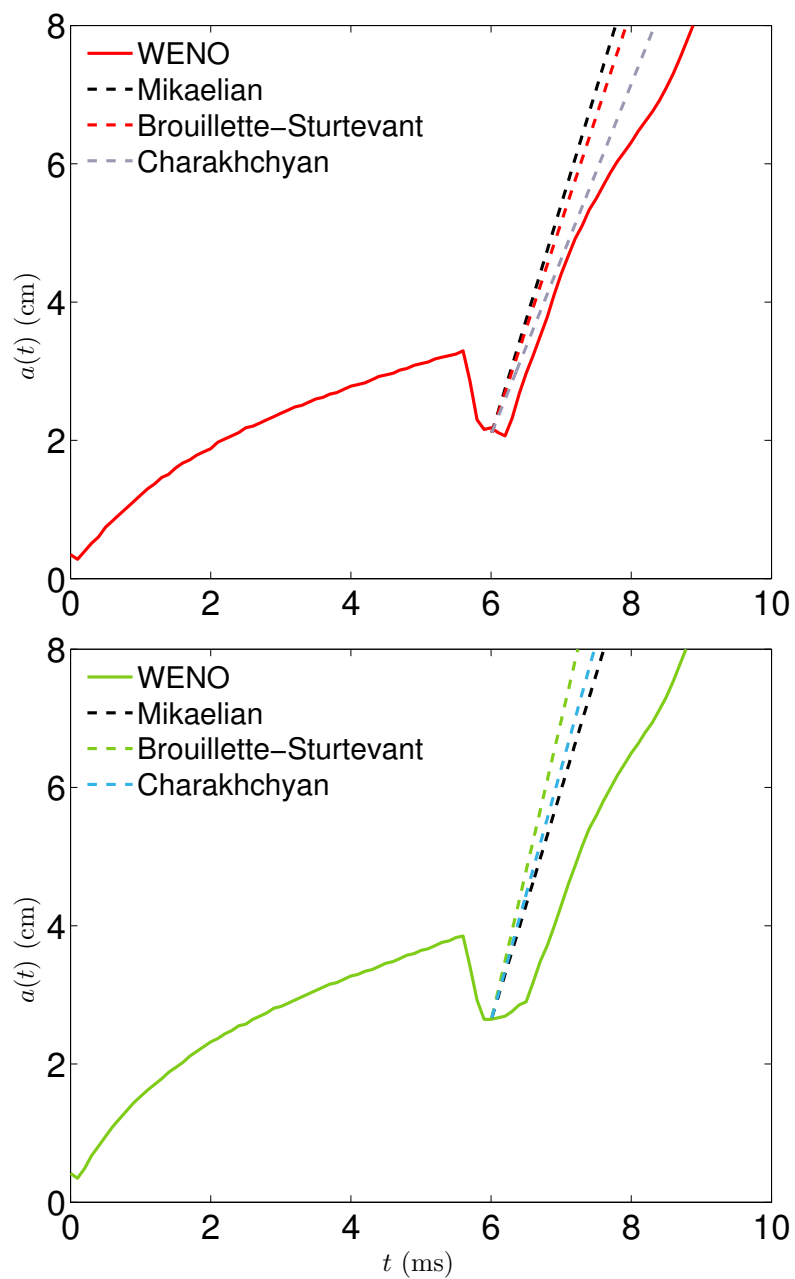


Figure 5.15. The mixing layer amplitude $a(t)$ versus time t from the three-dimensional WENO simulation with $a_0^- = 0.205$ cm (top) and $a_0^- = 0.29$ cm (bottom), together with the predictions of the Mikaelian, Brouillette-Sturtevant, and Charakhch'yan reshock models.

5.5 Atwood number study using the vorticity-streamfunction method

Presented here is a study of the effects of the Atwood number A on the evolution of the single-mode Richtmyer-Meshkov instability in three dimensions. Simulations using the VS method are performed for $A = 0, 0.2, 0.4, 0.6,$ and 0.8 , including visualization of the instability evolution using enstrophy and mass fraction isosurfaces and cross-sections of the density and vorticity fields (Sec. 5.5.1), and a comparison of the perturbation, bubble and spike amplitudes to the predictions of the Zhang-Sohn models (Sec. 5.5.2).

5.5.1 Comparison of instability evolution and vorticity dynamics

Presented here are visualizations of the mass fraction and enstrophy isosurfaces for $A = 0$ and 0.4 . The mass fraction isosurface illustrates the instability development in three dimensions, while the enstrophy isosurface illustrates the dynamics of vorticity. The visualizations illustrate the dynamics of both the spike and bubble. For all visualizations, the perspective is from the heavier fluid (or in the case of $A = 0$, from the fluid corresponding to $m = 1$).

Figure 5.16 shows the time-evolution of the mass fraction and enstrophy isosurfaces for $A = 0$. At 1 ms, the mass fraction isosurface shows the linear stage of the instability development with the growth of the bubble and spike. For $A = 0$, the bubble and spike are symmetric. In general, for $A \neq 0$ the spike contracts, while the bubble expands. At 3 ms, roll-ups are already visible and the vorticity assumes a ring-like structure. At 5 ms, roll-ups are further developed. At 7 ms, the roll-up is fully developed and is visible on the sides of the mass fraction isosurface. In three dimensions there are two regions where roll-ups occur; at the spike (as in two dimensions), and in the bubble region.

Figure 5.17 shows the time-evolution of the mass fraction and enstrophy isosurfaces for $A = 0.4$. As the Atwood number increases, the symmetry between the bubble and spike for $A = 0$ in Figure 5.16 is lost. Instead, as the instability develops, the bubble rises into the heavier fluid and expands, while the spike penetrates into the lighter fluid and contracts. This is already visible at 5 ms, where the size of the bubble roll-up is larger than the roll-up for the spike.

Figure 5.18 show the cross-sections of the density and components of the vorticity field. The cross-sections are taken in the longitudinal (x, z) -plane and correspond to the middle of the spike region at 0 ms. The cross-section for $\omega_3(x, z)$ is shown at 0.2 ms, as it is zero at the initial time. Only the spike region is shown, as the bubble region shows similar behavior. Visualizations at 1, 3, 5, and 7 ms illustrate the time-evolution of the instability. Results are compared for $A = 0, 0.2, 0.4, 0.6,$ and 0.8 to understand how the dynamics change as a function of the Atwood number.

Figure 5.19 shows the time-evolution of the density cross-section $\rho(x, y, z)$ as a function of time

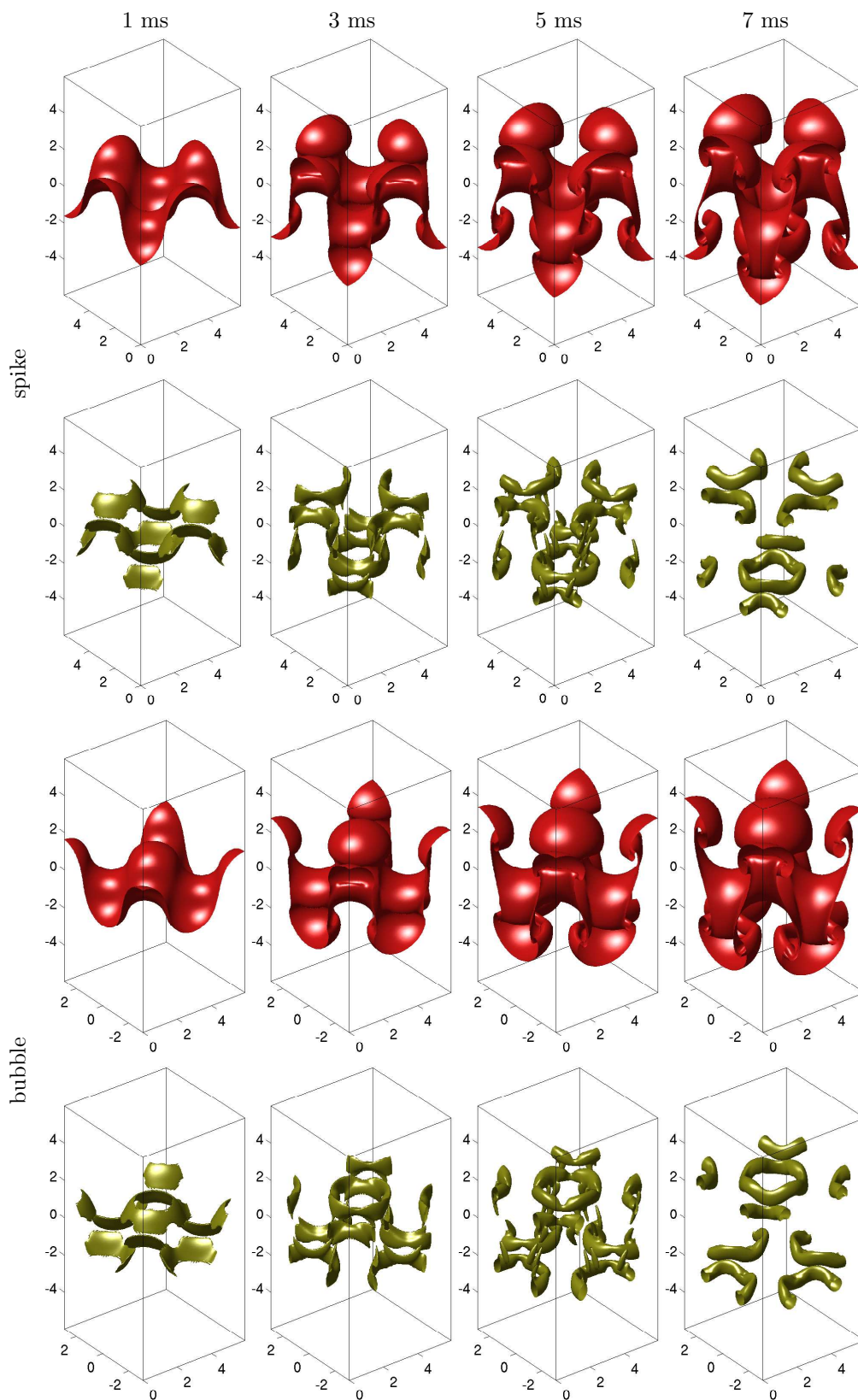
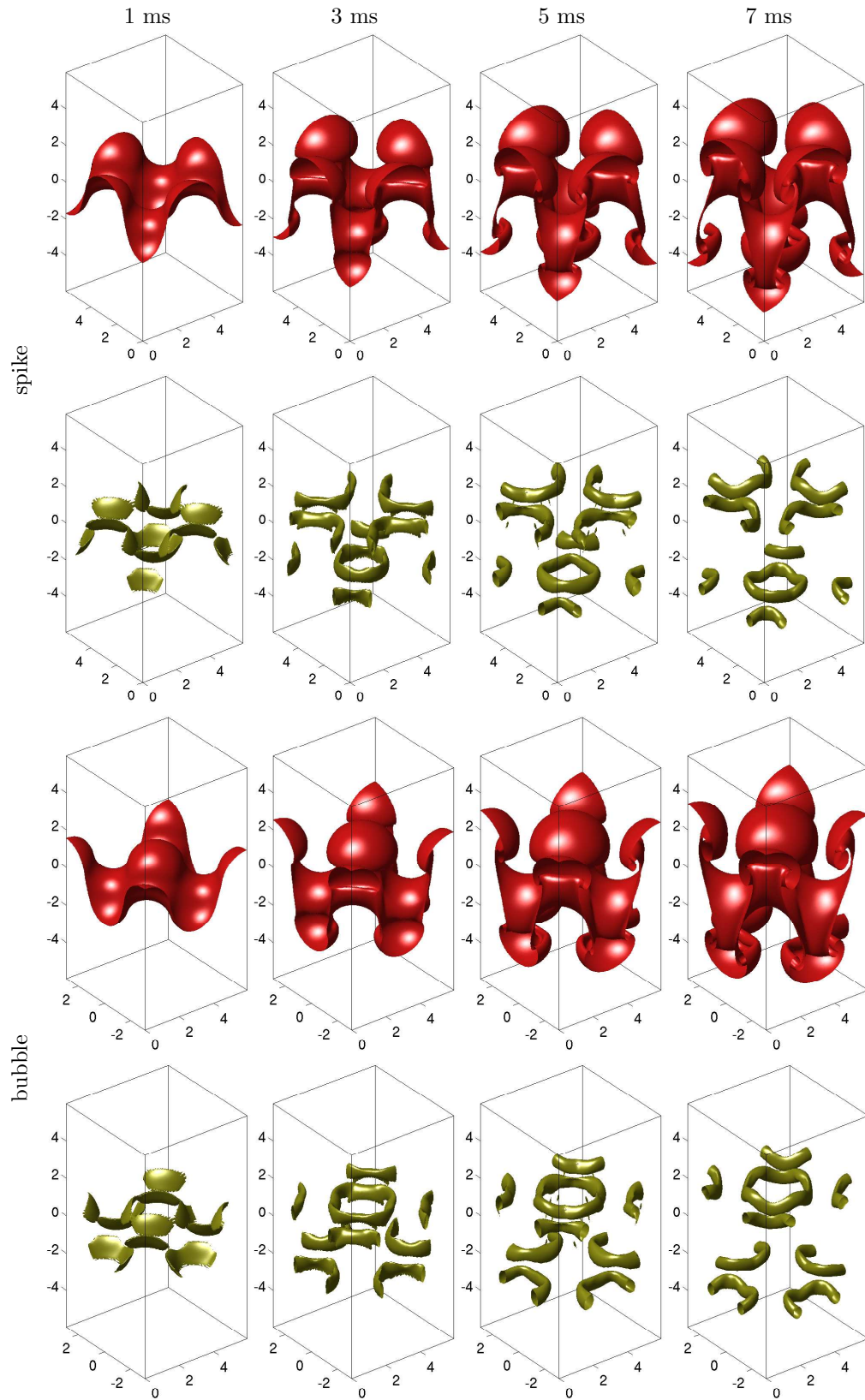


Figure 5.16. Time-evolution of the mass fraction and entropy isosurfaces for $A = 0$ at 1, 3, 5, and 7 ms from the VS simulation.

Figure 5.17. Same as Figure 5.16 but with $A = 0.4$.

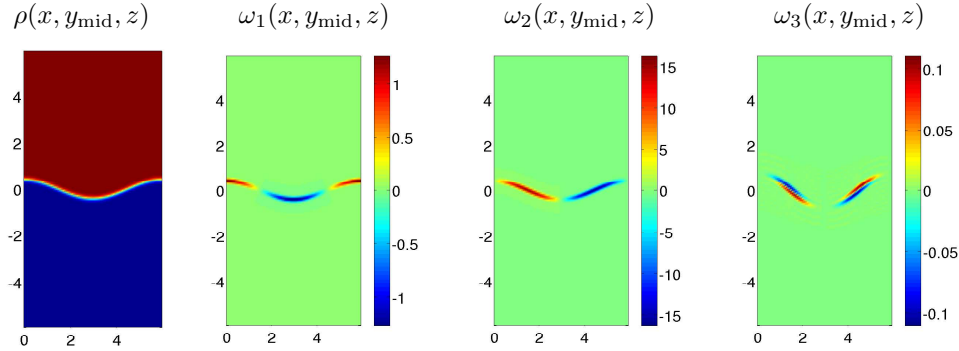


Figure 5.18. The density cross-section $\rho(x, y_{\text{mid}}, z)$ and cross-sections for the three components of the vorticity field, $\omega_1(x, y_{\text{mid}}, z)$, $\omega_2(x, y_{\text{mid}}, z)$ at 0 ms and $\omega_3(x, y_{\text{mid}}, z)$ at 0.2 ms.

and A . For $A = 0$, the image shown corresponds to the mass fraction cross-section $m(x, y, z)$ in the spike region. The visualization shows the initial growth of the spike and bubble at 1 ms. At 3 ms, the beginnings of the roll-ups in the bubble and spike region are visible. At 5 and 7 ms, the roll-up further develops, showing symmetry between the bubbles and spikes. Comparing the mass fraction cross-sections of the three-dimensional simulations with those of the two-dimensional simulations (Fig. 4.28) shows similarities in the development of the spike roll-up. In both cases, the spike roll-up develops at 3 ms, and a fully-developed roll-up forms at 5 ms. The $A = 0.2$ results show little differences compared with the $A = 0$ results except that the spike is now smaller. This trend is visible in the 5 ms cross-section for $A = 0.4$. As the Atwood number increases, the spike also penetrates further into the lighter fluid. The images corresponding to $A = 0.6$ and 0.8 show similar trends, including a smaller spike roll-up and deeper penetration of the spike.

Figure 5.20 shows the time-evolution of the cross-section of the first component of the vorticity field $\omega_1(x, y_{\text{mid}}, z)$ as a function of the Atwood number. At 0 ms, this component shows a negative region corresponding to the tip of the spike and a positive region corresponding to the tip of the bubble. The regions of strongest vorticity correspond to the mid-point between the bubble and spike tip. Consider now the case $A = 0$. As the instability develops at 1 ms, this component follows the growth of the bubble and spike, and intensifies in the region corresponding to the mid-point between the bubble and spike. At 3 ms, the vorticity is now concentrated in a bilayer of positive and negative vorticity in the region between the bubble and spike. At 5 ms, the vorticity rolls-up in the bubble and spike. At 7 ms, the center of the roll-up shows vorticity of opposite sign. As the Atwood number is increased to $A = 0.2$ and 0.4 , the vorticity follows the more elongated and thinner spike. For $A = 0.6$ at 3 ms, the vorticity field shows a negative layer corresponding to the tip of the spike. This layer rolls up at later time. For $A = 0.8$, the vorticity shows a strong negative region corresponding to the tip of the bubble at all times. A strong positive layer of vorticity is present in the region between the bubble and spike.

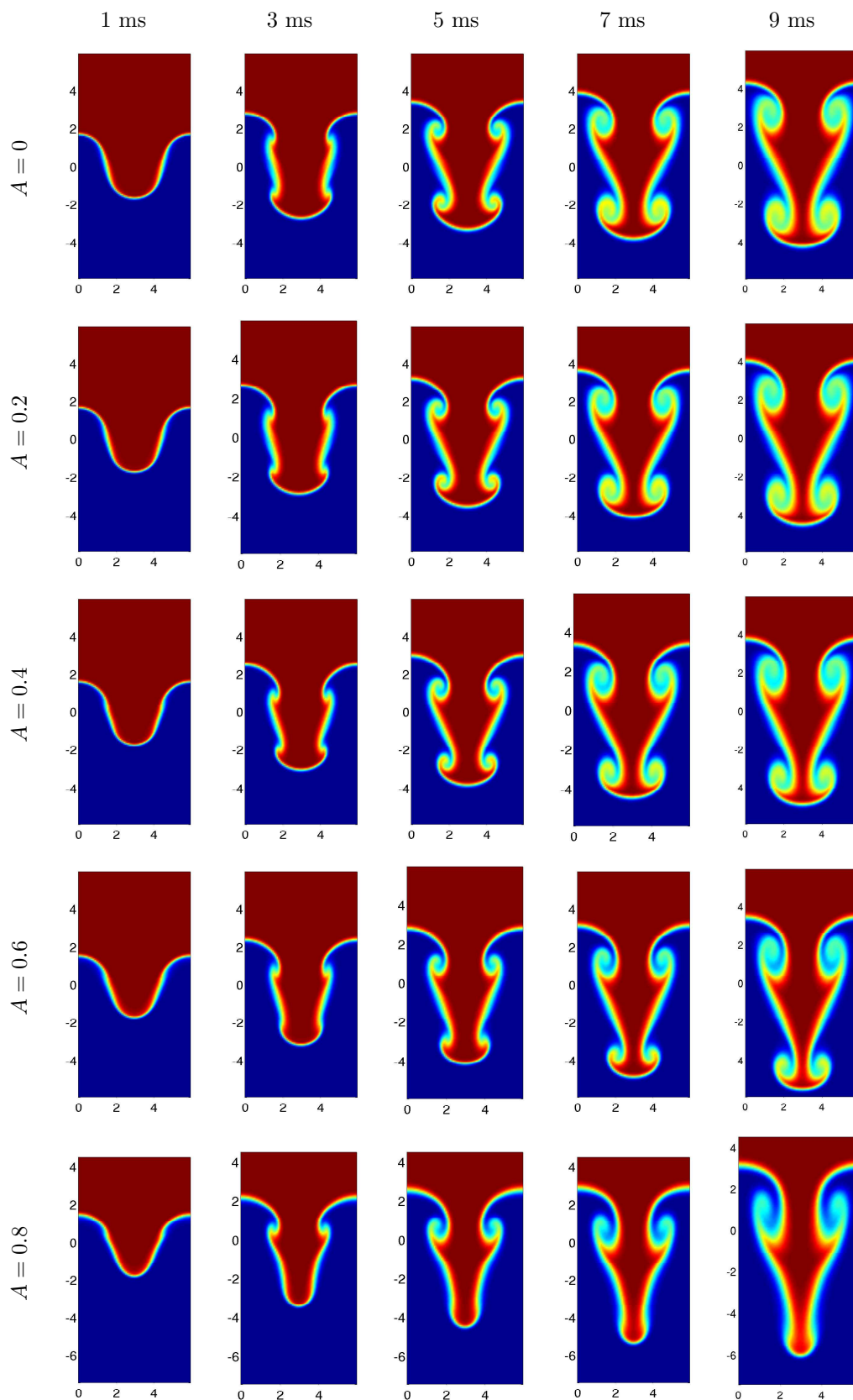


Figure 5.19. Time-evolution of the (x, z) -cross-section of the density field $\rho(x, y_{\text{mid}}, z)$ for $A = 0, 0.2, 0.4, 0.6,$ and 0.8 at 1, 3, 5, 7, and 9 ms from the VS simulation.

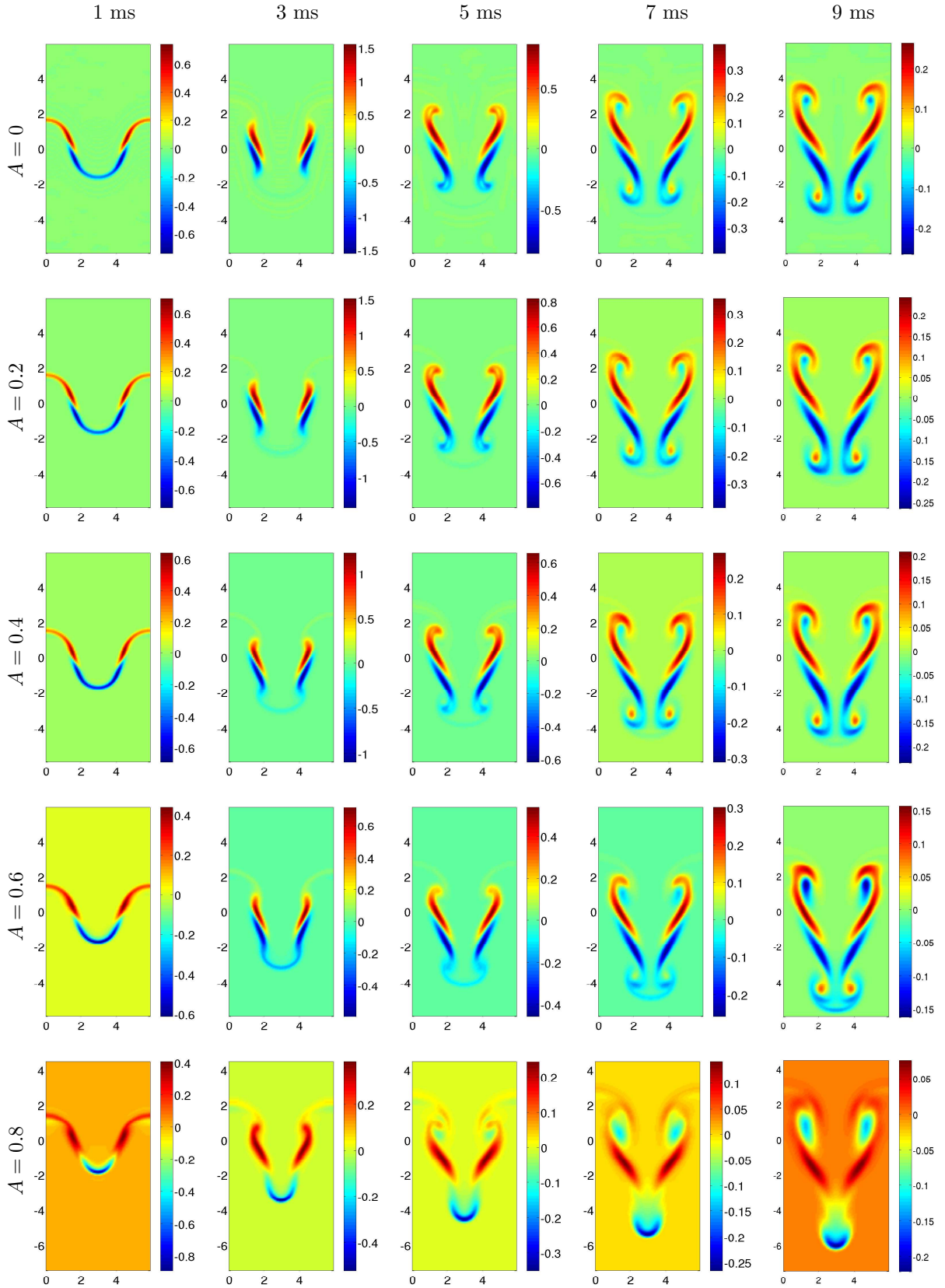


Figure 5.20. Time-evolution of the (x, z) -cross-section for the first component of the vorticity field $\omega_1(x, y_{\text{mid}}, z)$ for $A = 0, 0.2, 0.4, 0.6, \text{ and } 0.8$ at 1, 3, 5, 7, and 9 ms from the VS simulation.

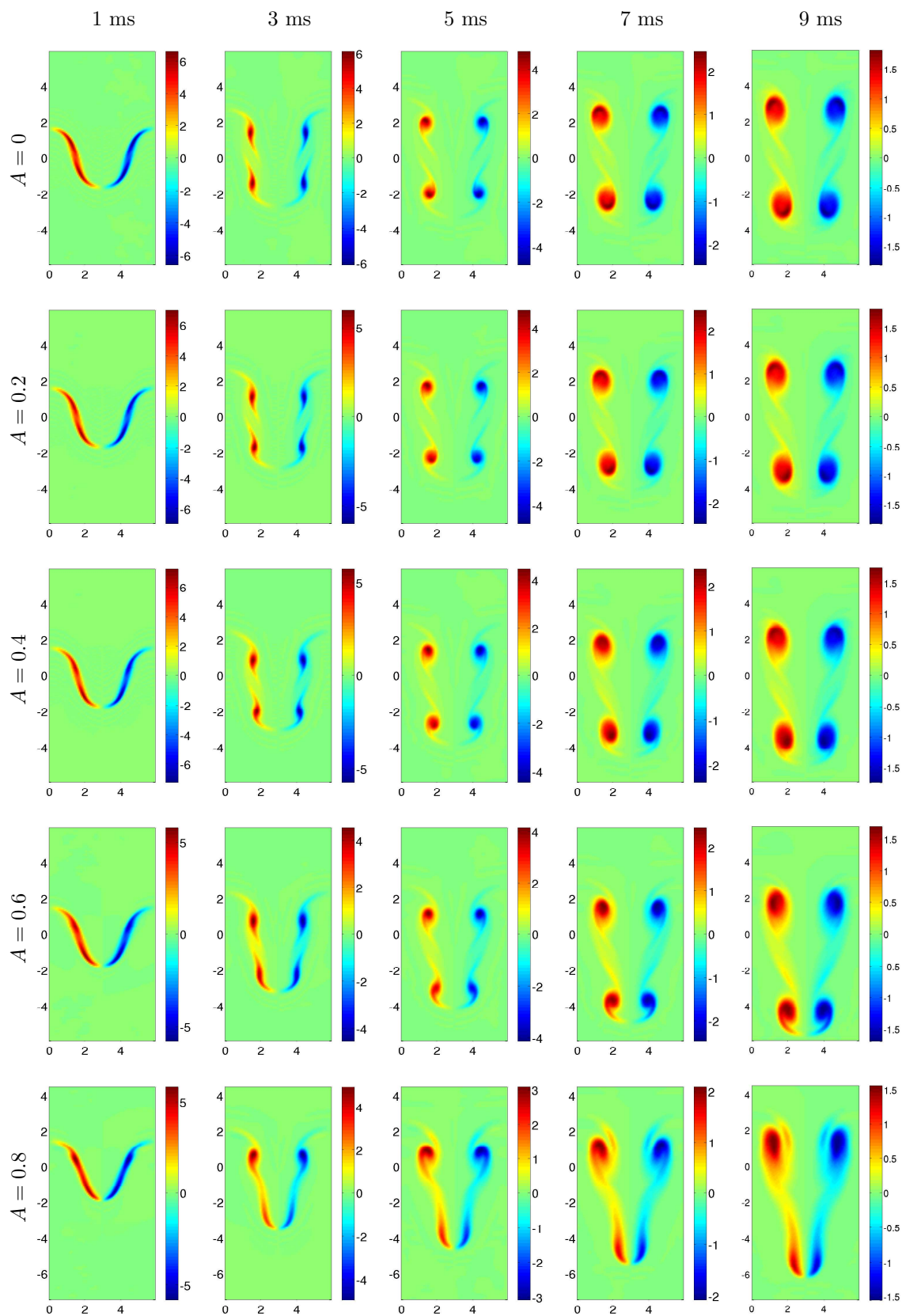


Figure 5.21. Same as Figure 5.20 but for the second component of the vorticity field $\omega_2(x, y_{\text{mid}}, z)$.

Figure 5.21 shows the time-evolution of the cross-section of the second component of the vorticity field $\omega_2(x, y_{\text{mid}}, z)$ as a function of the Atwood number. At 0 ms, this component has the same distribution observed in two dimensions, with a positive and negative layer on opposite sides of the tip of the spike. Consider now the evolution for $A = 0$. At 1 ms, as the bubble and spike grow, the vorticity forms two regions of strong positive and negative vorticity, one closer to the bubble tip and one closer to the spike tip. At 3 ms, the roll-ups of the bubble and spike are visible. At 5 and 7 ms, the cores become stronger and larger. For $A = 0$, the rotating cores corresponding to the tip of the bubble and spike are located one on top of the other. By contrast, as A increases, the cores corresponding to the spike are closer together, further indicating that the spike contracts while the bubble expands. For $A = 0.8$, the vorticity of the spike forms a layer that is close to rolling up at 7 ms.

Figure 5.22 shows the time-evolution of the cross-section of the third component of the vorticity field $\omega_3(x, y_{\text{mid}}, z)$ as a function of the Atwood number. This component is zero at 0 ms, corresponding to the initial distribution following linear instability theory. As a result, the time-evolution is only shown starting at 0.2 ms. For $A = 0$, this vorticity distribution corresponds to a vortex bilayer located at the mid-point between the bubble and spike, which shows positive vorticity on the bubble side and negative vorticity on the spike side. At 1 ms, the bilayer is still present and located in the region between the bubble and spike. The vorticity has intensified, going from a maximum magnitude of 0.1 to 0.5 ms^{-1} . At 3 ms, the bilayer is still present and further intensifies with a maximum value of 1.5 ms^{-1} . At 5 and 7 ms, a roll-up is observed, where the cores are represented by vorticity of opposite sign compared to the sign of the vorticity in the layer. As the Atwood number is increased, the bilayer at 0.2 ms shows one side becoming stronger. At late times, stronger positive and negative cores are observed in the roll-up regions.

5.5.2 Comparison of the perturbation, bubble, and spike amplitudes to the predictions of amplitude growth models

Presented here is a quantitative comparison of the perturbation, bubble, and spike amplitudes from the VS simulations with the predictions of the Zhang-Sohn model [157].

Figure 5.23 show a comparison of the amplitudes from the three-dimensional VS simulations as the Atwood number is varied. As A increases, the spike amplitude increases and the bubble amplitude decreases. However, the overall perturbation amplitude is nearly constant and increases only for $A = 0.6$ and 0.8 . This is in contrast to the perturbation amplitude in two dimensions (Fig. 4.38). The results suggest that in three dimensions, Atwood number effects are less pronounced than in two-dimensions.

Figure 5.24 shows a comparison of $a(t) - a(0^+)$ from the VS simulation with the prediction of the

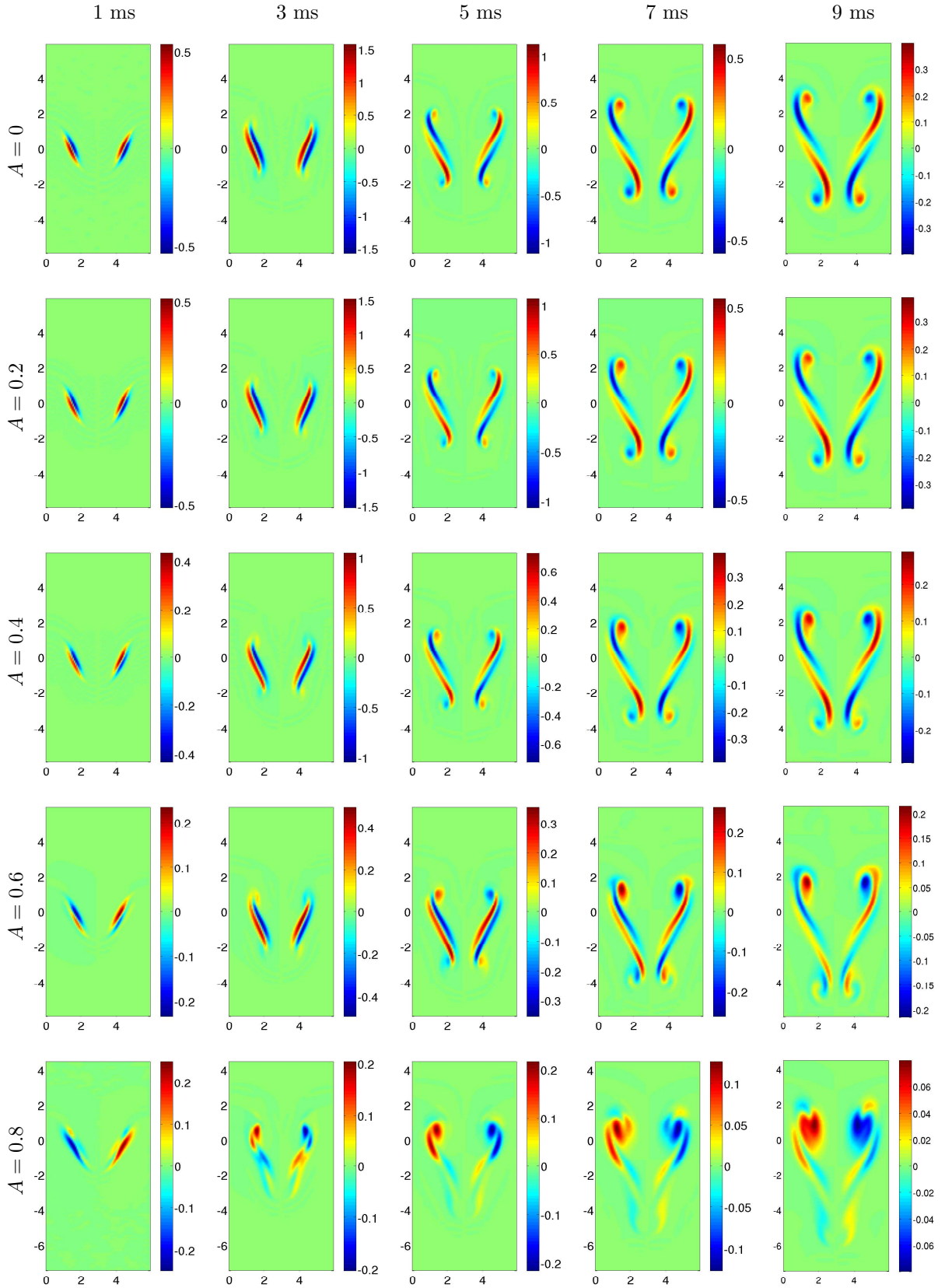


Figure 5.22. Same as Figure 5.20 but for the third component of the vorticity field $\omega_3(x, y_{\text{mid}}, z)$.

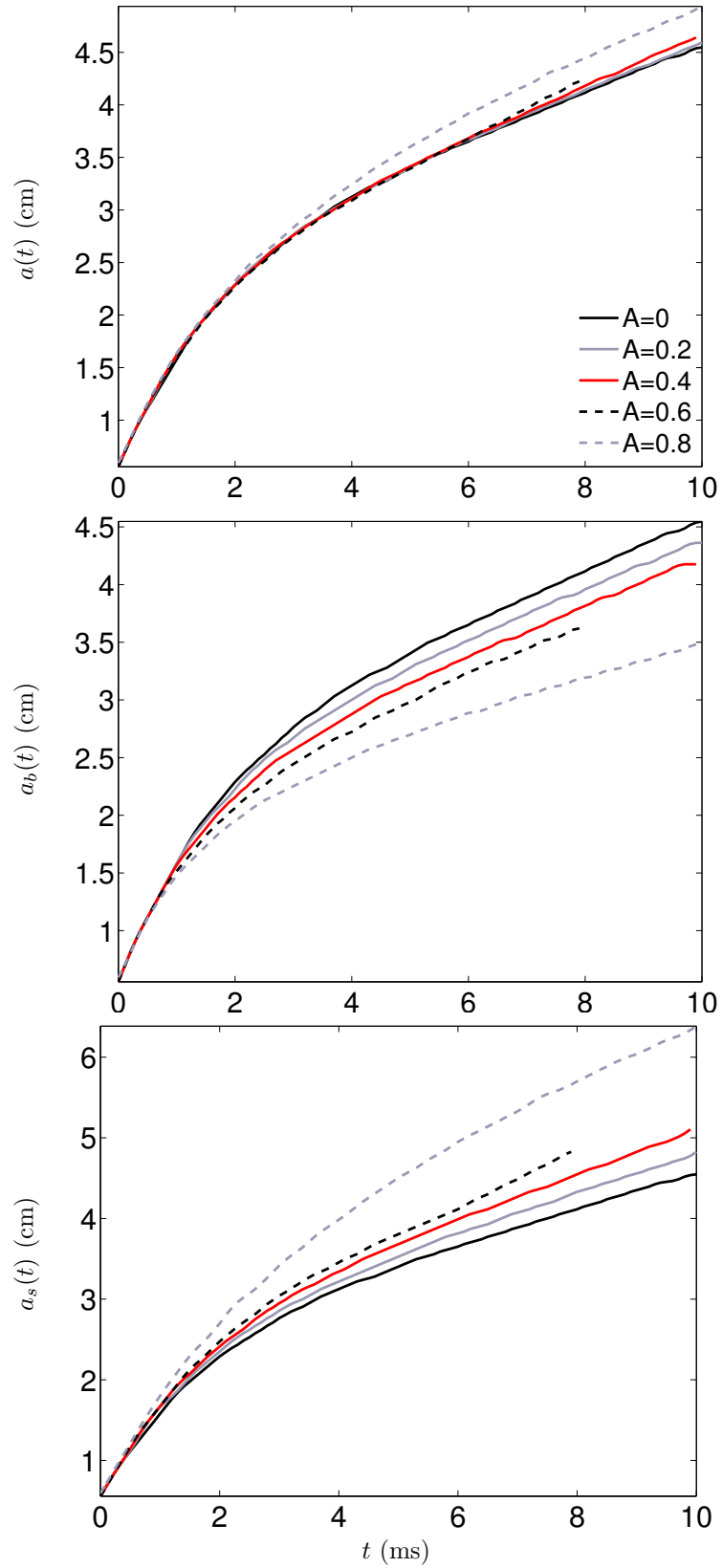


Figure 5.23. Comparison of the perturbation, bubble, and spike amplitudes, $a(t)$, $a_b(t)$ and $a_s(t)$, respectively, for $A = 0, 0.2, 0.4, 0.6,$ and 0.8 from the three-dimensional VS simulation.

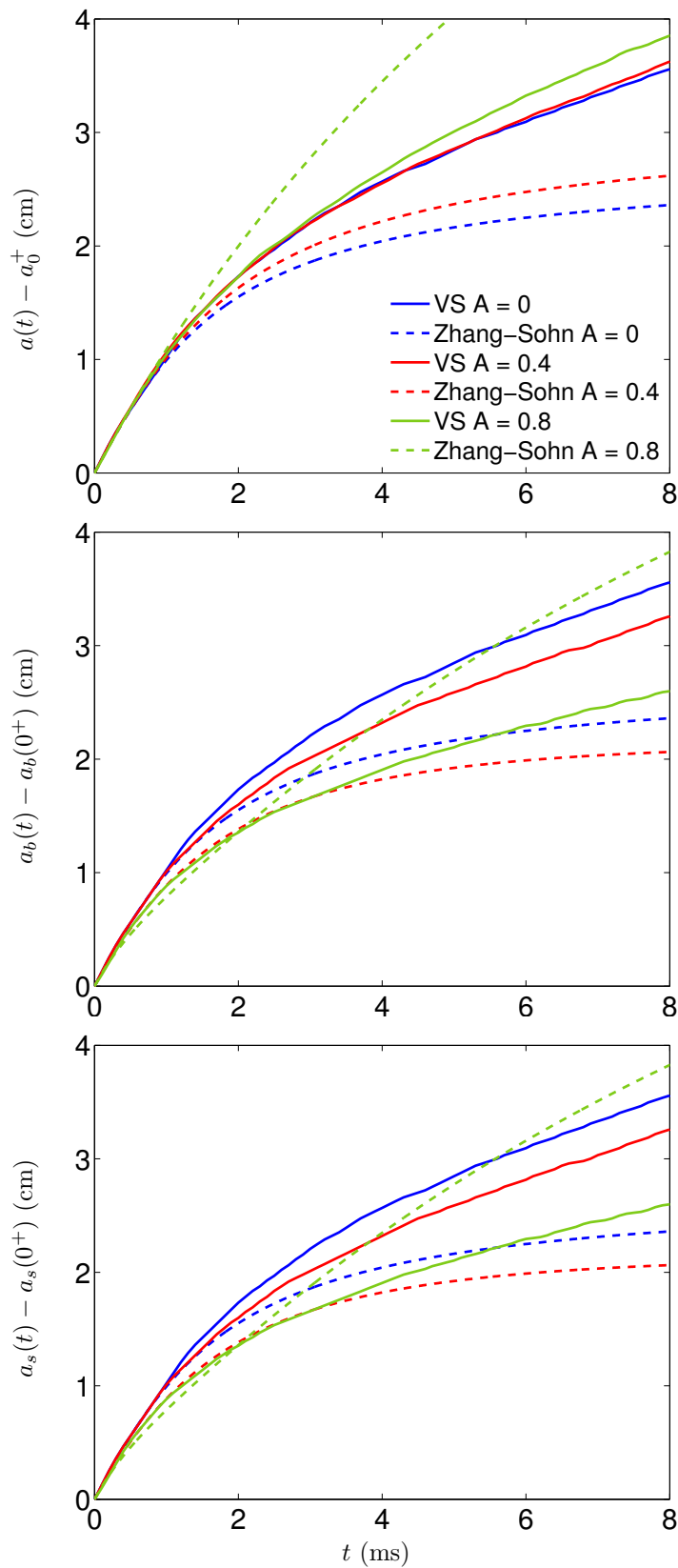


Figure 5.24. The perturbation, bubble, and spike amplitudes $a(t) - a(0^+)$, $a_b(t) - a_b(0^+)$, and $a_s(t) - a_s(0^+)$, respectively, from the VS simulations with $A = 0, 0.4$, and 0.8 and the predictions of the Zhang-Sohn model.

$A = 0$	Δ_{sim}
Zhang-Sohn Padé (all)	8.06
Zhang-Sohn Padé (bubble)	8.06
Zhang-Sohn Padé (spike)	8.06

$A = 0.2$	Δ_{sim}
Zhang-Sohn Padé (all)	8.12
Zhang-Sohn Padé (bubble)	12.05
Zhang-Sohn Padé (spike)	5.16

$A = 0.4$	Δ_{sim}
Zhang-Sohn Padé (all)	5.21
Zhang-Sohn Padé (bubble)	13.56
Zhang-Sohn Padé (spike)	1.82

$A = 0.6$	Δ_{sim}
Zhang-Sohn Padé (all)	2.23
Zhang-Sohn Padé (bubble)	11.94
Zhang-Sohn Padé (spike)	9.15

$A = 0.8$	Δ_{sim}
Zhang-Sohn Padé (all)	8.86
Zhang-Sohn Padé (bubble)	7.66
Zhang-Sohn Padé (spike)	15.8

Table 5.7. Average fractional deviation Δ_{sim} between the VS amplitude and the predictions of the Zhang-Sohn model for $A = 0, 0.2, 0.4, 0.6,$ and 0.8 .

Zhang-Sohn Padé model [Eq. (5.13)]. For $A = 0$, the Zhang-Sohn model shows agreement at early times before diverging. These observations apply also to $A = 0.4$. For $A = 0.8$, the Zhang-Sohn Padé models overpredict the perturbation amplitude. Figure 5.24 and shows a comparison of $a_b(t) - a_b(0^+)$ from the VS simulations at $A = 0, 0.4,$ and 0.8 and the predictions of the Zhang-Sohn bubble amplitude model [Eq. (5.14)]. For $A = 0$ and 0.4 , the Zhang-Sohn models show good agreement at early-to-intermediate times. At late times, the models underpredict the bubble amplitudes. For $A = 0.8$, the Zhang-Sohn model overpredicts the bubble amplitude from the simulations. Figure 5.24 also shows a comparison of the spike amplitude $a_s(t) - a_s(0^+)$ from the VS simulation and the prediction of the Zhang-Sohn model [Eq. (5.15)]. For $A = 0$ and 0.4 , the model is in good agreement with the simulation amplitudes at early times. At intermediate-to-late times, the models underpredict. For $A = 0.8$, the Zhang-Sohn model overpredicts the amplitudes. The agreement between the simulations and the model predictions can be made more quantitative by computing the average fractional deviation Δ_{sim} [Eq. (4.40)] shown in Table 5.7.

Chapter 6

Conclusions

A vorticity-streamfunction method was developed to investigate the single-mode Richtmyer-Meshkov instability in two and three dimensions. In the VS method, the vortex sheet representation of the shocked interface in classical vortex methods was thickened to obtain a vortex layer. Such thickening corresponds to the shocked diffuse interface in the experiments of Jacobs and Krivets [62], which serve as a model for the present investigation. The VS method was then applied to investigate the single-mode Richtmyer-Meshkov instability in two and three dimensions with a comparison to the compressible WENO method and to other incompressible vortex methods.

The formally high-order WENO method is a modern reconstruction-evolution shock-capturing scheme for the compressible simulations of complex flows with shocks. As such, simulations are performed *ab initio* with a shock launched in the air(acetone) refracting into the SF₆ following the interaction with the diffuse interface. The VS and WENO methods represent two different, yet complementary, approaches to investigate this instability.

Presented here is a summary of the major findings from each of the chapters in the thesis.

6.1 Development and numerical implementation of the vorticity-streamfunction method

A vorticity-streamfunction method for the incompressible simulations of the Richtmyer-Meshkov instability was developed in Chapter 2. The VS method, and more generally vortex methods, offers an alternative to compressible simulations and to nonlinear growth models to reach the nonlinear stages of the instability evolution. The VS method was motivated by limitations in vortex method approaches for investigating this instability. (1) In the purely Lagrangian vortex method (Sec. 2.1.2), the algorithm for the evolution of the vortex sheet required complex regularization procedures to overcome the formation of the singularity during roll-up [71, 13, 7]. In addition, the formation of singularities required a redistribution of the vortex markers [68], and the numerical method may also

cease to provide solutions at late times. (2) The velocity field from the hybrid Lagrangian-Eulerian vortex method based on the vortex-in-cell algorithm (Sec. 2.1.3) did not converge under grid refinement to the velocity field from the Biot-Savart law (Sec. 2.2.1). Oscillations in the velocity developed due to the singular limit represented by a (thin) vortex sheet [126]. When interpolation kernels based on central B-splines [109] with larger stencils were used, the oscillations still develop, but on finer grids. Higher order interpolation kernels obtained from Richardson extrapolation [109] developed oscillations on coarser grids. As a result, the classical VIC method can only be used to investigate the Richtmyer-Meshkov instability when fairly coarse Cartesian grids are used. To overcome this limitation, the vortex sheet was thickened using a Gaussian to obtain a vortex layer. The simultaneous reduction of the grid spacing and diffuse-interface thickness produced initial conditions that converged to the Biot-Savart solution (Sec. 2.2.2). The rate of convergence can be increased by using Richardson extrapolation. The thickening of the sheet has the desirable feature of providing a “physical” solution to the instability problem and is equivalent to the diffusive thickness in the Jacobs and Krivets [62] experiments. This is in contrast to the “unphysical” length-scale introduced by using vortex blobs (in the Lagrangian- γ method) and the grid spacing Δx (in the VIC method). Furthermore, the numerical method can be easily extended to three dimensions.

In the VS method (Sec. 2.3), the vorticity assigned on the grid using the technique from the VIC method (which ensured that the velocity field converged to the velocity of a vortex sheet in the limit of decreasing diffuse-interface width) was evolved using the vorticity equation augmented by the baroclinic vorticity production term to capture the effects of the instability. As a result, an auxiliary density equation was evolved with initial diffuse thickness given by a hyperbolic tangent [125, 94]. The pressure was obtained by solving the pressure Poisson equation with Neumann boundary conditions.

The equations were discretized using a semi-implicit fourth-order in space third-order in time Adams-Bashforth backward differentiation scheme (AB/BDI3) scheme, which uses multiple time-levels for both the time and spatial operators (Sec. 2.3.3). A stability analysis showed that the region of stability for this scheme is largest among other Adams-Bashforth backward differentiation schemes. Fourth-order finite-difference operators were used for the spatial derivatives. The vorticity-streamfunction Poisson equation was discretized using a fourth-order nine-point scheme. The fast Fourier transform was used to invert the block-Toeplitz-symmetric-tridiagonal (TST) finite-difference matrices (*Hockney’s method* [59]). When viscosity was present, the final implicit linear equation was a Helmholtz equation, which was solved by modifying the nine-point scheme for the Poisson equation. This method was extended to three dimensions.

6.2 Investigation of convergence of the vorticity-streamfunction method

The dependence of the evolution of the vortex layer on numerical parameters (including grid spacing Δx and time step Δt) and physical parameters (including the diffuse interface thickness δ_T , the viscosity ν , and mass diffusivity \mathcal{D}) was investigated in Chapter 3. Fourth-order in space and third-order in time point-wise convergence was demonstrated for a vortex layer with fixed thickness δ_T (Sec. 3.1). When $A = 0$ and $\nu = 0$, fourth-order spatial convergence was observed only at early times, demonstrating that the method is stable. As the instability developed, the heavy fluid pushed onto the lighter fluid, decreasing the thickness of the layer and increasing the gradients, resulting in the generation of oscillations. Increasing the grid resolution delayed but did not prevent, the onset of such oscillations. In fact, the fine-scale structure of the roll-up eventually created sufficiently steep gradients to generate oscillations. The oscillations became more severe at later times, decreasing the convergence rate of the method. To prevent the formation of steep gradients, viscosity ν and mass diffusivity \mathcal{D} were introduced, keeping the Schmidt number ($Sc \equiv \nu/\mathcal{D}$) unity, consistent with gas dynamics properties. This led to fourth-order pointwise spatial convergence for all times. The perturbation, bubble, and spike amplitudes, and the circulation also exhibited fourth-order spatial convergence.

Visualizations of the instability as the diffuse-interface thickness δ_T and viscosity ν vary (Sec. 3.2.1) showed that significant variation occurs in the small-scale features as δ_T decreases, while no significant difference was observed as ν decreases. As a result, a grid convergence study was performed for the smallest value of the viscosity as the diffuse-interface thickness was decreased (Sec. 3.2.2) to ensure that the solution was inside the region of convergence. All of the simulations exhibited fourth-order convergence at early times. At later times and for smaller values of the diffuse-interface thickness and viscosity, high order required sufficient resolution to resolve all small-scale structures. When insufficient resolution was used, the method generated oscillations that degraded the solution. Even when sufficient resolution was used to prevent the formation of oscillations, the resolution was still insufficient to guarantee fourth-order convergence. Regions with second- and third-order convergence were observed prior to full fourth-order convergence. In general, a resolution of $N_x = 512$ points per initial perturbation wavelength was sufficient to guarantee that the results were in the region of fourth-order convergence for the diffuse-interface thickness and viscosity used here. The perturbation, bubble, and spike amplitudes were in good agreement as δ_T and ν were varied, indicating that these quantities were not very sensitive to these parameters. The average fractional deviation (used to quantify the distance to the curve corresponding to the smallest δ_T and ν) became smaller as δ_T and ν decreased.

6.3 Investigation of the two-dimensional single-mode Richtmyer-Meshkov instability

The incompressible vorticity-streamfunction method was applied to investigate the two-dimensional single-mode Richtmyer-Meshkov instability in Chapter 4. Simulations were performed on a model of the Jacobs and Krivets [62] (Sec. 4.2.1) Mach 1.3 air(acetone)/SF₆ experiment to provide an element of validation. The results were compared to those from compressible WENO simulations.

The WENO method [12] (Sec. 4.1) is a shock-capturing scheme used in the investigation of the Richtmyer-Meshkov instability [78] and more generally flows with shocks. As with all other shock-capturing methods, at most first-order accuracy can be expected in the post-shock region [89, 108]. In fact, multiple families of characteristics intersect the shock, so that the error near the shock propagates to the entire post-shock region [36]. Despite the loss of accuracy, high-order shock-capturing methods remain desirable for the accurate evolution of high-frequency components and small-scale structure [21] present in the complex mixing layer of the Richtmyer-Meshkov instability, and for the reduced numerical dissipation associated with higher-order WENO flux reconstructions and finer grids [77]. As in other upwind schemes, the nonlinearity and upwinding in the WENO method removes the generation of spurious oscillations, making the method more stable. A comparison of the fifth- and ninth-order WENO methods for different grid resolutions (Sec. 4.3) indicated differences in the small-scale structure within the roll-ups, consistent with what is generally observed in simulations of this flow [78]. More importantly, the overall height and width of the stem did not vary. A convergence study for the perturbation, bubble, and spike amplitudes and circulation showed second-order convergence as the grid was refined, and no significant difference between the amplitude from the fifth- and ninth-order simulations.

In the present implementation of the WENO method, only a single value of the adiabatic exponent can be specified. As a result, the conditions of a mixture of 50% air(acetone) 50% SF₆ were adopted in the *mix initial conditions* (Sec. 4.2.2). The Mach number of the incident shock was adjusted so that the initial growth rate v_0 matched that in the experiment. An alternative approach to the mix initial conditions was the *upstream initial conditions*, where the adiabatic exponent of the air(acetone) mixture is used [78]. It was shown (Sec. 4.5.3) that using the mix and upstream initial conditions led to different wave velocities. However, the time of reshock was the same, the growth was very similar, and the agreement with the model predictions and experimental data points was the same. As a result, the choice of initial conditions did not affect the instability dynamics. As the VS simulation began immediately following the passage of the shock, the vorticity deposited in the WENO method was compared to the predictions of linear instability theory and the Samtaney-Zabusky [127, 128] circulation-deposition model (Sec. 4.2.3). Excellent agreement was found between the vorticity deposited by the shock and the predictions of the models. As a result, the VS method

was initialized using the linear instability model, due to the more direct physical interpretation of this initial condition (Sec. 4.2.4).

A comparison of the density fields from the fifth- and ninth-order WENO and VS methods with the experimental PLIF images (Sec. 4.4) showed agreement in the large-scale structures but differences in the small-scale structures. In particular, the WENO and PLIF images showed similar small-scale disordered structure within the roll-ups. Such structure was not captured by the VS method, which showed a strong rotating core. Despite these differences, the perturbation amplitudes from the WENO and VS methods were in good agreement and generally matched the experimental data points well (Sec. 4.5). The bubble and spike amplitudes showed differences, with the bubble amplitude from the WENO method smaller than that from the VS method, and the spike amplitude from the WENO method larger than that from the VS method. To understand this, simulations with different Mach numbers were compared (Sec. 4.6). For small Mach numbers, the bubble and spike amplitudes from the WENO and VS simulations were very similar. As the Mach number was increased, the agreement between the WENO and VS methods decreases. Furthermore, the bubble amplitude from the WENO $Ma_i = 1.45$ simulation was smaller than that from the $Ma_i = 1.31$ simulation. In fact, following shock refraction and the instantaneous deposition of vorticity on the interface, the corrugated transmitted shock stabilized, generating pressure waves which interacted with the layer, causing a decrease in the bubble growth and an increase in the spike growth [150]. In the incompressible VS method, such corrections were not present, explaining the discrepancy in the bubble and spike amplitudes. The perturbation amplitudes from the WENO and VS methods were also compared with the predictions of nonlinear amplitude growth models (Sec. 4.5.2), where the growth was reduced to account for the diffuse initial interface [34]. In general, the models agreed with the simulation amplitudes at early-to-intermediate times ($\tau < 4$) and underpredicted at later times, corresponding to the late nonlinear regime.

The WENO method was also used to investigate the reshock process (Sec. 4.7), which occurs when the transmitted shock reflects from the end wall of the test section and interacts with the evolving mixing layer. Reshock is of fundamental interest [129] as it imparts additional energy into the layer and contributes to the formation of complex disordered structures. The mixing layer amplitude was also compared to the predictions of reshock models and good agreement was found.

Finally, the VS method was developed for the evolution of a vortex layer, which naturally arises in shocked stratified flows and in the presence of viscosity. However, in the limit of small thickness, the vortex layer is expected to give results consistent with the evolution of a vortex sheet. As a result, the VS method was compared to the classical Lagrangian and vortex-in-cell methods as the Atwood number was varied (Sec. 4.8). For low Atwood numbers, all three methods were in agreement. As the Atwood number increased, the VS method showed differences in the bubble and spike amplitudes compared to the Lagrangian and VIC methods. This can be expected, as the

baroclinic vorticity production for a diffuse layer is different from that of an infinitely thin layer. The amplitudes from the simulations were also compared to the predictions of nonlinear amplitude growth models. In general, the models agreed with the simulation data at early-to-intermediate times and underpredicted at late times. The VS method and, more generally, vortex methods are valid methods to reach the late nonlinear regime.

6.4 Investigation of the three-dimensional single-mode Richtmyer-Meshkov instability

One of the main goals when developing the vorticity-streamfunction method was the ability to extend the formulation to three dimensions. In the present thesis, the VS method was extended to three dimensions and applied to the single-mode Richtmyer-Meshkov instability in Chapter 5.

The initial conditions for the simulations (Sec. 5.1) were the same as in two dimensions, but with an additional periodic dimension. The initial perturbation was a product of sinusoids, consistent with previous three-dimensional single-mode investigations [84, 157]. For these initial conditions, the effective wavenumber (which enters into the determination of the growth rate v_0) was larger than the corresponding two-dimensional value. As a result, simulations with larger v_0 and with a reduced amplitude (so that v_0 is the same as in two dimensions) were performed using both the WENO and VS methods. For the VS method, the initial conditions were taken from three-dimensional linear theory [47].

The instability evolution was visualized using the mass fraction isosurface (Sec. 5.2). In three dimensions two roll-ups formed, one corresponding to the spike roll-up (as in two dimensions) and one corresponding to the bubble roll-up. As the spike was compressed and the bubble expanded, the bubble roll-up was larger than the spike roll-up. The vorticity was visualized through the enstrophy isosurface showing the formation of a ring structure corresponding to the cores of the roll-ups. The WENO and VS simulations were in good agreement, with the WENO simulations showing additional complex structures in the cores.

The perturbation amplitudes from the WENO and VS methods were in excellent agreement for both initial conditions up to reshock (Sec. 5.3). The bubble and spikes amplitude were in good agreement at early times. At later times, the WENO bubble amplitude was smaller than the VS amplitude. The spike amplitude also showed agreement at early times, while at later times, the WENO spike amplitude was larger. This can also be explained by the same mechanism outlined for the two-dimensional simulations (Sec. 4.6). A comparison with the nonlinear Zhang-Sohn model [157] showed that the model agreed with the simulation data at early times and then underpredicted.

The investigation of reshock was also extended to three dimensions (Sec. 5.4) using the WENO method. In three dimensions, reshock produced a qualitative change in structures. In particular,

the enstrophy iso-surface showed that the vorticity was fragmented and formed small, short, tubular structures. This was in contrast to the two-dimensional vorticity, which formed strong cores. The mixing layer width from the simulations with different initial perturbation amplitudes were in excellent agreement, indicating that the width after reshock did not depend on the initial perturbation amplitude. A comparison with the predictions of reshock models showed that the Mikaelian model [101] was in best agreement with the amplitudes following reshock. In addition, the Mikaelian model was independent of the pre-shock amplitude.

Finally, the effects of Atwood number were investigated using the VS method (Sec. 5.5). A visualization of the density and vorticity field cross-sections illustrated the dynamics in three dimensions as a function of the Atwood number. The amplitudes from the simulations were compared to the predictions of the Zhang-Sohn model. At early times, the simulations and the models were in agreement. At late times, the models underpredicted.

This study is one of the few investigations of the single-mode instability in three dimensions.

6.5 Implications

The results presented here suggest that the VS method constitutes a valid numerical approach for investigating the late-time dynamics of the single-mode Richtmyer-Meshkov instability in two and three dimensions. This method offers an alternative to the more computationally expensive WENO simulations to determine the large-scale properties of the instability, including the shape of the roll-ups, provided that the Mach number is sufficiently low that compressibility effects are negligible.

The VS method constitutes an alternative to nonlinear amplitude growth models to accurately determine the perturbation, bubble, and spike amplitudes into the late nonlinear regime ($\tau > 4$). This is due to the fact that nonlinear models are based on Padé extensions of weakly-nonlinear expansions, which have a t^{-1} decay for the instability growth by construction. As shown in Peng, Zabusky, and Zhang [115], the late-time decay of the growth remains an open question, as vorticity coalesces into complex structures resulting in a decrease of the late-time decay. The VS method does not have such a priori scalings.

When compared to classical vortex methods developed for the evolution of a vortex sheet, the VS method resolves the questions of well-posedness and continued existence of the solution by thickening the sheet into a layer. The thickening is performed so that in the limit of small diffuse-interface thickness the evolution of a vortex sheet is recovered. This thickening also provides a physical lengthscale (corresponding to the diffuse-interface width) in contrast to other lengthscales such as the vortex blob core δ in the classical Lagrangian method, and the grid-spacing Δx in the vortex-in-cell method. In addition, the VS method is robust, so that the layer can be evolved to arbitrarily late times (provided that sufficient grid resolution is used to fully resolve the gradients).

Finally, the VS method was used here to investigate the large-scale bubble and spike features of the single-mode instability and to obtain accurate values for the perturbation, bubble, and spike amplitudes. However, the VS method contains additional information from the vorticity and density fields, which can be used to determine mixing rates, the spectrum of energy distribution, and other characteristic quantities [129]. In addition, only the single-mode instability was investigated here. However, complex multi-mode initial conditions can also be examined.

Bibliography

- [1] R. Abgrall, *How to prevent pressure oscillations in multicomponent flow calculations: a quasi-conservative approach*, J. Comput. Phys. **125** (1996), 150–160.
- [2] R. Abgrall and S. Karni, *Computations of compressible multifluids*, J. Comput. Phys **169** (2001), 594–623.
- [3] C. Anderson, *A vortex method for flows with slight density variations*, J. Comput. Phys. **61** (1985), 417–444.
- [4] D. Arnett, *The role of mixing in astrophysics*, Astrophys. J. Suppl. **127** (2000), 213–217.
- [5] W. D. Arnett, *Supernova theory and supernova 1987A*, Astrophys. J. **319** (1987), 136–142.
- [6] W. D. Arnett, B. A. Fryxell, and E. Müller, *Instabilities and nonradial motion in SN-1987A*, Astrophys. J. **341** (1989), L63–L66.
- [7] G. R. Baker and J. T. Beale, *Vortex blob methods applied to interfacial motion*, J. Comput. Phys. **196** (2004), 233–258.
- [8] G. R. Baker, D. I. Meiron, and S. A. Orszag, *Vortex simulations of the Rayleigh-Taylor instability*, Phys. Fluids **23** (1980), 1485–1490.
- [9] ———, *Generalized vortex methods for free-surface flow problems*, J. Fluid Mech. **123** (1982), 477–501.
- [10] ———, *Boundary integral methods for axisymmetric and three-dimensional Rayleigh-Taylor instability problems*, Physica D **12** (1984), 19–31.
- [11] G. R. Baker and M. J. Shelley, *On the connection between thin vortex layers and vortex sheets*, J. Fluid Mech. **215** (1990), 161–194.
- [12] D. Balsara and C.-W. Shu, *Monotonicity preserving weighted essentially non-oscillatory schemes with increasingly high order of accuracy*, J. Comput. Phys. **160** (2000), 405–452.
- [13] J. T. Beale and A. Majda, *High order accurate vortex methods with explicit velocity kernels*, J. Comput. Phys. **58** (1985), 188–208.

- [14] G. Birkhoff, *Taylor instability*, Tech. Report LA-1927, Los Alamos National Laboratory, 1956.
- [15] ———, *Helmholtz and Taylor instability*, Proc. Sympos. Appl. Math., Vol. XIII, American Mathematical Society, Providence, R.I., 1962, pp. 55–76.
- [16] ———, *Numerical fluid dynamics*, SIAM Rev. **25** (1983), 1–34.
- [17] M. Brouillette, *The Richtmyer-Meshkov instability*, Ann. Rev. Fluid Mech. **34** (2002), 445–468.
- [18] M. Brouillette and B. Sturtevant, *Growth induced by multiple shock waves normally incident on plane gaseous interfaces*, Physica D **37** (1989), 248–263.
- [19] ———, *Experiments on the Richtmyer-Meshkov instability: single-scale perturbations on a continuous interface*, J. Fluid Mech. **263** (1994), 271–292.
- [20] W. H. Cabot, O. Schilling, and Y. Zhou, *Influence of subgrid scales on resolvable turbulence and mixing in Rayleigh-Taylor flow*, Phys. Fluids **16** (2004), 495–508.
- [21] J. Casper and M. H. Carpenter, *Computational considerations for the simulation of shock-induced sound*, SIAM J. Sci. Comput. **22** (1998), 813–828.
- [22] A. A. Charakhch'yan, *Reshocking at the non-linear stage of Richtmyer-Meshkov instability*, Plasma Phys. Control. Fusion **43** (2001), 1169–1179.
- [23] A. J. Chorin and P. S. Bernard, *Discretization of a vortex sheet, with an example of roll-up*, J. Comput. Phys. **13** (1973), 423–429.
- [24] J. P. Christiansen, *Numerical simulation of hydrodynamics by method of point vortices*, J. Comput. Phys **13** (1973), 363–379.
- [25] T. J. Chung, *Computational Fluid Dynamics*, Cambridge University Press, New York, 2002.
- [26] P. Colella and P. R. Woodward, *The piecewise parabolic method (PPM) for gas-dynamical simulations*, J. Comput. Phys. **54** (1984), 174–201.
- [27] B. D. Collins and J. W. Jacobs, *PLIF flow visualization and measurements of the Richtmyer-Meshkov instability of an air/SF₆ interface*, J. Fluid Mech. **464** (2002), 113–136.
- [28] A. W. Cook and P. E. Dimotakis, *Transition stages of Rayleigh-Taylor instability between miscible fluids*, J. Fluid Mech. **443** (2001), 69–99, Corrigendum, J. Fluid Mech. **457** (2002), 410–411.
- [29] G.-H. Cottet and P. D. Koumoutsakos, *Vortex Methods: Theory and Practice*, Cambridge University Press, Cambridge, 2000.

- [30] W. S. Don, D. Gottlieb, and C.-W. Shu, *High order accurate simulations and physics of shock-induced turbulent mixing*, Contractor Report, Brown University (2004), 1–24.
- [31] R. P. Drake, *High-Energy-Density-Physics: From Inertial Fusion to Experimental Astrophysics*, Springer-Verlag, New York, 2006.
- [32] P. G. Drazin, *Introduction to Hydrodynamic Stability*, Cambridge Texts in Applied Mathematics, Cambridge University Press, Cambridge, 2002.
- [33] P. G. Drazin and W. H. Reid, *Hydrodynamic Stability*, second ed., Cambridge Mathematical Library, Cambridge University Press, Cambridge, 2004.
- [34] R. E. Duff, F. H. Harlow, and C. W. Hirt, *Effects of diffusion on interface instability between gases*, Phys. Fluids **5** (1962), 417–425.
- [35] J. S. Ely and G. R. Baker, *High-precision calculations of vortex sheet motion*, J. Comput. Phys. **111** (1994), 275–281.
- [36] B. Engquist and B. Sjögreen, *The convergence rate of finite difference schemes in the presence of shocks*, SIAM J. Numer. Anal. **35** (1998), 2464–2485.
- [37] S. W. Falk and W. D. Arnett, *A theoretical model for type II supernovae*, Astrophys. J. **180** (1973), L65–L68.
- [38] P. T. Fink and W. K. Soh, *New approach to roll-up calculations of vortex sheets*, Proc. Roy. Soc. London Ser. A **362** (1978), 195–209.
- [39] G. Fraley, *Rayleigh-Taylor stability for a normal shockwave-density discontinuity interaction*, Phys. Fluids **29** (1986), 376–386.
- [40] N. C. Freeman, *A theory of the stability of plane shock waves*, Proc. Roy. Soc. London. Ser. A. **228** (1955), 341–362.
- [41] S. K. Godunov, *A difference method for numerical calculation of discontinuous solutions of the equations of hydrodynamics*, Mat. Sb. **47 (89)** (1959), 271–306.
- [42] V. N. Goncharov, *Analytical model of nonlinear, single-mode, classical Rayleigh-Taylor instability at arbitrary Atwood numbers*, Phys. Rev. Lett. **88** (2002), 134501–1–134501–4.
- [43] S. Gottlieb, D. Gottlieb, and C.-W. Shu, *Recovering high-order accuracy in WENO computations of steady-state hyperbolic systems*, J. Sci. Comput. **28** (2006), 307–318.
- [44] J.-L. Guermond and L. Quartapelle, *Equivalence of \mathbf{u} - p and ζ - ψ formulations of the time-dependent Navier-Stokes equations*, Internat. J. Numer. Methods Fluids **18** (1994), 471–487.

- [45] F. H. Harlow, *Hydrodynamics problems involving large fluid distortions*, J. Assoc. Comput. Mach. **4** (1957), 137–142.
- [46] ———, *The particle-in-cell computing method in fluid dynamics*, Methods Comput. Phys. **3** (1964), 319–343.
- [47] D. J. Haroldsen and D. I. Meiron, *Numerical calculation of three-dimensional interfacial potential flows using the point vortex method*, SIAM J. Sci. Comput. **20** (1998), 648–683.
- [48] A. Harten, *High resolution schemes for hyperbolic conservation laws*, J. Comput. Phys. **49** (1983), 357–393.
- [49] A. Harten, B. Engquist, S. Osher, and S. R. Chakravarthy, *Uniformly high order accurate essentially non-oscillatory schemes, III*, J. Comput. Phys. **77** (1987), 231–303.
- [50] A. Harten and S. Osher, *Uniformly high-order accurate nonoscillatory schemes. I*, SIAM J. Numer. Anal. **24** (1987), 279–309.
- [51] J. F. Hawley and N. J. Zabusky, *Vortex paradigm for shock-accelerated density-stratified interfaces*, Phys. Rev. Lett. **63** (1989), 1241–1244.
- [52] J. Hecht, U. Alon, and D. Shvarts, *Potential flow models of Rayleigh-Taylor and Richtmyer-Meshkov bubble fronts*, Phys. Fluids **6** (1994), 4019–30.
- [53] H. von Helmholtz, *Über die integrale der hydromechanischen gleichung*, Crelles J. **55** (1858), 25.
- [54] ———, *On discontinuous movements of fluids*, Phil. Mag. **36** (1868), 337–346.
- [55] L. F. Henderson, *On the refraction of shock waves*, J. Fluid Mech. **198** (1989), 365–386.
- [56] G. J. Hendricks, *Two Mechanisms of Vorticity Generation in Combusting Flow Fields*, Ph.D. thesis, California Institute of Technology, 1986.
- [57] D. J. Hill, C. Pantano, and D. I. Pullin, *Large-eddy simulation and multiscale modelling of a Richtmyer-Meshkov instability with reshock*, J. Fluid Mech. **557** (2006), 29–61.
- [58] D. J. Hill and D. I. Pullin, *Hybrid tuned center-difference-WENO method for large eddy simulations in the presence of strong shocks*, J. Comput. Phys. **194** (2004), 435–450.
- [59] R. W. Hockney, *A fast direct solution of Poisson’s equation using Fourier analysis*, J. Assoc. Comput. Mach. **12** (1965), 95–113.
- [60] R. W. Hockney and J. W. Eastwood, *Computer Simulations Using Particles*, McGraw-Hill, New York, 1988.

- [61] A. Iserles, *A First Course in the Numerical Analysis of Differential Equations*, Cambridge Texts in Applied Mathematics, Cambridge University Press, Cambridge, 1996.
- [62] J. W. Jacobs and V. V. Krivets, *Experiments on the late-time development of single-mode Richtmyer-Meshkov instability*, Phys. Fluids **17** (2005), 034104–1–034105–10.
- [63] G.-S. Jiang and C.-W. Shu, *Efficient implementation of weighted ENO schemes*, J. Comput. Phys. **126** (1996), 202–228.
- [64] M. A. Jones and J. W. Jacobs, *A membraneless experiment for the study of Richtmyer-Meshkov instability of a shock-accelerated gas interface*, Phys. Fluids **9** (1997), 3078–3085.
- [65] S. Karni, *Multicomponent flow calculations by a consistent primitive algorithm*, J. Comput. Phys. **112** (1994), 31–43.
- [66] ———, *Hybrid multifluid algorithms*, SIAM J. Sci. Comput. **17** (1996), 1019–1039.
- [67] W. Kelvin, *Hydrokinetic solutions and observations*, Phil. Mag. **42** (1871), 362–377.
- [68] R. M. Kerr, *Simulation of Rayleigh-Taylor flows using vortex blobs*, J. Comput. Phys **76** (1988), 48–84.
- [69] A. D. Kotelnikov, J. Ray, and N. J. Zabusky, *Vortex morphologies on reaccelerated interfaces: Visualization, quantification and modeling of one- and two-mode compressible and incompressible environments*, Phys. Fluids **12** (2000), 3245–3264.
- [70] R. H. Kraichnan and D. Montgomery, *Two-dimensional turbulence*, Rep. Prog. Phys. **43** (1980), 547–619.
- [71] R. Krasny, *Desingularization of periodic vortex sheet roll-up*, J. Comput. Phys **65** (1986), 292–313.
- [72] ———, *A study of singularity formation in a vortex sheet by the point-vortex approximation*, J. Fluid Mech. **167** (1986), 65–93.
- [73] ———, *Computation of vortex sheet roll-up*, Vortex Methods, Lecture Notes in Math., vol. 1360, Springer-Verlag, Berlin, 1988, pp. 9–22.
- [74] C. B. Laney, *Computational Gasdynamics*, Cambridge University Press, New York, 1998.
- [75] M. Latini and O. Schilling, *Weighted Essentially Non-Oscillatory Simulations and Modeling of Complex Hydrodynamic Flows. Part 1. Regular Shock Refraction*, Tech. Report UCRL-TR-205132, Lawrence Livermore National Laboratory, 2004.

- [76] ———, *Weighted Essentially Non-Oscillatory Simulations and Modeling of Complex Hydrodynamic Flows. Part 2. Single-mode Richtmyer-Meshkov Instability with Reshock*, Tech. Report URCL-TR-212120, Lawrence Livermore National Laboratory, 2004.
- [77] M. Latini, O. Schilling, and W. S. Don, *Effects of WENO flux reconstruction order and spatial resolution on reshocked two-dimensional Richtmyer-Meshkov instability*, J. Comput. Phys. (2007), in press.
- [78] ———, *High-resolution simulations and modeling of reshocked single-mode Richtmyer-Meshkov instability: comparison to experimental data and to amplitude growth model predictions*, Phys. Fluids (2007), in press.
- [79] P. D. Lax, *Accuracy and resolution in the computation of solutions of linear and nonlinear equations*, Recent Advances in Numerical Analysis (C. De Boor and G. Golub, eds.), Academic Press, New York, 1978, pp. 293–298.
- [80] D. Layzer, *On the instability of superposed fluids in a gravitational field*, Astrophys. J. **122** (1955), 1–12.
- [81] A. Leonard, *Vortex methods for flow simulation*, J. Comput. Phys. **37** (1980), 289–335.
- [82] R. J. LeVeque, *Numerical Methods for Conservation Laws*, second ed., Lectures in Mathematics ETH Zürich, Birkhäuser Verlag, Basel, 1992.
- [83] ———, *Finite Volume Methods for Hyperbolic Problems*, Cambridge Texts in Applied Mathematics, Cambridge University Press, New York, 2002.
- [84] X. L. Li and Q. Zhang, *A comparative numerical analysis of the Richtmyer-Meshkov instability with nonlinear analysis in two and three dimensions*, Phys. Fluids **9** (1997), 3069–3077.
- [85] J. D. Lindl, *Development of the indirect-drive approach to inertial confinement fusion and the target physics basis for ignition and gain*, Phys. Plasmas **2** (1995), 3933–4024.
- [86] ———, *Inertial Confinement Fusion: The Quest for Ignition and Energy Gain Using Indirect Drive*, AIP Press, New York, 1998.
- [87] P. J. Linstrom and W. G. Mallard, *NIST Chemistry WebBook*, NIST Standard Reference Database, no. 69, National Institute of Standards and Technology, Gaithersburg, MD, 2005, <http://webbook.nist.gov>.
- [88] X.-D. Liu, S. Osher, and T. Chan, *Weighted essentially non-oscillatory schemes*, J. Comput. Phys. **115** (1994), 200–212.

- [89] A. Majda and S. Osher, *Propagation of error into regions of smoothness for accurate difference approximations to hyperbolic equations*, Comm. Pure Appl. Math. **30** (1977), 671–705.
- [90] A. Marquina and P. Mulet, *A flux-split algorithm applied to conservative models for multicomponent compressible flows*, J. Comput. Phys **185** (2003), 120–138.
- [91] C. Matsuoka, K. Nishihara, and Y. Fukuda, *Nonlinear evolution of an interface in the Richtmyer-Meshkov instability*, Phys. Rev. E **67** (2003), 036301–1–036301–14.
- [92] D. I. Meiron, G. R. Baker, and S. A. Orszag, *Analytic structure of vortex sheet dynamics. Part 1. Kelvin-Helmholtz instability*, J. Fluid Mech. **114** (1982), 283–298.
- [93] D. I. Meiron and M. Meloon, *Richtmyer-Meshkov instability in compressible stratified fluids*, Proceedings of the 6th International Workshop on the Physics of Compressible Turbulence and Mixing (G. Jourdan and L. Hovas, eds.), Institut Universitaire Thermiques Industriels, Marseille, France, 1997, pp. 337–342.
- [94] M. R. Meloon, *Models of Richtmyer-Meshkov Instability in Continuously Stratified Fluids*, Ph.D. thesis, California Institute of Technology, 1998.
- [95] R. Menikoff and C. Zemach, *Rayleigh-Taylor instability and the use of conformal maps for ideal fluid flow*, J. Comput. Phys **51** (1983), 28–64.
- [96] E. E. Meshkov, *Instability of the interface of two gases accelerated by a shock wave*, Sov. Fluid Dyn. **4** (1969), 101–108.
- [97] K. A. Meyer and P. J. Blewett, *Numerical investigation of the stability of a shock accelerated interface between two fluids*, Phys. Fluids **15** (1972), 753–759.
- [98] K. O. Mikaelian, *Normal-modes and symmetries of the Rayleigh-Taylor instability in stratified fluids*, Phys. Rev. Lett. **48** (1982), 1365–1368.
- [99] ———, *Rayleigh-Taylor instabilities in stratified fluids*, Phys. Rev. A **26** (1982), 2140–2158.
- [100] ———, *Approximate treatment of density gradients in Rayleigh-Taylor instabilities*, Phys. Rev. A **26** (1986), 1216–1222.
- [101] ———, *Turbulent mixing generated by Rayleigh-Taylor and Richtmyer-Meshkov instabilities*, Physica D **36** (1989), 343–357.
- [102] ———, *Density gradient stabilization of the Richtmyer-Meshkov instability*, Phys. Fluids A **3** (1991), 2638–2643.
- [103] ———, *Growth rate of the Richtmyer-Meshkov instability at shocked interfaces*, Phys. Rev. Lett. **71** (1993), 2903–2906.

- [104] ———, *Freeze-out and the effect of compressibility in the Richtmyer-Meshkov instability*, Phys. Fluids **6** (1994), 356–368.
- [105] ———, *Analytic approach to nonlinear Rayleigh-Taylor and Richtmyer-Meshkov instabilities*, Phys. Rev. Lett. **80** (1998), 508–511.
- [106] ———, *Explicit expressions for the single-mode Rayleigh-Taylor and Richtmyer-Meshkov instabilities at arbitrary Atwood numbers*, Phys. Rev. E **67** (2003), 026319–1–026319–7.
- [107] A. R. Miles, B. Blue, M. J. Edwards, J. A. Greenough, J. F. Hansen, and H. F. Robey, *Transition to turbulence and effect of initial conditions on three-dimensional compressible mixing in planar blast-wave-driven systems*, Phys. Plasmas **12** (2005), 056317–1–056317–10.
- [108] M. Mock and P. Lax, *The computation of discontinuous solutions of linear hyperbolic equations*, Comm. Pure Appl. Math. **31** (1978), 423–430.
- [109] J. J. Monaghan, *Extrapolating B-splines for interpolation*, J. Comput. Phys. **60** (1985), 253–262.
- [110] D. W. Moore, *Numerical study of roll-up of a finite vortex sheet*, J. Fluid Mech. **63** (1974), 225–235.
- [111] ———, *The spontaneous appearance of a singularity in the shape of an evolving vortex sheet*, Proc. Roy. Soc. London Ser. A **365** (1979), 105–119.
- [112] C. E. Niederhaus, *Experiments on the Richtmyer-Meshkov Instability of Incompressible Fluids*, Ph.D. thesis, University of Arizona, 2000.
- [113] C. E. Niederhaus and J. W. Jacobs, *Experimental study of the Richtmyer-Meshkov instability of incompressible fluids*, J. Fluid Mech. **485** (2003), 243–277.
- [114] Sadot O., L. Erez, U. Alon, D. Oron, and L. A. Levin, *Study of nonlinear evolution of single-mode and two bubble interaction under Richtmyer-Meshkov instability*, Phys. Rev. Lett. **80** (1998), 1654–1657.
- [115] G. Peng, N. J. Zabusky, and S. Zhang, *Vortex-accelerated secondary baroclinic vorticity deposition and late-intermediate time dynamics of a two-dimensional Richtmyer-Meshkov interface*, Phys. Fluids **15** (2003), 3730–3744.
- [116] C. S. Peskin, *Numerical-analysis of blood-flow in heart*, J. Comput. Phys **25** (1977), 220–252.
- [117] R. Peyret, *Spectral Methods for Incompressible Viscous Flow*, Applied Mathematical Sciences, vol. 148, Springer-Verlag, New York, 2002.

- [118] J. J. Quirk and S. Karni, *On the dynamics of a shock-bubble interaction*, J. Fluid Mech. **318** (1996), 129–163.
- [119] J. W. S. Rayleigh, *Investigation of the character of the equilibrium of an incompressible heavy fluid of variable density*, Proc. Roy. Soc. London **14** (1883), 170–177.
- [120] K. I. Read, *Experimental investigation of turbulent mixing by Rayleigh-Taylor instability*, Physica D **12** (1984), 45–58.
- [121] R. D. Richtmyer, *Taylor instability in shock acceleration of compressible fluids*, Comm. Pure Appl. Math. **8** (1960), 297–319.
- [122] L. Rosenhead, *The point vortex approximation of a vortex sheet*, Proc. Roy. Soc. London Ser. A **134** (1932), 170–192.
- [123] P. G. Saffman, *Vortex Dynamics*, Cambridge University Press, New York, 1992.
- [124] P. G. Saffman and G. R. Baker, *Vortex interactions*, Ann. Rev. Fluid Mech. **11** (1979), 95–121.
- [125] P. G. Saffman and D. I. Meiron, *Kinetic energy generated by the incompressible Richtmyer-Meshkov instability in a continuously stratified fluid*, Phys. Fluids A **1** (1989), 1767–1771.
- [126] R. Samtaney and D. I. Pullin, *On initial-value and self-similar solutions of the compressible Euler equations*, Phys. Fluids **8** (1996), 2650–2655.
- [127] R. Samtaney and N. J. Zabusky, *On shock polar analysis and analytical expressions for vorticity deposition in shock-accelerated density-stratified interfaces*, Phys. Fluids **5** (1993), 1285–1287.
- [128] ———, *Circulation deposition on shock-accelerated planar and curved density stratified interfaces: models and scaling laws*, J. Fluid Mech. **269** (1994), 45–78.
- [129] O. Schilling, M. Latini, and W. S. Don, *Physics of reshock and mixing in single-mode Richtmyer-Meshkov instability*, Phys. Rev. E (2007), in preparation.
- [130] I. J. Schoenberg, *Cardinal Spline Interpolation*, Society for Industrial and Applied Mathematics (SIAM), Philadelphia, 1973, Conference Board of the Mathematical Sciences Regional Conference Series in Applied Mathematics, No. 12.
- [131] J. Shi, Y.-T. Zhang, and C.-W. Shu, *Resolution of high order WENO schemes for complicated flow structures*, J. Comput. Phys **186** (2003), 690–696.
- [132] C.-W. Shu, *Essentially non-oscillatory and weighted essentially non-oscillatory schemes for hyperbolic conservation laws*, Advanced numerical approximation of nonlinear hyperbolic equations (Cetraro, 1997), Lecture Notes in Math., vol. 1697, Springer, Berlin, 1998, pp. 325–432.

- [133] C.-W Shu and S. Osher, *Efficient implementation of essentially nonoscillatory shock-capturing schemes*, J. Comput. Phys. **77** (1988), 439–471.
- [134] S.-I. Sohn, *Simple potential-flow model of Rayleigh-Taylor and Richtmyer-Meshkov instabilities for all density ratios*, Phys. Rev. E **67** (2003), 026301–1–026301–5.
- [135] ———, *Density dependence of a Zuffria-type model for Rayleigh-Taylor bubble fronts*, Phys. Rev. E **70** (2004), 045301–1–045301–4.
- [136] ———, *Vortex model and simulation for Rayleigh-Taylor and Richtmyer-Meshkov instabilities*, Phys. Rev. E **69** (2004), 036703–1–036703–11.
- [137] S.-I. Sohn and Q. Zhang, *Late time behavior of bubbles at unstable interfaces in two dimensions*, Phys. Fluids **13** (2001), 3493–3495.
- [138] A. Suresh and H. T. Huynh, *Accurate monotonicity-preserving schemes with Runge-Kutta time stepping*, J. Comput. Phys. **136** (1997), 83–99.
- [139] G. I. Taylor, *The instability of liquid surfaces when accelerated in a direction perpendicular to their planes*, Proc. R. Soc. Lond. A Mat. **201** (1950), 192–196.
- [140] N. Themelis, *Transport and Chemical Rate Phenomena*, Taylor and Francis, New York, 1995.
- [141] G. Tryggvason, *Numerical simulations of the Rayleigh-Taylor instability*, J. Comput. Phys. **75** (1988), 253–282.
- [142] ———, *Simulations of vortex sheet roll-up by vortex methods*, J. Comput. Phys **80** (1989), 1–16.
- [143] B. Van Leer, *Towards the ultimate conservative difference scheme IV*, J. Comput. Phys. **23** (1977), 276–299.
- [144] ———, *Towards the ultimate conservative difference scheme V*, J. Comput. Phys. **32** (1979), 101–136.
- [145] M. Vandenboomgaerde, S. Gauthier, and C. Mügler, *Nonlinear regime of a multimode Richtmyer-Meshkov instability: a simplified perturbation theory*, Phys. Fluids **14** (2002), 1111–1122.
- [146] M. Vandenboomgaerde, C. Mügler, and S. Gauthier, *Impulsive model for the Richtmyer-Meshkov instability*, Phys. Rev. E **58** (1998), 1874–1882.
- [147] A. L. Velikovich, P. L. Dahlburg, A. J. Schmitt, J. H. Gardner, L. Phillips, F. L. Cochran, Y. K. Chong, G. Dimonte, and N. Metzler, *Richtmyer-Meshkov-like instabilities and early-time perturbation growth in laser targets and Z-pinch loads*, Phys. Plasmas **7** (2000), 1662–1671.

- [148] V. Wheatley, *On the Richtmyer-Meshkov Instability in Magnetohydrodynamics*, Ph.D. thesis, California Institute of Technology, 2005.
- [149] V. Wheatley, D. I. Pullin, and R. Samtaney, *Stability of an impulsively accelerated density interface in magnetohydrodynamics*, Phys. Rev. Lett. **95** (2005), 125002–1–125002–4.
- [150] J. G. Wouchuk and K. Nishihara, *Linear perturbation growth at a shocked interface*, Phys. Plasmas **3** (1996), 3761–3776.
- [151] ———, *Asymptotic growth in the linear Richtmyer-Meshkov instability*, Phys. Plasmas **4** (1997), 1028–1038.
- [152] J. Yang, T. Kubota, and Zukoski E. E., *Applications of shock-induced mixing to supersonic combustion*, AIAA J. **31** (1993), 854–862.
- [153] D. L. Youngs, *Numerical simulation of turbulent mixing by Rayleigh-Taylor instability*, Physica D **12** (1984), 32–44.
- [154] N. J. Zabusky, *Vortex paradigm for accelerated inhomogeneous flows: Visiometrics for the Rayleigh-Taylor and Richtmyer-Meshkov environments*, Ann. Rev. Fluid Mech. **31** (1999), 495–536.
- [155] Q. Zhang, *Analytical solution of Layzer-type approach to unstable interfacial fluid mixing*, Phys. Rev. Lett. **81** (1998), 3391–3394.
- [156] Q. Zhang and S.-I. Sohn, *Non-linear theory of unstable fluid mixing driven by shock wave*, Phys. Fluids **9** (1997), 1106–1124.
- [157] ———, *Quantitative theory of Richtmyer-Meshkov instability in three dimensions*, Z. Angew. Math. Phys. **50** (1999), 1–46.
- [158] J. A. Zufria, *Bubble competition in Rayleigh-Taylor instability*, Phys. Fluids **31** (1988), 440–446.
- [159] ———, *Vortex-in-cell simulation of bubble competition in a Rayleigh-Taylor instability*, Phys. Fluids **31** (1988), 3199–3212.
- [160] ———, *Linear analysis of the vortex-in-cell algorithm applied to Rayleigh-Taylor instability*, J. Comput. Phys. **80** (1989), 387–402.